Journal of
Mechanics of
Materials and Structures

msp

JOURNAL OF MECHANICS OF MATERIALS AND STRUCTURES

msp.org/jomms

Founded by Charles R. Steele and Marie-Louise Steele

Cover photo: Ev Shafrir

See msp.org/jomms for submission guidelines.
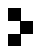
msp

THE ROLE OF RHEOLOGY IN MODELLING ELASTIC WAVES WITH GAS BUBBLES IN GRANULAR FLUID-SATURATED MEDIA

ADHAM A. ALI AND DMITRY V. STRUNIN

Elastic waves in fluid-saturated granular media depend on the rheology which includes elements representing the fluid and, if necessary, gas bubbles. We investigated the effect of different rheological schemes, including and excluding the bubbles, on the linear Frenkel–Biot waves of P1 type. For the wave with the bubbles the scheme consists of three segments representing the solid continuum, fluid continuum, and a bubble surrounded by the fluid. We derived the Nikolaevskiy-type equations describing the velocity of the solid matrix in the moving reference system. The equations are linearized to yield the decay rate λ as a function of the wave number k. We compared the $\lambda(k)$-dependence for the cases with and without the bubbles, using typical values of the input mechanical parameters. For the both cases, the $\lambda(k)$-curve lies entirely below zero, which is in line with the notion of the elastic wave being an essentially passive system. We found that the increase of the radius of the bubbles leads to faster decay, while the increase in the number of the bubbles leads to slower decay of the elastic wave.

A list of symbols can be found on page 16.

1. Introduction

The problem of wave propagation in porous media is of interest in various fields of science and engineering. Over the recent years, researchers studied diverse phenomena of this type in large-scale earthquakes, soil mechanics, acoustics, earthquake engineering, and many other disciplines. The fundamentals of the theory of the wave propagation in porous elastic solids can be found in [Biot 1956a; 1956b] or in a more recent review [Frenkel 2005]. Biot [1956a; 1956b] generalized the first principles of linear elasticity and today, most studies in acoustics, geophysical, and geological mechanics rely on his theory. Biot [1962a; 1962b] also deduced the dynamical equations for the wave propagation in poroelastic media. According to Frenkel–Biot's theory, there are two types of longitudinal waves propagating in a saturated porous medium. The wave of the first type is fast and weakly damped (P1-wave), whereas the wave of the second type is slow and strongly damped (P2-wave). Yang et al. [2014] showed that the dispersion of velocity and attenuation of the P1-wave are greatly affected by the viscoelasticity of the medium.

Liu et al. [1976] demonstrated that rheology based on the scheme often referred to as Generalized Standard Linear Solid (GSLS) helps to better describe measured characteristics of seismic waves in earth continua. The importance of complex multicomponent GSLS was acknowledged by Bohlen [2002] who employed the rheology with many Maxwell bodies connected in parallel. Nikolaevskiy [1989] used complex stress-strain relations in a fluid-saturated grain, where the solid matrix and fluid are in contact.

Keywords: Frenkel–Biot's waves, bubbles, rheology, porous media.

This resulted, in the final analysis, in the nonlinear higher-order partial differential equation of the form

$$\frac{\partial v}{\partial t} + v\frac{\partial v}{\partial x} = \sum_{p=1}^{5} \varepsilon^{p-1} A_{p+1} \frac{\partial^{p+1} v}{\partial x^{p+1}}, \qquad (1)$$

where v is the particle velocity of the solid matrix, ε is the small parameter reflecting slow evolution of the wave (this is discussed below), and A_{p+1} are the coefficients linked to mechanical parameters of the system. From the standpoint of wave dynamics, the even derivatives in (1) are responsible for the dissipation and odd derivatives for the dispersion effects. Equation (1) assumes the form of the Korteweg–de Vries–Burgers equation if the index p goes from just 1 and 2. But with the range of p going further as shown, the equation manifests an extension of this classical equation to include high-order spatial derivatives. As explained below, this extension results from the complex rheology of the system.

Experimental evidence indicates that the presence of gas bubbles changes the characteristics of the wave [Dunin and Nikolaevskiy 2005; Van Wijngaarden 1968; Anderson 1980]. Typically, in rocks saturated with fluids, the P1-wave is the only observable wave [Nikolaevskiy 2008]. However, the presence of gas, even in small proportion, can affect the wave type [Nikolaevskiy and Strunin 2012], so that the P2-wave may also be visible. Dunin et al. [2006] studied the effect of gas bubbles on linear P1- and P2-waves, and derived the dispersion relation connecting the frequency and wave number. Of special interest was the transformation of the wave type due to the bubbles. They found that the transformation was due to the change in the motion of the liquid in the porous space. Instead of the overflow between the pores incurring large Darcy friction, which is characteristic of the P2-waves, the liquid may be displaced into the volume released when a bubble is compressed. In this case the oscillations of the porous matrix and of the bubbles occur in phase and, as a result, the decay of the P2-wave diminishes due to the reduction in the Darcy friction. As far as the rheology is concerned, Dunin et al. [2006] used a rather simple stress-strain relation, $\sigma = Ee$, in standard notations. Various aspects of the wave propagation in multifluid and bubbly flows were studied in [Papageorgiou and Chapman 2015; Tisato et al. 2015; Brunner and Spetzler 2001; Collier et al. 2006]. For example, Collier et al. [2006] explored the influence of the gas bubbles on attenuation in volcanic magma, where the bubbles grow not only due to gas expansion, but also due to the exsolution of volatiles, such as water, from the melt into the bubbles. In our present study we do not consider such kind of thermodynamic disequilibrium conditions.

The rheological scheme used in [Nikolaevskiy 1989], despite containing several Maxwell bodies, did not include an element representing gas bubble. Nikolaevskiy and Strunin [2012] pointed out the place in this scheme which the bubble element should occupy; see Figure 1. In the present work we aim to include the bubble element into the rheological scheme and then derive and analyze the equation of the type (1), where the coefficients A_p too depend on the bubble-related parameters. The resulting equation will describe the decay (or attenuation) of the freely propagating seismic wave. We will investigate the influence of the bubble-related parameters, including their radius and concentration, on the decay rate.

During its propagation the seismic wave decays due to the viscous friction both within individual phases, e.g., fluid, and between the phases. The decay may be described in terms of the decay rate in time as in [Nikolaevskiy 1989], or decay rate in space via the attenuation factor as in [Dunin et al. 2006]. These descriptions are closely connected and just correspond to different realizations of the wave. To illustrate this, let us represent Fourier modes of the linear wave as $\exp(i\xi_1)$, where $\xi_1 = wt + kx$, w is
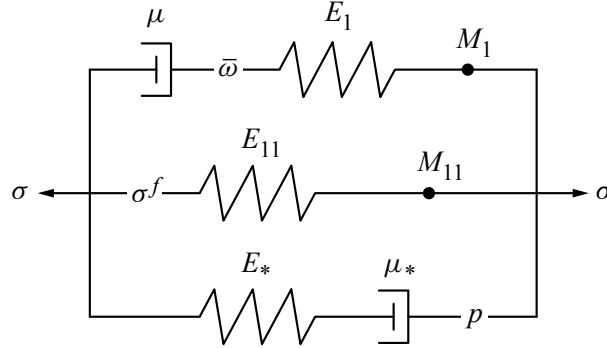
Figure 1. Rheological scheme with the branch ϖ corresponding to a bubble [Niko-laevskiy and Strunin 2012].

the frequency, and k the wave number connected with each other via the dispersion relation. Writing this relation in the form $w = w(k)$ with k being real-valued, we can find the corresponding complex-valued w. Its imaginary part determines how fast the wave decays in time. Physically this situation corresponds to the wave in an unbounded medium, which decays as time goes. Alternatively, one may write down the dispersion relation as $k = k(w)$ and consider the real-valued frequency w as the argument, whereas the wave number k becomes complex-valued. Imaginary part of k governs the decay of the wave in space. From physical standpoint this realization can be associated with the wave which propagates, say, from the surface into underground. The decay of such a wave against the distance is characterized by the attenuation factor.

Importantly, the dynamics of the fluid in porous media may exhibit boundary layers. They form when the frequency of the seismic wave is relatively high. This contrasts the low-frequency waves where the viscous forces dominate throughout the fluid volume so that inertial effects may be neglected. However, at high frequencies the inertial effects dominate in the bulk of the fluid, while the viscous friction concentrates within narrow boundary layers near solid walls due to the no-slip conditions. Allowing for the boundary layers in the analysis significantly affects the frequency dependence of the attenuation of the wave. Namely the low- and high-frequency branches of the attenuation curve become asymmetric. Masson et al. [2006] confirmed this effect by numerical computations of the governing mechanics equations. The model that we use in our present paper is one-dimensional; therefore, it disregards the boundary layers.

In our study of the wave decay we choose to analyze the decay in time, that is, the $w = w(k)$ form of the dispersion relation. We will execute a procedure similar to [Nikolaevskiy 2008], where one-dimensional (x-dependent) dynamics are considered, and all the functions of interest are decomposed into series in small parameter ε characterizing slow evolution of the wave in space and time. Let us denote the phase velocity of the wave by c. Introducing the running variable ξ and using ε to scale the distance x and time t as

$$\xi = \varepsilon(x - ct), \quad \tau = \left(\tfrac{1}{2}\varepsilon^2\right)t, \tag{2}$$

we seek the velocity of the solid matrix in the form

$$v = \varepsilon v_1 + \varepsilon^2 v_2 + \cdots$$

We will show, in line with Nikolaevskiy [2008], that the complex rheology generates higher-order time derivatives [Nikolaevskiy 1989]. They, in turn, translate into high-order derivatives in ξ in the resulting equation (1) because, using (2),

$$\frac{\partial}{\partial t} = \left(\tfrac{1}{2}\varepsilon^2\right)\frac{\partial}{\partial \tau} - \varepsilon c\frac{\partial}{\partial \xi} \approx -\varepsilon c\frac{\partial}{\partial \xi},$$

where the quadratic term in the small parameter ε is neglected in comparison with the linear term. Once derived, (1) gives the dispersion relation, which is the main point of interest in this paper. Our focus is on the dissipation controlled by the even x-derivatives. Therefore, we will study a truncated form of (1):

$$\frac{\partial v}{\partial t} + v\frac{\partial v}{\partial \xi} = A_2\frac{\partial^2 v}{\partial \xi^2} + \varepsilon^2 A_4\frac{\partial^4 v}{\partial \xi^4} + \varepsilon^4 A_6\frac{\partial^6 v}{\partial \xi^6}. \tag{3}$$

Equation (3) can be complemented by spatially periodic boundary conditions, leading to a spatially periodic solution. Substituting the Fourier modes of the solution, $v \sim \exp(\lambda t + ikx)$, into (3) gives

$$\lambda = -A_2 k^2 + \varepsilon^2 A_4 k^4 - \varepsilon^4 A_6 k^6, \tag{4}$$

with k being the wave number associated with the scaled length ξ. When analyzing (4) we remember that k is not allowed to be too large, otherwise the assumption of the slow variation of the wave in space will be violated. As we noted, the slowness is facilitated by the smallness of ε. Therefore, in (4) the term $\varepsilon^2 A_4 k^4$ should be treated just as a correction to the leading term $A_2 k^2$, and the following term $\varepsilon^4 A_6 k^6$ as a correction to the term $\varepsilon^2 A_4 k^4$. Thus, the value of λ remains negative at all plausible values of the mechanical parameters of the system (such as elastic moduli and viscosities). This reflects the essentially dissipative nature of the seismic wave, or, in other words, the impossibility of self-excitation of motion. In view of the crucial presence of the small parameter ε in (3) and (4) we revise our earlier attempt [Strunin 2014] to guarantee this important property of the freely propagating seismic wave in the model. In [Strunin 2014] a popular form of (3) was considered where the small parameter ε was omitted. It was reasoned that the mechanical parameters, of which A_4 and A_6 are composed, should therefore assume special limited values, in order to guarantee that $\lambda < 0$. However, negativity of λ is simply ensured by the smallness of ε, which is the essential part of (3) as explicitly shown.

2. Basic equations of one-dimensional dynamics

2.1. *Conservation of mass and momentum.* For a one-dimensional case the momentum and mass balance equations are [Nikolaevskiy 1990]

$$\frac{\partial}{\partial t}(1-m)\rho^{(s)}v + \frac{\partial}{\partial x}(1-m)\rho^{(s)}vv = \frac{\partial}{\partial x}\sigma^{(ef)} - (1-m)\frac{\partial p}{\partial x} - I,$$

$$\frac{\partial}{\partial t}m\rho^{(f)}u + \frac{\partial}{\partial x}m\rho^{(f)}uu = -m\frac{\partial p}{\partial x} + I,$$

$$\frac{\partial}{\partial t}(1-m)\rho^{(s)} + \frac{\partial}{\partial x}(1-m)\rho^{(s)}v = 0, \tag{5}$$

$$\frac{\partial}{\partial t}m\rho^{(f)} + \frac{\partial}{\partial x}m\rho^{(f)}u = 0,$$

where the subscripts s and f label the solid and gas-liquid mixture respectively, ρ, v, and u are the corresponding densities and mass velocities, m is the porosity, $\sigma^{(ef)}$ is the effective Terzaghi stress, p is the pore pressure, and I is the interfacial viscous force approximated by

$$I = \delta m(v - u), \quad \delta = \frac{\mu^{(f)}m}{\ell},$$

where $\mu^{(f)}$ is the gas-liquid mixture viscosity and ℓ is the intrinsic permeability.

2.2. *Dynamics of bubbles.*
The equation of the dynamics of a bubble [Dunin et al. 2006] has the form

$$R\frac{\partial^2}{\partial t^2}R + \frac{3}{2}\left(\frac{\partial}{\partial t}R\right)^2 + \frac{4\mu}{\rho^{(L)}}\left(\frac{1}{R} + \frac{m}{4\ell}R\right)\frac{\partial}{\partial t}R = (p_g - p)/\rho^{(L)}, \tag{6}$$

where R is the bubble radius, p is the pressure in the liquid, $p_g = p_0(R_0/R)^\chi$ is the gas pressure inside the bubble (here $\chi = 3\zeta$, and ζ is the adiabatic exponent), $\rho^{(L)}$ is the density of the liquid without the bubbles, and μ is the viscosity of the liquid without the bubbles. The density equations for the solid and liquid without gas are

$$\rho^{(s)} = \rho_0^{(s)}(1 - \beta^{(s)}\sigma) = \rho_0^{(s)}\left[1 + \beta^{(s)}p - \frac{\beta^{(s)}\sigma^{(ef)}}{1-m}\right] \approx \rho_0^{(s)}[1 + \beta^{(s)}p - \beta^{(s)}\sigma^{(ef)}], \tag{7}$$

$$\rho^{(L)} = \rho_0^{(L)}(1 + \beta^{(L)}p). \tag{8}$$

The mean density of the gas-liquid mixture is

$$\rho^{(f)} = (1 - \phi)\rho^{(L)} + \phi\rho^{(g)}, \tag{9}$$

where

$$\phi = \frac{4\pi}{3}R^3 n_0.$$

Here σ is the true stress, ϕ is the volume gas content and n_0 is the number density of the bubbles per unit volume. In (9) we can neglect the density of the gas $\rho^{(g)}$ due to the low gas content. The change in ϕ is due to the change in the bubble radius R. Then (9) becomes

$$\rho^{(f)} = \rho_0^{(L)}(1 + \beta^{(L)}p)\left(1 - \frac{4\pi}{3}R_0^3 n_0\right). \tag{10}$$

Similarly to [Dunin et al. 2006] we also assume that the pore pressure p is equal to the pressure in the liquid far from the bubble.

2.3. *Stress-strain relation.*
In this section we derive the stress-strain relation for the viscoelastic medium based on the rheological Maxwell–Voigt model, which includes the gas bubble. The model includes two friction elements with viscosities μ_1 and μ_2, three elastic springs with the elastic moduli E_1, E_2, and E_3, and three oscillating masses M_1, M_2, and M_3. The total stress in denoted σ. We also denote the displacements of the elements of the model by e with respective subscripts as shown in Figure 2. Now we write the second Newton's law for the elements and the kinematic relations:

$$M_1\frac{d^2e_1}{dt^2} + M_2\frac{d^2e_2}{dt^2} = \sigma - E_1e_1 - E_2e_2, \qquad e = e_2 = e_1 + e_3 + e_4 + e_5,$$

$$M_3\frac{d^2e_3}{dt^2} = E_1e_1 - E_3e_3, \qquad E_3e_3 = \mu_2\frac{de_4}{dt} = \mu_1\frac{de_5}{dt}. \tag{11}$$
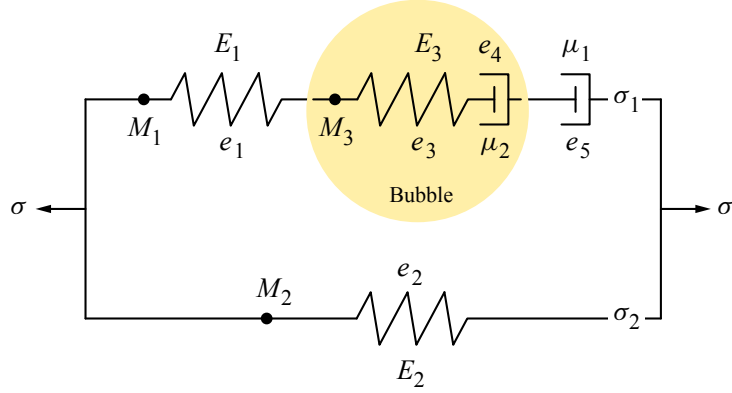
Figure 2. Rheological scheme including a gas bubble.

Equations (11) generate the following relation between the stress and strain:

$$\left[E_1 E_3\left(\frac{1}{\mu_1}+\frac{1}{\mu_2}\right)\right]\sigma + (E_3+E_1)\frac{d\sigma}{dt}+M_3\frac{d^3\sigma}{dt^3}$$

$$= \left[E_1 E_2 E_3\left(\frac{1}{\mu_1}+\frac{1}{\mu_2}\right)\right]e + [(E_2+E_1)E_3+E_1 E_2]\frac{de}{dt}+\left[E_1 E_3 M_2\left(\frac{1}{\mu_1}+\frac{1}{\mu_2}\right)\right]\frac{d^2 e}{dt^2}$$

$$+ [((E_2+E_1)M_3+(E_3+E_1)M_2)+E_3 M_1]\frac{d^3 e}{dt^3}+[(M_2+M_1)M_3]\frac{d^5 e}{dt^5}. \quad (12)$$

Generalizing (12) using a similar approach to [Nikolaevskiy 2008], we get

$$\sigma^{(ef)}+\eta\sum_{q=1,3}b_q\frac{D^q\sigma^{(ef)}}{Dt^q}=E_2 e+\beta^{(s)}k_b p+\eta\sum_{q=1,2,3,5}a_q\frac{D^q e}{Dt^q}, \quad (13)$$

where $\sigma^{(ef)}$ is the effective stress, $\eta=[E_1 E_3(1/\mu_1+1/\mu_2)]^{-1}$, k_b is the bulk elastic module of the porous matrix, and the coefficients a_q and b_q are expressed as

$$a_1=[(E_2+E_1)E_3+E_1 E_2], \quad a_2=M_2, \quad a_3=[(E_2+E_1)M_3+(E_3+E_1)M_2+E_3 M_1],$$
$$a_5=[(M_2+M_1)M_3], \quad b_1=(E_3+E_1), \quad b_3=M_3.$$

Finally, we add the closing relation between the deformation e and the velocity v of the solid:

$$\frac{De}{Dt}\equiv\frac{\partial e}{\partial t}+v\frac{\partial e}{\partial x}=\frac{\partial v}{\partial x}. \quad (14)$$

3. Elastic waves in saturated media including gas bubbles

Following the approach of Nikolaevskiy [2008], we consider the P1-wave in a porous media under the full saturation. Accordingly we assume that the mass velocities v and u have the same sign:

$$v=u+O(\varepsilon v), \quad (15)$$

where ε is the small parameter. The Darcy force has the order as shown:

$$I = \varepsilon^\gamma \delta m (v - u) = \varepsilon^\gamma \delta m v, \quad \delta = m\mu/k = O(1). \tag{16}$$

Describing a weakly nonlinear wave we use the running coordinate system with simultaneous scale change:

$$\xi = \varepsilon(x - ct), \quad \tau = \tfrac{1}{2}\varepsilon^2 t, \quad \frac{\partial}{\partial x} = \varepsilon \frac{\partial}{\partial \xi}, \quad \frac{\partial}{\partial t} = \varepsilon\left(\tfrac{1}{2}\varepsilon \frac{\partial}{\partial \tau} - c\frac{\partial}{\partial \xi}\right). \tag{17}$$

Thus, the constitutive law (13) transforms into the form

$$\sigma^{(ef)} + \eta \sum_{q=1,3} b_q \varepsilon^q \left(\tfrac{1}{2}\varepsilon \frac{\partial}{\partial \tau} + (v - c)\frac{\partial}{\partial \xi}\right)^q \sigma^{(ef)}$$

$$= E_2 e + \beta^{(s)} k_b p + \eta \sum_{q=1,2,3,5} a_q \varepsilon^q \left(\tfrac{1}{2}\varepsilon \frac{\partial}{\partial \tau} + (v - c)\frac{\partial}{\partial \xi}\right)^q e. \tag{18}$$

Now, we seek the unknown functions as power series:

$$\begin{aligned}
v &= \varepsilon v_1 + \varepsilon^2 v_2 + \cdots, & u &= \varepsilon u_1 + \varepsilon^2 u_2 + \cdots, \\
\sigma^{ef} &= \sigma_0^{(ef)} + \varepsilon \sigma_1^{(ef)} + \varepsilon^2 \sigma_2^{(ef)} + \cdots, & p &= p_0 + \varepsilon p_1 + \varepsilon^2 p_2 + \cdots, \\
m &= m_0 + \varepsilon m_1 + \varepsilon^2 m_2 + \cdots, & e &= e_0 + \varepsilon e_1 + \varepsilon^2 e_2 + \cdots, \\
\phi &= \phi_0 + \varepsilon \phi_1 + \varepsilon^2 \phi_2 + \cdots, & R &= R_0(1 + \varepsilon R_1 + \varepsilon^2 R_2 + \cdots).
\end{aligned} \tag{19}$$

3.1. *The first approximation.* Using series (19) in the mass and momentum equations (5), (6), and the stress-strain relation (13) and collecting linear terms $\sim \varepsilon$, we eventually arrive at the system

$$(1 - \beta^{(s)} E_2)v_1 + (B - k_b \beta^{(s)} \beta^{(s)})p_0 \chi R_1 c = 0, \tag{20}$$

$$(E_2 - \rho_0 c^2)v_1 - (A - k_b \beta^{(s)})p_0 \chi R_1 c = 0. \tag{21}$$

We address the reader to Appendix A for details of derivation of (20) and (21).

Equations (20) and (21) must coincide, therefore,

$$\begin{vmatrix} (1 - \beta^{(s)} E_2) & (B - k_b \beta^s \beta^s)p_0 \chi \\ (E_2 - \rho_0 c^2) & -(A - k_b \beta^{(s)})p_0 \chi \end{vmatrix} = 0. \tag{22}$$

Equation (22) gives the velocity of the wave,

$$c^2 = \frac{(A - k_b \beta^{(s)})Z_1 + E_2}{\rho_0}, \tag{23}$$

where

$$Z_1 = \frac{1 - \beta^{(s)} E_2}{B - k_b \beta^{(s)} \beta^{(s)}}.$$

Thus, all the variables are expressed through any one selected variable; for example, the velocity v_1:

$$e_1 = -\frac{v_1}{c}, \quad \sigma_1^{(ef)} = -(E_2 - k_b \beta^{(s)} Z_1)\frac{v_1}{c}, \quad p_1 = Z_1\frac{v_1}{c}, \quad R_1 = -\frac{Z_1}{p_0\chi}\frac{v_1}{c},$$

$$m_1 = [((1 - m_0) - k_b\beta^{(s)})\beta^{(s)} Z_1 + \beta^{(s)} E_2 - (1 - m_0)]\frac{v_1}{c},$$

$$\rho_1^{(f)} = \rho_0^{(L)} Z_1\left(\beta^{(L)}\kappa_1 + \frac{\kappa_2 4\pi n_0 R_0^3}{p_0\chi}\right)\frac{v_1}{c},$$

$$\rho_1^{(s)} = \rho_0^{(s)}\beta^{(s)}[Z_1(1 - k_b\beta^{(s)}) + E_2]\frac{v_1}{c}.$$

3.2. The second approximation. In the second approximation, we collect quadratic terms $\sim \varepsilon^2$ in the mass and momentum equations (5), (6), and stress-strain relation (13) and come to the following system:

$$\frac{\partial}{\partial\xi}[(E_2 - \rho_0 c^2)v_2 - (1 - \beta^{(s)}k_b)p_0\chi R_2 c] = E_2 F - c\Sigma + c\frac{\partial T}{\partial\xi} - c(1 - \beta^{(s)}k_b)\frac{\partial\Gamma}{\partial\xi}, \quad (24)$$

$$\frac{\partial}{\partial\xi}\left[(1 - E_2\beta^{(s)})v_2 - \left(\omega_1 p_0\chi - \frac{4\pi m_0 n_0 R_0^3}{\kappa_1}\right)R_2 c\right]$$

$$= \Lambda - \beta^{(s)} E_2 F - c\beta^{(s)}\frac{\partial T}{\partial\xi} - c\omega_1\frac{\partial\Gamma}{\partial\xi} + c\omega_2\frac{\partial R_1^2}{\partial\xi}. \quad (25)$$

The details of the derivation of (24) and (25) are provided in Appendix B. The determinant of the left-hand side of the system of equations (24) and (25) coincides with the determinant of (22), which equals zero. A nonzero solution for v_2 exists only if the following compatibility condition takes place:

$$\begin{vmatrix} (E_2 - \rho_0 c^2) & \frac{\partial}{\partial\xi}\left(E_2 F - c\Sigma + c\frac{\partial T}{\partial\xi} - (1 - \beta^{(s)}k_b)c\frac{\partial\Gamma}{\partial\xi}\right) \\ (1 - E_2\beta^{(s)}) & \frac{\partial}{\partial\xi}\left[\Lambda - \beta^{(s)} E_2 F - c\beta^{(s)}\frac{\partial T}{\partial\xi} - c\omega_1\frac{\partial\Gamma}{\partial\xi} + c\omega_2\frac{\partial R_1^2}{\partial\xi}\right] \end{vmatrix} = 0 \quad (26)$$

(see Appendix C). This is the evolution equation with respect to $v \cong v_1$:

$$cM\frac{\partial\Gamma}{\partial\xi} - cN\frac{\partial T}{\partial\xi} + c\omega_2\psi\frac{\partial R_1^2}{\partial\xi} + \Lambda\psi + c\Sigma(1 - E_2\beta^{(s)}) - E_2 F N = 0, \quad (27)$$

where

$$\psi = (E_2 - \rho_0 c^2), \quad M = (1 - \beta^{(s)}k_b)(1 - E_2\beta^{(s)}) - \omega_1\psi, \quad N = (1 - \beta^{(s)}\rho_0 c^2).$$

Now, we rewrite (27) in terms of v and regroup:

$$\frac{1}{2}\left[Y_1 + \psi\left((1 - \kappa_1\kappa_2)\bar{m}_1 - E_2\beta^{(s)} - \left(Y_2 + \frac{4\pi n_0 R_0^3}{p_0\chi}\right)Z_1\right)\right]\frac{\partial v}{\partial\tau}$$

$$-\left[N\eta c^2(a_1 - b_1(E_2 - k_b\beta^{(s)} Z_1)) + \frac{M Z_1\mu c^2}{p_0\chi}\left(4 + \frac{m_0 R_0^2}{\ell}\right)\right]\frac{\partial^2 v}{\partial\xi^2} + \varepsilon N\eta c^3 a_2\frac{\partial^3 v}{\partial\xi^3}$$

$$-\varepsilon^2 N\eta c^4[a_3 - b_3(E_2 - k_b\beta^{(s)} Z_1)]\frac{\partial^4 v}{\partial\xi^4} - \varepsilon^4 N\eta a_5 c^6\frac{\partial^6 v}{\partial\xi^6} - [\zeta_1 + \zeta_2]\frac{\partial vv}{\partial\xi} = 0, \quad (28)$$

where

$$\bar{m}_1 = ((1-m_0)-k_b\beta^{(s)})\beta^{(s)}Z_1+\beta^{(s)}E_2-(1-m_0),$$

$$Y_1 = (E_2N+c^2\rho_0(1-E_2\beta^{(s)})), \quad Y_2 = m_0(\kappa_1\beta^{(L)}-\beta^{(s)})+\beta^{(s)}(1-\beta^{(s)}k_b),$$

$$\zeta_1 = \psi\Bigg(\bar{m}_1-(1-m_0)\beta^{(s)}Z_1+\beta^{(s)}(E_2-k_b\beta^{(s)}Z_1)(1-\bar{m}_1)-\beta^{(s)}Z_1\bar{m}_1$$

$$+\kappa_1\beta^{(L)}Z_1\bar{m}_1-\kappa_1\kappa_2+4\pi n_0\kappa_2 R_0^3\frac{Z_1}{p_0\chi}(\bar{m}_1-m_0)-m_0\kappa_1\beta^{(L)}Z_1+\omega_2\frac{Z_1^2}{(p_0\chi)^2}\Bigg),$$

$$\zeta_2 = c^2(1-E_2\beta^{(s)})\Bigg(\rho_0-\rho_0\kappa_1\beta Z_1-\rho_0^{(s)}\beta^{(s)}(E_2-k_b\beta^{(s)}Z_1)-m_0\kappa_2\rho^{(L)}\frac{Z_1}{p_0\chi}+\bar{m}_1(\rho^{(s)}-\kappa_1\kappa_2\rho^{(L)})\Bigg)$$

$$+\frac{M(\chi+1)}{2p_0\chi}Z_1^2+E_2N.$$

In short, the evolution equation (28) can be written as

$$C_1\frac{\partial v}{\partial\tau}-C_2\frac{\partial^2 v}{\partial\xi^2}+\varepsilon C_3\frac{\partial^3 v}{\partial\xi^3}-\varepsilon^2 C_4\frac{\partial^4 v}{\partial\xi^4}-\varepsilon^4 C_6\frac{\partial^6 v}{\partial\xi^6}-\zeta\frac{\partial vv}{\partial\xi}=0, \tag{29}$$

where

$$C_1 = \frac{1}{2}\Bigg[Y_1+\psi\Bigg((1-\kappa_1\kappa_2)\bar{m}_1-E_2\beta^{(s)}-\Bigg(Y_2+\frac{4\pi n_0 R_0^3}{p_0\chi}\Bigg)Z_1\Bigg)\Bigg],$$

$$C_2 = \Bigg[N\eta c^2(a_1-b_1(E_2-k_b\beta^{(s)}Z_1))+\frac{MZ_1\mu c^2}{p_0\chi}\Bigg(4+\frac{m_0 R_0^2}{\ell}\Bigg)\Bigg], \quad C_3 = N\eta c^3 a_2,$$

$$C_4 = N\eta c^4(a_3-b_3(E_2-k_b\beta^{(s)}Z_1)), \quad C_6 = N\eta a_5 c^6, \quad \zeta = \zeta_1+\zeta_2.$$

4. Elastic waves in saturated media without gas bubbles

Our goal is to study the effect of inclusion of gas bubbles into the rheological scheme on the elastic wave decay. For this purpose we will remove the bubble-representing segment from Figure 2 and rederive the wave equation (note that our rheological scheme consists of only two branches: one for the solid and the other for the bubble-fluid mixture). This differs from the original Nikolaevskiy scheme, which includes three parallel branches [Nikolaevskiy 1989; 2008].

4.1. Stress-strain relation. By removing the bubble segment from the rheological scheme, we get Figure 3. The second Newton's law for the scheme and the kinematic relation are

$$M_1\frac{d^2 e_1}{dt^2}+M_2\frac{d^2 e}{dt^2}=\sigma-E_1 e_1-E_2 e, \quad e=e_1+e_3, \quad E_1 e_1=\mu_1\frac{de_3}{dt}. \tag{30}$$

Equations (30) lead to the well-known stress-strain relation [Nikolaevskiy 1985]

$$\sigma+\theta\frac{d\sigma}{dt}=E_2 e+(E_1+E_2)\theta\frac{de}{dt}+M_2\frac{d^2 e}{dt^2}+(M_1+M_2)\theta\frac{d^3 e}{dt^3}, \tag{31}$$
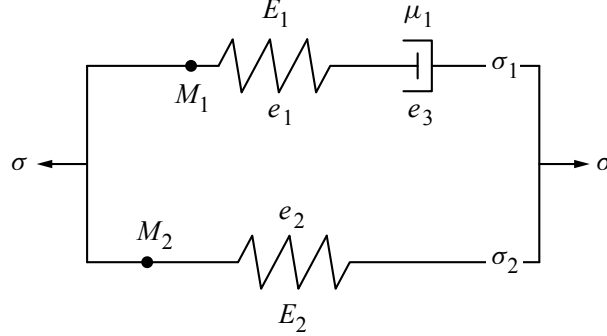
Figure 3. Rheological scheme without gas bubble.

where $\theta = \mu_1/E_1$. Hence, the constitutive law (31) will be written as

$$\sigma^{(ef)} + b_1 \varepsilon \left(\tfrac{1}{2} \varepsilon \frac{\partial}{\partial \tau} + (v - c) \frac{\partial}{\partial \xi} \right) \sigma^{(ef)} = E_2 e + \beta^{(s)} k_b p + \sum_{q=1}^{3} a_q \varepsilon^q \left(\tfrac{1}{2} \varepsilon \frac{\partial}{\partial \tau} + (v - c) \frac{\partial}{\partial \xi} \right)^q e, \quad (32)$$

where

$$a_1 = (E_1 + E_2)\theta, \quad a_2 = M_2, \quad a_3 = (M_1 + M_2)\theta, \quad b_1 = \theta.$$

4.2. *First approximation of the system without gas bubbles.* Following the approach of Section 3.1, in the first approximation for the system without bubbles we arrive at the system

$$(1 - \beta^{(s)} E_2) v_1 = (\beta - \beta^{(s)} \beta^{(s)} k_b) c p_1, \quad (33)$$

$$(\rho_0 c^2 - E_2) v_1 = (1 - \beta^{(s)} k_b) c p_1. \quad (34)$$

Appendix D provides the derivation details of these equations. The determinant of the system of equations (33) and (34) gives the wave velocity c:

$$\begin{vmatrix} (1 - \beta^{(s)} E_2) & -(\beta - \beta^{(s)} \beta^{(s)} k_b) \\ (\rho_0 c^2 - E_2) & -(1 - \beta^{(s)} k_b) \end{vmatrix} = 0. \quad (35)$$

Thus,

$$c^2 = \frac{E_2 + Z_2 (1 - \beta^{(s)} k_b)}{\rho_0}, \quad (36)$$

where

$$Z_2 = \frac{(1 - \beta^{(s)} E_2)}{(\beta - \beta^{(s)} \beta^{(s)} k_b)}.$$

Again we can express all the variables through the velocity v_1:

$$e_1 = -\frac{v_1}{c}, \quad p_1 = Z_2 \frac{v_1}{c}, \quad \rho_1^{(s)} = \rho^{(s)} \beta^{(s)} [Z_2 (1 - \beta^{(s)} k_b) + E_2] \frac{v_1}{c},$$

$$\rho_1^{(L)} = \rho^{(L)} \beta^{(L)} Z_2 \frac{v_1}{c}, \quad m_1 = [(1 - m_0) \beta^{(s)} Z_2 + \beta^{(s)} (E_2 - \beta^{(s)} k_b Z_2) - (1 - m_0)] \frac{v_1}{c},$$

$$\sigma_1^{(ef)} = -(E_2 - \beta^{(s)} k_b Z_2) \frac{v_1}{c}.$$

4.3. *Second approximation for the system without gas bubbles.* Following the approach of Section 3.2, in the second approximation we arrive at the system

$$\frac{\partial}{\partial \xi}[(E_2 - \rho_0 c^2)v_2 + (1 - \beta^{(s)}k_b)cp_2] = E_2 F - c\Sigma + c\frac{\partial T}{\partial \xi}, \tag{37}$$

$$\frac{\partial}{\partial \xi}[(1 - E_2\beta^{(s)})v_2 - (\beta - \beta^{(s)}\beta^{(s)})cp_2] = \Lambda - \beta^{(s)}E_2 F - c\beta^{(s)}\frac{\partial T}{\partial \xi}. \tag{38}$$

See Appendix E for the derivation details. In analogy to (26), the compatibility condition for the system of equations (37), (38) has the form

$$\begin{vmatrix} (E_2 - \rho_0 c^2) & \frac{\partial}{\partial \xi}\left(E_2 F - c\Sigma + c\frac{\partial T}{\partial \xi}\right) \\ (1 - E_2\beta^{(s)}) & \frac{\partial}{\partial \xi}\left(\Lambda - \beta^{(s)}E_2 F - c\beta^{(s)}\frac{\partial T}{\partial \xi}\right) \end{vmatrix} = 0. \tag{39}$$

Then the evolution equation for $v \cong v_1$ is

$$\Lambda \psi - cN\frac{\partial T}{\partial \xi} + c\Sigma(1 - E_2\beta^{(s)}) - E_2 F N = 0. \tag{40}$$

Rearranging, we arrive at

$$c^2\rho_0(1 - E_2\beta^{(s)})\frac{\partial v}{\partial \tau} - Nc^2(a_1 - b_1(E_2 - \beta^{(s)}k_b Z_2))\frac{\partial^2 v}{\partial \xi^2}$$

$$+ \varepsilon Na_2 c^3\frac{\partial^3 v}{\partial \xi^3} - \varepsilon^2 Na_3 c^4\frac{\partial^4 v}{\partial \xi^4} + [G_1 + G_2]\frac{\partial vv}{\partial \xi} = 0, \quad (41)$$

where

$$\hat{m}_1 = (1 - m_0)\beta^{(s)}Z_2 + \beta^{(s)}(E_2 - \beta^{(s)}k_b Z_2) - (1 - m_0),$$

$$G_1 = \psi\left(-((1 - m_0) + \hat{m}_1)\beta^{(s)}Z_2 - \beta^{(s)}(E_2 - \beta^{(s)}k_b Z_2)\left(1 + \frac{\hat{m}_1}{(1 - m_0)}\right) + \beta^{(L)}Z_2\hat{m}_1 - m_0\beta^{(L)}Z_2\right),$$

$$G_2 = c^2(1 - E_2\beta^{(s)})(\rho_0 - \rho_0\beta Z_2 - \rho^{(s)}\beta^{(s)}(E_2 - \beta^{(s)}k_b Z_2) + \hat{m}_1(\rho^{(s)} - \rho^{(L)})) + E_2(1 - \beta^{(s)}\rho_0 c^2).$$

Finally, we rewrite the evolution equation (41) as

$$D_1\frac{\partial v}{\partial \tau} - D_2\frac{\partial^2 v}{\partial \xi^2} + \varepsilon D_3\frac{\partial^3 v}{\partial \xi^3} - \varepsilon^2 D_4\frac{\partial^4 v}{\partial \xi^4} + G\frac{\partial vv}{\partial \xi} = 0, \tag{42}$$

where

$$D_1 = c^2\rho_0(1 - E_2\beta^{(s)}), \quad D_2 = Nc^2(a_1 - b_1(E_2 - \beta^{(s)}k_b Z_2)),$$

$$D_3 = Na_2 c^3, \quad D_4 = Na_3 c^4, \quad G = G_1 + G_2.$$

We remark that for the wave propagating to the left, that is, with $\xi = \varepsilon(x + ct)$, one obtains (as we checked) the same equation (42).

5. Linearized model

In this section we investigate the linearized versions of the model with and without the bubbles, that is, (29) and (42). Our particular interest is in its dissipative part responsible for decay of the wave.

5.1. *Evaluation of the parameters and the wave velocity.* From [Dunin et al. 2006; Nikolaevskiy 1985; 2016; Sutton and Biblarz 2016; Carcione 1998; Mikhailov 2010; Smeulders 2005], the values of the parameters are: the density $\rho_0^{(L)} = 1000\,\text{kg/m}^3$ for water, $\rho^{(g)} = 2\,\text{kg/m}^3$ for gas, $\rho_0^{(s)} = 2500\,\text{kg/m}^3$ for solid; porosity $m_0 = 0.25$; bulk modulus $k_b = 1.7 \times 10^9\,\text{Pa}$ for the matrix, $k_b = 30 \times 10^9\,\text{Pa}$ for the solid; compressibility $\beta^{(L)} = 2 \times 10^{-9}\,\text{Pa}^{-1}$ for water, $\beta^{(L)} = 2.4 \times 10^{-6}\,\text{Pa}^{-1}$ for gas, $\beta^{(s)} = 2 \times 10^{-10}\,\text{Pa}^{-1}$ for solid; steady pressure $p_0 = 10^5\,\text{Pa}$; bubble radius $R_0 = 5 \times 10^{-5}\,\text{m}$; volume gas content $\phi_0 = 10^{-3}$; viscosity $\mu_1 = 10^{-3}\,\text{Pa·s}$ for water, $\mu_2 = 2 \times 10^{-5}\,\text{Pa·s}$ for gas; adiabatic exponent $\zeta = 1.4$, and permeability $\ell = 2 \times 10^{-11}\,\text{m}^2$. Using the data from [Nikolaevskiy and Strunin 2012; Nikolaevskiy 1985; 2016; Nikolaevskiy and Stepanova 2005], the values of the parameters of the rheological scheme in Figure 2 are

$$M_1 = \rho^{(L)}L_s^2 = 10^{-2}\,\text{kg/m}, \quad M_2 = \rho^{(s)}L_s^2 = 0.02\,\text{kg/m}, \quad M_3 = \rho^{(g)}L_s^2 = 2 \times 10^{-6}\,\text{kg/m},$$

and

(a) $$E_1 = 1/\beta^{(L)} = 4 \times 10^5\,\text{Pa}, \quad E_2 = c^2\rho_0 = 2 \times 10^7\,\text{Pa}, \quad E_3 = 3\chi p_0 = 4 \times 10^7\,\text{Pa},$$

where we used, just for the purpose of evaluating of E_i and M_i, the typical velocity $c \sim 100\,\text{m/s}$ and the linear size of the oscillator $L_s = 0.3\,\text{cm}$ from [Nikolaevskiy 1985; Vilchinska et al. 1985]. Note that the above values of E_i are known only approximately. With this in mind, in the present study we also explore other the values of E_i that are considerably different from variant (a):

(b) $$E_1 = 5 \times 10^5\,\text{Pa}, \quad E_2 = 5 \times 10^8\,\text{Pa}, \quad E_3 = 5 \times 10^4\,\text{Pa},$$

(c) $$E_1 = 6 \times 10^5\,\text{Pa}, \quad E_2 = 2 \times 10^9\,\text{Pa}, \quad E_3 = 5 \times 10^3\,\text{Pa}.$$

The reason for this choice is that the two different rheological schemes that we use (for the wave with and without the bubbles) give close values of λ when we put $R_0 = 0$ and $n_0 = 0$.

Now we apply the formulas for the wave velocity (23) and (36) to show that they give reasonable orders of magnitude. For variant (a) formula (23) for the wave with the bubbles gives $c \approx 577\,\text{m/s}$, and formula (36) for the wave without the bubbles gives $c \approx 2100\,\text{m/s}$. For variant (b) the wave with the bubbles has the velocity $c \approx 726\,\text{m/s}$ and the wave without the bubbles the velocity $c \approx 2000\,\text{m/s}$. For variant (c) the wave with the bubbles has $c \approx 1100\,\text{m/s}$, and the wave without the bubbles $c \approx 1800\,\text{m/s}$. This illustrates, in line with the previous studies, that the bubbles may result in a considerable change of the wave velocity. However, our main interest in this study is the dissipation rate of the wave, which we explore in the next section.

5.2. *Dispersion (dissipation) relation.* Analyzing the linearized model, we are interested in the influence of the bubbles on the wave dissipation. This effect is controlled by the even derivatives, so we truncate the linearized equations (29) to the form

$$\frac{\partial v}{\partial \tau} = \frac{C_2}{C_1}\frac{\partial^2 v}{\partial \xi^2} + \varepsilon^2\frac{C_4}{C_1}\frac{\partial^4 v}{\partial \xi^4} + \varepsilon^4\frac{C_6}{C_1}\frac{\partial^6 v}{\partial \xi^6}. \tag{43}$$

For the Fourier modes $v \sim \exp(\lambda t + ikx)$, we get the dispersion (or dissipation) relation

$$\lambda(k) = -\frac{C_2}{C_1}k^2 + \varepsilon^2\frac{C_4}{C_1}k^4 - \varepsilon^4\frac{C_6}{C_1}k^6, \tag{44}$$
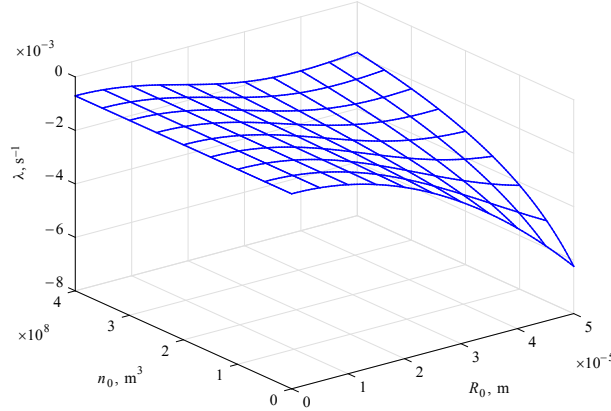
Figure 4. The decay rate by formula (44) for variant (a), $k_* = 0.25\,\text{m}^{-1}$.
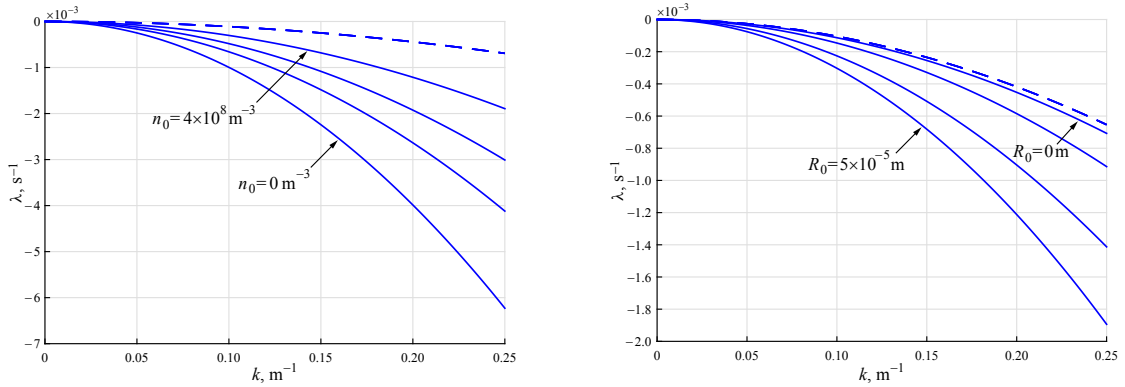
Figure 5. The decay rate by formulas (44) and (46) for variant (a). Left: n_0 varies, $R_0 = 5 \times 10^{-5}$. Right: R_0 varies, $n_0 = 4 \times 10^8$.

where λ is the decay rate and k is the wave number. For the model without the bubbles, the linearized form of (42) is

$$\frac{\partial v}{\partial \tau} = \frac{D_2}{D_1}\frac{\partial^2 v}{\partial \xi^2} + \varepsilon^2 \frac{D_4}{D_1}\frac{\partial^4 v}{\partial \xi^4} \tag{45}$$

(we again consider only even derivatives). Accordingly, the dispersion relation is

$$\lambda(k) = -\frac{D_2}{D_1}k^2 + \varepsilon^2 \frac{D_4}{D_1}k^4. \tag{46}$$

Figure 4 shows the decay rate by formula (44) at fixed $k_* = 0.25\,\text{m}^{-1}$ [Nikolaevskiy 1989] against R_0 and n_0. See that the increase in R_0 significantly affects the decay rate and makes its absolute value larger due to the bubbles increasing their role through the pressure $p_1 = -p_0 \chi R_1$. As for n_0, one should disregard the region of small n_0 in Figure 4 since the equations of continuum mechanics in the form adopted in the model become invalid when there are too few bubbles. This is because one can no longer assume that every fluid particle contains its own bubble (as suggested by (6)) because this would imply that the fluid particles are no longer small and, hence, the continuum mechanics description fails.
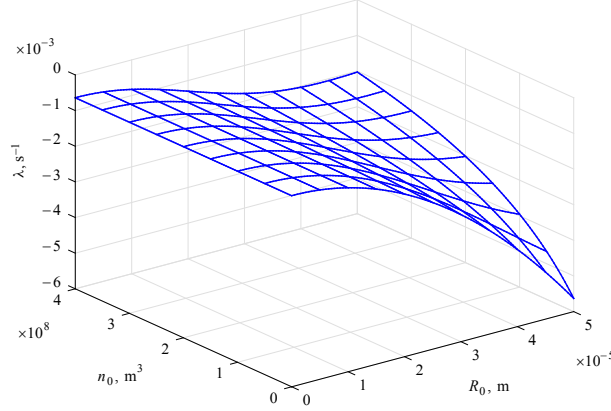
Figure 6. The decay rate by formula (44) for variant (b), $k_* = 0.25\,\text{m}^{-1}$.
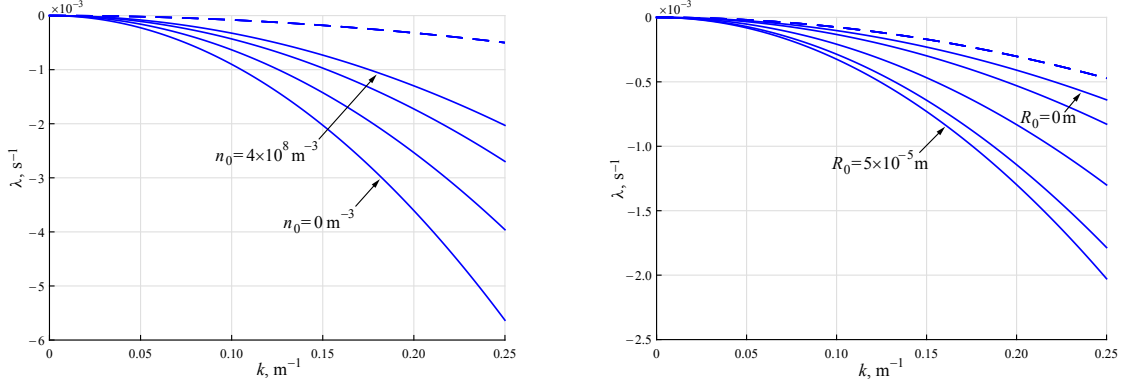
Figure 7. The decay rate by formulas (44) and (46) for variant (b). Left: n_0 varies, $R_0 = 5 \times 10^{-5}$. Right: R_0 varies, $n_0 = 4 \times 10^8$.

Figure 5 compares the dispersion curves of the wave with the bubbles and the wave without the bubbles. The dashed line describes the case without the bubbles and the solid lines correspond to the wave with the bubbles. The figure on the left is for varying n_0 and fixed R_0; the figure on the right is for varying R_0 and fixed n_0. The decay rate depends on the number and radius of the bubbles. We note that this result agrees with the conception discussed in [Strunin 2014; Strunin and Ali 2016] about the passive nature of the freely propagating elastic wave. Similar results are obtained for variants (b) and (c) as shown in Figures 6–9.

For a different $k_* = 0.52\,\text{m}^{-1}$ [Beresnev and Nikolaevskiy 1993], the results are similar; see Figures 10 and 11.

6. Conclusions

We studied the effect of rheology with and without gas bubbles and of the bubble dynamics on the dissipation of elastic waves in porous solids. The Frenkel–Biot waves of P1 type are analyzed in the
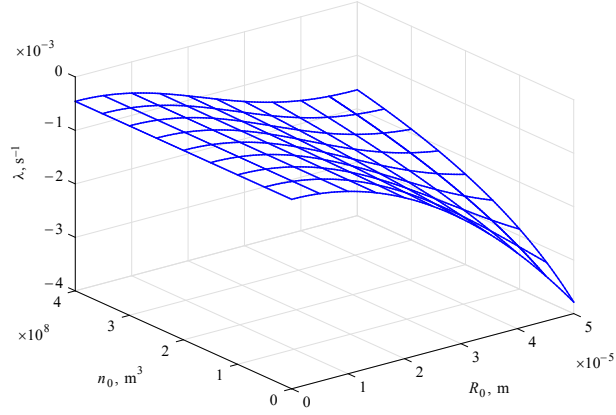
Figure 8. The decay rate by formula (44) for variant (c), $k_* = 0.25\,\mathrm{m}^{-1}$.
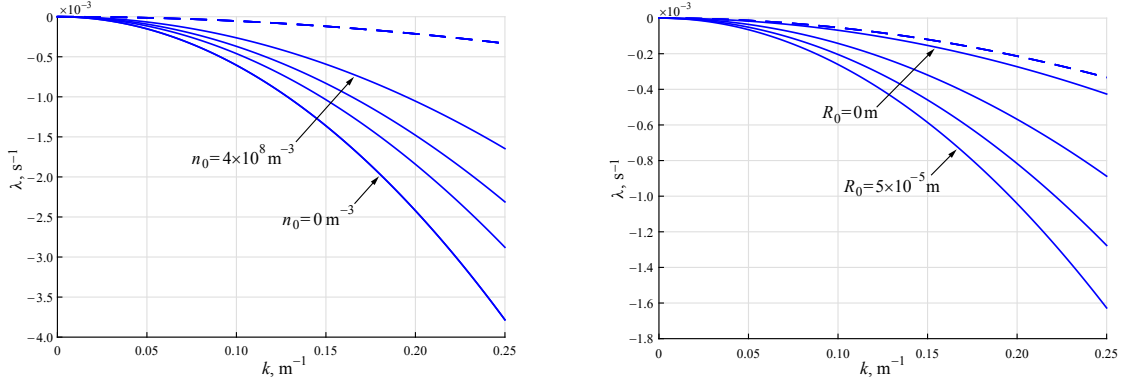
Figure 9. The decay rate by formulas (44) and (46) for variant (c). Left: n_0 varies, $R_0 = 5 \times 10^{-5}$. Right: R_0 varies, $n_0 = 4 \times 10^8$.
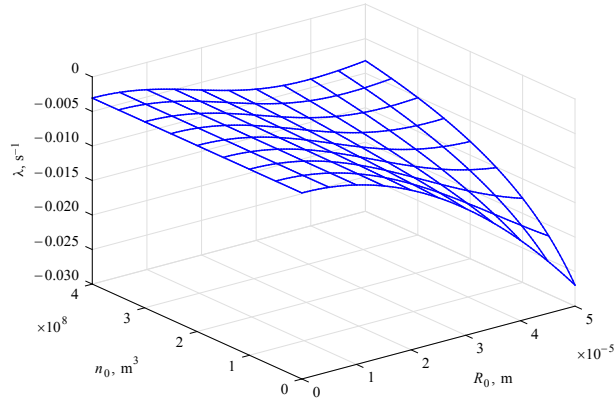
Figure 10. The decay rate by formula (44) for variant (a), $k_* = 0.52\,\mathrm{m}^{-1}$.
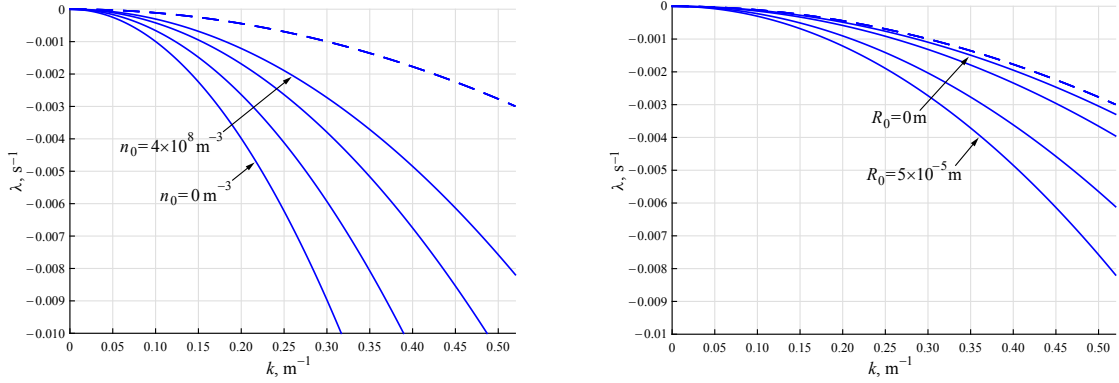
Figure 11. The decay rate by formulas (44) and (46) for variant (a). Left: n_0 varies, $R_0 = 5 \times 10^{-5}$. Right: R_0 varies, $n_0 = 4 \times 10^8$.

fluid-saturated environment. Using the three-segment rheological scheme (with the bubbles) and two-segment scheme (without the bubbles), we derived the Nikolaevskiy-type equations for the velocity of the solid matrix. The linearized versions of the equations are compared in terms of the decay rate $\lambda(k)$ of the Fourier modes. For the both cases — with and without the bubbles — the $\lambda(k)$-curve lies entirely below the zero. We found out that $|\lambda(k)|$ increases with the increase of the radius of the bubbles but decreases with the increase of the number of the bubbles.

List of symbols

$\beta^{(s)}$	:	compressibility of solid (Pa^{-1})	M_i	:	masses (kg/m)
$\beta^{(L)}$	:	compressibility of water and gas (Pa^{-1})	k_b	:	bulk modulus (Pa)
$\rho_0^{(s)}$	:	density of solid (kg/m^3)	p	:	pressure (Pa)
$\rho_0^{(L)}$	:	density of water (kg/m^3)	$\sigma^{(ef)}$	:	effective stress (Pa)
$\rho_0^{(g)}$	:	density of gas (kg/m^3)	ϕ	:	volume gas content
R_0	:	bubble radius (m)	m	:	porosity
ε	:	small parameter	ζ	:	adiabatic exponent
n_0	:	number of bubbles (m^{-3})	k	:	wave number (m^{-1})
μ	:	viscosity (Pa·s)	c	:	wave velocity (m/s)
ℓ	:	permeability (m^2)	v	:	particle velocity (m/s)
E_i	:	elastic moduli (Pa)	λ	:	decay rate (s^{-1})

Appendix A

Using equations (19), we collect the linear terms $\sim \varepsilon$ in system (5):

$$-(1-m_0)\rho_0^{(s)}c\frac{\partial v_1}{\partial \xi} = \frac{\partial \sigma_1^{(ef)}}{\partial \xi} - (1-m_0)\frac{\partial p_1}{\partial \xi},$$

$$-m_0\rho_0^{(f)}c\frac{\partial u_1}{\partial \xi} = -m_0\frac{\partial p_1}{\partial \xi},$$

$$\rho_0^{(s)}c\frac{\partial m_1}{\partial \xi} - (1-m_0)c\frac{\partial \rho_1^{(s)}}{\partial \xi} + (1-m_0)\rho_0^{(s)}\frac{\partial v_1}{\partial \xi} = -\tfrac{1}{2}(1-m_0)\frac{\partial \rho_0^{(s)}}{\partial \tau},$$

$$-m_0 c\frac{\partial \rho_1^{(f)}}{\partial \xi} - \rho_0^{(f)}c\frac{\partial m_1}{\partial \xi} + m_0\rho_0^{(f)}\frac{\partial u_1}{\partial \xi} = -\tfrac{1}{2}m_0\frac{\partial \rho_0^{(f)}}{\partial \tau}. \tag{47}$$

The system (47) gives the integrals

$$(1-m_0)\rho_0^{(s)}cv_1 = -\sigma_1^{(ef)} + (1-m_0)p_1, \qquad m_0\rho_0^{(f)}cu_1 = m_0 p_1,$$

$$(1-m_0)\rho_0^{(s)}v_1 = ((1-m_0)\rho_1^{(s)} - \rho_0^{(s)}m_1)c, \qquad m_0\rho_0^{(f)}u_1 = (\rho_0^{(f)}m_1 + m_0\rho_1^{(f)})c. \tag{48}$$

According to (7) and (10) the terms $\sim \varepsilon$ in the density series are

$$\rho_1^{(s)} = \rho_0^{(s)}\left(\beta^{(s)}p_1 - \frac{\beta^{(s)}\sigma_1^{(ef)}}{(1-m_0)}\right), \quad \rho_1^{(f)} = \rho_0^{(L)}(\beta^{(L)}\kappa_1 p_1 - 4\pi n_0\kappa_2 R_0^3 R_1), \tag{49}$$

and also

$$\rho_0^{(f)} = \kappa_1\kappa_2\rho_0^{(L)}, \tag{50}$$

where

$$\kappa_1 = 1 - \tfrac{4\pi}{3}R_0^3 n_0, \quad \kappa_2 = 1 + \beta^{(L)}p.$$

Inserting (49) and (50) into the last two equations in (48) (mass equations), we get

$$(1-m_0)v_1 = [(1-m_0)\beta^{(s)}p_1 - \beta^{(s)}\sigma_1^{(ef)} - m_1]c, \tag{51}$$

$$m_0 u_1 = \left[m_1 + \frac{m_0\beta^{(L)}p_1}{\kappa_2} - \frac{4\pi n_0 m_0 R_0^3 R_1}{\kappa_1}\right]c. \tag{52}$$

The combination of (51) and (52) gives

$$(1-m_0)v_1 + m_0 u_1 = \left[\frac{(\beta + (1-m_0)\beta^{(s)}\beta^{(L)}p_0)p_1}{\kappa_2} - \beta^{(s)}\sigma_1^{(ef)} - \frac{4\pi n_0 m_0 R_0^3 R_1}{\kappa_1}\right]c, \tag{53}$$

where $\beta = (1-m_0)\beta^{(s)} + m_0\beta^{(L)}$.

The condition (15) means $v_1 = u_1$, therefore (53) becomes

$$v_1 = \left[\frac{(\beta + (1-m_0)\beta^{(s)}\beta^{(L)}p_0)p_1}{\kappa_2} - \beta^{(s)}\sigma_1^{(ef)} - \frac{4\pi n_0 m_0 R_0^3 R_1}{\kappa_1}\right]c. \tag{54}$$

Due to the conditions $v_1 = u_1$, $\rho_0 = (1-m_0)\rho_0^{(s)} + m_0\rho_0^{(L)}$ and using (50), the first two of the momentum equations (48) give

$$\rho_0 cv_1 = -\sigma_1^{(ef)} + Ap_1, \tag{55}$$

where

$$A = (1-m_0) + \frac{m_0}{\kappa_1\kappa_2}.$$

Now, the linear terms $\sim \varepsilon$ in relations (14) and (18) give

$$\frac{1}{2}\frac{\partial e_0}{\partial \tau} - c\frac{\partial e_1}{\partial \xi} + v_1\frac{\partial e_0}{\partial \xi} = \frac{\partial v_1}{\partial \xi}, \tag{56}$$

$$\sigma_1^{(ef)} - E_2 e_1 - \beta^{(s)}k_b p_1 = T, \tag{57}$$

where

$$T \equiv \eta\left[\sum_{q=1,2,3,5} a_q(-c)^q \varepsilon^{q-1}\frac{\partial^q e_0}{\partial \xi^q} + \sum_{q=1,3} b_q c^q \varepsilon^{q-1}\frac{\partial^q \sigma_0^{(ef)}}{\partial \xi^q}\right].$$

The linear terms $\sim \varepsilon$ in the bubble (6) give

$$-\frac{\mu c}{\rho_0^{(L)}\kappa_2}\left[\frac{4}{R_0} + \frac{m_0 R_0}{\ell}\right]\frac{\partial R_0}{\partial \xi} = -\frac{1}{\rho_0^{(L)}\kappa_2}(p_0 \chi R_1 + p_1). \tag{58}$$

Equations (56), (57), and (58) lead to the integrals

$$e_1 = -\frac{v_1}{c}, \quad \sigma_1^{(ef)} = E_2 e_1 + \beta^{(s)}k_b p_1, \quad p_1 = -p_0 \chi R_1. \tag{59}$$

The effective stress $\sigma_1^{(ef)}$ in (59) can be rewritten as

$$\sigma_1^{(ef)} = -\left[\frac{E_2 v_1}{c} + p_0 \chi \beta^{(s)}k_b R_1\right]. \tag{60}$$

Substituting (60) and the value of p_1 from (59) into (54) leads to

$$(1 - \beta^{(s)}E_2)v_1 + (B - k_b\beta^{(s)}\beta^{(s)})p_0 \chi R_1 c = 0, \tag{61}$$

where

$$B = \frac{(\beta + (1 - m_0)\beta^{(s)}\beta^{(L)}p_0)}{\kappa_2} + \frac{4\pi n_0 m_0 R_0^3}{\kappa_1 p_0 \chi}.$$

Now, from (55) and using the value of p_1 from (59), we obtain the effective stress as

$$\sigma_1^{(ef)} = -(\rho_0 c v_1 + A)p_0 \chi R_1. \tag{62}$$

The combination of (60) and (62) results in

$$(E_2 - \rho_0 c^2)v_1 - (A - k_b\beta^{(s)})p_0 \chi R_1 c = 0. \tag{63}$$

Appendix B

Collecting the quadratic terms $\sim \varepsilon^2$ in (18), we get

$$\sigma_2^{(ef)} - E_2 e_2 - \beta^{(s)}k_b p_2 = T, \tag{64}$$

where

$$T \equiv \eta\left[\sum_{q=1,2,3,5} a_q(-c)^q \varepsilon^{q-1}\frac{\partial^q e_1}{\partial \xi^q} + \sum_{q=1,3} b_q c^q \varepsilon^{q-1}\frac{\partial^q \sigma_1^{(ef)}}{\partial \xi^q}\right].$$

Note that here we keep (as Nikolaevskiy [2008] did) the higher powers of ε to represent small corrections to the leading terms. These corrections will eventually translate into small corrections in the derived Nikolaevskiy equation further in this paper; they will be the object of our study. Thus,

$$\frac{\partial \sigma_2^{(ef)}}{\partial \xi} - E_2 \frac{\partial e_2}{\partial \xi} - \beta^{(s)} k_b \frac{\partial p_2}{\partial \xi} = \frac{\partial T}{\partial \xi}. \tag{65}$$

From (14) in the order $\sim \varepsilon^2$, we get

$$\frac{\partial}{\partial \xi}(ce_2 + v_2) = F, \quad F = -\frac{1}{c}\left(\frac{1}{2}\frac{\partial v_1}{\partial \tau} + \frac{\partial v_1 v_1}{\partial \xi}\right). \tag{66}$$

Therefore,

$$\frac{\partial e_2}{\partial \xi} = \frac{F}{c} - \frac{1}{c}\frac{\partial v_2}{\partial \xi}. \tag{67}$$

Substituting (67) into (65) we obtain

$$\frac{\partial}{\partial \xi}(c\sigma_2^{(ef)} + E_2 v_2 - c\beta^{(s)} k_b p_2) = E_2 F + c\frac{\partial T}{\partial \xi}. \tag{68}$$

From the momentum equations (5) for the solid and liquid, we get

$$(1 - m_0)\rho_0^{(s)} c \frac{\partial v_2}{\partial \xi} + \frac{\partial \sigma_2^{(ef)}}{\partial \xi} - (1 - m_0)\frac{\partial p_2}{\partial \xi} = \Sigma_1, \tag{69}$$

where

$$\Sigma_1 = (1 - m_0)\rho_0^{(s)}\left(\frac{1}{2}\frac{\partial v_1}{\partial \tau} + \frac{\partial v_1 v_1}{\partial \xi}\right) - (1 - m_0)\rho_1^{(s)} c \frac{\partial v_1}{\partial \xi} + m_1\rho_0^{(s)} c \frac{\partial v_1}{\partial \xi} - m_1\frac{\partial p_1}{\partial \xi} + \varepsilon^{\gamma-1}\delta m_0 v_1$$

and

$$m_0\rho_0^{(f)} c \frac{\partial u_2}{\partial \xi} - m_0\frac{\partial p_2}{\partial \xi} = \Sigma_2, \tag{70}$$

where

$$\Sigma_2 = m_0\rho_0^{(f)}\left(\frac{1}{2}\frac{\partial u_1}{\partial \tau} + \frac{\partial u_1 u_1}{\partial \xi}\right) - m_0\rho_1^{(f)} c \frac{\partial u_1}{\partial \xi} - m_1\rho_0^{(f)} c \frac{\partial u_1}{\partial \xi} + m_1\frac{\partial p_1}{\partial \xi} - \varepsilon^{\gamma-1}\delta m_0 u_1.$$

Due to the condition (15), the combination of (69) with (70) gives

$$\rho_0 c \frac{\partial v_2}{\partial \xi} + \frac{\partial \sigma_2^{(ef)}}{\partial \xi} - \frac{\partial p_2}{\partial \xi} = \Sigma, \tag{71}$$

where $\Sigma = \Sigma_1 + \Sigma_2$, so that

$$\Sigma = \rho_0\left(\frac{1}{2}\frac{\partial v_1}{\partial \tau} + \frac{\partial v_1 v_1}{\partial \xi}\right) - c((1 - m_0)\rho_0^{(s)}\beta^{(s)} + m_0\rho_0^{(L)}\beta^{(L)}\kappa_1)\frac{\partial p_1 v_1}{\partial \xi}$$

$$+ c\rho_0^{(s)}\beta^{(s)}\frac{\partial \sigma_1^{(ef)} v_1}{\partial \xi} + c\rho_0^{(L)} 4\pi n_0 m_0\kappa_2 R_0^3 \frac{\partial R_1 v_1}{\partial \xi} + c(\rho_0^{(s)} - \kappa_1\kappa_2\rho_0^{(L)})\frac{\partial m_1 v_1}{\partial \xi}.$$

Equations (68) and (71) result in

$$\frac{\partial}{\partial \xi}[(E_2 - \rho_0 c^2)v_2 + (1 - \beta^{(s)} k_b)cp_2] = E_2 F - c\Sigma + c\frac{\partial T}{\partial \xi}. \tag{72}$$

From the bubble equation (6), in the order $\sim \varepsilon^2$,

$$\frac{-\mu c}{\rho_0^{(L)}\kappa_2}\left(4 + \frac{m_0 R_0^2}{\ell}\right)\frac{\partial R_1}{\partial \xi} = \frac{1}{\rho_0^{(L)}\kappa_2}\left[\frac{\beta^{(L)}p_0\chi}{\kappa_2}p_1 R_1 + \frac{\beta^{(L)}}{\kappa_2}p_1^2 + \frac{p_0\chi(\chi+1)}{2}R_1^2 - p_0\chi R_2 - p_2\right]. \quad (73)$$

We rewrite (73) as

$$p_2 = \Gamma - p_0\chi R_2, \quad (74)$$

where

$$\Gamma = \mu c\left(4 + \frac{m_0 R_0^2}{\ell}\right)\frac{\partial R_1}{\partial \xi} + \frac{\beta^{(L)}p_1}{\kappa_2}(p_0\chi R_1 + p_1) + \tfrac{1}{2}p_0\chi(\chi+1)R_1^2.$$

Now we substitute the value of p_2 from (74) into (72) to get

$$\frac{\partial}{\partial \xi}[(E_2 - \rho_0 c^2)v_2 - (1 - \beta^{(s)}k_b)p_0\chi R_2 c] = E_2 F - c\Sigma + c\frac{\partial T}{\partial \xi} - c(1 - \beta^{(s)}k_b)\frac{\partial \Gamma}{\partial \xi}. \quad (75)$$

In the second order, the mass balances (5) for the solid and liquid-gas mixture have the form

$$\frac{\partial}{\partial \xi}((1 - m_0)v_2 - [(1 - m_0)\beta^{(s)}p_2 - \beta^{(s)}\sigma_2^{(ef)} - m_2]c) = \Lambda^{(s)}/\rho_0^{(s)}, \quad (76)$$

$$\frac{\partial}{\partial \xi}\left(m_0 u_2 - \left[m_2 + \frac{m_0\beta^{(L)}p_2}{\kappa_2} - \frac{4\pi m_0 n_0 R_0^3(R_2 + R_1^2)}{\kappa_1} + \frac{4\pi m_0 n_0 R_0^3 p_0\chi\beta^{(L)}R_1^2}{\kappa_1\kappa_2}\right]c\right) = \frac{\Lambda^{(L)}}{\rho_0^{(L)}}, \quad (77)$$

where

$$\Lambda^{(s)} = \rho_0^{(s)}\frac{1}{2}\frac{\partial}{\partial \tau}[(m_1 - (1 - m_0)\beta^{(s)}p_1 + \beta^{(s)}\sigma_1^{(ef)})]$$

$$+ \rho_0^{(s)}\frac{\partial}{\partial \xi}\left[m_1 v_1 - ((1 - m_0)p_1 + \sigma_1^{(ef)})\beta^{(s)}v_1 - c\beta^{(s)}m_1\left(p_1 - \frac{\sigma_1^{(ef)}}{(1 - m_0)}\right)\right], \quad (78)$$

$$\Lambda^{(L)} = -\rho_0^{(L)}\frac{1}{2}\frac{\partial}{\partial \tau}[\kappa_1(m_1\kappa_2 + m_0\beta^{(L)}p_1) - 4\pi n_0\kappa_2 R_0^3 R_1]$$

$$+ \rho_0^{(L)}\frac{\partial}{\partial \xi}[(\beta^{(L)}\kappa_1 p_1 - 4\pi n_0\kappa_2 R_0^3 R_1)(cm_1 - m_0 u_1)] - \kappa_1\kappa_2\rho_0^{(L)}\frac{\partial m_1 u_1}{\partial \xi}. \quad (79)$$

The combination of (76) and (77) gives

$$\frac{\partial}{\partial \xi}\left[v_2 - \left(\frac{(\beta + (1 - m_0)\beta^{(s)}\beta^{(L)}p_0)p_2}{\kappa_2} - \beta^{(s)}\sigma_2^{(ef)}\right.\right.$$

$$\left.\left. - \frac{4\pi m_0 n_0 R_0^3(R_2 + R_1^2)}{\kappa_1} + \frac{4\pi m_0 n_0 R_0^3 p_0\chi\beta^{(L)}R_1^2}{\kappa_1\kappa_2}\right)c\right] = \Lambda, \quad (80)$$

where

$$\Lambda \equiv \Lambda^{(s)}/\rho_0^{(s)} + \Lambda^{(L)}/\rho_0^{(L)}.$$

From (68) we have

$$\frac{\partial \sigma_2^{(ef)}}{\partial \xi} = \frac{\partial}{\partial \xi}\left(T + k_b\beta^{(s)}\Gamma - k_b\beta^{(s)}p_0\chi R_2 - \frac{E_2}{c}v_2\right) + \frac{1}{c}E_2 F. \quad (81)$$

Now we insert (81) and the value of p_2 represented by (74) into (80),

$$\frac{\partial}{\partial \xi}\left[(1 - E_2 \beta^{(s)})v_2 - \left(\omega_1 p_0 \chi - \frac{4\pi m_0 n_0 R_0^3}{\kappa_1}\right)R_2 c\right]$$

$$= \Lambda - \beta^{(s)} E_2 F - c\beta^{(s)}\frac{\partial T}{\partial \xi} - c\omega_1 \frac{\partial \Gamma}{\partial \xi} + c\omega_2 \frac{\partial R_1^2}{\partial \xi}, \quad (82)$$

where

$$\omega_1 = k_b \beta^{(s)} \beta^{(s)} + \frac{\beta + (1 - m_0)\beta^{(s)}\beta^{(L)}p_0}{\kappa_2}, \quad \omega_2 = \frac{4\pi m_0 n_0 R_0^3 \beta^{(L)}p_0 \chi}{\kappa_1 \kappa_2} - \frac{4\pi m_0 n_0 R_0^3}{\kappa_1}.$$

Appendix C

Equation (26) can be illustrated by the following simple example

$$v_1 + cR_1 = 0, \quad 2v_1 + 4R_1 = 0.$$

A nonzero solution of the system exists only if $c = 2$ (the eigenvalue of the problem). Here v_1 and R_1 are analogous to the first approximation from our main text. The second approximation, v_2 and R_2, satisfies the system

$$v_2 + cR_2 = f[v_1], \quad 2v_2 + 4R_2 = g[v_1],$$

which is solvable only if the right-hand sides satisfy the condition $g[v_1] = 2f[v_1]$. This solvability condition is the analogy to the Nikolaevskiy-type equation that we aim to derive.

Appendix D

The first approximations for the momentum and mass-balance equations without gas bubbles are the same as for the system (5). As for the density equations, the solid density remains unchanged but for gas-liquid mixture we neglect the volume gas content ϕ in (9):

$$\rho^{(f)} = \rho^{(L)} = \rho_0^{(L)}(1 + \beta^{(L)}p). \quad (83)$$

The first approximation of (83) is

$$\rho_1^{(L)} = \rho_0^{(L)}\beta^{(L)}p_1. \quad (84)$$

Inserting this into the mass equation for the fluid (48), we get

$$m_0 u_1 = [m_1 + m_0 \beta^{(L)}p_1]c. \quad (85)$$

Now, the combination of (51) and (85) yields

$$(1 - m_0)v_1 + n_0 u_1 = [(1 - m_0)\beta^{(s)}p_1 - \beta^{(s)}\sigma_1^{(ef)} + m_0 \beta^{(L)}p_1]c. \quad (86)$$

Due to the condition (15), Equation (86) becomes

$$v_1 = [(1 - m_0)\beta^{(s)}p_1 - \beta^{(s)}\sigma_1^{(ef)} + m_0 \beta^{(L)}p_1]c. \quad (87)$$

After we apply the conditions

$$v_1 = u_1, \quad \rho_0 = (1 - m_0)\rho_0^{(s)} + m_0\rho_0^{(L)},$$

the first two equations in (48) give

$$\rho_0 c v_1 = -\sigma_1^{(ef)} + p_1. \tag{88}$$

The first approximation of relation (32) is

$$\sigma_1^{(ef)} - E_2 e_1 - \beta^{(s)} k_b p_1 = \sum_{q=1}^{3} a_q (-c)^q \varepsilon^{q-1} \frac{\partial^q e_0}{\partial \xi^q} + b_1 c \frac{\partial \sigma_0^{(ef)}}{\partial \xi}. \tag{89}$$

Equations (89) and (56) result in the integral

$$\sigma_1^{ef} = -\frac{E_2 v_1}{c} + \beta^{(s)} k_b p_1. \tag{90}$$

Substituting (90) into (87), we get

$$(1 - \beta^{(s)} E_2)v_1 = c(1 - m_0)\beta^{(s)} p_1 + cm_0\beta^{(L)} p_1 - \beta^{(s)}\beta^{(s)} k_b c p_1. \tag{91}$$

As $\beta = (1 - m_0)\beta^{(s)} + m_0\beta^{(L)}$, (91) becomes

$$(1 - \beta^{(s)} E_2)v_1 = (\beta - \beta^{(s)}\beta^{(s)} k_b)c p_1. \tag{92}$$

From (88) we obtain

$$\sigma_1^{(ef)} = p_1 - \rho_0 c v_1. \tag{93}$$

Therefore, the combination of (93) with (90) yields

$$(\rho_0 c^2 - E_2)v_1 = (1 - \beta^{(s)} k_b)c p_1. \tag{94}$$

Appendix E

In the second approximation for the system without the bubbles we again arrive at an equation of the form (72), except the formulas for Σ and T are changed:

$$\frac{\partial}{\partial \xi}[(E_2 - \rho_0 c^2)v_2 + (1 - \beta^{(s)} k_b)c p_2] = E_2 F - c\Sigma + c\frac{\partial T}{\partial \xi}, \tag{95}$$

where

$$\Sigma = \rho_0 \left(\frac{1}{2}\frac{\partial v_1}{\partial \tau} + \frac{\partial v_1 v_1}{\partial \xi} \right) - c\rho_0 \beta \frac{\partial p_1 v_1}{\partial \xi} + c\rho_0^{(s)}\beta^{(s)} \frac{\partial \sigma_1^{(ef)} v_1}{\partial \xi} + c(\rho_0^{(s)} - \rho_0^{(L)})\frac{\partial m_1 v_1}{\partial \xi},$$

$$T = \sum_{q=1}^{3} a_q(-c)^q \varepsilon^{q-1} \frac{\partial^q e_1}{\partial \xi^q} + b_1 c \frac{\partial \sigma_1^{(ef)}}{\partial \xi}.$$

The second approximation of the mass balance for the solid is the same as (76), while for the fluid it takes the form

$$\frac{\partial}{\partial \xi}[m_0 u_2 - (m_2 + m_0\beta^{(L)} p_2)c] = \Lambda^{(L)}/\rho_0^{(L)}, \tag{96}$$

where

$$\Lambda^{(L)} = -\tfrac{1}{2}\rho_0^{(L)}\frac{\partial}{\partial\tau}[m_1 + m_0\beta^{(L)}p_1] + \rho_0^{(L)}\frac{\partial}{\partial\xi}[cm_1\beta^{(L)}p_1 - m_0\beta^{(L)}p_1u_1 - m_1u_1].$$

The combination of (76) and (96) results in

$$\frac{\partial}{\partial\xi}[v_2 - (\beta p_2 - \beta^{(s)}\sigma_2^{(ef)})c] = \Lambda, \tag{97}$$

where

$$\Lambda = (\Lambda^{(s)}/\rho_0^{(s)}) + (\Lambda^{(L)}/\rho_0^{(L)}).$$

From (68) we find

$$\frac{\partial\sigma_2^{(ef)}}{\partial\xi} = \frac{\partial}{\partial\xi}\left(T + k_b\beta^{(s)}p_2 - \frac{E_2}{c}v_2\right) + \frac{1}{c}E_2F. \tag{98}$$

Substituting (98) into (97) we get

$$\frac{\partial}{\partial\xi}[(1 - E_2\beta^{(s)})v_2 - (\beta - \beta^{(s)}\beta^{(s)})cp_2] = \Lambda - \beta^{(s)}E_2F - c\beta^{(s)}\frac{\partial T}{\partial\xi}. \tag{99}$$

References

[Anderson 1980] A. L. Anderson, "Acoustics of gas-bearing sediments, I: Background", *J. Acoust. Soc. Am.* **67**:6 (1980), 1865–1889.

[Beresnev and Nikolaevskiy 1993] I. A. Beresnev and V. N. Nikolaevskiy, "A model for nonlinear seismic waves in a medium with instability", *Physica D* **66**:1-2 (1993), 1–6.

[Biot 1956a] M. A. Biot, "Theory of propagation of elastic waves in a fluid-saturated porous solid, I: Low-frequency range", *J. Acoust. Soc. Am.* **28**:2 (1956), 168–178.

[Biot 1956b] M. A. Biot, "Theory of propagation of elastic waves in a fluid-saturated porous solid, II: Higher frequency range", *J. Acoust. Soc. Am.* **28**:2 (1956), 179–191.

[Biot 1962a] M. A. Biot, "Generalized theory of acoustic propagation in porous dissipative media", *J. Acoust. Soc. Am.* **34**:9A (1962), 1254–1264.

[Biot 1962b] M. A. Biot, "Mechanics of deformation and acoustic propagation in porous media", *J. Appl. Phys.* **33**:4 (1962), 1482–1498.

[Bohlen 2002] T. Bohlen, "Parallel 3-D viscoelastic finite difference seismic modelling", *Comput. Geosci.* **28**:8 (2002), 887–899.

[Brunner and Spetzler 2001] W. Brunner and H. A. Spetzler, "Observations of time-dependent meniscus behavior with implications for seismic attenuation in three-phase systems", *Geophys. Res. Lett.* **28**:9 (2001), 1867–1870.

[Carcione 1998] J. M. Carcione, "Viscoelastic effective rheologies for modelling wave propagation in porous media", *Geophys. Prospecting* **46**:3 (1998), 249–270.

[Collier et al. 2006] L. Collier, J. W. Neuberg, N. Lensky, V. Lyakhovsky, and O. Navon, "Attenuation in gas-charged magma", *J. Volcanology Geotherm. Res.* **153**:1-2 (2006), 21–36.

[Dunin and Nikolaevskiy 2005] S. Z. Dunin and V. N. Nikolaevskii, "Nonlinear waves in porous media saturated with live oil", *Acoust. Phys.* **51**:Suppl. 1 (2005), S61–S66.

[Dunin et al. 2006] S. Z. Dunin, D. N. Mikhailov, and V. N. Nikolayevskii, "Longitudinal waves in partially saturated porous media: the effect of gas bubbles", *J. Appl. Math. Mech.* **70**:2 (2006), 251–263.

[Frenkel 2005] J. Frenkel, "On the theory of seismic and seismoelectric phenomena in a moist soil", *J. Eng. Mech.* (*ASCE*) **131**:9 (2005), 879–887.

[Liu et al. 1976] H.-P. Liu, D. L. Anderson, and H. Kanamori, "Velocity dispersion due to anelasticity: implications for seismology and mantle composition", *Geophys. J. Int.* **47**:1 (1976), 41–58.

[Masson et al. 2006] Y. J. Masson, S. R. Pride, and K. T. Nihei, "Finite difference modeling of Biot's poroelastic equations at seismic frequencies", *J. Geophys. Res. Solid Earth* **111**:B10 (2006), art. id. B10305.

[Mikhailov 2010] D. N. Mikhailov, "The influence of gas saturation and pore pressure on the characteristics of the Frenkel–Biot *P* waves in partially saturated porous media", *Fiz. Zemli* **2010**:10 (2010), 99–112. In Russian; translated in *Izv. Phys. Solid Earth* **46**:10 (2010), 897–909.

[Nikolaevskiy 1985] V. N. Nikolaevskiy, "Viscoelasticity with internal oscillators as a possible model of seismoactive medium", *Dokl. Akad. Nauk SSSR* **283**:6 (1985), 1321–1324. In Russian.

[Nikolaevskiy 1989] V. N. Nikolaevskii, "Dynamics of viscoelastic media with internal oscillators", pp. 201–221 in *Recent advances in engineering science*, edited by S. L. Koh and C. G. Speziale, Lect. Notes Eng. **39**, Springer, 1989.

[Nikolaevskiy 1990] V. N. Nikolaevskij, *Mechanics of porous and fractured media*, Series Theor. Appl. Mech. **8**, World Sci., Teaneck, NJ, 1990.

[Nikolaevskiy 2008] V. N. Nikolaevskiy, "Non-linear evolution of *P*-waves in viscous-elastic granular saturated media", *Transp. Porous Media* **73**:2 (2008), 125–140.

[Nikolaevskiy 2016] V. N. Nikolaevskiy, "A real *P*-wave and its dependence on the presence of gas", *Fiz. Zemli* **2016**:1 (2016), 3–14. In Russian; translated in *Izv. Phys. Solid Earth* **52**:1 (2016), 1–13.

[Nikolaevskiy and Stepanova 2005] V. N. Nikolaevskiĭ and G. S. Stepanova, "Nonlinear seismics and the acoustic action on the oil recovery from an oil pool", *Acoust. Phys.* **51**:Suppl. 1 (2005), S131–S139.

[Nikolaevskiy and Strunin 2012] V. Nikolaevskiy and D. Strunin, "The role of natural gases in seismics of hydrocarbon reservoirs", pp. 25–29 Int. Conf. Elastic Wave Effect on Fluid in Porous Media **3**, 2012.

[Papageorgiou and Chapman 2015] G. Papageorgiou and M. Chapman, "Multifluid squirt flow and hysteresis effects on the bulk modulus-water saturation relationship", *Geophys. J. Int.* **203**:2 (2015), 814–817.

[Smeulders 2005] D. M. Smeulders, "Experimental evidence for slow compressional waves", *J. Eng. Mech.* (*ASCE*) **131**:9 (2005), 908–917.

[Strunin 2014] D. V. Strunin, "On dissipative nature of elastic waves", *J. Coupled Syst. Multiscale Dyn.* **2**:2 (2014), 70–73.

[Strunin and Ali 2016] D. V. Strunin and A. A. Ali, "On nonlinear dynamics of neutral modes in elastic waves in granular media", *J. Coupled Syst. Multiscale Dyn.* **4**:3 (2016), 163–169.

[Sutton and Biblarz 2016] G. P. Sutton and O. Biblarz, *Rocket propulsion elements*, 9th ed., Wiley, Hoboken, NJ, 2016.

[Tisato et al. 2015] N. Tisato, B. Quintal, S. Chapman, Y. Podladchikov, and J.-P. Burg, "Bubbles attenuate elastic waves at seismic frequencies: first experimental evidence", *Geophys. Res. Lett.* **42**:10 (2015), 3880–3887.

[Van Wijngaarden 1968] L. Van Wijngaarden, "On the equations of motion for mixtures of liquid and gas bubbles", *J. Fluid Mech.* **33**:3 (1968), 465–474.

[Vilchinska et al. 1985] N. Vilchinska, V. N. Nikolaevskiy, and V. Lisin, "Slow waves and natural oscillations in sandy marine soils", *Izv. Acad. Nauk SSSR Oceanology* **25**:4 (1985), 656–663. In Russian.

[Yang et al. 2014] L. Yang, D. Yang, and J. Nie, "Wave dispersion and attenuation in viscoelastic isotropic media containing multiphase flow and its application", *Sci. China G Phys. Mech. Astronom.* **57**:6 (2014), 1068–1077.

ADHAM A. ALI: u1054916@umail.usq.edu.au
Department of Mathematics, Kirkuk University, Kirkuk, Iraqi

and

Computational Engineering and Science Research Centre, Faculty of Health, Engineering and Sciences,
University of Southern Queensland, Toowoomba, Australia

DMITRY V. STRUNIN: strunin@usq.edu.au
Computational Engineering and Science Research Centre, Faculty of Health, Engineering and Sciences,
University of Southern Queensland, Toowoomba, Australia

msp

SOME GENERAL THEOREMS FOR LOCAL GRADIENT THEORY OF ELECTROTHERMOELASTIC DIELECTRICS

OLHA HRYTSYNA AND HALYNA MOROZ

Using the basic equations of local gradient theory of electrothermoelastic nonferromagnetic polarized solids, which accounts for the local mass displacement and its effect on mechanical, thermal and electromagnetic fields, the governing set of equations is obtained for a linear approximation. On this basis, the coupled initial-boundary-value problems corresponding to this gradient-type theory are formulated. The reciprocity and uniqueness theorems for non-stationary problems of the local gradient electrothermoelasticity are proved.

1. Introduction

As a result of the rapid development of nanotechnologies, the past several decades have been marked by significant scientific attention to the construction of nonlocal theories of the deformation of solids. At a continuous level, such theories account for the long-range effects and the impact of a material's microstructure on its macro-properties. Nonlocal theories have allowed for the description of a range of experimentally-observed phenomena [Liu et al. 2006; Nam et al. 2006; Nysten et al. 2005; Kumikov and Khokonov 1983] that cannot be duly explained by the classical (local) theories. Within the scope of a continuous description, gradient-type theories of dielectrics are constructed by introducing into the space of constitutive parameters of internal variables, or gradients of the strain, polarization, electric field [Hadjigeorgiou et al. 1999; Nowacki 1983; Kafadar 1971; Kalpakidis et al. 1995; Kalpakidis and Agiasofitou 2002; Maugin 1979; 1988; Mindlin 1972; Sahin and Dost 1988; Yang 2006; Yan and Jiang 2007].

In 1987, Burak proposed a new continuum-thermodynamic approach to the construction of a non-local theory of the deformation of thermoelastic solids, which consisted in accounting for local mass displacement and its impact on the mechanical and heat fields in the model description [Burak 1987]. In doing so, he linked the local mass displacement to changes in the material structure of a fixed small element of the body. By employing this approach, articles [Burak et al. 2007; 2008] present the foundations of a gradient-type theory of the deformation of electrothermo-elastic nonferromagnetic polarized solids. The mentioned theory is grounded on accounting for the local mass displacement and its effect to mechanical, heat, and electromagnetic fields [Burak et al. 2007; 2008; Kondrat and Hrytsyna 2008; 2012]. The developed theory was called a local gradient theory of dielectrics. This theory enabled us to explain theoretically some observed phenomena, namely, the near-surface and size phenomena [Burak et al. 2007; 2008], high-frequency dispersion of longitudinal elastic waves [Kondrat and Hrytsyna 2010],

Mead's anomaly [Chapla et al. 2009], piezoelectric effect in high symmetry crystalline dielectrics [Hrytsyna 2012], the existence of anti-plane shear surface SH waves in homogeneous isotropic half-space [Hrytsyna 2017] etc. Note that the above phenomena are not accounted for in the classical theory of dielectrics.

The objective of the proposed paper is to state the boundary value problems of the local gradient theory of dielectrics and to prove the Reciprocity Theorem and the Uniqueness Theorem for the coupled linear problems of this theory. To this end, Section 2 presents a nonlinear complete set of relations of the said theory. Basing on these relations, Section 3 obtains a linearized governing set of equations and shows the possibility of its division into two subsystems of differential equations that can be solved consecutively. Boundary conditions for local gradient theory of dielectrics are presented in Section 4. Section 5 and Section 6 present and prove the Uniqueness and Reciprocity Theorems for linear local gradient theory of electrothermoelastic nonferromagnetic dielectrics.

2. Basic preliminaries

In this Section, we briefly present the basic ideas and equations that describe the coupled fields in the framework of a local gradient theory of electrothermoelastic nonferromagnetic dielectrics, according to Burak et al. [Burak et al. 2007; 2008; Kondrat and Hrytsyna 2008].

We consider a thermoelastic polarized solid body occupying a finite domain (V) bounded by a smooth boundary (Σ). The body is subjected to an action of external forces, thermal and electromagnetic loads. As a result the mechanical, heat, and electromagnetic processes are occurring within a body, potentially followed by changes in the material structure of a fixed small element of the body. Such changes in structure can be observed, for instance, in the near-surface regions of newly-created surfaces. They are caused by a violation of the atom force balance in these regions. In a local gradient theory of electrothermoelastic nonferromagnetic dielectrics, the said changes in material structure are described by mass fluxes $\boldsymbol{J}_{ms}$ of a non-diffusive and non-convective nature [Burak et al. 2007; 2008]. The mentioned changes in material structure are further related to the process of the local mass displacement.

Burak and co-workers [Burak et al. 2007; 2008] use the Cauchy stress tensor $\hat{\sigma}$ and strain tensor $\hat{e}$ to describe the mechanical fields, as well as the density of the heat flux $\boldsymbol{J}_q$, the absolute temperature T, and the entropy S to describe the process of heat conductivity. They characterize the electromagnetic field by the vectors of electric $\boldsymbol{D}$ and magnetic $\boldsymbol{B}$ inductions, electric $\boldsymbol{E}$ and magnetic $\boldsymbol{H}$ fields, and the polarization vector $\boldsymbol{\Pi}_e$. They introduce the vector of local mass displacement $\boldsymbol{\Pi}_m$, the density of the induced mass $\rho_{m\pi} = -\nabla \cdot \boldsymbol{\Pi}_m$, as well as the potential μ_π to describe the process of local mass displacement [Burak et al. 2008]. Here ∇ is the Hamilton operator; the dot denotes the scalar product. Note that the potential μ_π is defined as an energy measure of the effect of the local mass displacement on internal energy [Burak et al. 2008].

The result of accounting in the model description for the local mass displacement and its coupling to the mechanical, heat, and electromagnetic fields is a modification of the Gibbs equation. Along with the generally-accepted in classic electrothermoelasticity pairs of conjugate parameters of state (stress and strain tensors, temperature and entropy, polarization and electric field), the generalized Gibbs equation contains two additional pairs of parameters. The modified chemical potential $\mu'_\pi = \mu_\pi - \mu$ and specific density of induced mass comprise one pair of the parameters of state, while the specific vector of local

mass displacement $\boldsymbol{\pi}_m = \boldsymbol{\Pi}_m / \rho$ and the gradient of the modified chemical potential $\nabla \mu'_\pi$ comprise the other. Here, μ is chemical potential. Thus, within the scope of the developed theory, the Gibbs equation takes the following form [Burak et al. 2008]:

$$df = \frac{1}{\rho} \hat{\boldsymbol{\sigma}}_* : d\hat{\boldsymbol{e}} - s \, dT - \boldsymbol{\pi}_e \cdot d\boldsymbol{E}_* + \mu'_\pi d\rho_m + \boldsymbol{\pi}_m \cdot d\nabla \mu'_\pi. \tag{1}$$

Here, ρ is the mass density, $s = S/\rho$, $\boldsymbol{\pi}_e = \boldsymbol{\Pi}_e / \rho$, f is the free energy, $\boldsymbol{E}_* = \boldsymbol{E} + \boldsymbol{v} \times \boldsymbol{B}$, $\boldsymbol{v}$ is the velocity vector, and the symbol "$\times$" denotes the vector product.

The consequence of accounting for the processes of polarization and the local mass displacement is the modification of the stress tensor, which is now defined by the formula $\hat{\boldsymbol{\sigma}}_* = \hat{\boldsymbol{\sigma}} - \rho[\boldsymbol{\pi}_e \cdot \boldsymbol{E}_* + \rho_m \mu'_\pi - \boldsymbol{\pi}_m \cdot \nabla \mu'_\pi] \hat{\boldsymbol{I}}$, where $\hat{\boldsymbol{I}}$ is the unit tensor.

Using the differential 1-forms (1) for the generalized theory of dielectrics, we obtain the following constitutive equations:

$$\hat{\boldsymbol{\sigma}}_* = \rho \frac{\partial f}{\partial \hat{\boldsymbol{e}}}, \quad s = -\frac{\partial f}{\partial T}, \quad \boldsymbol{\pi}_e = -\frac{\partial f}{\partial \boldsymbol{E}_*}, \quad \mu'_\pi = \frac{\partial f}{\partial \rho_m}, \quad \boldsymbol{\pi}_m = \frac{\partial f}{\partial (\nabla \mu'_\pi)}. \tag{2}$$

The set of relations of local gradient electrothermomechanics of dielectrics includes the nonlocal constitutive equations (2), as well as the balance equations of mass, induced mass, and induced electric charge

$$\frac{\partial \rho}{\partial t} + \nabla \cdot (\rho \boldsymbol{v}) = 0, \tag{3}$$

$$\frac{\partial \rho_{m\pi}}{\partial t} + \nabla \cdot \boldsymbol{J}_{ms} = 0, \tag{4}$$

$$\frac{\partial \rho_{e\pi}}{\partial t} + \nabla \cdot \boldsymbol{J}_{es} = 0, \tag{5}$$

the momentum equation and the entropy balance equation

$$\rho \frac{d\boldsymbol{v}}{dt} = \nabla \cdot \hat{\boldsymbol{\sigma}}_* + \boldsymbol{F}_e + \rho(\boldsymbol{F} + \boldsymbol{F}'_*), \tag{6}$$

$$T \frac{\partial S}{\partial t} = -\nabla \cdot \boldsymbol{J}_q + \frac{1}{T} \boldsymbol{J}_q \cdot \nabla T - T \nabla \cdot (S \boldsymbol{v}) + T \sigma_s + \rho \mathfrak{R}, \tag{7}$$

the Maxwell equations and the conservation law of induced electric charges

$$\nabla \times \boldsymbol{E} = -\frac{\partial \boldsymbol{B}}{\partial t}, \quad \nabla \times \boldsymbol{H} = \boldsymbol{J}_e + \varepsilon_0 \frac{\partial \boldsymbol{E}}{\partial t} + \frac{\partial \boldsymbol{\Pi}_e}{\partial t}, \quad \nabla \cdot \boldsymbol{B} = 0, \quad \nabla \cdot \boldsymbol{D} = \rho_e, \tag{8}$$

$$\frac{\partial \rho_e}{\partial t} + \nabla \cdot \boldsymbol{J}_e = 0, \tag{9}$$

the constitutive relations

$$\boldsymbol{B} = \mu_0 \boldsymbol{H}, \qquad\qquad \boldsymbol{D} = \varepsilon_0 \boldsymbol{E} + \boldsymbol{\Pi}_e, \tag{10}$$

$$\boldsymbol{J}_q = \boldsymbol{J}_q\left(-\frac{\nabla T}{T^2}, \frac{\boldsymbol{E}_*}{T}\right), \quad \boldsymbol{J}_{e*} = \boldsymbol{J}_{e*}\left(-\frac{\nabla T}{T^2}, \frac{\boldsymbol{E}_*}{T}\right), \tag{11}$$

the geometric relations

$$\boldsymbol{v} = \frac{d\boldsymbol{u}}{dt}, \quad \hat{\boldsymbol{e}} = \tfrac{1}{2}[\boldsymbol{\nabla} \otimes \boldsymbol{u} + (\boldsymbol{\nabla} \otimes \boldsymbol{u})^T], \tag{12}$$

the relations for additional mass force $\boldsymbol{F}_*'$ and ponderomotive force $\boldsymbol{F}_e$

$$\boldsymbol{F}_*' = \rho_m \boldsymbol{\nabla} \mu_\pi' - (\boldsymbol{\nabla} \otimes \boldsymbol{\nabla} \mu_\pi') \cdot \boldsymbol{\pi}_m, \tag{13}$$

$$\boldsymbol{F}_e = \rho_e \boldsymbol{E}_* + \left[\boldsymbol{J}_{e*} + \frac{\partial(\rho \boldsymbol{\pi}_e)}{\partial t} \right] \times \boldsymbol{B} + \rho(\boldsymbol{\nabla} \otimes \boldsymbol{E}_*) \cdot \boldsymbol{\pi}_e, \tag{14}$$

the expression for the entropy production

$$\sigma_s = -\boldsymbol{J}_q \cdot \frac{\boldsymbol{\nabla} T}{T^2} + \boldsymbol{J}_{e*} \cdot \frac{\boldsymbol{E}_*}{T}, \tag{15}$$

the formulae

$$\boldsymbol{J}_{ms} = \frac{\partial \boldsymbol{\Pi}_m}{\partial t}, \quad \boldsymbol{J}_{es} = \frac{\partial \boldsymbol{\Pi}_e}{\partial t}, \tag{16}$$

and a corresponding series for the free energy $f = f(\hat{\boldsymbol{e}}, T, \boldsymbol{E}_*, \rho_m, \boldsymbol{\nabla} \mu_\pi')$.

Here t denotes the time variable, $\boldsymbol{u}$ is the displacement vector, $\boldsymbol{F}$ is the mass force, σ_s is the entropy production per unit of volume and time, $\mathfrak{R}$ denotes the distributed thermal sources, $\boldsymbol{J}_{ms}$ is the density of non-convective and non-diffusive mass flux, ρ_e denotes the density of free electric charges, $\rho_{e\pi} = -\boldsymbol{\nabla} \cdot \boldsymbol{\Pi}_e$ is the density of induced electric charge, $\boldsymbol{J}_e$ is the density of the electric current (convection and conduction currents), $\boldsymbol{J}_{es}$ is the polarization current, ε_0 and μ_0 are electric and magnetic constants, $\boldsymbol{J}_{e*} = \boldsymbol{J}_e - \rho_e \boldsymbol{v}$, $\otimes$ is the dyadic product, an upper index T denotes a transposed tensor, and $(d\dots/dt) = (\partial\dots/\partial t) + \boldsymbol{v} \cdot \boldsymbol{\nabla}\dots$.

In comparison to the classical theory of elasticity, Burak [1987] introduced into the space of constitutive parameters one additional pair of conjugate constitutive parameters, namely, the vector of the local mass displacement $\boldsymbol{\Pi}_m$ and the gradient of the chemical potential $\boldsymbol{\nabla}\mu$. Note that according to the generalized Gibbs equations (1), the set of conjugate variables for the thermoelastic dielectrics is complemented by two additional pairs of variables (μ_π', ρ_m) and $(\boldsymbol{\pi}_m, \boldsymbol{\nabla}\mu_\pi')$, related to the local mass displacement. The equation of motion (6) takes into account the additional stresses

$$\hat{\boldsymbol{\sigma}}_*' = -\rho(\rho_m \mu_\pi' - \boldsymbol{\pi}_m \cdot \boldsymbol{\nabla}\mu_\pi')\hat{\boldsymbol{I}}$$

and nonlinear mass force $\boldsymbol{F}'$ (see formula (13)), induced within the body by the local mass displacement.

In general, the set of equations (2)–(16) is nonlinear. The number of equations in this set can be reduced by substituting the geometric (12) and physical relations (2), (10), and (11), as well as the expression for the entropy production (15) into the Maxwell equations (8) and the balance equations (3)–(7), and (9).

Below we present a governing set of equations for a linear approximation. To this end, we should write the constitutive equations (2) and the kinetic equations (11) in the explicit form. For isotropic materials,

we obtain [Burak et al. 2008]:

$$\hat{\sigma}_* = 2G\hat{e} + \left[\left(K - \frac{2}{3}G\right)e - K(\alpha_T\theta + \alpha_\rho\rho_m)\right]\hat{I} \tag{17a}$$

$$s = s_o + \frac{G_V}{T_o}\theta + \frac{K\alpha_T}{\rho_o}e + \beta_{T_\rho}\rho_m, \tag{17b}$$

$$\mu'_\pi = \mu'_{\pi o} + d_\rho\rho_m - \beta_{T_\rho}\theta - \frac{K\alpha_\rho}{\rho_o}e, \tag{17c}$$

$$\boldsymbol{\pi}_e = \chi_E\boldsymbol{E} - \chi_{Em}\nabla\mu'_\pi, \tag{17d}$$

$$\boldsymbol{\pi}_m = -\chi_m\nabla\mu'_\pi + \chi_{Em}\boldsymbol{E}, \tag{17e}$$

$$\boldsymbol{J}_q = -\lambda\nabla\theta + \pi_t\boldsymbol{J}_e, \quad \boldsymbol{J}_e = \sigma_e\boldsymbol{E} - \eta\nabla\theta, \tag{18}$$

where, K, G, α_T, α_ρ, C_V, β_{T_ρ}, d_ρ, χ_E, χ_m, χ_{Em}, λ, σ_e, π_t, and η are the material characteristics, $e = \hat{e} : \hat{I}$, $\theta = T - T_o$, T_o, s_o, and $\mu'_{\pi o}$ are the temperature, entropy and modified chemical potential μ'_π in the reference state. Here, the reference state is considered to be an infinite medium without any disturbances of fields, that is, $\hat{e} = 0$, $\hat{\sigma}_* = 0$, $\boldsymbol{E}_* = 0$, $\boldsymbol{\pi}_e = 0$, $\boldsymbol{\pi}_m = 0$, $\nabla\mu'_\pi = 0$, $T = T_o$, $s = s_o$, $\rho_m = 0$, and $\mu'_\pi = \mu'_{\pi o}$.

3. Governing equations

Note that within the framework of a linear approximation, we have the following formula for the specific density of induced mass

$$\rho_m = -\nabla \cdot \boldsymbol{\pi}_m. \tag{19}$$

Substituting the formulas (10), (12), (16)–(19) into the balance equations (4), (6), (7) and the Maxwell equations (8), we obtain the following governing set of linearized equations to determine the functions $\boldsymbol{u}$, θ, $\tilde{\mu}'_\pi = \mu'_\pi - \mu'_{\mu o}$, $\boldsymbol{E}$, and $\boldsymbol{B}$:

$$\rho_o\frac{\partial^2\boldsymbol{u}}{\partial t^2} = \left(\bar{K} + \frac{1}{3}G\right)\nabla(\nabla \cdot \boldsymbol{u}) + G\Delta\boldsymbol{u} - K\bar{\alpha}_T\nabla\theta - K\frac{\alpha_\rho}{d_\rho}\nabla\tilde{\mu}'_\pi + \rho_o\boldsymbol{F}, \tag{20}$$

$$\rho_o\bar{C}_V\frac{\partial\theta}{\partial t} + KT_o\bar{\alpha}_T\frac{\partial(\nabla \cdot \boldsymbol{u})}{\partial t} + \rho_oT_o\frac{\beta_{T_\rho}}{d_\rho}\frac{\partial\tilde{\mu}'_\pi}{\partial t} = (\lambda + \pi_t\eta)\Delta\theta - \sigma_e\pi_t\nabla \cdot \boldsymbol{E} + \rho_o\mathfrak{R}, \tag{21}$$

$$\Delta\tilde{\mu}'_\mu - \lambda_\mu^2\tilde{\mu}'_\pi = \lambda_\mu^2\left(K\frac{\alpha_\rho}{\rho_o}\nabla \cdot \boldsymbol{u} + \beta_{T_\rho}\theta\right) + \frac{\chi_{Em}}{\chi_m}\nabla \cdot \boldsymbol{E}, \tag{22}$$

$$\nabla \times \boldsymbol{E} = -\frac{\partial\boldsymbol{B}}{\partial t}, \quad \nabla \times \boldsymbol{B} = \mu_0\sigma_e\boldsymbol{E} - \mu_0\eta\nabla\theta + \varepsilon\mu_0\frac{\partial}{\partial t}(\boldsymbol{E} - \kappa_E\nabla\tilde{\mu}'_\pi), \tag{23}$$

$$\nabla \cdot \boldsymbol{B} = 0, \quad \nabla \cdot \boldsymbol{E} - \kappa_E\Delta\tilde{\mu}'_\pi = \frac{\rho_e}{\varepsilon}. \tag{24}$$

Here, Δ is the Laplacian, and coefficients $\bar{K}$, $\bar{\alpha}_T$, $\bar{C}_V$, ε, and κ_E are defined by the formulae

$$\bar{K} = K - \frac{K^2\alpha_\rho^2}{\rho_od_\rho}, \quad \bar{\alpha}_T = \alpha_T + \beta_{T_\rho}\frac{\alpha_\rho}{d_\rho}, \quad \bar{C}_V = C_V + T_o\frac{\beta_{T_\rho}^2}{d_\rho},$$

$$\lambda_\mu = \left|\sqrt{d_\rho\chi_m}\right|^{-1}, \quad \varepsilon = \varepsilon_0 + \rho_o\chi_E, \quad \kappa_E = \rho_o\chi_{Em}/\varepsilon. \tag{25}$$

The parameter $l_* = 1/\lambda_\mu$ is a material constant, with the dimension of length, and is a characteristic length for near-surface phenomena [Burak et al. 2008]. The appearance of such a constant is related to the consideration in the material model of the local mass displacement. Such a parameter is absent in the classical theory, based on local constitutive relations. The characteristic length l_* may be determined by experiment methods (for example, the electron diffraction measurements), by methods of discrete analysis or the theory of crystal lattice dynamics, etc. Using the methods of lattice dynamics, Mindlin [1972] and Maugin [1988] showed that the characteristic length is the magnitude of the order of distance between the nearest atoms (for example, for Sodium chloride $l_* = 0.73 \cdot 10^{-10}$ m and for Potassium chloride $l_* = 0.93 \cdot 10^{-10}$ m [Mindlin 1972]).

Note that the ponderomotive force is absent in the momentum equation (20), as is Joule heat in the heat conduction equation (21). This is because in the chosen reference state the ponderomotive force and Joule heat are nonlinear functions of the perturbation of fields. We can see that compared to the classical theory of electrothermoelastic dielectrics, as a result of accounting for the process of the local mass displacement, an additional equation (22) appears in the governing set of equations. Another consequence of accounting for local mass displacement is a modification of the equation of motion (20), heat conduction (21), and electrodynamics (23)–(24), which now also contain addends related to the local mass displacement. The consideration of the impact of the gradient of modified chemical potential in the motion equation (20) may be quantitatively interpreted as the emergence of an additional mass force within the body, proportional to $\nabla \tilde{\mu}'_\pi$, while in the equation of heat conduction it may be interpreted as the emergence of a source of heat in the body of the power $-\rho_o T_o (\beta_{T_\rho}/d_\rho)(\partial \tilde{\mu}'_\pi/\partial t)$.

Note that the governing set of equations (20)–(24) can be easily divided into two unrelated subsystems, eliminating the electric field from the second and third equations of this set. Indeed, using the relations (24), equations (21) and (22) can be presented as follows:

$$\rho_o \bar{C}_V \frac{\partial \theta}{\partial t} + K T_o \bar{\alpha}_T \frac{\partial (\nabla \cdot \boldsymbol{u})}{\partial t} + \rho_o T_o \frac{\beta_{T_\rho}}{d_\rho} \frac{\partial \tilde{\mu}'_\pi}{\partial t} = (\lambda + \pi_t \eta) \Delta\theta - \sigma_e \pi_t \kappa_E \left(\Delta \tilde{\mu}'_\pi + \frac{\rho_e}{\rho_o \chi_{Em}} \right) + \rho_o \mathfrak{R}, \quad (26)$$

$$\Delta \tilde{\mu}'_\pi - \lambda^2_{\mu E} \tilde{\mu}'_\pi = \lambda^2_{\mu E} \left(K \frac{\alpha_\rho}{\rho_o} \nabla \cdot \boldsymbol{u} + \beta_{T_\rho}\theta \right) + \lambda^2_{\mu E} \chi_{Em} d_\rho \frac{\rho_e}{\varepsilon}. \quad (27)$$

Here, $\lambda^2_{\mu E} = \lambda^2_\mu (1 - \kappa_E \chi_{Em}/\chi_m)^{-1}$.

Now the formulated problem can be solved consecutively. To determine the functions $\boldsymbol{u}$, θ, and $\tilde{\mu}'_\pi$, we use the related set of equations (20), (26), and (27). The vectors of the electromagnetic field are derived from the equations (23) and (24), where the functions $\boldsymbol{u}$, θ, and $\tilde{\mu}'_\pi$ are known.

For ideal dielectrics, the governing set of equations above is simplified and looks as follows:

$$\rho_o \frac{\partial^2 \boldsymbol{u}}{\partial t^2} = \left(\bar{K} + \frac{1}{3}G \right) \nabla(\nabla \cdot \boldsymbol{u}) + G \Delta\boldsymbol{u} - K \bar{\alpha}_T \nabla\theta - K \frac{\alpha_\rho}{d_\rho} \nabla \tilde{\mu}'_\pi + \rho_o \boldsymbol{F}, \quad (28)$$

$$\rho_o \bar{C}_V \frac{\partial \theta}{\partial t} + T_o K \bar{\alpha}_T \frac{\partial (\nabla \cdot \boldsymbol{u})}{\partial t} + \rho_o T_o \frac{\beta_{T_\rho}}{d_\rho} \frac{\partial \tilde{\mu}'_\pi}{\partial t} = \lambda \Delta\theta + \rho_o \mathfrak{R}, \quad (29)$$

$$\Delta \tilde{\mu}'_\pi - \lambda^2_{\mu E} \tilde{\mu}'_\pi = \lambda^2_{\mu E} \left(K \frac{\alpha_\rho}{\rho_o} \nabla \cdot \boldsymbol{u} + \beta_{T_\rho}\theta \right), \quad (30)$$

$$\nabla \times \boldsymbol{E} = -\frac{\partial \boldsymbol{B}}{\partial t}, \quad \nabla \cdot \boldsymbol{B} = \varepsilon\mu_0 - \frac{\partial}{\partial t}(\boldsymbol{E} - \kappa_E \nabla \tilde{\mu}'_\pi), \quad (31)$$

$$\nabla \cdot \boldsymbol{B} = 0, \quad \nabla \cdot \boldsymbol{E} - \kappa_E \Delta \tilde{\mu}'_\pi = 0. \tag{32}$$

4. Boundary conditions

To complete the problems of the local gradient electrothermoelasticity, the boundary (or jump) conditions and initial conditions must be adjoined to the derived set of differential equations. These conditions ensure the uniqueness of the solution of the formulated problem. We proceed to specifying them below.

We assume the polarized solid is subjected to the following boundary conditions:

- mechanical conditions (displacement or traction (force per unit area) are prescribed):

$$\boldsymbol{u} = \boldsymbol{u}_a \quad \text{or} \quad \hat{\boldsymbol{\sigma}}_* \cdot \boldsymbol{n} = \sigma_a, \tag{33}$$

- thermal boundary conditions (temperature, normal heat flux or condition of convective heat exchange are prescribed):

$$T = T_a \quad \text{or} \quad \boldsymbol{J}_q \cdot \boldsymbol{n} = J_{qa}, \quad \text{or} \quad \boldsymbol{J}_q \cdot \boldsymbol{n} - H_*(T - T_c) = 0, \tag{34}$$

- condition for local mass displacement:

$$\mu'_\pi = \mu'_{\pi a}, \tag{35}$$

- electromagnetic boundary conditions are written as a prescribing of a tangential components of vectors of electric and magnetic fields:

$$\boldsymbol{E} \times \boldsymbol{n} = \boldsymbol{E}_a, \quad \boldsymbol{H} \times \boldsymbol{n} = \boldsymbol{H}_a. \tag{36}$$

In the relations (33)–(36): $\boldsymbol{n}$ is the outward unit normal to the smooth boundary (Σ); $\boldsymbol{u}_a$, $\boldsymbol{\sigma}_a$, $\boldsymbol{E}_a$, $\boldsymbol{H}_a$, J_{qa}, T_a, and $\mu'_{\pi a}$ are given on the surface (Σ) values of the displacement vector, of traction, of the electric and magnetic fields, of the normal component of heat flux, of temperature, and of the modified chemical potential μ'_π; H_* is a heat transfer coefficient from the surface and is the surrounding environment temperature.

In some cases, certain conditions for the body surface can be formulated as boundary, while others — as jump conditions. Indeed, let the body be in contact with a vacuum or an environment with similar properties. In this case, mechanical conditions may be formulated as displacement (kinematic) boundary conditions (if displacements are known on the body surface) or traction boundary conditions (corresponding to a traction-free surface). Thermal boundary conditions should correspond to the prescription of the surface temperature (if we can control it) or the flux from the surface. Now, the equality between the potential μ'_π and zero is a condition for the local mass displacement. Since the perturbation of the electrothermomechanical processes within the body will cause the radiation of the electromagnetic field into the vacuum, the electromagnetic conditions on the body surface should be formulated as contact conditions. Therefore, the Maxwell equations in a vacuum (domain (V_v)) need to be added to the governing set of equations:

$$\nabla \times \boldsymbol{E}_v = -\frac{\partial \boldsymbol{B}_v}{\partial t}, \quad \nabla \times \boldsymbol{H}_v = \frac{\partial \boldsymbol{D}_v}{\partial t}, \quad \nabla \cdot \boldsymbol{B}_v = 0, \quad \nabla \cdot \boldsymbol{D}_v = 0, \tag{37}$$

$$\boldsymbol{D}_v = \varepsilon_0 \boldsymbol{E}_v, \quad \boldsymbol{B}_v = \mu_0 \boldsymbol{H}_v, \tag{38}$$

where $\boldsymbol{E}_v$, $\boldsymbol{H}_v$, $\boldsymbol{D}_v$, and $\boldsymbol{B}_v$ are the electric and magnetic fields, and inductions in vacuum.

The jump conditions take the following form

$$(\boldsymbol{E} - \boldsymbol{E}_v) \times \boldsymbol{n} = 0, \qquad (\boldsymbol{H} - \boldsymbol{H}_v) \times \boldsymbol{n} = \boldsymbol{i}_s + \rho_{es}\boldsymbol{v}_s, \tag{39}$$

$$(\boldsymbol{D} - \boldsymbol{D}_v) \cdot \boldsymbol{n} = -\rho_{es}, \qquad (\boldsymbol{B} - \boldsymbol{B}_v) \cdot \boldsymbol{n} = 0. \tag{40}$$

Here, ρ_{es} and $\boldsymbol{i}_s$ are the surface densities of electric charges and current; $\boldsymbol{v}_s$ is a tangent component of velocity to the body surface.

To solve non-stationary problems, it is necessary to write the corresponding initial conditions. We write them as follows

$$\boldsymbol{u} = \boldsymbol{u}^0, \quad \frac{\partial \boldsymbol{u}}{\partial t} = \boldsymbol{v}^0, \quad \theta = 0, \quad \tilde{\mu}'_\pi = 0, \quad \boldsymbol{E} = \boldsymbol{E}^0, \quad \boldsymbol{B} = \boldsymbol{B}^0, \quad \text{at} \quad t = 0. \tag{41}$$

Note that in conditions (41) it is assumed that the initial time corresponds to the reference equilibrium state of the thermodynamic system.

The coupled initial-boundary-value problem is to determine the displacement vector $\boldsymbol{u}(\boldsymbol{r}, t)$, temperature change $\theta(\boldsymbol{r}, t)$, modified chemical potential $\tilde{\mu}'_\pi(\boldsymbol{r}, t)$, electric field $\boldsymbol{E}(\boldsymbol{r}, t)$ and magnetic induction $\boldsymbol{B}(\boldsymbol{r}, t)$ of $C^{(2)}$ in the medium, governed by the equations (28)–(32) and subject to the boundary conditions (33)–(35), jump conditions (39), (40), and initial conditions (41). We define the electric field $\boldsymbol{E}_v(\boldsymbol{r}, t)$ and magnetic induction $\boldsymbol{B}_v(\boldsymbol{r}, t)$ in a vacuum using the equations (37) and (38).

5. Uniqueness theorem

As shown above, the set of differential equations for local gradient electrothermoelasticity can be divided into two uncoupled subsystems. In view of this, we study the conditions of uniqueness of the solution to the corresponding problems in mathematical physics in two stages: separately for the equations of motion (20), heat conduction (26) and modified chemical potential (27), and separately for the equations of electrodynamics (31) and (32).

Theorem 1. *For a domain* (V) *bounded by a smooth surface* (Σ), *and positive* G, $K - \frac{2}{3}G - K^2\alpha_\rho^2/(\rho_o d_\rho)$, C_V, d_ρ, χ_m, *and* H_* *there is no more than one set of functions* $\boldsymbol{u}(\boldsymbol{r}, t)$, $\theta(\boldsymbol{r}, t)$, *and* $\tilde{\mu}'_\pi(\boldsymbol{r}, t)$ *that*

- $\forall \boldsymbol{r} \in (V) \cup (\Sigma) : (\boldsymbol{u}, \theta, \tilde{\mu}'_\pi) \in C^{(2)}$;

- $\forall \boldsymbol{r} \in (V)$ *satisfies the set of differential equations* (28)–(30);

- $\forall \boldsymbol{r} \in (V) \cup (\Sigma)$ *satisfies the strain-displacement relation* (12)$_2$, *the constitutive equations* (17) *and* (18)$_1$;

- *satisfies the boundary and initial conditions*:

$$\hat{\boldsymbol{\sigma}}_* \cdot \boldsymbol{n} = \boldsymbol{\sigma}^a, \quad \boldsymbol{J}_q \cdot \boldsymbol{n} - H_*(\theta - \theta_c) = 0, \quad \tilde{\mu}'_\pi = \mu'_{\pi a}, \quad \forall \boldsymbol{r} \in (\Sigma),$$

$$\boldsymbol{u} = \boldsymbol{u}^0, \quad \frac{\partial \boldsymbol{u}}{\partial t} = \boldsymbol{v}^0, \quad \theta = 0, \quad \tilde{\mu}'_\pi = 0, \quad \text{at} \quad t = 0.$$

Proof. For the linear problems, the material time derivative is equal to Eulerian time derivative. Then, using the Gibbs equation (1) and the Legendre transformation $u = f + Ts + \boldsymbol{E}_* \cdot \boldsymbol{\pi}_e - \nabla\mu'_\pi \cdot \boldsymbol{\pi}_m$, for the

specific internal energy u, we can write

$$\rho_o \frac{\partial u}{\partial t} = \rho_o T_o \frac{\partial s}{\partial t} + \rho_o \mu'_{\pi o} \frac{\partial \rho_m}{\partial t} + \hat{\boldsymbol{\sigma}}_* : \frac{\partial \hat{\boldsymbol{e}}}{\partial t} + \rho_o \theta \frac{\partial s}{\partial t} + \rho_o \tilde{\mu}'_\pi \frac{\partial \rho_m}{\partial t} - \rho_o \nabla \tilde{\mu}'_\pi \cdot \frac{\partial \boldsymbol{\pi}_m}{\partial t}. \tag{42}$$

We substitute the constitutive equations (17) into nonlinear summands of the relation (42). After some transformations, we obtain:

$$\rho_o \frac{\partial u}{\partial t} = \rho_o T_o \frac{\partial s}{\partial t} + \rho_o \mu'_{\pi 0} \frac{\partial \rho_m}{\partial t}$$
$$+ \frac{1}{2} \frac{\partial}{\partial t} \left[\left(\bar{K} - \frac{2}{3}G \right) I_1^2 + 2G I_2 + \rho_o \frac{\bar{C}_V}{T_o} \theta^2 + \frac{\rho_o}{d_\rho} (\tilde{\mu}'_\pi)^2 + \rho_o \chi_m \nabla \tilde{\mu}'_\pi \cdot \nabla \tilde{\mu}'_\pi + 2\rho_o \frac{\beta_{T_\rho}}{d_\rho} \theta \tilde{\mu}'_\pi \right]. \tag{43}$$

The proof of the theorem will be based on the energy balance equation, which for the model of the thermoelastic solid has the form [Kondrat and Hrytsyna 2009]

$$\frac{\partial}{\partial t} \int_{(V)} \rho_o \left(u + \frac{1}{2} v^2 \right) dV = \int_{(V)} \rho_o (\boldsymbol{F} \cdot \boldsymbol{v} + \mathfrak{R}) \, dV - \oint_{(\Sigma)} \left(\boldsymbol{J}_q - \hat{\boldsymbol{\sigma}}_* \cdot \boldsymbol{v} + \mu'_\pi \frac{\partial \boldsymbol{\Pi}_m}{\partial t} \right) \cdot \boldsymbol{n} \, d\Sigma.$$

Hence, making use of the expression (43), formula (19), kinetic equation (18)$_1$, entropy balance equation (7) and divergence theorem, we can write

$$\frac{\partial \mathscr{E}_*}{\partial t} = \int_{(V)} \left(\rho_o \boldsymbol{F} \cdot \boldsymbol{v} + \rho_o \mathfrak{R} \frac{\theta}{T} - T_o \sigma_s \right) dV + \oint_{(\Sigma)} \left[\boldsymbol{\sigma}_n \cdot \boldsymbol{v} - \frac{H_*}{T} \theta^2 + \frac{\theta}{T} \left(\lambda \frac{\partial \theta}{\partial n} + H_* \theta \right) - \rho_o \tilde{\mu}'_\pi \frac{\partial \pi_{mn}}{\partial t} \right] d\Sigma. \tag{44}$$

Here, $(\partial \theta / \partial n) = \nabla \theta \cdot \boldsymbol{n}$, $\pi_{mn} = \boldsymbol{\pi}_m \cdot \boldsymbol{n}$, and

$$\mathscr{E}_* = \frac{1}{2} \int_{(V)} \left[\rho_o v^2 + \left(\bar{K} - \frac{2}{3}G \right) I_1^2 + 2G I_2 + \rho_o \frac{C_V}{T_o} \theta^2 + \rho_o \chi_m (\nabla \tilde{\mu}'_\pi)^2 + \frac{\rho_o}{d_\rho} (\tilde{\mu}'_\pi + \beta_{T_\rho} \theta)^2 \right] dV. \tag{45}$$

The energy balance (44) makes it possible to prove the uniqueness of the solution.

We assume that two distinct solutions $\boldsymbol{u}_1(\boldsymbol{r}, t)$, $\theta_1(\boldsymbol{r}, t)$, $\tilde{\mu}'_{\pi 1}(\boldsymbol{r}, t)$ and $\boldsymbol{u}_2(\boldsymbol{r}, t)$, $\theta_2(\boldsymbol{r}, t)$, $\tilde{\mu}'_{\pi 2}(\boldsymbol{r}, t)$ satisfy the equations (28)–(30) and the appropriate boundary and initial conditions. Their difference $\boldsymbol{u} = \boldsymbol{u}_1 - \boldsymbol{u}_2$, $\theta = \theta_1 - \theta_2$, and $\tilde{\mu}'_\pi = \tilde{\mu}'_{\pi 1} - \tilde{\mu}'_{\pi 2}$ therefore satisfies the homogeneous equations (28)–(30) and the homogeneous boundary and initial conditions:

$$\forall \boldsymbol{r} \in (\Sigma): \hat{\boldsymbol{\sigma}}_* \cdot \boldsymbol{n} = 0, \quad \lambda \frac{\partial \theta}{\partial n} + H_* \theta = 0, \quad \tilde{\mu}'_\pi = 0, \tag{46}$$

$$\boldsymbol{u} = 0, \quad \frac{\partial \boldsymbol{u}}{\partial t} = 0, \quad \theta = 0, \quad \tilde{\mu}'_\pi = 0, \quad \text{at} \quad t = 0. \tag{47}$$

In view of the homogeneity of the equations and boundary conditions (46), from the equation of energy balance (44) we obtain

$$\frac{\partial \mathscr{E}_*}{\partial t} = - \int_{(V)} T_o \sigma_s \, dV - \oint_{(\Sigma)} \frac{H_*}{T} \theta^2 \, d\Sigma.$$

Because $\sigma_s \geq 0$ and $(H_*/T) \geq 0$, the following inequality should hold

$$\frac{\partial \mathscr{E}_*}{\partial t} \leq 0. \tag{48}$$

The difference of solutions satisfies the zero initial conditions, and, therefore $\mathscr{E}_*$ equals zero at the initial moment of time. Thus, from inequality (48) it follows that the function $\mathscr{E}_*$ is either negative or zero: $\mathscr{E}_* \leq 0$. On the other hand, according to (45) we have that $\mathscr{E}_* > 0$ since G, $K - (2/3)G - (K^2\alpha_\rho^2/\rho_o d_\rho)$, C_V, d_ρ, and χ_m are positive-definite. The above two inequalities can be fulfilled only if $\mathscr{E}_* = 0$. Consequently, taking into account the formula (45), we can write

$$\int_{(V)}\left[\rho_o \boldsymbol{v}^2 + \left(\bar{K} - \frac{2}{3}G\right)I_1^2 + 2G\,I_2 + \rho_o\frac{C_V}{T_o}\theta^2 + \rho_o\chi_m(\boldsymbol{\nabla}\tilde{\mu}'_\pi)^2 + \frac{\rho_o}{d_\rho}(\tilde{\mu}'_\pi + \beta_{T_\rho}\theta)^2\right]dV = 0.$$

Since $K - (2/3)G - (K^2\alpha_\rho^2/\rho_o d_\rho) > 0$, $G > 0$, $C_V > 0$, $d_\rho > 0$, and $\chi_m > 0$ and the relation in brackets is positive-definite, from last formula we get: $\boldsymbol{v} = 0$, $\hat{\boldsymbol{e}} = 0$, $\theta = 0$, $\tilde{\mu}'_\pi = 0$, and $\boldsymbol{\nabla}\tilde{\mu}'_\pi = 0$. Using the constitutive equation (17), we also obtain that $\rho_m = 0$ and $\boldsymbol{\pi}_m = 0$. So: $\boldsymbol{u}_1 = \boldsymbol{u}_2$, $\theta_1 = \theta_2$, and $\tilde{\mu}'_{\pi 1} = \tilde{\mu}'_{\pi 2}$. Therefore the coupled initial-boundary-value problem of local gradient thermoelasticity has only one solution, which is what we set out to demonstrate. $\qquad\square$

Theorem 2. *If ε_0, μ_0, χ_E, σ_e are positive and the functions $\boldsymbol{u}(\boldsymbol{r}, t)$, $\theta(\boldsymbol{r}, t)$, and $\tilde{\mu}'_\pi(\boldsymbol{r}, t)$ are known, then for the body domain (V) and vacuum (V_ν), separated by a smooth surface (Σ), there is not more than one set of functions $(\boldsymbol{E}, \boldsymbol{H}, \boldsymbol{E}_\nu, \boldsymbol{H}_\nu)$, such that*

- *$\forall \boldsymbol{r} \in (V) \cup (\Sigma)$ and $\forall \boldsymbol{r}_\nu \in (V_\nu) \cup (\Sigma) : (\boldsymbol{E}, \boldsymbol{H}, \boldsymbol{E}_\nu, \boldsymbol{H}_\nu) \in C^{(2)}$;*

- *$\forall \boldsymbol{r} \in (V)$ satisfy the differential equations (8) and $\forall \boldsymbol{r}_\nu \in (V_\nu)$ satisfy the equation (37), respectively;*

- *$\forall \boldsymbol{r} \in (V) \cup (\Sigma)$ satisfy the constitutive relations (10), (17d) and the kinetic equation (18)$_2$, and $\forall \boldsymbol{r}_\nu \in (V_\nu) \cup (\Sigma)$ satisfy the constitutive relations (38), respectively;*

- *$\forall \boldsymbol{r}, \boldsymbol{r}_\nu \in (\Sigma)$ fulfils the jump conditions (39) and the initial conditions*

$$\boldsymbol{E} = \boldsymbol{E}^0, \quad \boldsymbol{H} = \boldsymbol{H}^0, \quad \boldsymbol{E}_\nu = \boldsymbol{E}_\nu^0, \quad \boldsymbol{H}_\nu = \boldsymbol{H}_\nu^0, \quad \text{at} \quad t = 0.$$

Proof. Suppose that the two sets of fields $(\boldsymbol{E}_1, \boldsymbol{H}_1, \boldsymbol{E}_{\nu 1}, \boldsymbol{H}_{\nu 1})$ and $(\boldsymbol{E}_2, \boldsymbol{H}_2, \boldsymbol{E}_{\nu 2}, \boldsymbol{H}_{\nu 2})$ solve the above problem. The difference fields $\boldsymbol{E} = \boldsymbol{E}_1 - \boldsymbol{E}_2$, $\boldsymbol{H} = \boldsymbol{H}_1 - \boldsymbol{H}_2$, $\boldsymbol{E}_\nu = \boldsymbol{E}_{\nu 1} - \boldsymbol{E}_{\nu 2}$, and $\boldsymbol{H}_\nu = \boldsymbol{H}_{1\nu} - \boldsymbol{H}_{2\nu}$ satisfy the relations (8), (37), the trivial initial conditions, the constitutive relations (10), (38), as well as

$$\boldsymbol{\Pi}_e = \rho_o \chi_E \boldsymbol{E}, \tag{49}$$

and the kinetic equation

$$\boldsymbol{J}_e = \sigma_e \boldsymbol{E}. \tag{50}$$

These functions satisfy the following energy balance equations for the electromagnetic field [Burak et al. 2008]:

$$\frac{\partial U_e}{\partial t} + \boldsymbol{\nabla} \cdot \boldsymbol{S}_e + \left(\boldsymbol{J}_e + \frac{\partial \boldsymbol{\Pi}_e}{\partial t}\right) \cdot \boldsymbol{E} = 0, \tag{51}$$

$$\frac{\partial U_{ev}}{\partial t} + \boldsymbol{\nabla} \cdot \boldsymbol{S}_{ev} = 0, \tag{52}$$

where

$$U_e = \frac{1}{2}(\varepsilon_0 \boldsymbol{E}^2 + \mu_0 \boldsymbol{H}^2), \quad \boldsymbol{S}_e = \boldsymbol{E} \times \boldsymbol{H}, \tag{53}$$

$$U_{ev} = \frac{1}{2}(\varepsilon_0 \boldsymbol{E}_v^2 + \mu_0 \boldsymbol{H}_v^2), \quad \boldsymbol{S}_{ev} = \boldsymbol{E}_v \times \boldsymbol{H}_v. \tag{54}$$

Substituting the formulae (53), (49), and (50) into (51), after some manipulations we obtain

$$\frac{1}{2}\frac{\partial}{\partial t}(\varepsilon \boldsymbol{E}^2 + \mu_0 \boldsymbol{H}^2) + \nabla \cdot (\boldsymbol{E} \times \boldsymbol{H}) + \sigma_e \boldsymbol{E} \cdot \boldsymbol{E} = 0.$$

Here, ε is defined by the formula $(25)_1$. By integrating the obtained expression over the region (V), and using the divergence theorem, we obtain

$$\frac{1}{2}\int_{(V)}\frac{\partial}{\partial t}(\varepsilon \boldsymbol{E}^2 + \mu_0 \boldsymbol{H}^2)\,dV = -\int_{(\Sigma)}(\boldsymbol{E} \times \boldsymbol{H}) \cdot \boldsymbol{n}\,d\Sigma - \sigma_e \int_{(V)} \boldsymbol{E}^2\,dV. \tag{55}$$

Substituting the formula (54) into the equation (52) and integrating the obtained result over the domain (V_v), we obtain

$$\frac{1}{2}\int_{(V_v)}\frac{\partial}{\partial t}(\varepsilon_0 \boldsymbol{E}_v^2 + \mu_0 \boldsymbol{H}_v^2)\,dV = \int_{(\Sigma)}(\boldsymbol{E}_v \times \boldsymbol{H}_v) \cdot \boldsymbol{n}\,d\Sigma. \tag{56}$$

Combining the expressions (55) and (56), we find that

$$\frac{\partial U_e^t}{\partial t} = -\int_{(\Sigma)}[(\boldsymbol{E} \times \boldsymbol{H}) - (\boldsymbol{E}_v \times \boldsymbol{H}_v)] \cdot \boldsymbol{n}\,d\Sigma - \sigma_e \int_{(V)} \boldsymbol{E}^2\,dV, \tag{57}$$

where

$$U_e^t = \frac{1}{2}\left[\int_{(V)}(\varepsilon \boldsymbol{E}^2 + \mu_0 \boldsymbol{H}^2)\,dV + \int_{(V_v)}(\varepsilon_0 \boldsymbol{E}_v^2 + \mu_0 \boldsymbol{H}_v^2)\,dV\right] \geq 0. \tag{58}$$

In view of the jump conditions (39), we can write the expression (57) as follows

$$\frac{\partial U_e^t}{\partial t} = -\int_{(\Sigma)}\boldsymbol{E}_s \cdot \boldsymbol{i}_s\,d\Sigma - \sigma_e \int_{(V)} \boldsymbol{E}^2\,dV.$$

Since $\boldsymbol{i}_s = \sigma_e \boldsymbol{E}_s$, where $\boldsymbol{E}_s$ is the tangential component of vector of the electric field, we have

$$\frac{\partial U_e^t}{\partial t} = -\sigma_e \int_{(\Sigma)}\boldsymbol{E}_s^2\,d\Sigma - \sigma_e \int_{(V)} \boldsymbol{E}^2\,dV. \tag{59}$$

From the formula (59) it follows that $(\partial U_e^t / \partial t) \leq 0$, since σ_e is positive. Thus, U_e^t is either a decreasing function, or a constant. Since at the initial time $t = 0$ the functions $\boldsymbol{E}$, $\boldsymbol{H}$, $\boldsymbol{E}_v$, $\boldsymbol{H}_v$ satisfy the trivial initial conditions, then the function U_e^t is equal to zero at the initial moment in time. Hence $U_e^t \leq 0$. At the same time, as follows from (58), the function U_e^t is positive definite or equal to zero: $U_e^t \geq 0$. The last two inequalities hold only if $U_e^t = 0$. Thus

$$U_e^t = \frac{1}{2}\left[\int_{(V)}(\varepsilon \boldsymbol{E}^2 + \mu_0 \boldsymbol{H}^2)\,dV + \int_{(V_v)}(\varepsilon_0 \boldsymbol{E}_v^2 + \mu_0 \boldsymbol{H}_v^2)\,dV\right] = 0.$$

Since $\varepsilon_0 > 0$, $\mu_0 > 0$, $\varepsilon = \varepsilon_0 + \rho_o \chi_E > 0$, from above equation we obtain that $\boldsymbol{E} = \boldsymbol{E}_1 - \boldsymbol{E}_2 = 0$, $\boldsymbol{H} = \boldsymbol{H}_1 - \boldsymbol{H}_2 = 0$, $\boldsymbol{E}_\nu = \boldsymbol{E}_{\nu 1} - \boldsymbol{E}_{\nu 2} = 0$, and $\boldsymbol{H}_\nu = \boldsymbol{H}_{1\nu} - \boldsymbol{H}_{2\nu} = 0$. Thus $\boldsymbol{E}_1 = \boldsymbol{E}_2$, $\boldsymbol{H}_1 = \boldsymbol{H}_2$, $\boldsymbol{E}_{\nu 1} = \boldsymbol{E}_{\nu 2}$, and $\boldsymbol{H}_{1\nu} = \boldsymbol{H}_{2\nu}$, which is what had to be proved. This completes the proof. $\qquad \square$

6. Reciprocal theorem

We consider two different stress-strain states of dielectric solid, caused by two sets of external loading, namely, the mass force $\boldsymbol{F}_*$ and $\boldsymbol{F}'_*$; the thermal sources $\mathfrak{R}$ and $\mathfrak{R}'$; the surface loadings $\boldsymbol{\sigma}_*$ and $\boldsymbol{\sigma}'_*$ on the surface (Σ_σ); the displacements $\boldsymbol{u}$ and $\boldsymbol{u}'$ on the surface (Σ_u); the surface electric charges $\boldsymbol{\Pi}_e \cdot \boldsymbol{n}$ and $\boldsymbol{\Pi}'_e \cdot \boldsymbol{n}$ on the surface (Σ_p); the electric potentials φ_e and φ'_e on the surface (Σ_φ); the disturbance of the temperature θ and θ' on the surface (Σ_θ); the heat fluxes $\boldsymbol{J}_q$ and $\boldsymbol{J}'_q$ on the surface (Σ_J); the vectors of local mass displacement $\boldsymbol{\pi}_m$ and $\boldsymbol{\pi}'_m$ on the surface (Σ_π) and the potentials $\tilde{\mu}'_\pi$ and $(\tilde{\mu}'_\pi)'$ on the surface (Σ_μ). Here, $(\Sigma_\sigma) \cup (\Sigma_u) = (\Sigma)$, $(\Sigma_\sigma) \cap (\Sigma_u) = \varnothing$, $(\Sigma_\theta) \cup (\Sigma_J) = (\Sigma)$, $(\Sigma_\theta) \cap (\Sigma_J) = \varnothing$, $(\Sigma_\varphi) \cup (\Sigma_p) = (\Sigma)$, $(\Sigma_\varphi) \cap (\Sigma_p) = \varnothing$, $(\Sigma_\pi) \cup (\Sigma_\mu) = (\Sigma)$, $(\Sigma_\pi) \cap (\Sigma_\mu) = \varnothing$. The consequence of such an external action is the two states of the body, which we can be described by the stress tensors $\hat{\boldsymbol{\sigma}}_*$, $\hat{\boldsymbol{\sigma}}'_*$ and strain tensors $\hat{\boldsymbol{e}}$, $\hat{\boldsymbol{e}}'$, by disturbances of temperature θ, and θ' specific entropies s, s', by specific densities of induced mass ρ_m, ρ'_m and modified potentials $\tilde{\mu}'_\pi$, $(\tilde{\mu}'_\pi)'$, by the specific vectors of local mass displacement $\boldsymbol{\pi}_m$, $\boldsymbol{\pi}'_m$ and gradients of potentials $\nabla \tilde{\mu}'_\pi$, $(\nabla \tilde{\mu}'_\pi)'$, as well as by the specific vectors of polarization $\boldsymbol{\pi}_e$, $\boldsymbol{\pi}'_e$ and the electric fields $\boldsymbol{E}$, $\boldsymbol{E}'$ correspondingly.

We apply a one-sided Laplace transform

$$\mathscr{L}[f(\boldsymbol{r}, t)] = f^L(\boldsymbol{r}, \zeta) = \int_0^\infty f(\boldsymbol{r}, t)\, e^{-\zeta t}\, dt,$$

to the equations of the local gradient theory of dielectrics that are provided in Section 2. Here, $f(\boldsymbol{r}, t) = \{\hat{\boldsymbol{\sigma}}_*, \hat{\boldsymbol{e}}, \boldsymbol{F}_*, \boldsymbol{u}, \boldsymbol{B}, \boldsymbol{E}, \boldsymbol{D}, \boldsymbol{H}, \boldsymbol{\pi}_e, \boldsymbol{\pi}_m, \theta, \mu'_\pi, \rho_m, \mathfrak{R}\}$, and ζ is a parameter of the Laplace transform.

Assume that all initial conditions for the perturbation of functions are equal to zero. For the considered two systems of external loads, applying a Laplace transform to the linearized momentum equation (6), we obtain

$$\nabla \cdot \hat{\boldsymbol{\sigma}}_*^L + \rho_o \boldsymbol{F}_*^L = \rho_o \zeta^2 \boldsymbol{u}^L, \tag{60}$$

$$\nabla \cdot \hat{\boldsymbol{\sigma}}_*^{\prime L} + \rho_o \boldsymbol{F}_*^{\prime L} = \rho_o \zeta^2 \boldsymbol{u}^{\prime L}. \tag{61}$$

Multiplying the equations (60) and (61) by the displacement vectors $\boldsymbol{u}^{\prime L}$ and $\boldsymbol{u}^L$, respectively, taking a difference between the obtained relations and integrating the result over the body volume (V), we obtain the following formula:

$$\int_{(V)} \left[(\nabla \cdot \hat{\boldsymbol{\sigma}}_*^L) \cdot \boldsymbol{u}^{\prime L} + \rho_o \boldsymbol{F}_*^L \cdot \boldsymbol{u}^{\prime L} - (\nabla \cdot \hat{\boldsymbol{\sigma}}_*^{\prime L}) \cdot \boldsymbol{u}^L - \rho_o \boldsymbol{F}_*^{\prime L} \cdot \boldsymbol{u}^L \right] dV = 0. \tag{62}$$

Making use of the relations

$$(\nabla \cdot \hat{\boldsymbol{\sigma}}_*^L) \cdot \boldsymbol{u}^{\prime L} = \nabla \cdot (\hat{\boldsymbol{\sigma}}_*^L \cdot \boldsymbol{u}^{\prime L}) - \hat{\boldsymbol{\sigma}}_*^L : \nabla \boldsymbol{u}^{\prime L}, \quad (\nabla \cdot \hat{\boldsymbol{\sigma}}_*^{\prime L}) \cdot \boldsymbol{u}^L = \nabla \cdot (\hat{\boldsymbol{\sigma}}_*^{\prime L} \cdot \boldsymbol{u}^L) - \hat{\boldsymbol{\sigma}}_*^{\prime L} : \nabla \boldsymbol{u}^L,$$

the formula $(12)_2$ and the divergence theorem, from the integral equation (62), we arrive at

$$\int_{(\Sigma)} \left(\boldsymbol{\sigma}_*^L \cdot \boldsymbol{u}'^L - \boldsymbol{\sigma}_*'^L \cdot \boldsymbol{u}^L \right) d\Sigma + \int_{(V)} \rho_o \left(\boldsymbol{F}_*^L \cdot \boldsymbol{u}'^L - \boldsymbol{F}_*'^L \cdot \boldsymbol{u}^L \right) dV = \int_{(V)} \left(\hat{\boldsymbol{\sigma}}_*^L : \hat{\boldsymbol{e}}'^L - \hat{\boldsymbol{\sigma}}_*'^L : \hat{\boldsymbol{e}}^L \right) dV.$$

Here $\boldsymbol{\sigma}_*^L = \hat{\boldsymbol{\sigma}}_*^L \cdot \boldsymbol{n}$, and $\boldsymbol{\sigma}_*'^L = \hat{\boldsymbol{\sigma}}_*'^L \cdot \boldsymbol{n}$.

Substituting the constitutive equation (17a) into the right-hand side of the obtained equation leads to the following result:

$$\int_{(\Sigma)} \left(\boldsymbol{\sigma}_*^L \cdot \boldsymbol{u}'^L - \boldsymbol{\sigma}_*'^L \cdot \boldsymbol{u}^L \right) d\Sigma + \int_{(V)} \rho_o \left(\boldsymbol{F}_*^L \cdot \boldsymbol{u}'^L - \boldsymbol{F}_*'^L \cdot \boldsymbol{u}^L \right) dV$$

$$= K\alpha_T \int_{(V)} (\theta'^L e^L - \theta^L e'^L) \, dV - K\alpha_\rho \int_{(V)} \left(\rho_m^L e'^L - \rho_m'^L e^L \right) dV. \quad (63)$$

Let us return to the equation of entropy balance (7). Making use of constitutive equations (17b) and $(18)_1$, from this equation in linear approximation we obtain the following heat equation for ideal dielectrics

$$\rho_o C_V \frac{\partial \theta}{\partial t} = \lambda \Delta\theta - T_o K \alpha_T \frac{\partial e}{\partial t} - \rho_o T_o \beta_{T_\rho} \frac{\partial \rho_m}{\partial t} + \rho_o \mathfrak{R}. \quad (64)$$

Applying a Laplace transform to the equation (64), for two systems of external loads, we can write

$$\rho_o C_V \zeta \theta^L = \lambda \Delta\theta^L - T_o K \alpha_T \zeta e^L - \rho_o T_o \beta_{T_\rho} \zeta \rho_m^L + \rho_o \mathfrak{R}^L, \quad (65)$$

$$\rho_o C_V \zeta \theta'^L = \lambda \Delta\theta'^L - T_o K \alpha_T \zeta e'^L - \rho_o T_o \beta_{T_\rho} \zeta \rho_m'^L + \rho_o \mathfrak{R}'^L. \quad (66)$$

Multiplying the equations (65) and (66) by the functions θ'^L and θ^L, respectively, taking a difference between the obtained expressions and integrating the result over the region (V), eventually we find that

$$\lambda \int_{(V)} (\theta'^L \Delta\theta^L - \theta^L \Delta\theta'^L) \, dV - T_o K \alpha_T \zeta \int_{(V)} (\theta'^L e^L - \theta^L e'^L) \, dV$$

$$- \rho_o T_o \beta_{T_\rho} \zeta \int_{(V)} \left(\theta'^L \rho_m^L - \theta^L \rho_m'^L \right) dV + \rho_o \int_{(V)} (\theta'^L \mathfrak{R}^L - \theta^L \mathfrak{R}'^L) \, dV = 0.$$

In the first integral of the formula obtained above, we take into account the following expressions: $\theta'^L \Delta\theta^L - \theta^L \Delta\theta'^L = \nabla \cdot (\theta'^L \nabla\theta^L - \theta^L \nabla\theta'^L)$. Making use the divergence theorem, we can rewrite this relation as follows

$$\frac{\lambda}{\zeta T_o} \int_{(\Sigma)} (\theta'^L \nabla\theta^L - \theta^L \nabla\theta'^L) \cdot \boldsymbol{n} \, d\Sigma - K\alpha_T \int_{(V)} (\theta'^L e^L - \theta^L e'^L) \, dV$$

$$- \rho_o \beta_{T_\rho} \int_{(V)} \left(\theta'^L \rho_m^L - \theta^L \rho_m'^L \right) dV + \frac{\rho_o}{\zeta T_o} \int_{(V)} (\theta'^L \mathfrak{R}^L - \theta^L \mathfrak{R}'^L) \, dV = 0. \quad (67)$$

We restrict ourselves to considering a quasi-static electric field and assume that: $\boldsymbol{E} = -\nabla\varphi_e$. In view of constitutive equation $(10)_2$, applying a Laplace transform to the equation $(8)_4$, we obtain

$$-\varepsilon_0 \nabla^2 \varphi_e^L + \nabla \cdot \boldsymbol{\Pi}_e^L = 0, \quad -\varepsilon_0 \nabla^2 \varphi_e'^L + \nabla \cdot \boldsymbol{\Pi}_e'^L = 0. \quad (68)$$

We multiply these equations by the functions $\varphi_e'^L$ and φ_e^L. Proceeding in a similar manner, we obtain

$$-\varepsilon_0 \int_{(V)} \left[\nabla \cdot (\nabla\varphi_e^L)\,\varphi_e'^L - \nabla \cdot (\nabla\varphi_e'^L)\,\varphi_e^L \right] dV = \int_{(V)} \left[(\nabla \cdot \boldsymbol{\Pi}_e^L)\,\varphi_e'^L - (\nabla \cdot \boldsymbol{\Pi}_e'^L)\,\varphi_e^L \right] dV. \qquad (69)$$

Further, we take into account the following expressions

$$\begin{aligned}
&\nabla \cdot (\nabla\varphi_e^L)\,\varphi_e'^L - \nabla \cdot (\nabla\varphi_e'^L)\,\varphi_e^L = \nabla \cdot \left[(\nabla\varphi_e^L)\,\varphi_e'^L \right] - \nabla \cdot \left[(\nabla\varphi_e'^L)\,\varphi_e^L \right], \\
&(\nabla \cdot \boldsymbol{\Pi}_e^L)\,\varphi_e'^L - (\nabla \cdot \boldsymbol{\Pi}_e'^L)\,\varphi_e^L = \nabla \cdot (\boldsymbol{\Pi}_e^L \varphi_e'^L) - \nabla \cdot (\boldsymbol{\Pi}_e'^L \varphi_e^L) + \boldsymbol{\Pi}_e'^L \cdot (\nabla\varphi_e^L) - \boldsymbol{\Pi}_e^L \cdot (\nabla\varphi_e'^L).
\end{aligned} \qquad (70)$$

In view of the relations (70) and the divergence theorem, the equation (69) may be written as follows:

$$\int_{(\Sigma)} (\varphi_e'^L \boldsymbol{D}^L - \varphi_e^L \boldsymbol{D}'^L) \cdot \boldsymbol{n}\, d\Sigma = \int_{(V)} (\boldsymbol{\Pi}_e^L \cdot \nabla\varphi_e'^L - \boldsymbol{\Pi}_e'^L \cdot \nabla\varphi_e^L)\, dV. \qquad (71)$$

Combining the equations (63), (67), and (71) yields

$$\begin{aligned}
\int_{(\Sigma)} & \left[\boldsymbol{\sigma}_*^L \cdot \boldsymbol{u}'^L - \boldsymbol{\sigma}_*'^L \cdot \boldsymbol{u}^L + (\varphi_e'^L \boldsymbol{D}^L - \varphi_e^L \boldsymbol{D}'^L) \cdot \boldsymbol{n} \right] d\Sigma \\
& - \frac{\lambda}{\zeta T_o} \int_{(\Sigma)} (\theta'^L \nabla\theta^L - \theta^L \nabla\theta'^L) \cdot \boldsymbol{n}\, d\Sigma \\
& + \rho_o \int_{(V)} (\boldsymbol{F}_*^L \cdot \boldsymbol{u}'^L - \boldsymbol{F}_*'^L \cdot \boldsymbol{u}^L)\, dV - \frac{\rho_o}{\zeta T_o} \int_{(V)} (\theta'^L \mathfrak{R}^L - \theta^L \mathfrak{R}'^L)\, dV \\
& = \int_{(V)} [\boldsymbol{\Pi}_e^L \cdot \nabla\varphi'^L - \boldsymbol{\Pi}_e'^L \cdot \nabla\varphi^L]\, dV \\
& \qquad - \int_{(V)} \left[K\alpha_\rho(\rho_m^L e'^L - \rho_m'^L e^L) + \rho_o \beta_{T_\rho}(\theta'^L \rho_m^L - \theta^L \rho_m'^L) \right] dV. \qquad (72)
\end{aligned}$$

We simplify the integrand in the right-hand side of the equation (72). First, we transform the integrand in the last line of this equation. Using the constitutive relation (17c) we obtain the following formulae

$$K\alpha_\rho e^L = -\rho_o \tilde{\mu}_\pi'^L + \rho_o d_\rho \rho_m^L - \rho_o \beta_{T_\rho}\theta^L, \qquad K\alpha_\rho e'^L = -\rho_o (\tilde{\mu}_\pi')'^L + \rho_o d_\rho \rho_m'^L - \rho_o \beta_{T_\rho}\theta'^L. \qquad (73)$$

Substituting the expressions (73) into the integrand, we can write

$$K\alpha_\rho \left(\rho_m^L e'^L - \rho_m'^L e^L \right) + \rho_o \beta_{T_\rho} \left(\theta'^L \rho_m^L - \theta^L \rho_m'^L \right) = \rho_o \left[\rho_m'^L \tilde{\mu}_\pi'^L - \rho_m^L (\tilde{\mu}_\pi')'^L \right]. \qquad (74)$$

In view of the constitutive relations (17), it can be shown that the following expression are true for a quasi-static electric field

$$\boldsymbol{\Pi}_e^L \cdot \nabla\varphi_e'^L - \boldsymbol{\Pi}_e'^L \cdot \nabla\varphi_e^L = \rho_o \left[(\nabla\tilde{\mu}_\pi')^L \cdot \boldsymbol{\pi}_m'^L - (\nabla\tilde{\mu}_\pi')'^L \cdot \boldsymbol{\pi}_m^L \right]. \qquad (75)$$

Using the constitutive relations (74) and (75), as well as the formula (19), we transform the right-hand side of the equation (72) to obtain

$$\begin{aligned}
\int_{(V)} & \left[\boldsymbol{\Pi}_e^L \cdot \nabla\varphi_e'^L - \boldsymbol{\Pi}_e'^L \cdot \nabla\varphi_e^L - K\alpha_\rho \left(\rho_m^L e'^L - \rho_m'^L e^L \right) + \rho_o \beta_{T_\rho} \left(\theta'^L \rho_m^L - \theta^L \rho_m'^L \right) \right] dV \\
& = -\rho_o \int_{(V)} \nabla \cdot \left[\boldsymbol{\pi}_m^L (\tilde{\mu}_\pi')'^L - \boldsymbol{\pi}_m'^L \tilde{\mu}_\pi'^L \right] dV. \qquad (76)
\end{aligned}$$

Finally, substituting the expression (76) into (72) and taking into account the divergence theorem, we obtain the generalized reciprocity theorem in the transformed domain:

$$\zeta T_o \left\{ \int_{(\Sigma)} \left[\boldsymbol{\sigma}_*^L \cdot \boldsymbol{u}'^L - \boldsymbol{\sigma}_*'^L \cdot \boldsymbol{u}^L + (\varphi_e'^L \boldsymbol{D}^L - \varphi_e^L \boldsymbol{D}'^L) \cdot \boldsymbol{n} \right. \right.$$

$$\left. + \rho_o \left(\boldsymbol{\pi}_m^L (\tilde{\mu}_\pi')'^L - \boldsymbol{\pi}_m'^L \tilde{\mu}_\pi'^L \right) \cdot \boldsymbol{n} \right] d\Sigma + \rho_o \int_{(V)} (\boldsymbol{F}_*^L \cdot \boldsymbol{u}'^L - \boldsymbol{F}_*'^L \cdot \boldsymbol{u}^L) \, dV \right\}$$

$$+ \lambda \int_{(\Sigma)} (\theta^L \nabla \theta'^L - \theta'^L \nabla \theta^L) \cdot \boldsymbol{n} \, d\Sigma + \rho_o \int_{(V)} (\theta^L \mathfrak{R}'^L - \theta'^L \mathfrak{R}^L) \, dV = 0.$$

Inverting the Laplace transform yields the reciprocity theorem in the desired form

$$T_o \left\{ \int_{(\Sigma)} \left[\boldsymbol{\sigma}_* \odot \boldsymbol{u}' - \boldsymbol{\sigma}_*' \odot \boldsymbol{u} + \varphi_e' \bigcirc (\boldsymbol{D} \cdot \boldsymbol{n}) - \varphi_e \bigcirc (\boldsymbol{D}' \cdot \boldsymbol{n}) \right. \right.$$

$$\left. + \rho_o (\boldsymbol{\pi}_m \cdot \boldsymbol{n}) \bigcirc (\tilde{\mu}_\pi')' - \rho_o (\boldsymbol{\pi}_m' \cdot \boldsymbol{n}) \bigcirc \tilde{\mu}_\pi' \right] d\Sigma + \rho_o \int_{(V)} (\boldsymbol{F}_* \odot \boldsymbol{u}' - \boldsymbol{F}_*' \odot \boldsymbol{u}) \, dV \right\}$$

$$+ \lambda \int_{(\Sigma)} \left[\theta * (\nabla \theta' \cdot \boldsymbol{n}) - \theta' * (\nabla \theta \cdot \boldsymbol{n}) \right] d\Sigma + \rho_o \int_{(V)} (\theta * \mathfrak{R}' - \theta' * \mathfrak{R}) \, dV = 0. \quad (77)$$

Here we use the following notation to indicate the time convolutions:

$$\boldsymbol{f} \odot \boldsymbol{g} = \int_0^t \boldsymbol{f}(\boldsymbol{r}, t - \tau) \cdot \frac{\partial \boldsymbol{g}(\boldsymbol{r}, t)}{\partial \tau} \, d\tau,$$

$$f \bigcirc g = \int_0^t f(\boldsymbol{r}, t - \tau) \frac{\partial g(\boldsymbol{r}, \tau)}{\partial \tau} \, d\tau,$$

$$f * g = \int_0^t f(\boldsymbol{r}, t - \tau) \, g(\boldsymbol{r}, \tau) \, d\tau.$$

The equation (77) corresponds to the reciprocity theorem generalized to non-stationary problems of the linear theory of local gradient electrothermoelasticity. It is worth noting that the occurrence of convolutions $\rho_o(\boldsymbol{\pi}_m \cdot \boldsymbol{n}) \odot (\tilde{\mu}_\pi')'$ and $\rho_o(\boldsymbol{\pi}_m' \cdot \boldsymbol{n}) \odot \tilde{\mu}_\pi'$ in (77) is caused by the accounting for local mass displacement. In the absence of the local mass displacement effects, the equation (77) reduces to the reciprocity relation of the classical thermopiezoelectricity obtained by Nowacki [1965; 1983].

For stationary processes, the equations (77) simplifies to the following form

$$\int_{(\Sigma)} \left\{ \boldsymbol{\sigma}_* \cdot \boldsymbol{u}' - \boldsymbol{\sigma}_*' \cdot \boldsymbol{u} + (\varphi_e' \boldsymbol{D} - \varphi_e \boldsymbol{D}') \cdot \boldsymbol{n} + \rho_o \left[(\tilde{\mu}_\pi')' \boldsymbol{\pi}_m - \tilde{\mu}_\pi' \boldsymbol{\pi}_m' \right] \cdot \boldsymbol{n} \right\} d\Sigma$$

$$+ \rho_o \int_{(V)} \left[\boldsymbol{F}_* \cdot \boldsymbol{n}' - \boldsymbol{F}_*' \cdot \boldsymbol{u} + \beta_{T_\rho} (\rho_m' \theta - \rho_m \theta') + \frac{K \alpha_T}{\rho_o} (e'\theta - e\theta') \right] dV = 0. \quad (78)$$

7. Conclusion

The paper presents a complete set of equations of a continuum-type local gradient model of electrothermo-elastic nonferromagnetic solid dielectrics that accounts for the processes of deformation, heat conduction, polarization, and local mass displacement. A governing set of equations and the corresponding boundary conditions are obtained at a linear approximation. It is shown that this set of equations can be divided into two subsets that can be solved consecutively. This allows us to investigate the uniqueness of the

solution to the stated linear boundary problems in mathematical physics in two stages: (i) by proving the uniqueness of solution to the problem for a thermoelastic continuum, which accounts for the relationship between thermomechanic processes and the local mass displacement, and (ii) by proving the uniqueness of solution to Maxwell equations with the corresponding jump conditions. Using Laplace transforms, the reciprocity theorem is extended to the linear boundary-value problems of local gradient theory of electrothermoelastic dielectrics. This theorem may be used in the development of analytical methods of computation of the stress-strain state of nonferromagnetic polarized bodies, accounting for the process of local mass displacement.

Acknowledgement

References

[Burak 1987] Y. Burak, "Constitutive equations of locally gradient thermomechanics", *Dopovidi Akad. Nauk URSR = Proc. Acad. Sci. Ukrain. SSR* **12** (1987), 19–23. In Ukrainian.

[Burak et al. 2007] Y. I. Burak, V. F. Kondrat, and O. R. Hrytsyna, "Subsurface mechanoelectromagnetic phenomena in thermoelastic polarized bodies in the case of local displacements of mass", *Fiz.-Khim. Mekh. Mater.* **43**:4 (2007), 5–17. In Ukrainian; translated in *Mater. Sci.* **43**:4 (2007), 449–463.

[Burak et al. 2008] Y. Burak, V. Kondrat, and O. Hrytsyna, "An introduction of the local displacements of mass and electric charge phenomena into the model of the mechanics of polarized electromagnetic solids", *J. Mech. Mater. Struct.* **3**:6 (2008), 1037–1046.

[Chapla et al. 2009] Y. Chapla, S. Kondrat, O. Hrytsyna, and V. Kondrat, "On electromechanical phenomena in thin dielectric films", *Task Quart.* **13**:1-2 (2009), 145–154.

[Hadjigeorgiou et al. 1999] E. P. Hadjigeorgiou, V. K. Kalpakides, and C. V. Massalas, "A general theory for elastic dielectrics – Part I: the vectorial approach", *Int. J. Non-Linear Mech.* **34**:5 (1999), 831–841.

[Hrytsyna 2012] O. R. Hrytsyna, "Oscillations of a layer of a crystal with cubic symmetry under the action of harmonic electric field", *Fiz.-Khim. Mekh. Mater.* **48**:5 (2012), 88–96. In Ukrainian; translated in *Mater. Sci.* **48**:5 (2013), 653–663.

[Hrytsyna 2017] O. R. Hrytsyna, "Influence of subsurface inhomogeneity on the propagation of SH waves in isotropic materials", *Fiz.-Khim. Mekh. Mater.* **53**:2 (2017), 128–134. In Ukrainian; translated in *Mater. Sci.* **53**:2 (2017), 272–281.

[Kafadar 1971] C. B. Kafadar, "The theory of multipoles in classical electromagnetism", *Int. J. Eng. Sci.* **9**:9 (1971), 831–853.

[Kalpakidis and Agiasofitou 2002] V. K. Kalpakidis and E. K. Agiasofitou, "On material equations in second order gradient electroelasticity", *J. Elasticity* **67** (2002), 205–227.

[Kalpakidis et al. 1995] V. K. Kalpakidis, E. P. Hadjigeorgiou, and C. V. Massalas, "A variational principle for elastic dielectrics with quadruple polarization", *Int. J. Eng. Sci.* **33**:6 (1995), 793–801.

[Kondrat and Hrytsyna 2008] V. Kondrat and O. Hrytsyna, "The equations of electro-magneto-thermo-mechanics of polarized nonferromagnetic solids taking into account a local displacement of mass", *Fiz.-mat. modelyuvannya ta inform. technologii = Physico-Mathematical Modeling and Information Technologies* **8** (2008), 69–83. In Ukrainian.

[Kondrat and Hrytsyna 2009] V. F. Kondrat and O. R. Hrytsyna, "Equations of thermomechanics of deformable bodies with regard for irreversibility of local displacement of mass", *J. Math. Sci.* **160**:4 (2009), 492–502.

[Kondrat and Hrytsyna 2010] V. F. Kondrat and O. R. Hrytsyna, "Mechanoelectromagnetic interaction in isotropic dielectrics with regard for the local displacement of mass", *J. Math. Sci.* **168**:5 (2010), 688–698.

[Kondrat and Hrytsyna 2012] V. Kondrat and O. Hrytsyna, "Local gradient theory of dielectrics with polarization inertia and irreversibility of local mass displacement", *J. Mech. Mater. Struct.* **7**:3 (2012), 285–296.

[Kumikov and Khokonov 1983] V. K. Kumikov and K. B. Khokonov, "On the measurement of surface free energy and surface tension of solid metals", *J. Appl. Phys.* **54**:3 (1983), 1346–1350.

[Liu et al. 2006] K. H. Liu, W. L. Wang, Z. Xu, L. Liao, X. D. Bai, and E. G. Wang, "*In situ* probing mechanical properties of individual tungsten oxide nanowires directly grown on tungsten tips inside transmission electron microscope", *Appl. Phys. Lett.* **89**:22 (2006), 221908.

[Maugin 1979] G. A. Maugin, "Nonlocal theories or gradient-type theories: a matter of convenience", *Arch. Mech.* **31** (1979), 15–26.

[Maugin 1988] G. A. Maugin, *Continuum mechanics of electromagnetic solids*, Noth Holland, Amsterdam, 1988.

[Mindlin 1972] R. D. Mindlin, "Elasticity, piezoelectricity and crystal lattice dynamics", *J. Elasticity* **2**:4 (1972), 217–282.

[Nam et al. 2006] C.-Y. Nam, P. Jaroenapibal, D. Tham, D. E. Luzzi, S. Evoy, and J. E. Fischer, "Diameter-dependent electromechanical properties of GaN nanowires", *Nano Lett.* **6**:2 (2006), 153–158.

[Nowacki 1965] W. Nowacki, "A reciprocity theorem for coupled mechanical and thermoelectric fields in piezoelectric crystals", *Proc. Vibr. Probl.* **6**:1 (1965), 3–11.

[Nowacki 1983] W. Nowacki, *Efekty elektromagnetyczne w stałych ciałach odkształcalnych*, Państwowe Wydawnictwo Naukowe, Warszawa, 1983.

[Nysten et al. 2005] B. Nysten, C. Fretigny, and S. Cuenot, "Elastic modulus of nanomaterials: resonant contact-AFM measurement and reduced-size effect", *Proc. Soc. Photo-Opt. Ins.* **5766** (2005), 78–88.

[Sahin and Dost 1988] E. Sahin and S. Dost, "A strain-gradient theory of elastic dielectrics with spatial dispersion", *Int. J. Eng. Sci.* **26**:12 (1988), 1231–1245.

[Yan and Jiang 2007] Z. Yan and L. Jiang, "Modified continuum mechanics modeling on size-dependent properties of piezoelectric nanomaterials: a review", *Nanomaterials* **7**:2 (2007), 27p.

[Yang 2006] J. Yang, "Review of a few topics in piezoelectricity", *Appl. Mech. Rev.* (*ASME*) **59**:6 (2006), 335–345.

OLHA HRYTSYNA: gryt045@gmail.com
Center of Mathematical Modeling of Pidstryhach Institute for Applied Problems of Mechanics and Mathematics,
National Academy of Sciences of Ukraine, Lviv, Ukraine

and

Institute of Construction and Architecture, Slovak Academy of Sciences, Bratislava, Slovak Republic

HALYNA MOROZ: halynamoroz.ua@gmail.com
Center of Mathematical Modeling of Pidstryhach Institute for Applied Problems of Mechanics and Mathematics,
National Academy of Sciences of Ukraine, Lviv, Ukraine

■msp

EFFECT OF SURFACE ELASTICITY
ON STRESS INTENSITY FACTORS
NEAR MODE-III CRACK TIPS

Xian-Fang Li

This paper studies a nanoscale mode-III crack in a homogeneous isotropic material. Classical elasticity, incorporating surface elasticity, is applied to solve a mixed boundary value problem. An emphasis is placed on the influence of surface elasticity on the stress intensity factors. Using the Fourier transform, the problem is reduced to a hypersingular integro-differential equation, then to a singular integro-differential equation with Cauchy kernel or a weakly singular integral equation with logarithmic kernel of the second kind. Using the Galerkin method, a solution of the resulting singular integro-differential equation is determined through expanding the out-of-plane displacement jump across crack faces as a series of Chebyshev polynomials. The influences of surface material properties on the stress intensity factor are examined and displayed graphically. For most materials, the surface effect decreases the stress intensity factors and enhances the effective fracture toughness of most nanoscale materials with a crack.

1. Introduction

With the development of nano/micro-techniques in recent years, the mechanical behavior of small scale materials and structures is quite significant for better understanding structural integrity, reliability, and stability. In particular, some defects such as dislocations, grain boundaries, cracks, holes, etc., inevitably appear in these structures because of fabrication techniques. It is well recognized that for nano/micro-scale materials and structures, in addition to macro bulk materials, small scale parameters play a crucial role in affecting mechanical properties. For example, as a key elastic property, Young's modulus of carbon nanotubes and graphene are measured to reach 1 TPa or more [Wong et al. 1997; Lee et al. 2008], much larger than that for conventional materials. Fracture of graphene has been analyzed and commented [Zhang et al. 2014; 2015]. A prevailing point of view is that taking into account large specific surface area for a nano/micro-material, surface effects including surface elasticity and surface residual tension should be included in assessing the overall material properties [Sharma and Ganti 2004; Duan et al. 2005], although they are negligible as compared to those for macro bulk materials. In this field, Gurtin and Murdoch (GM) [Gurtin and Murdoch 1975; Gurtin et al. 1998] first introduced surface/interface elasticity along with surface residual stress to extend the classical theory of elasticity. Based on surface elasticity theory, Ru [2010] put forward a simple geometrical explanation of the GM surface elasticity theory and gave several simplified surface constitutive relations. Consideration of surface properties strongly affects static and dynamic response of nanoscale materials and structures [Wu et al. 2017; Chen et al. 2017; Xiao and Li 2018].

Based on the GM model, Dingreville et al. [2005] exploited the surface free energy to describe its effect on the elastic behavior of nanomaterials and derived an overall prediction of the material properties for an elastic bulk material with nanosized particles, wires, and films. By means of the complex potential method, based on the GM model, Mogilevskaya et al. [2008] studied the interaction of elastic fields of multiple circular nanoinhomogeneities or/and nanopores in a two-dimensional elastic medium. Wu [1999] solved the effect of surface stresses on deformation of an elliptical hole and found the surface stress to change stress intensity factors. Wang et al. [2008] examined the surface effects on the crack-tip stresses for both mode-I and mode-III cracks and found that when the curvature radius of a blunt crack front decreases to nanometers, surface energy strongly affects the stress intensities near the crack tip. For a mode-II nanoscale crack, Fu et al. [2008] gave a similar analysis. Using a double cantilever beam model, Wang et al. [2013] addressed the influence of surface residual tension on stress intensity factors at the crack tips. Nan and Wang [2012] analyzed that effect of crack face residual stress on the fracture of nanoscale materials. Yang et al. [2018] established a thin plate model with surface effect to simulate the growth of a nanoscale penny-shaped crack and derived an accurate expression for calculating size-dependent energy release rates. In a review paper, Duan et al. [2009] commented some progress of the classical theory of elasticity incorporating the GM model of surface elasticity. On the other hand, the fundamental solution of a concentrated force at the surface of a half-plane or half-space with consideration of surface stresses as well as surface elasticity has been obtained [Wang and Feng 2007; Gao et al. 2013; 2014], and this solution can be used to treat a class of contact problems related to surface elasticity. Hu et al. [Hu et al. 2018; Hu and Li 2018] solved mode-I and II crack and rigid inclusion problems for a thin-film with surface effect and derived a closed-form solution of surface properties-dependent stress intensity factors or stress singularity coefficients. Utilizing the complex potential method, Kim et al. [2009; 2011a; 2011b; 2011c] investigated the effects of surface elasticity for a classical mode-III crack embedded in a linearly elastic material or bimaterial and further extended their results to mode-I and mode-II (interface) cracks for plane deformation. They found that surface elasticity leads to the disappearance of singular stresses near the crack tip. On the contrary, Walton [Walton 2012; Kim et al. 2013] also examined the tip-field singularity of a crack and found a logarithmic singularity of stresses near the crack tip when surface elasticity of the crack faces is considered. The influence of the surface effect on the stress intensity factors for a nanoscale crack has been analyzed for a bridged crack and an arc-shaped crack by Wang and Schiavone [2016] and Wang [2015], who found a weak logarithmic singularity outside the crack and a strong square root singularity on the crack faces.

In this paper, we analyze the stress field near the crack tip for a nanoscale crack embedded in an elastic medium with surface elasticity. First, a routine approach via the Fourier integral transform technique is employed to reduce the problem to a singular integro-differential equation. By use of the Galerkin method, we construct an approximate solution. Obtained results show that surface properties affect the stress intensity factors. Numerical results illustrate the strong influence of surface material parameters on stress intensity factors for nano/microscale cracks. Finally, some conclusions are drawn.

2. Statement of the problem

For a homogeneous isotropic linear bulk material, the stress-strain relations are governed by [Lurie and Belyaev 2005]

$$\sigma_{ij} = \lambda \varepsilon_{ll} \delta_{ij} + 2\mu \varepsilon_{ij}, \tag{1}$$
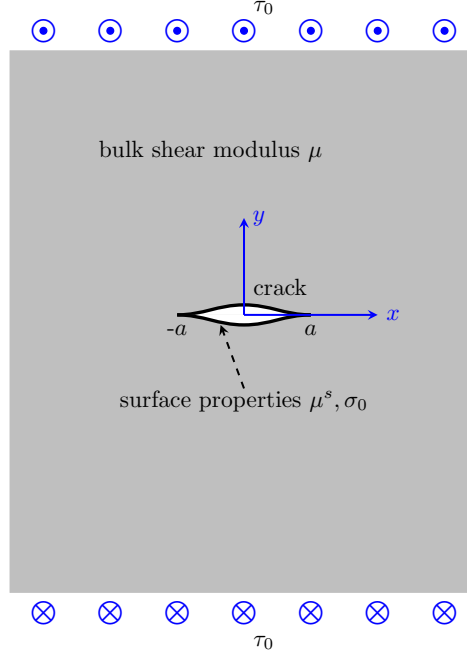
Figure 1. Schematic of a cracked medium with surface effect under remote antiplane shear loading.

where λ and μ are the Lamé constants, σ_{ij} is the Cauchy stress tensor, and ε_{ij} is the strain tensor. For a homogeneous isotropic surface material, the surface stress-strain relations read as follows [Gurtin and Murdoch 1975]:

$$\sigma^s_{\alpha\beta} = \sigma_0\delta_{\alpha\beta} + (\lambda^s + \sigma_0)\varepsilon^s_{\gamma\gamma}\delta_{\alpha\beta} + 2(\mu^s - \sigma_0)\varepsilon^s_{\alpha\beta} + \sigma_0 u^s_{\alpha,\beta}, \tag{2}$$

$$\sigma^s_{\alpha 3} = \sigma_0 u^s_{3,\alpha}, \tag{3}$$

where λ^s and μ^s are the surface Lamé constants independent of the surface residual stress, σ_0 is the surface residual stress under unconstrained conditions, $\sigma^s_{\alpha j}$ are the Piola–Kirchhoff surface stresses, $\varepsilon^s_{\alpha\beta}$ are the surface strains, and u_α are the elastic displacement components. In the above, δ_{ij} or $\delta_{\alpha\beta}$ is the Kronecker delta, Latin subscripts i, j, l take values from 1 to 3, and Greek subscripts α, β, γ range from 1 to 2, a comma in the subscript denotes differentiation with respect to the spatial variable following the comma, and the Einstein convention of summation over repeated lower-case indices has been used.

In this paper a cracked material subjected to antiplane shear loading is studied, as shown in Figure 1 For convenience, a tunnel crack of length $2a$ is assumed to be located at the x-axis, i.e., $|x| < a$. In other words, in the present study we consider a nanoscale mode-III crack in plane strain state. Since antiplane shear loading is applied, there is only a unique out-of-plane displacement component, denoted as w and other displacement components along the x- and y-axes vanish. With w, the constitutive equation (1) for bulk material becomes

$$\sigma_{xz} = \mu\frac{\partial w}{\partial x}, \quad \sigma_{yz} = \mu\frac{\partial w}{\partial y}, \tag{4}$$

where μ denotes shear modulus of the material. Inserting the above constitutive equations for bulk material into the equilibrium equation

$$\frac{\partial \sigma_{xz}}{\partial x} + \frac{\partial \sigma_{yz}}{\partial y} = 0 \tag{5}$$

yields the following governing equation:

$$\frac{\partial^2 w}{\partial x^2} + \frac{\partial^2 w}{\partial y^2} = 0. \tag{6}$$

For a nanoscale mode-III crack embedded in a material, due to the presence of the crack, surface elasticity at the crack faces affects the mechanical behavior of a cracked material. To model a nanoscale crack, we adopt the surface elasticity formulated originally by Gurtin and Murdoch [1975]. Namely, the surface stresses of the crack faces satisfy the surface constitutive equations (2) and (3). They along with the bulk stresses satisfy the following equilibrium equations at the crack faces:

$$[\![\sigma_{ij} n_j e_i]\!] + \sigma^s_{\alpha\beta,\beta} e_\alpha = 0, \tag{7}$$

$$[\![\sigma_{ij} n_i n_j]\!] = \kappa_{\alpha\beta} \sigma^s_{\alpha\beta}, \tag{8}$$

where $\alpha, \beta = 1, 3$, $\kappa_{\alpha\beta}$ denotes the curvature tensor of surface, e_i is the unit vector component along the x_i direction, and $[\![*]\!] = (*)^+ - (*)^-$ stands for the jump of a quantity across the surface film. For the present problem under consideration, the above equilibrium equations (7) and (8) reduce to

$$\frac{\partial \sigma^s_{xx}}{\partial x} + \frac{\partial \sigma^s_{zx}}{\partial z} + [\![\sigma_{yx}]\!] = 0, \tag{9}$$

$$\frac{\partial \sigma^s_{xz}}{\partial x} + \frac{\partial \sigma^s_{zz}}{\partial z} + [\![\sigma_{yz}]\!] = 0, \tag{10}$$

$$[\![\sigma_{yy}]\!] = -\sigma_0 \left(\frac{\partial^2 v}{\partial x^2} + \frac{\partial^2 v}{\partial z^2} \right), \tag{11}$$

where v is the elastic displacement component along the y-axis. Only the out-of-plane displacement exists for an antiplane shear problem, and other displacement components are nil. Thus, using the surface stress-strain relation (2) with $\alpha = 1$, $\beta = 3$ or

$$\sigma^s_{xz} = (\mu^s - \sigma_0) \frac{\partial w}{\partial x}, \tag{12}$$

where μ^s is the surface shear modulus, σ_0 is the surface residual stress, and the surface displacement is assumed to be identical to that for the bulk displacement at a local position. From (9)–(11) we obtain

$$(\mu^s - \sigma_0) \frac{\partial^2 w}{\partial x^2} + [\![\sigma_{yz}]\!] = 0. \tag{13}$$

Finally, when applied loading at the crack faces is given, (13) can be rewritten as

$$\sigma^{\pm}_{yz}(x, 0) = q(x) \mp (\mu^s - \sigma_0) \frac{\partial^2 w(x, 0)}{\partial x^2}, \quad |x| < a, \tag{14}$$

where $q(x)$ is the prescribed loading at the crack faces. It represents the negative of applied antiplane shear loading without crack. Two typical cases are respectively analyzed in what follows. Case A

corresponds to an even loading $q_e(x)$ such as constant loading $-\tau_0$, which is equivalent to the application of a remote constant loading, and Case B corresponds to an odd loading $q_o(x)$ such as $-\tau_0 x/a$, which is equivalent to the application of a torque around the y-axis.

3. Derivation of singular integro-differential equation

This section is devoted to the derivation of singular integro-differential equation for the problem in question. To this end, we employ the Fourier transform technique to achieve our purpose. In addition to the boundary condition at the crack faces, we need to provide the boundary condition at the crack-free portion in the x-axis, i.e.,

$$w(x, 0) = 0, \quad |x| > a. \tag{15}$$

3.1. *Case A.* First the case of an even function loading $q_e(x)$ with respect to x is studied. Using the Fourier transform, we find that the out-of-plane displacement in the upper half-plane can be chosen as

$$w(x, y) = \frac{2}{\pi} \int_0^\infty A(\xi) \exp(-\xi y) \cos(\xi x) \, d\xi, \quad y \geq 0, \tag{16}$$

where $A(\xi)$ is an unknown function in ξ to be determined from the boundary conditions. Due to the symmetry of the problem, it is sufficient to determine the elastic field in the upper half-plane, and that in the lower half-plane can be directly written by symmetry. Plugging the expression (16) for the out-of-plane displacement into the constitutive relations (4) leads to an integral representation for the bulk stress components:

$$\sigma_{xz}(x, y) = -\frac{2\mu}{\pi} \int_0^\infty \xi A(\xi) \exp(-\xi y) \sin(\xi x) \, d\xi, \tag{17}$$

$$\sigma_{yz}(x, y) = -\frac{2\mu}{\pi} \int_0^\infty \xi A(\xi) \exp(-\xi y) \cos(\xi x) \, d\xi. \tag{18}$$

In order to derive a singular integro-differential equation, we define the so-called continuous screw dislocation pile-up or out-of-plane displacement jump across the crack faces as $2g(x)$, i.e.,

$$g(x) = w(x, 0). \tag{19}$$

Obviously, making use of the condition (15), one performs the Fourier cosine transform to (16) as $y = 0$. Thus we can express $A(\xi)$ in terms of $g(x)$ through the following integral:

$$A(\xi) = \int_0^a g(s) \cos(\xi s) \, ds. \tag{20}$$

Next, inserting (20) into (18) for $y = 0$ leads to

$$\sigma_{yz}(x, 0) = -\frac{2\mu}{\pi} \int_0^a g(s) \, ds \int_0^\infty \xi \cos(\xi s) \cos(\xi x) \, d\xi. \tag{21}$$

Recalling the well-known integral identity

$$\int_0^\infty \xi \cos(\xi x) \cos(\xi s) \, d\xi = -\frac{1}{2} \left[\frac{1}{(s+x)^2} + \frac{1}{(s-x)^2} \right], \tag{22}$$

we have

$$\sigma_{yz}(x,0) = \frac{\mu}{\pi} \int_0^a g(s) \left[\frac{1}{(s+x)^2} + \frac{1}{(s-x)^2} \right] ds. \tag{23}$$

Considering that $g(x)$ is an even function, we immediately obtain

$$\int_0^a \frac{g(s)}{(s+x)^2} \, ds = \int_{-a}^0 \frac{g(s)}{(s-x)^2} \, ds, \tag{24}$$

and the stress (23) at the upper crack face is then rewritten as

$$\sigma_{yz}(x,0) = \frac{\mu}{\pi} \int_{-a}^a \frac{g(s)}{(s-x)^2} \, ds. \tag{25}$$

Now we substitute (25) into the remaining boundary condition (14) at the upper crack face and get the following hypersingular integro-differential equation:

$$\frac{\mu}{\pi} \int_{-a}^a \frac{g(s)}{(s-x)^2} \, ds + (\mu^s - \sigma_0)g''(x) = q_e(x), \quad |x| < a, \tag{26}$$

where the double prime denotes second-order derivative with respect to x, and $q_e(x)$ is a prescribed even function. Due to the kernel $1/(s-x)^2$ having singularity of order 2, such a strongly singular integral equation with another differential term is called hypersingular integro-differential equation. Here, hypersingular integral is understood in the sense of Hadamard finite-part integral [Kaya and Erdogan 1987]. In fact, hypersingular integral equations have been widely used to tackle the classical crack problems [Ioakimidis 1982; Chan et al. 2003; Li 2003; Li et al. 2013]. In the above, besides the hypersingular integral term, the last term of the left-hand side of (26) is related to surface elasticity and it reflects the contribution of surface effect. Evidently, if neglecting the term related to $g''(x)$, the hypersingular integral equation for the classical mode-III crack is recovered. It is mentioned that if denoting $g'(x) = \eta(x)$, owing to $g(\pm a) = 0$ we perform integration by parts and get

$$\int_{-a}^a \frac{g(s)}{(s-x)^2} \, ds = \int_{-a}^a \frac{\eta(s)}{s-x} \, ds. \tag{27}$$

Thus the above equation (26) is equivalent to the following singular integro-differential equation:

$$(\mu^s - \sigma_0)\eta'(x) + \frac{\mu}{\pi} \int_{-a}^a \frac{\eta(s)}{s-x} \, ds = q_e(x), \tag{28}$$

identical to that obtained by Kim et al. [2009], who employed the complex variable method to derive the singular integro-differential equation (28) for a mode-III crack in an infinite elastic medium with surface elasticity. It is readily found that the unknown function $\eta(x)$ corresponds to the strain component physically. Strictly speaking, the behavior of $\eta(\pm a)$ is not obvious. In fact, it is the condition $\eta(\pm a) = 0$ that gives rise to no singularity occurring near the crack tips [Walton 2012; Kim et al. 2013]. Instead, for the unknown function $g(x)$ that stands for the displacement jump, the requirement of $g(\pm a) = 0$ is evident, which implies the single-value condition at the crack tips. As a consequence, although the singular integro-differential equation (28) is identical in form to that derived in [Kim et al. 2009], the

physical meaning of the unknown functions involved is completely different. A further simplification to (26) is achieved by integrating both sides of (26):

$$\frac{\mu}{\pi} \int_{-a}^{a} \frac{g(s)}{s-x} \, ds + (\mu^s - \sigma_0) g'(x) = \int_0^x q_e(s) \, ds, \quad |x| < a, \tag{29}$$

where a vanishing integration constant has been used since $g'(x)$ and $\int_{-a}^{a} g(s)/(s-x) \, ds$ are both odd functions with respect to x. Thus we have derived a singular integro-differential equation (29) for the out-of-plane displacement at the upper crack face $g(x)$, rather than its derivative $\eta(x)$.

3.2. *Case B.* In this subsection, we turn our attention to the case of antisymmetric odd loading $q_o(x)$. To treat this case, it is convenient to replace the out-of-plane displacement (16) by the following Fourier integral

$$w(x, y) = \frac{2}{\pi} \int_0^{\infty} B(\xi) \exp(-\xi y) \sin(\xi x) \, d\xi, \quad y \geq 0, \tag{30}$$

where $B(\xi)$ is an unknown function in ξ to be determined from the boundary conditions. In a similar manner, using the constitutive relations, we have the bulk stress components

$$\sigma_{xz}(x, y) = \frac{2\mu}{\pi} \int_0^{\infty} \xi B(\xi) \exp(-\xi y) \cos(\xi x) \, d\xi, \tag{31}$$

$$\sigma_{yz}(x, y) = -\frac{2\mu}{\pi} \int_0^{\infty} \xi B(\xi) \exp(-\xi y) \sin(\xi x) \, d\xi. \tag{32}$$

Under the same notation $g(x) = w(x, 0)$, $B(\xi)$ can be expressed in terms of $g(x)$ through the following integral:

$$B(\xi) = \int_0^{a} g(s) \sin(\xi s) \, ds, \tag{33}$$

which is inserted back into (32) for $y = 0$, giving

$$\sigma_{yz}(x, y) = -\frac{2\mu}{\pi} \int_0^{a} g(s) \, ds \int_0^{\infty} \xi \sin(\xi s) \sin(\xi x) \, d\xi. \tag{34}$$

With the aid of the well-known integral identity

$$\int_0^{\infty} \xi \sin(\xi s) \sin(\xi x) \, d\xi = \frac{1}{2} \left[\frac{1}{(s+x)^2} - \frac{1}{(s-x)^2} \right], \tag{35}$$

we have

$$\sigma_{yz}(x, 0) = -\frac{\mu}{\pi} \int_0^{a} g(s) \left[\frac{1}{(s+x)^2} - \frac{1}{(s-x)^2} \right] ds. \tag{36}$$

Considering the fact that $g(x)$ is an odd function, we immediately obtain

$$\int_0^{a} \frac{g(s)}{(s+x)^2} \, ds = -\int_{-a}^{0} \frac{g(s)}{(s-x)^2} \, ds, \tag{37}$$

and the stress (36) at the upper crack face is then rewritten as

$$\sigma_{yz}(x, 0) = \frac{\mu}{\pi} \int_{-a}^{a} \frac{g(s)}{(s-x)^2} \, ds. \tag{38}$$

Note that the above result is the same as (25). So applying the boundary condition at the upper crack face, the following hypersingular integro-differential equation can be derived:

$$\frac{\mu}{\pi} \int_{-a}^{a} \frac{g(s)}{(s-x)^2} \, ds + (\mu^s - \sigma_0) g''(x) = q_o(x), \quad |x| < a. \tag{39}$$

After integrating both sides of the above equation, one gets

$$\frac{\mu}{\pi} \int_{-a}^{a} \frac{g(s)}{s-x} ds + (\mu^s - \sigma_0) g'(x) = \int_{0}^{x} q_o(s) \, ds + C, \quad |x| < a, \tag{40}$$

where C denotes an integration constant. Differing from the previous result in the foregoing subsection, C does not vanish, but must be determined through the following supplementary condition, i.e.,

$$C = \frac{\mu}{\pi} \int_{-a}^{a} \frac{g(s)}{s} \, ds + (\mu^s - \sigma_0) g'(0). \tag{41}$$

As a result, we have also derived a singular integro-differential equation (40) but with an unknown constant C, which satisfies the condition (41).

4. Solution to the singular integro-differential equation

In order to derive the solution of the resulting integro-differential equation, we introduce the following dimensionless quantities:

$$\bar{g}(\bar{x}) = \frac{g(x)}{a}, \qquad \qquad \theta = \frac{\mu^s - \sigma_0}{a\mu}, \tag{42}$$

$$q(x) = \tau_0 \bar{q}(\bar{x}), \quad \int_{0}^{x} q(s) \, ds = \tau_0 \zeta(\bar{x}) - C, \tag{43}$$

$$\bar{x} = \frac{x}{a}, \qquad \qquad \bar{s} = \frac{s}{a}, \tag{44}$$

where $\zeta(\bar{x})$ is a prescribed function, which may contain an undetermined constant to ensure that the right-hand side vanishes as $\bar{x} = 0$. That is, we require $\zeta(0) \neq 0$ and it satisfies (41) for an even function $\zeta(\bar{x})$ corresponding to the case of an odd loading. The resulting equations for Cases A and B can be written as a unified form

$$\theta g''(\bar{x}) + \frac{1}{\pi} \int_{-1}^{1} \frac{\bar{g}(\bar{s})}{(\bar{s} - \bar{x})^2} \, d\bar{s} = \frac{\tau_0}{\mu} \bar{q}(\bar{x}), \quad |\bar{x}| < 1, \tag{45}$$

or

$$\theta \bar{g}'(\bar{x}) + \frac{1}{\pi} \int_{-1}^{1} \frac{\bar{g}(\bar{s})}{\bar{s} - \bar{x}} \, d\bar{s} = \frac{\tau_0}{\mu} \zeta(\bar{x}), \quad |\bar{x}| < 1. \tag{46}$$

The former is a hypersingular integro-differential equation, and the latter is a singular integro-differential equation.

Since the out-of-plane displacement at the upper crack face vanishes at both crack tips, i.e.,

$$\bar{g}(\pm 1) = 0, \tag{47}$$

we still give an alternative weakly singular integral equation with logarithmic kernel as follows:

$$\theta \bar{g}'(\bar{x}) - \frac{1}{\pi} \int_{-1}^{1} \bar{g}'(\bar{s}) \ln|\bar{s} - \bar{x}| \, d\bar{s} = \frac{\tau_0}{\mu} \zeta(\bar{x}), \quad |\bar{x}| < 1. \tag{48}$$

The asymptotic behavior of the unknown function $\bar{g}(\bar{x})$ near the crack tips is, however, still unknown. As a consequence, a key task is to seek a solution to (46) subject to (47). Prior to the presentation of an appropriate solution, let us have a glance at the behavior of the solution to (46) subject to (47). If the parameter θ is sufficiently large, implying that the second term on the left-hand side of (46) is negligible as compared to the first term, after removing the second term one integrates both sides of (46) with respect to $\bar{x}$ and finds that $\bar{g}(\bar{x})$ has a behavior like $(1 - \bar{x}^2)$ near $\bar{x} = \pm 1$ in view of $\zeta(0) \neq 0$. Conversely, if the parameter θ is sufficiently small, implying that the first term on the left-hand side of (46) is negligible as compared to the second term, after removing the first term (46) reduces to a standard singular integral equation with Cauchy kernel of the first kind, the solution of which under the condition (47) has a square-root behavior like $\sqrt{1 - \bar{x}^2}$ near $\bar{x} = \pm 1$ [Muskhelishvili 1977]. In fact, this conclusion may be seen from what follows. By rewriting (46) as

$$\frac{1}{\pi} \int_{-1}^{1} \frac{\bar{g}(\bar{s})}{\bar{s} - \bar{x}} \, d\bar{s} = \frac{\tau_0}{\mu} \zeta(\bar{x}) - \theta \bar{g}'(\bar{x}), \tag{49}$$

with the well-known solution of a singular integral equation with the Cauchy kernel of the first kind [Muskhelishvili 1977, p. 155], by virtue of (47) we arrive at that the solution $\bar{g}(\bar{x})$ should satisfy the following relations:

$$\bar{g}(\bar{x}) = -\frac{\sqrt{1 - \bar{x}^2}}{\mu \pi} \int_{-1}^{1} \frac{\tau_0 \zeta(\bar{s}) - \mu \theta \bar{g}'(\bar{s})}{(\bar{s} - \bar{x})\sqrt{1 - \bar{s}^2}} \, d\bar{s} \tag{50}$$

and

$$\int_{-1}^{1} \frac{\tau_0 \zeta(\bar{s}) - \mu \theta \bar{g}'(\bar{s})}{\sqrt{1 - \bar{s}^2}} \, d\bar{s} = 0. \tag{51}$$

Based on the above analysis, we reasonably approximate the out-of-plane displacement $\bar{g}(\bar{x})$ by the following finite-term sum of the Chebyshev polynomials of the second kind [Frankel 1995; Bhattacharya and Mandal 2008]:

$$\bar{g}_N(\bar{x}) = \frac{\tau_0}{\mu} \sqrt{1 - \bar{x}^2} \sum_{n=0}^{N} b_n U_n(\bar{x}), \tag{52}$$

where the coefficients b_n are unknown coefficients, and N is a positive integer. Due to the completeness of $U_n(\bar{x})$, N is often chosen so large that the sum of the first finite terms converges the desired one, i.e., $\bar{g}_N(\bar{x}) \to \bar{g}(\bar{x})$ as $N \to \infty$. Hereafter we still denote $\bar{g}_N(\bar{x})$ as $\bar{g}(\bar{x})$, if no confusion is caused. Notice that if $\bar{g}_N(\bar{x})$ is even, only even terms $U_{2n}(\bar{x})$ are maintained in (52), whereas if $\bar{g}_N(\bar{x})$ is odd, only odd terms $U_{2n+1}(\bar{x})$ remain. In the above, the Chebyshev polynomial of the second kind $U_n(\bar{x})$ is defined as

$$U_n(\bar{x}) = \frac{\sin[(n+1)\cos^{-1}\bar{x}]}{\sin(\cos^{-1}\bar{x})}, \quad n \geq 0. \tag{53}$$

We stress that the assumption of the expression (52) is completely different from those used in [Kim et al. 2009; Wang 2015]. A solution in the form (52) is based on the out-of-plane displacement at the

upper crack face, not its derivative. Besides, different from most derivations, we use the Chebyshev polynomials of the second kind, not the first kind, and such a choice greatly simplifies the derivation. It is mentioned that an analogous expression of using the Chebyshev polynomial of the second kind has been applied in [Paulino et al. 2003]. Of course, it is also feasible to choose an expansion of the Chebyshev polynomials of the first kind such as $\bar{g}'_N(\bar{x}) = \mu^{-1}\tau_0 \sum_{n=0}^{N} b_n T_n(\bar{x})/\sqrt{1-\bar{x}^2}$ in place of (52), and we don't go on along this approach.

The remaining task is to determine the unknown coefficients b_n. We substitute the expansion (52) into (46), yielding

$$\sum_{n=0}^{N} b_n \left\{ \theta \frac{d}{d\bar{x}}[\sqrt{1-\bar{x}^2}U_n(\bar{x})] + \frac{1}{\pi} \int_{-1}^{1} \frac{\sqrt{1-\bar{s}^2}U_n(\bar{s})}{\bar{s}-\bar{x}} \, d\bar{s} \right\} = \zeta(\bar{x}), \quad |\bar{x}| < 1. \tag{54}$$

Taking account of the following properties of derivatives and integrals involving the Chebyshev polynomials:

$$\frac{d}{d\bar{x}}[U_n(\bar{x})\sqrt{1-\bar{x}^2}] = -\frac{(n+1)T_{n+1}(\bar{x})}{\sqrt{1-\bar{x}^2}}, \quad |\bar{x}| < 1, \tag{55}$$

$$\frac{1}{\pi} \int_{-1}^{1} \frac{U_n(\bar{s})\sqrt{1-\bar{s}^2}}{\bar{s}-\bar{x}} \, d\bar{s} = -T_{n+1}(\bar{x}), \qquad |\bar{x}| < 1, \tag{56}$$

where $T_n(\bar{x})$ is the Chebyshev polynomial of the first kind, defined by

$$T_n(\bar{x}) = \cos(n\cos^{-1}\bar{x}), \quad n \geq 0, \tag{57}$$

one finds that (54) reduces to

$$\sum_{n=0}^{N} b_n \left[\frac{(n+1)\theta}{\sqrt{1-\bar{x}^2}} + 1 \right] T_{n+1}(\bar{x}) = -\zeta(\bar{x}), \quad |\bar{x}| < 1. \tag{58}$$

After multiplying both sides of (58) by $T_{m+1}(\bar{x})$, we then integrate both sides with respect to $\bar{x}$ from -1 to 1. Applying the orthogonality of the Chebyshev polynomials:

$$\int_{-1}^{1} \frac{T_m(\bar{x})T_n(\bar{x})}{\sqrt{1-\bar{x}^2}} \, d\bar{x} = \begin{cases} 0, & m \neq n, \\ \pi, & m = n = 0, \\ \frac{1}{2}\pi, & m = n, \ m \neq 0, \end{cases} \tag{59}$$

and the closed-form integral formula

$$\int_{-1}^{1} T_m(\bar{x})T_n(\bar{x}) \, d\bar{x} = \frac{1+(-1)^{m-n}}{2} \left[\frac{1}{1-(m-n)^2} + \frac{1}{1-(m+n)^2} \right], \tag{60}$$

we obtain linear algebraic equations for the unknown constants b_n $(n = 0, 1, \ldots, N)$:

$$\sum_{n=0}^{N} \left[\frac{(n+1)\theta\pi}{2}\delta_{mn} + a_{mn} \right] b_n = f_m, \quad m = 0, 1, 2, \ldots, N, \tag{61}$$

where δ_{mn} denotes the Kronecker delta symbol, and

$$a_{mn} = \frac{1 + (-1)^{m-n}}{2} \left[\frac{1}{1 - (m-n)^2} + \frac{1}{1 - (m+n+2)^2} \right], \tag{62}$$

$$f_m = -\int_{-1}^{1} \zeta(\bar{x}) T_{m+1}(\bar{x}) \, d\bar{x}. \tag{63}$$

For the case of an even loading, (61) forms a system of $(N+1)$ linear algebraic equations with $(N+1)$ unknowns. Solving the above system through a standard method, one gets the desired solution. For the case of an odd loading, an additional unknown constant C appears in (40), which can be determined by another supplementary condition (41). In other words, besides the above $N+1$ equations (61) we must add another equation, i.e.,

$$\sum_{n=0}^{N} b_n [(n+1)\theta + 1] \cos \frac{(1+n)\pi}{2} = -\zeta(0). \tag{64}$$

Therefore, (61) together with (64) form a system of $(N+2)$ linear algebraic equations with $(N+2)$ unknowns including $b_n (0, 1, 2, \ldots, N)$ and $\zeta(0)$. Thus the resulting system is uniquely solvable.

Once the unknown coefficients b_n are determined, the stress singularity near the crack tips is readily derived. To this end, substituting (52) into (25) we get the stress along the crack line through the following integral:

$$\sigma_{yz}(x, 0) = \frac{\tau_0}{\pi} \sum_{n=0}^{N} b_n \int_{-1}^{1} \frac{U_n(\bar{s})\sqrt{1 - \bar{s}^2}}{(\bar{s} - \bar{x})^2} \, d\bar{s}. \tag{65}$$

Remembering the following properties of the Chebyshev polynomials [Paulino et al. 2003]:

$$\frac{1}{\pi} \int_{-1}^{1} \frac{U_n(\bar{s})\sqrt{1 - \bar{s}^2}}{(\bar{s} - \bar{x})^2} \, d\bar{s} = \begin{cases} -(n+1)U_n(\bar{x}), & |\bar{x}| < 1, \\ (n+1)(|\bar{x}|/\sqrt{\bar{x}^2 - 1} - 1)(\bar{x} - \bar{x}/|\bar{x}|\sqrt{\bar{x}^2 - 1})^n, & |\bar{x}| > 1, \end{cases} \tag{66}$$

for $n \geq 0$, we have

$$\sigma_{yz}(x, 0) = \tau_0 \sum_{n=0}^{N} b_n (n+1) \left(\frac{|\bar{x}|}{\sqrt{\bar{x}^2 - 1}} - 1 \right) \left(\bar{x} - \frac{\bar{x}}{|\bar{x}|} \sqrt{\bar{x}^2 - 1} \right)^n, \quad |\bar{x}| > 1. \tag{67}$$

From the above stress field, we find that the stress field exhibits the usual inverse square-root singularity near the crack tips. If defining the stress intensity factor by

$$K_{III}^+ = \lim_{x \to a^+} \sqrt{2\pi(x - a)} \sigma_{yz}(x, 0), \quad K_{III}^- = \lim_{x \to -a^-} \sqrt{-2\pi(a + x)} \sigma_{yz}(x, 0), \tag{68}$$

we can give the explicit expression for stress intensity factor as

$$K_{III}^+ = \tau_0 \sqrt{\pi a} \sum_{n=0}^{N} (n+1) b_n, \quad K_{III}^- = \tau_0 \sqrt{\pi a} \sum_{n=0}^{N} (-1)^n (n+1) b_n. \tag{69}$$

To get the stress distribution, from (25) and (46) one acquires the stress at the crack-free part:

$$\sigma_{yz}(x, 0) = \tau_0 \sum_{n=0}^{N} (n+1)b_n [x/a - x/|x|\sqrt{(x/a)^2 - 1}]^{n+1} [\sqrt{(x/a)^2 - 1}]^{-1}, \quad |x| > a. \quad (70)$$

It is obvious from the above result that bulk stress still exhibits an inverse square-root singularity unless $b_0 \neq 0$. This conclusion is different from the previous results. The reason is that Kim et al. [2009; 2011b] assumed a vanishing out-of-plane displacement gradient at the crack tips and found no singularity at the crack tips. Their treatment in fact corresponds to $b_0 = 0$. Finally, it is worth noting that on account of the influence of surface stress, the bulk stresses at the crack faces are not equal to applied loading at the crack faces. Or rather, using (38) and (39) one gets the bulk stress at the crack faces in the upper half-plane:

$$\sigma_{yz}(x, 0^+) = -\tau_0 \left\{ 1 - \theta \sum_{n=0}^{N} b_n(n+1) \left[\frac{(n+1)aU_n(x/a)}{\sqrt{a^2 - x^2}} + \frac{a^2 x T_{n+1}(x/a)}{(a^2 - x^2)^{3/2}} \right] \right\}, \quad |x| < a, \quad (71)$$

where in deriving the above result, (55) and

$$\frac{dT_{n+1}(x)}{dx} = (n+1)U_n(x) \quad (72)$$

have been used. It is readily found that because of consideration of surface effect, the bulk stress at the crack face exhibits a singular behavior near the crack tips, rather than a constant, although applied antiplane shear loading is uniform. When the surface effect is neglected, i.e., $\theta = 0$, applied constant loading is recovered, as expected.

5. Numerical results and discussion

In this section, numerical examples are presented to examine the influence of surface effect on stress intensity factors, crack face displacement, and stress distribution. In addition to bulk shear modulus μ, only the parameter θ enters the final equation (46). It indicates that all surface parameters including surface elasticity and surface residual stress in connection with crack length are combined into a dimensionless parameter θ.

We first examine the influence of the parameter θ on the stress intensity factors. As such, the following numerical results are only presented for uniform loading, i.e., $q(x) = -\tau_0$. Under such circumstances, we have $\zeta(\bar{x}) = -\bar{x}$ and (61) becomes

$$\sum_{n=0}^{N} \left[\frac{(2n+1)\pi}{2} \theta \delta_{mn} + \frac{1}{1 - 4(m-n)^2} + \frac{1}{1 - 4(m+n+1)^2} \right] b_n = \frac{2}{3 - 4m(1+m)}, \quad m = 0, 1, \dots, N. \quad (73)$$

It is clear that the coefficients b_n are dependent on the parameter θ alone. By solving the above linear equations, the b_n are determined and the stress intensity factors are evaluated by (69). According to the estimate of Kim et al. [2009], the range of θ is not in excess of 0.1. Considering the occurrence of a negative parameter θ [Hu et al. 2018], Table 1 examines the convergence of the numerical results of the normalized stress intensity factor $K_{III}/\tau_0\sqrt{\pi a}$ for various values of θ. From Table 1, one finds that if taking $\theta = 10^{-8}$, meaning that surface effect is nearly negligible, the normalized stress intensity factors

$\theta \downarrow$ $N \rightarrow$ 20	40	60	80	100
-10^{-4}	1.06148	1.28376	1.9920	9.87854	-
-10^{-6}	1.00058	1.00217	1.0048	1.00848	1.01324
-10^{-8}	1.00001	1.00002	1.00005	1.00008	1.00013
0	1	1	1	1	1
10^{-8}	0.999994	0.999978	0.999952	0.999916	0.999869
10^{-6}	0.999424	0.997837	0.995247	0.991669	0.987129
10^{-4}	0.945787	0.824715	0.686202	0.562309	0.462943
10^{-3}	0.646534	0.357601	0.230787	0.168227	0.132117
10^{-2}	0.206562	0.0998366	0.0659344	0.0492867	0.039375
10^{-1}	0.0561862	0.0284717	0.0190879	0.0143603	0.0115109

Table 1. The normalized stress intensity factor $K_{III}^{+}/\tau_0\sqrt{\pi a}$.

are almost equal to unity. Since θ is inversely proportional to the crack length, as shown in (42), that is to say that when the crack length arrives at a macroscale such as centimeter or larger, the value of θ is close to 10^{-8}, and the classical stress intensity factor is then recovered. Moreover, for such θ values, the convergence of the numerical results is very satisfactory. However, with the crack length decreasing, or θ rising, we find that the influence of surface effect is enhanced, and the normalized stress intensity factors obviously decline if the same term number N is chosen. It implies that when the crack length drops, the surface effect gives rise to a reduction of the stress intensity factor. That is, consideration of the surface effect enhances apparent fracture toughness of the material. This conclusion agrees well with theoretical prediction [Wang et al. 2013; Yang et al. 2018] and some experimental observation [Gojny et al. 2004; Kim et al. 2008; Liu et al. 2011]. Additionally, for a given θ value, $\theta = 0.001$, say, one views that the evaluated normalized stress intensity factors take 0.65 for $N = 20$ and 0.13 for $N = 100$, respectively. That implies that the convergence rate becomes quite slow, particularly for larger values of θ. This conclusion is attributed to the contribution of the first term of the left-hand side of (46) containing an unbounded derivative operator, which plays an amplification role for small values, particularly when the term number is large enough. This characteristic belongs to the nature of the derivative operator. For most cases, θ is positive. However, for a few cases with a negative θ value, the stress intensity factors increase with θ being larger in magnitude, which is capable of promoting crack growth or decreasing apparent fracture toughness. In the following, $N = 100$ is chosen unless otherwise stated.

If the coefficients b_n are determined by solving the resulting algebraic equations, the dimensionless out-of-plane displacement $\mu\bar{g}(\bar{x})/\tau_0$ is numerically calculated through the expansion (52), and the corresponding profiles at the upper crack-face are plotted in Figure 2 for several different θ values. From Figure 2, one finds that when θ is less than 10^{-3}, the profile curve of the dimensionless out-of-plane displacement $\mu\bar{g}(\bar{x})/\tau_0$ almost does not vary. For larger values such as $\theta = 0.05, 0.1$, the profile curve has a relatively large deviation.

Figure 3 shows the variation of bulk stress $\sigma_{zy}(x, 0)/\tau_0$ as a function of x for various values of θ. From Figure 3, it is seen that the bulk stress nearly takes a constant at the crack face ($|x| < a$) and the influence of surface effect is undetectable since the dimensionless parameter $\theta = 10^{-8}$ is sufficiently small. If setting $\theta = 0$, the bulk stress at the crack face identically takes a constant -1, which reduces
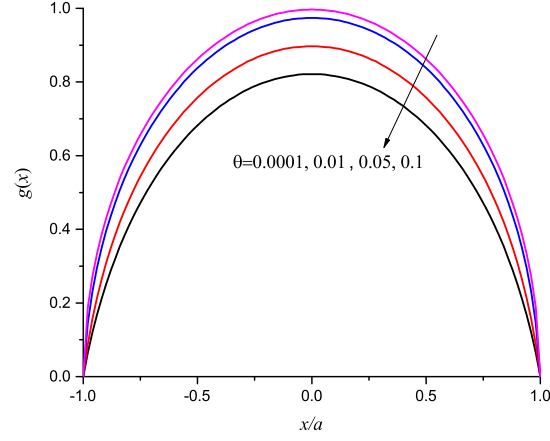
Figure 2. Profile of the dimensionless out-of-plane displacement $\mu \bar{g}(\bar{x})/\tau_0$ at the upper crack-face.
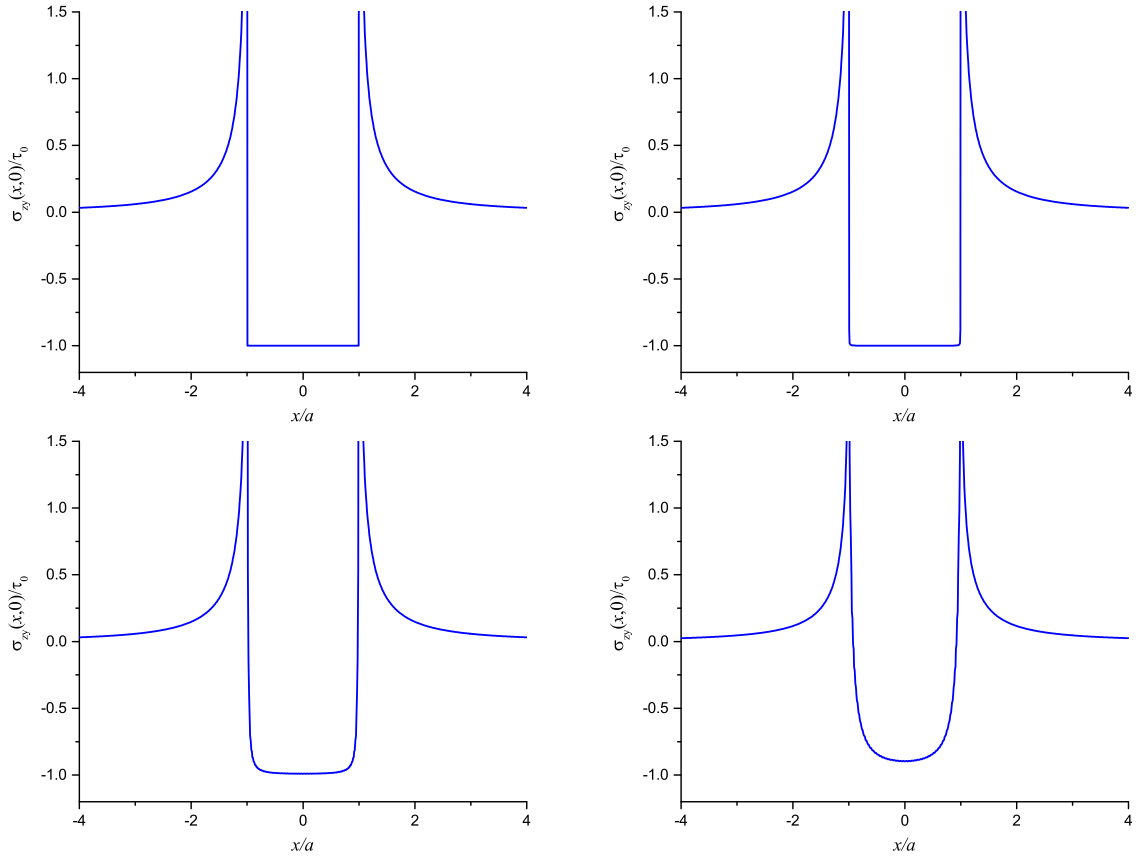

Figure 3. The variation of bulk stress $\sigma_{zy}(x, 0)/\tau_0$ as a function of x for various values of θ. Top left: $\theta = 10^{-8}$. Top right: $\theta = 10^{-4}$. Bottom left: $\theta = 10^{-2}$. Bottom right: $\theta = 10^{-1}$.

to the classical result. With θ rising, the surface effect alters the stress distribution. For example, for $\theta = 10^{-2}, 10^{-1}$, it is seen in Figure 3, bottom, that the bulk stress at the crack face varies. At the crack-free part, the bulk stress always exhibits inverse square-root singularity, as shown in Figure 3.

For practical situations, the θ values need to be given beforehand. Usually, bulk and surface material properties cover a large range. For example, the material properties of GaN, composed of a mixture of nitrified aluminum (Al), gallium (Ga) and indium (In) take the following values: $1.7\,\text{GPa} \leq \mu \leq 168\,\text{GPa}$, $0.7\,\text{N/m} < \sigma_0 < 2\,\text{N/m}$, $\mu^s = 161.73\,\text{J/m}^2$ [Sharma and Ganti 2004]. A copper single crystal with $E = 123.5\,\text{GPa}$, $11.6\,\text{N/m}$, $\sigma_0 = 1.5\,\text{N/m}$ [Choi et al. 2010], and an anodic alumina with $E = 70\,\text{GPa}$, $E^s = 5.19\,\text{N/m}$, $\sigma_0 = 0.91\,\text{N/m}$ [Shenoy 2005]. Therefore, in what follows we consider several typical values of $(\mu^s - \sigma_0)/\mu$, reflecting the surface characteristic length, and plot the variation of the stress intensity factors against the crack half-length a in Figure 4. From Figure 4, left, we see that for those materials with $(\mu^s - \sigma_0)/\mu = 10^{-10}$m, when the crack half-length is lower than 10μm, the surface effect comes into play and rapidly decreases the stress intensity factor, and when the crack half-length arrives at nanometer order, the stress intensity factor nearly equals zero, implying very weak singularity near the crack tips. In other words, the load-carrying capacity is effectively enhanced. Furthermore, if the surface shear modulus μ^s is raised, which causes $(\mu^s - \sigma_0)/\mu$ to rise, $(\mu^s - \sigma_0)/\mu = 10^{-8}$ m, say, one finds that the influence of surface effect is apparently observed for those cracks with length of millimeter order. Moreover, when the crack length drops to micrometer, the stress singularity almost disappears. This also sheds light on a mechanism that it is more difficult for micro/nanometer cracks to grow since the surface effect decreases the stress singularity and impedes crack advance. Or rather, the effective fracture toughness of cracked materials is enhanced when the crack length is reduced. This conclusion is verified by some experimental evidence. For example, Zhang et al. [2014] demonstrated that fracture stress is raised when the crack length is lowered for a bilayer graphene with a precrack. Cohen-Tanugi and Grossman [2014] showed an increase in fracture stress with nanopore radius decreasing in nanoporous graphene. Since most materials give a positive value of the parameter θ, it is worth noting that a negative value of θ for a few materials increases the stress intensity factors, as seen in Figure 4, right, which speeds crack advance. This trend is opposite to that for the case of $\theta > 0$.
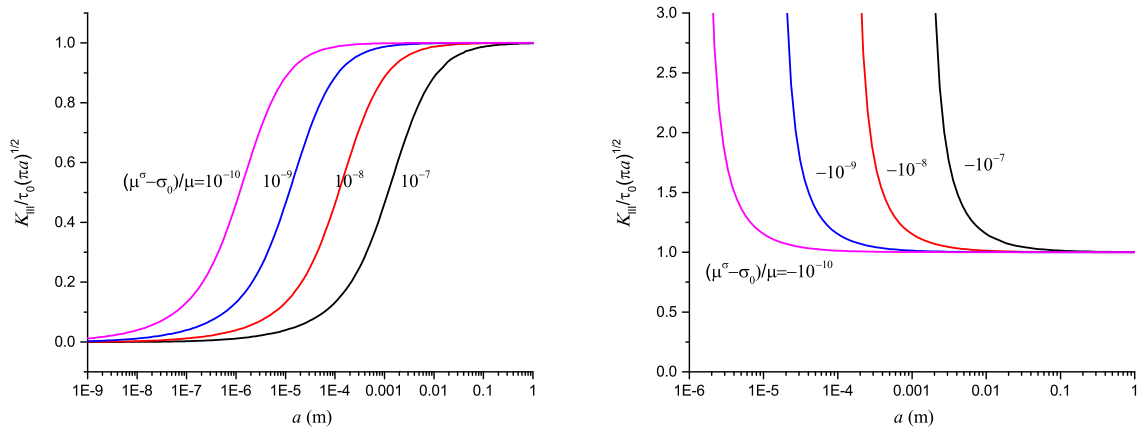
Figure 4. Dimensionless stress intensity factor $K_{III}/\tau_0\sqrt{\pi a}$ against the crack half-length a (m) for typical values of (left) positive and (right) negative $(\mu^s - \sigma_0)/\mu$ (m).

6. Conclusions

In this paper, we analyzed a mode-III crack embedded in an isotropic homogeneous medium with surface effect and examined the influence of surface material properties on a stress singularity near the crack tips. Using the Fourier transform, we first derived a hypersingular integro-differential equation. The Galerkin method was adopted to solve the resulting equation. Based on the expansion of the out-of-plane displacement jump across crack faces in terms of Chebyshev polynomials, the unknown coefficients were determined. The stress intensity factors were obtained and displayed for different surface properties. Obtained results show that for most materials with positive values of the parameter θ, consideration of surface effect decreases the stress intensity factors, or the effective fracture toughness is enhanced for materials with nano/microscale crack. Conversely, negative θ values increase the stress intensity factors or reduce the effective fracture toughness.

Acknowledgments

References

[Bhattacharya and Mandal 2008] S. Bhattacharya and B. N. Mandal, "Numerical solution of a singular integro-differential equation", *Appl. Math. Comput.* **195**:1 (2008), 346–350.

[Chan et al. 2003] Y.-S. Chan, A. C. Fannjiang, and G. H. Paulino, "Integral equations with hypersingular kernels: theory and applications to fracture mechanics", *Int. J. Eng. Sci.* **41**:7 (2003), 683–720.

[Chen et al. 2017] D. Q. Chen, D. L. Sun, and X.-F. Li, "Surface effects on resonance frequencies of axially functionally graded Timoshenko nanocantilevers with attached nanoparticle", *Compos. Struct.* **173** (2017), 116–126.

[Choi et al. 2010] J. Choi, M. Cho, and W. Kim, "Surface effects on the dynamic behavior of nanosized thin film resonator", *Appl. Phys. Lett.* **97**:17 (2010), art. id. 171901.

[Cohen-Tanugi and Grossman 2014] D. Cohen-Tanugi and J. C. Grossman, "Mechanical strength of a nanoporous graphene as a desalination membrane", *Nano Lett.* **14**:11 (2014), 6171–6178.

[Dingreville et al. 2005] R. Dingreville, J. Qu, and M. Cherkaoui, "Surface free energy and its effect on the elastic behavior of nano-sized particles, wires and films", *J. Mech. Phys. Solids* **53**:8 (2005), 1827–1854.

[Duan et al. 2005] H. L. Duan, J. Wang, Z. P. Huang, and B. L. Karihaloo, "Size-dependent effective elastic constants of solids containing nano-inhomogeneities with interface stress", *J. Mech. Phys. Solids* **53**:7 (2005), 1574–1596.

[Duan et al. 2009] H. L. Duan, J. Wang, and B. L. Karihaloo, "Theory of elasticity at the nanoscale", *Adv. Appl. Mech.* **42** (2009), 1–68.

[Frankel 1995] J. I. Frankel, "A Galerkin solution to a regularized Cauchy singular integro-differential equation", *Quart. Appl. Math.* **53**:2 (1995), 245–258.

[Fu et al. 2008] X. L. Fu, G.-F. Wang, and X. Q. Feng, "Surface effects on the near-tip stress fields of a mode-II crack", *Int. J. Fract.* **151**:2 (2008), 95–106.

[Gao et al. 2013] X. Gao, F. Hao, D. Fang, and Z. Huang, "Boussinesq problem with the surface effect and its application to contact mechanics at the nanoscale", *Int. J. Solids Struct.* **50**:16-17 (2013), 2620–2630.

[Gao et al. 2014] X. Gao, F. Hao, Z. Huang, and D. Fang, "Mechanics of adhesive contact at the nanoscale: the effect of surface stress", *Int. J. Solids Struct.* **51**:3-4 (2014), 566–574.

[Gojny et al. 2004] F. H. Gojny, M. H. G. Wichmann, U. Köpke, B. Fiedler, and K. Schulte, "Carbon nanotube-reinforced epoxy-composites: enhanced stiffness and fracture toughness at low nanotube content", *Compos. Sci. Technol.* **64**:15 (2004), 2363–2371.

[Gurtin and Murdoch 1975] M. E. Gurtin and A. I. Murdoch, "A continuum theory of elastic material surfaces", *Arch. Ration. Mech. Anal.* **57** (1975), 291–323. Addenda in **59**:4 (1975), 389–390.

[Gurtin et al. 1998] M. E. Gurtin, J. Weissmüller, and F. Larché, "A general theory of curved deformable interfaces in solids at equilibrium", *Philos. Mag. A* **78**:5 (1998), 1093–1109.

[Hu and Li 2018] Z.-L. Hu and X.-F. Li, "A rigid line inclusion in an elastic film with surface elasticity", *Z. Angew. Math. Phys.* **69**:4 (2018), art. id. 92.

[Hu et al. 2018] Z.-L. Hu, K. Y. Lee, and X.-F. Li, "Crack in an elastic thin-film with surface effect", *Int. J. Eng. Sci.* **123** (2018), 158–173.

[Ioakimidis 1982] N. I. Ioakimidis, "Application of finite-part integrals to the singular integral equations of crack problems in plane and three-dimensional elasticity", *Acta Mech.* **45**:1-2 (1982), 31–47.

[Kaya and Erdogan 1987] A. C. Kaya and F. Erdogan, "On the solution of integral equations with strongly singular kernels", *Quart. Appl. Math.* **45**:1 (1987), 105–122.

[Kim et al. 2008] B. C. Kim, S. W. Park, and D. G. Lee, "Fracture toughness of the nano-particle reinforced epoxy composite", *Compos. Struct.* **86**:1-3 (2008), 69–77.

[Kim et al. 2009] C. I. Kim, P. Schiavone, and C.-Q. Ru, "The effects of surface elasticity on an elastic solid with mode-III crack: complete solution", *J. Appl. Mech. (ASME)* **77**:2 (2009), art. id. 021011.

[Kim et al. 2011a] C. I. Kim, P. Schiavone, and C.-Q. Ru, "Analysis of plane-strain crack problems (mode-I and mode-II) in the presence of surface elasticity", *J. Elasticity* **104**:1-2 (2011), 397–420.

[Kim et al. 2011b] C. I. Kim, P. Schiavone, and C.-Q. Ru, "The effect of surface elasticity on a mode-III interface crack", *Arch. Mech. Stos.* **63**:3 (2011), 267–286.

[Kim et al. 2011c] C. I. Kim, P. Schiavone, and C.-Q. Ru, "Effect of surface elasticity on an interface crack in plane deformations", *Proc. R. Soc. Lond. A* **467**:2136 (2011), 3530–3549.

[Kim et al. 2013] C. I. Kim, C.-Q. Ru, and P. Schiavone, "A clarification of the role of crack-tip conditions in linear elasticity with surface effects", *Math. Mech. Solids* **18**:1 (2013), 59–66.

[Lee et al. 2008] C. Lee, X. Wei, J. W. Kysar, and J. Hone, "Measurement of the elastic properties and intrinsic strength of monolayer graphene", *Science* **321**:5887 (2008), 385–388.

[Li 2003] X.-F. Li, "Electroelastic analysis of an internal interface crack in a half-plane consisting of two bonded dissimilar piezoelectric quarter-planes", *Meccanica (Milano)* **38**:3 (2003), 309–323.

[Li et al. 2013] X.-F. Li, G.-J. Tang, and B.-Q. Tang, "Stress field around a strike-slip fault in orthotropic elastic layers via a hypersingular integral equation", *Comput. Math. Appl.* **66**:11 (2013), 2317–2326.

[Liu et al. 2011] H.-Y. Liu, G.-T. Wang, Y.-W. Mai, and Y. Zeng, "On fracture toughness of nano-particle modified epoxy", *Compos. B Eng.* **42**:8 (2011), 2170–2175.

[Lurie and Belyaev 2005] A. I. Lurie and A. Belyaev, *Theory of elasticity*, Springer, 2005.

[Mogilevskaya et al. 2008] S. G. Mogilevskaya, S. L. Crouch, and H. K. Stolarski, "Multiple interacting circular nano-inhomogeneities with surface/interface effects", *J. Mech. Phys. Solids* **56**:6 (2008), 2298–2327.

[Muskhelishvili 1977] N. I. Muskhelishvili, *Some basic problems of the mathematical theory of elasticity*, Springer, 1977.

[Nan and Wang 2012] H. Nan and B. Wang, "Effect of residual surface stress on the fracture of nanoscale materials", *Mech. Res. Commun.* **44** (2012), 30–34.

[Paulino et al. 2003] G. H. Paulino, A. C. Fannjiang, and Y.-S. Chan, "Gradient elasticity theory for mode III fracture in functionally graded materials, I: Crack perpendicular to the material gradation", *J. Appl. Mech. (ASME)* **70**:4 (2003), 531–542.

[Ru 2010] C.-Q. Ru, "Simple geometrical explanation of Gurtin–Murdoch model of surface elasticity with clarification of its related versions", *Sci. China G Phys. Mech. Astronom.* **53**:3 (2010), 536–544.

[Sharma and Ganti 2004] P. Sharma and S. Ganti, "Size-dependent Eshelby's tensor for embedded nano-inclusions incorporating surface/interface energies", *J. Appl. Mech. (ASME)* **71**:5 (2004), 663–671.

[Shenoy 2005] V. B. Shenoy, "Atomistic calculations of elastic properties of metallic fcc crystal surfaces", *Phys. Rev. B* **71**:9 (2005), art. id. 094104. Correction in **74**:14 (2006, art. id. 149901.

[Walton 2012] J. R. Walton, "A note on fracture models incorporating surface elasticity", *J. Elasticity* **109**:1 (2012), 95–102.

[Wang 2015] X. Wang, "A mode III arc-shaped crack with surface elasticity", *Z. Angew. Math. Phys.* **66**:4 (2015), 1987–2000.

[Wang and Feng 2007] G.-F. Wang and X. Q. Feng, "Effects of surface stresses on contact problems at nanoscale", *J. Appl. Phys.* **101**:1 (2007), art. id. 013510.

[Wang and Schiavone 2016] X. Wang and P. Schiavone, "Bridged cracks of mode III with surface elasticity", *Mech. Mater.* **95** (2016), 125–135.

[Wang et al. 2008] G.-F. Wang, X.-Q. Feng, T.-J. Wang, and W. Gao, "Surface effects on the near-tip stresses for mode-I and mode-III cracks", *J. Appl. Mech.* (*ASME*) **75**:1 (2008), art. id. 011001.

[Wang et al. 2013] H. Wang, X. Li, G. Tang, and Z. Shen, "Effect of surface stress on stress intensity factors of a nanoscale crack via double cantilever beam model", *J. Nanosci. Nanotechnol.* **13**:1 (2013), 477–482.

[Wong et al. 1997] E. W. Wong, P. E. Sheehan, and C. M. Lieber, "Nanobeam mechanics: elasticity, strength, and toughness of nanorods and nanotubes", *Science* **277**:5334 (1997), 1971–1975.

[Wu 1999] C. H. Wu, "The effect of surface stress on the configurational equilibrium of voids and cracks", *J. Mech. Phys. Solids* **47**:12 (1999), 2469–2492.

[Wu et al. 2017] J.-X. Wu, X.-F. Li, A.-Y. Tang, and K. Y. Lee, "Free and forced transverse vibration of nanowires with surface effects", *J. Vib. Control* **23**:13 (2017), 2064–2077.

[Xiao and Li 2018] Q.-X. Xiao and X.-F. Li, "Flutter and divergence instability of rectangular plates under nonconservative forces considering surface elasticity", *Int. J. Mech. Sci.* **149** (2018), 254–261.

[Yang et al. 2018] Y. Yang, K. Y. Lee, and X.-F. Li, "Surface effects on delamination of a thin film bonded to an elastic substrate", *Int. J. Fract.* **210**:1-2 (2018), 81–94.

[Zhang et al. 2014] P. Zhang, L. Ma, F. Fan, Z. Zeng, C. Peng, P. E. Loya, Z. Liu, Y. Gong, J. Zhang, X. Zhang, P. M. Ajayan, T. Zhu, and J. Lou, "Fracture toughness of graphene", *Nat. Commun.* **5** (2014), art. id. 3782.

[Zhang et al. 2015] T. Zhang, X. Li, and H. Gao, "Fracture of graphene: a review", *Int. J. Fract.* **196**:1-2 (2015), 1–31.

XIAN-FANG LI: xfli@csu.edu.cn
School of Civil Engineering, Central South University, Changsha, 410075, China

◾◾
◾msp

ANALYTICAL INVESTIGATION OF FREE VIBRATIONS OF A BOUNDED NONLINEAR BULK-ELASTIC MEDIUM IN A FIELD OF MASS FORCES

EUGENE I. RYZHAK AND SVETLANA V. SINYUKHINA

Free vibrations of a homogeneous nonlinear bulk-elastic medium, namely a solid with negligible shear stiffness, occupying a bounded domain and nonuniformly deformed under the action of a field of mass forces are investigated through variational methods. The nonlinear constitutive law of bulk elasticity is assumed to be arbitrary, the applied field of mass forces is assumed to be an arbitrary potential field, and conditions of free sliding are prescribed on the whole boundary. The associated problem of free vibrations corresponds to significantly nonuniform distribution of mechanical parameters of the medium, which results in significantly varying coefficients of governing equations — a case where standard methods are inapplicable and results of analysis are almost absent. A crucial element of presented variational analysis is the use of derived by the authors earlier the canonical form for the second variation of the total potential energy. This canonical form enables to state and prove a modified spectral theorem, and additionally a comparison theorem for the free vibration frequencies of different media in different fields of mass forces, provided the media occupy domains possessing the same or similar shapes. For some special shapes, the bilateral bounds for all the free vibration frequencies are obtained. The results are illustrated by clarifying examples.

1. Introduction

"Vibration problems for inhomogeneous structural elements present a challenge to the acoustics and vibration community. In contrast to classical problems for homogeneous strings, rods, membranes or plates for which exact solutions and a variety of approximate methods are available for finding frequencies and mode shapes, analogous results for inhomogeneous bodies are relatively scarce" [Horgan and Chan 1999]. This kind of problems is addressed in the present paper, considering the free vibrations of nonlinear bulk-elastic media occupying bounded domains. The nonuniformity of initial state of the medium is a result of 'stratification', namely, nonuniform strain produced by the action of a mass force field. With the term "bulk-elastic media" we mean nonlinearly elastic media characterized by an elastic potential depending exclusively on the volumetric strain (for instance, compressible fluids and gases), so that bulk-elastic media have a null shear stiffness. Although, strictly speaking, the presented analysis is based on constitutive relations of this very type, one can expect that the results may be extended to media characterized by shear moduli which are small as compared to their bulk moduli (say, gels, foams, etc.).

The considered problem is related to numerous technical devices, for instance, gas storage tanks, distillation columns, and pipeline sections (in the cases when there is a significant variation in altitude along the pipe). In addition to engineering equipment, some mechanical systems of natural origin (for instance atmospheres of planets) can be of interest in geophysics, atmospheric physics, or astrophysics.

In technical devices (especially those of large size) the vibrations are an undesirable (but inevitable) phenomenon, which may result even in the failure of the device. To prevent the excitation of resonant vibrations of large amplitude, it is desirable to know at least the ranges for free vibration frequencies, i.e. to find bilateral bounds for them, and also to understand how they depend on the mechanical properties of the bulk-elastic medium and on geometry of the domain. In the case of the gravity field for the domains large in the vertical dimension, the nonuniformity of density and bulk modulus distributions under the action of gravity is significant, which affects free vibrations. For large natural systems, as well as for rotating devices, where mass forces are implemented as the centrifugal forces, the nonuniformity of mass forces (that can manifest itself both as nonuniformity in absolute value and nonuniformity in the direction) can also play an important role.

Free vibrations of bulk-elastic media in bounded domains were not previously explored with regard for significantly nonuniform distribution of mechanical parameters of a medium. The well-known analytical solutions (based on equations with constant coefficients) are applicable only if nonuniformity of distribution of mechanical parameters of a compressible medium due to the action of mass forces is neglected (see e.g. Landau and Lifshitz 1987), that can be justified only in cases of low compressibility, or low mass forces, or small "vertical" dimension of the system. It should be mentioned that the particular case of constant sound velocity in a heavy medium (independent of pressure) and the resulting exponential distribution of density over depth, has been studied analytically and numerically by means of some special method (see e.g. Gaziev and Kopachevsky 2013). Nevertheless, this particular case does not exhaust the general problem, and its relevance motivates the purpose of the present article, namely, the general study of free vibrations of bulk-elastic media in bounded domains with regard for the action of mass forces. The bulk-elastic media are assumed to be constitutively homogeneous with an arbitrary nonlinear bulk-elastic law. The field of mass forces is assumed to be an arbitrary potential field. The domains are assumed to be bounded, simply connected, and having a piecewise smooth boundary (obeying some additional requirements which will be specified in detail in formulation of the lemma proved in Appendix A). The domains of several special shapes are studied separately.

Note that the problem setting is highly general, so that one can hardly expect to obtain any definite analytical results for the characteristics of free vibrations. In particular, the conventional methods of solving the corresponding problems in the presence of significant nonuniformity of coefficients and for rather arbitrary shape of the domain are not effective. The only known method that can be effective in this case is the variational method: the free vibration modes are the extremals of a well-known functional, and the squares of eigenfrequencies are the corresponding extremal values. The functional mentioned is the ratio of two quadratic functionals, namely, the second variation of the total potential energy of the system and its doubled kinetic energy (in the latter the velocity field is replaced by the field of small displacements). *The analytical expression for the second variation of the total potential energy is derived in principle easily and briefly through linearization of the equations of nonlinear elasticity, but this rather cumbersome expression yields almost nothing for investigation of free vibrations. A truly effective research tool is the usage of derived earlier by the authors* [Ryzhak et al. 2017]*: the canonical form of the second variation of the total potential energy. We use the term "canonical form" in the same sense as it is used in linear algebra with regard to quadratic forms: it does reveal the structure (in particular, the sign) of the quadratic functional representing the second variation. In contrast to the*
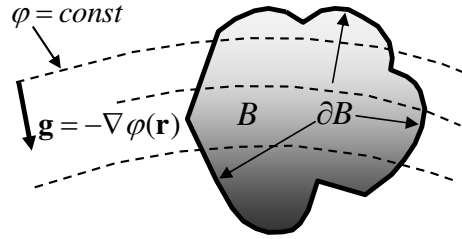
Figure 1. The mechanical system under investigation.

general case, when canonical form of the second variation consists of four terms [Ryzhak et al. 2017]; *in the problem under consideration it is especially simple and consists of a single term.*

In this paper, the investigation of free vibrations is carried out by the variational method, the crucial element of which being the usage of the above-mentioned canonical form of the second variation. Firstly, the canonical form reveals the not evident fact that for a homogeneous bulk-elastic medium the mass forces affect free vibrations only indirectly, specifically via resulting nonuniformity of equilibrium distribution of mechanical parameters of a medium. Secondly, the usage of the canonical form allows to prove for the considered class of problems some appropriate modifications of fundamental theorems of the theory of free vibrations for elastic solids. The modified theorems are applied both to compare the free vibration frequencies for different bulk-elastic media in domains of identical or similar shapes and to obtain analytical bilateral bounds for the frequencies in the case of domains that have the shape of either a rectangular parallelepiped or some different polyhedra, depending on the quantities characterizing nonuniformity of the equilibrium state of a medium and the geometry of a domain.

In Section 7 the general analytical results are illustrated by examples, where for a bulk-elastic medium of some specific type there are studied various situations characterized by different relations between gravity, geometry, and mechanical properties of the medium. The considered examples allow both to compare our results with the classical ones, corresponding to the case of governing equations with constant coefficients, and to clarify the situation where classical methods are inapplicable.

2. The investigated classes of mechanical systems and some elements of their kinematics in reference description

We assume that the potential of mass forces $\varphi(\boldsymbol{r})$, where $\boldsymbol{r}$ is the space position vector, is a continuously differentiable function with nonzero bounded gradient. The mass forces field intensity $\boldsymbol{g}$ is a vector opposite to the gradient of φ:

$$\boldsymbol{g} = -\nabla\varphi(\boldsymbol{r}). \tag{2-1}$$

The mechanical system under investigation consists of a constitutively homogeneous bulk-elastic medium occupying a domain with fixed and perfectly smooth boundary (Figure 1). A law of bulk elasticity is supposed to be arbitrary. In spite of constitutive homogeneity, the equilibrium state of the medium is nonuniform due to stratification caused by the action of mass forces. The boundary conditions of free sliding are posed on the whole of the boundary of the domain. The kinematical part of conditions of sliding specify the class of kinematically admissible motions of the medium at deviations of considered mechanical system from the equilibrium state which is assumed to be stable.

In all subsequent calculations we use the reference description of the continua considered (see for example Truesdell 1972). As a reference configuration κ (which is fixed in principle) it is taken the equilibrium configuration of the system. Material points of a continuum are identified by their position vectors x in the reference configuration; for each material point its identifier x is invariable. The actual position of a material point x is specified by the image of mapping

$$r = r(x, t), \qquad (2\text{-}2)$$

which will be called the "transformation"; here t is a time, $r(x, t)$ is the position vector of a given material point at a given time instant. Without loss of generality, we assume that the reference configuration coincides with the actual one at $t = 0$:

$$r(x, 0) = x. \qquad (2\text{-}3)$$

The domain occupied by the medium in the reference equilibrium state will be denoted B (Figure 1). The domain B is supposed to be bounded and simply connected. Its boundary ∂B is supposed to be piecewise smooth (Figure 1). Since the boundary is immovable, the domain occupied by the medium in any actual configuration is the same.

3. Some formulas of coordinateless tensor calculus and the relations associated with the reference and spatial descriptions of continua

We introduce some notations related to the reference description and derive equations permanently used in further analysis.

For any physical field $\Psi(x, t)$ (scalar, vector or tensor) its derivative with respect to t at a constant x will be called the "material" time derivative, conventionally denoted by a dot over a symbol:

$$\dot{\Psi}(x, t) := \left(\frac{\partial \Psi}{\partial t}\right)_x. \qquad (3\text{-}1)$$

Note that the velocity and acceleration are the first and the second material derivatives of the position vector $r(x, t)$:

$$v(x, t) = \dot{r}(x, t), \qquad (3\text{-}2)$$

$$\dot{v}(x, t) = \ddot{r}(x, t). \qquad (3\text{-}3)$$

Along with the material derivatives with respect to time, in some cases there will be used the "spatial" derivatives (i.e., the derivatives with respect to time at a constant r), which will be denoted $(\partial \Psi / \partial t)_r$. The material and spatial derivatives with respect to time are related to each other by the well-known Euler's formula which will be presented below.

Throughout the paper we use the coordinateless tensor calculus in the notation, almost coinciding with the system of tensor notation of J. W. Gibbs. Presented below is a summary of the main formulas used in this work: just the minimum necessary to enable us to avoid citing any additional sources.

The main strain-rotation quantity in the reference description is the transformation gradient:

$$F(x, t) := \nabla_\kappa \otimes r(x, t), \qquad (3\text{-}4)$$

$$dr(x, t, dx) = dx \cdot \nabla_\kappa \otimes r(x, t). \qquad (3\text{-}5)$$

The transformation gradient $\boldsymbol{F}(\boldsymbol{x}, t)$ is a tensor of rank two (TR(2)), i.e. the linear operator that specifies the principal linear part of mapping of the vicinity of a material point $\boldsymbol{x}$ in the reference configuration into the vicinity of corresponding point $\boldsymbol{r}(\boldsymbol{x}, t)$ in the actual configuration.

The subscript "κ" referred to the symbol "nabla" in the gradient notation indicates that this is a "reference" gradient, i.e. differentiation is carried out with respect to $\boldsymbol{x}$. The gradient of a tensor field of rank k is defined in a completely similar way:

$$dM(\boldsymbol{x}, t, d\boldsymbol{x}) = d\boldsymbol{x} \cdot \nabla_k \otimes M(\boldsymbol{x}, t), \tag{3-6}$$

i.e. $\nabla_\kappa \otimes M(\boldsymbol{x}, t)$ is a TR($k+1$) that specifies the principal linear part of the increment of the rank-k tensor field $M(\boldsymbol{x}, t)$ in the vicinity of a point x in the reference configuration. In the case of a scalar field gradient, the tensor product sign $\otimes$ in the gradient notation is omitted ($\chi(\boldsymbol{x}, t) \leftrightarrow \nabla_\kappa \chi(\boldsymbol{x}, t)$).

Along with the reference description sometimes it is needed to use the spatial description with the independent variables $(\boldsymbol{r}, t)$. For the gradient with respect to $\boldsymbol{r}$ we will use the symbol ∇ (without a subscript):

$$dM(\boldsymbol{r}, t, d\boldsymbol{r}) = d\boldsymbol{r} \cdot \nabla \otimes M(\boldsymbol{r}, t). \tag{3-7}$$

Due to (3-5) we have

$$\nabla_\kappa \otimes M = \boldsymbol{F} \cdot \nabla \otimes M, \quad \nabla \otimes M = \boldsymbol{F}^{-1} \cdot \nabla_\kappa \otimes M. \tag{3-8}$$

Mentioned above Euler's formula is represented by the following equality:

$$\dot{M}(\boldsymbol{r}, t) = \left(\frac{\partial M}{\partial t}\right)_{\boldsymbol{r}}(\boldsymbol{r}, t) + \boldsymbol{v}(\boldsymbol{r}, t) \cdot \nabla \otimes M(\boldsymbol{r}, t). \tag{3-9}$$

The reference and space divergences of a tensor field of rank k are the TR($k-1$) specified by the following equalities:

$$\nabla_\kappa \cdot M(\boldsymbol{r}, t) := \boldsymbol{I} : \nabla_\kappa \otimes M(\boldsymbol{x}, t), \tag{3-10}$$

$$\nabla \cdot M(\boldsymbol{r}, t) := \boldsymbol{I} : \nabla \otimes M(\boldsymbol{r}, t), \tag{3-11}$$

where $\boldsymbol{I}$ is the unit TR(2) (the unit linear operator in a vector space).

4. The nonlinear and linearized (incremental) relations of the theory of elasticity used in the work

We present without derivation those known formulas of the theory of elastic constitutive relations, which are used subsequently.

Let $\sigma_\kappa(\boldsymbol{F}, \boldsymbol{x})$ be the reference volume density of the elastic energy of a material at the point $\boldsymbol{x}$ of the reference configuration. Due to the principle of material objectivity [Truesdell 1972], it does not depend on rotations, i.e. for any proper orthogonal TR(2) $\boldsymbol{Q}$ (a rotation) and for any $\boldsymbol{F}$ (having a positive determinant), the following equality holds:

$$\sigma_\kappa(\boldsymbol{F} \cdot \boldsymbol{Q}, \boldsymbol{x}) = \sigma_\kappa(\boldsymbol{F}, \boldsymbol{x}). \tag{4-1}$$

The Piola stress tensor $T_\kappa(F, x)$ is related to $\sigma_\kappa(F, x)$ by the following equivalent equalities:

$$\delta\sigma_\kappa(F, x) = \delta F : T_\kappa(F, x), \tag{4-2}$$

$$T_\kappa(F, x) = \frac{\partial\sigma_\kappa}{\partial F}(F, x). \tag{4-3}$$

The surface force vector df, which acts on a surface element with the normal n and the area $d\Sigma$ in the actual configuration, whose pre-image in the reference configuration is the surface element with the normal n_κ and the area $d\Sigma_\kappa$, can be expressed in terms of the Cauchy stress tensor $T(F, x)$ and the Piola stress tensor $T_\kappa(F, x)$ as follows:

$$df = d\Sigma\, n \cdot T = d\Sigma_\kappa\, n_\kappa \cdot T_\kappa, \tag{4-4}$$

which results in the known relationship between the two stress tensors:

$$T_\kappa = (\det F)(F^{-1})^T \cdot T, \quad T = \frac{1}{\det F} F^T \cdot T_\kappa. \tag{4-5}$$

Due to the principle of material objectivity and in accordance with their own specific properties, the Piola and Cauchy stress tensors differently depend on rotations:

$$T_\kappa(F \cdot Q) = T_\kappa(F) \cdot Q \tag{4-6}$$

$$T(F \cdot Q) = Q^T \cdot T(F) \cdot Q =: T(F) * Q. \tag{4-7}$$

The following incremental (linearized) constitutive relations correspond to nonlinear relations $T(F)$ and $T_\kappa(F)$ (with regard for the principle of material objectivity and equalities (4-5)), the linearization being carried out in the vicinity of reference configuration (where $t = 0$, $r = x$, $F = I$, $\nabla = \nabla_\kappa$):

$$\delta T = L : \delta\varepsilon + T \cdot \delta\omega - \delta\omega \cdot T, \tag{4-8}$$

$$\delta T_\kappa|_{F=I} = L : \delta\varepsilon + T(I : \delta\varepsilon) - \delta\varepsilon \cdot T + T \cdot \delta\omega. \tag{4-9}$$

Here, with regard for coincidence of the actual configuration with the reference one at $t = 0$, the incremental tensors of strain $\delta\varepsilon$ and rotation $\delta\omega$ are related to the small displacement field $\delta u(x)$ by the following equalities:

$$\delta\varepsilon = \tfrac{1}{2}(\nabla_\kappa \otimes \delta u + \nabla_\kappa \otimes \delta u^T), \quad \delta\omega = \tfrac{1}{2}(\nabla_\kappa \otimes \delta u - \nabla_\kappa \otimes \delta u^T), \quad \delta\varepsilon + \delta\omega = \nabla_\kappa \otimes \delta u. \tag{4-10}$$

A TR(4) $L(F)$ is one of conventional elastic moduli tensors, the values of TR(4) $L(F)$ being different for different states of one and the same elastic material.

Since $\delta\varepsilon$ is symmetric, whereas $\delta\omega$ is skew-symmetric, we have

$$I : \delta\varepsilon = I : \nabla_\kappa \otimes \delta u = \nabla_\kappa \cdot \delta u. \tag{4-11}$$

If $T = -pI$, the stress state is called hydrostatic with pressure p. In the neighborhood of such a state the equalities (4-8) and (4-9) are simplified and take the form

$$\delta T = L : \delta\varepsilon, \quad \delta T_\kappa|_{F=I} = L : \delta\varepsilon - p(\nabla_\kappa \cdot \delta u)I + p\nabla_\kappa \otimes \delta u^T. \tag{4-12}$$

In what follows it will be assumed that the investigated equilibrium (unperturbed) configuration is characterized by a hydrostatic stress state in the entire domain B. The elastic potential of a bulk-elastic

medium is characterized by the property that its dependence on the transformation gradient $\boldsymbol{F}$ is reduced to dependence on its determinant (i.e. on the volume change coefficient):

$$\sigma_\kappa(\boldsymbol{F}, \boldsymbol{x}) = \psi(\det \boldsymbol{F}, \boldsymbol{x}), \tag{4-13}$$

$$\boldsymbol{T}_\kappa(\boldsymbol{F}, \boldsymbol{x}) = \frac{d(\det \boldsymbol{F})}{d\boldsymbol{F}} \frac{\partial \psi}{\partial(\det \boldsymbol{F})}(\det \boldsymbol{F}, \boldsymbol{x}) = (\det \boldsymbol{F})(\boldsymbol{F}^{-1})^T \frac{\partial \psi}{\partial(\det \boldsymbol{F})}(\det \boldsymbol{F}, \boldsymbol{x}), \tag{4-14}$$

$$\boldsymbol{T}(\boldsymbol{F}, \boldsymbol{x}) = \frac{\partial \psi}{\partial(\det \boldsymbol{F})}(\det \boldsymbol{F}, \boldsymbol{x})\boldsymbol{I} =: -p(\det \boldsymbol{F}, \boldsymbol{x})\boldsymbol{I}, \tag{4-15}$$

$$\delta \boldsymbol{T}(\boldsymbol{F}, \boldsymbol{x})|_{\boldsymbol{F}=\boldsymbol{I}} = -\frac{\partial p}{\partial(\det \boldsymbol{F})}(1, \boldsymbol{x})\, \delta(\det \boldsymbol{F})|_{\boldsymbol{F}=\boldsymbol{I}}\boldsymbol{I}$$

$$= -\frac{\partial p}{\partial(\det \boldsymbol{F})}(1, \boldsymbol{x})\, \boldsymbol{I}\,(\boldsymbol{I} : \delta\boldsymbol{\varepsilon}) =: K(1, \boldsymbol{x})\, \boldsymbol{I}\,(\boldsymbol{I} : \delta\boldsymbol{\varepsilon}), \tag{4-16}$$

$$\implies \quad \boldsymbol{L}(1, \boldsymbol{x}) = K(1, \boldsymbol{x})\, \boldsymbol{I} \otimes \boldsymbol{I} \quad \iff \quad \boldsymbol{L}_\kappa(\boldsymbol{x}) = K_\kappa(\boldsymbol{x})\, \boldsymbol{I} \otimes \boldsymbol{I}, \tag{4-17}$$

where $K_\kappa(\boldsymbol{x})$ is the bulk modulus field of a medium in the reference configuration.

We emphasize that the reference configuration is neither unloaded nor uniform: there is a nonzero pressure distribution $p(1, \boldsymbol{x})$ characterizing the equilibrium state in the field of mass forces.

5. The problem of finding the free vibration frequencies and modes as a variational problem

The concept of free vibrations is known to be related to the linearized problem of motion of an elastic body (in particular, a bulk-elastic medium) in the neighborhood of stable equilibrium state.

To derive the linearized equations of motion and the linearized boundary conditions, we first consider the exact equations and boundary conditions and then linearize them in displacements and their gradients.

The exact equations of motion in a nonuniform potential field of mass forces $\boldsymbol{g}$ and the exact boundary conditions are as follows:

$$\rho_\kappa(\boldsymbol{x})\, \ddot{\boldsymbol{r}}(\boldsymbol{x}, t) = \nabla_\kappa \cdot \boldsymbol{T}_\kappa(\boldsymbol{x}, \boldsymbol{F}(\boldsymbol{x}, t)) + \rho_\kappa(\boldsymbol{x})\boldsymbol{g}, \quad \boldsymbol{g} = -\nabla \varphi(\boldsymbol{r}(\boldsymbol{x}, t)), \tag{5-1}$$

$$\boldsymbol{r}(\boldsymbol{x}, t)|_{\boldsymbol{x} \in \partial B} \in \partial B, \tag{5-2}$$

$$\boldsymbol{n}_\kappa(\boldsymbol{x}) \cdot \boldsymbol{T}_\kappa(\boldsymbol{x}, \boldsymbol{F}(\boldsymbol{x}, t)) \cdot \big(\boldsymbol{I} - \boldsymbol{n}_\kappa(\boldsymbol{r}(\boldsymbol{x}, t)) \otimes \boldsymbol{n}_\kappa(\boldsymbol{r}(\boldsymbol{x}, t))\big)\big|_{\boldsymbol{x} \in \partial B} = 0. \tag{5-3}$$

We introduce the displacement field that is supposed to be small in what follows:

$$\delta\boldsymbol{u}(\boldsymbol{x}, t) := \boldsymbol{r}(\boldsymbol{x}, t) - \boldsymbol{x} \quad \iff \quad \boldsymbol{r}(\boldsymbol{x}, t) = \boldsymbol{x} + \delta\boldsymbol{u}(\boldsymbol{x}, t). \tag{5-4}$$

It is obvious that

$$\dot{\boldsymbol{r}}(\boldsymbol{x}, t) = \delta\dot{\boldsymbol{u}}(\boldsymbol{x}, t), \quad \ddot{\boldsymbol{r}}(\boldsymbol{x}, t) = \delta\ddot{\boldsymbol{u}}(\boldsymbol{x}, t), \quad \boldsymbol{F}(\boldsymbol{x}, t) = \boldsymbol{I} + \nabla_\kappa \otimes \delta\boldsymbol{u}(\boldsymbol{x}, t). \tag{5-5}$$

In the equilibrium state we have

$$\delta\boldsymbol{u}(\boldsymbol{x}, 0) = 0 \quad \iff \quad \boldsymbol{r}(\boldsymbol{x}, 0) = \boldsymbol{x}, \quad \boldsymbol{F}(\boldsymbol{x}, 0) = \boldsymbol{I}, \quad \boldsymbol{n}_\kappa\big(\boldsymbol{r}(\boldsymbol{x}, 0)\big) = \boldsymbol{n}_\kappa(\boldsymbol{x}), \tag{5-6}$$

$$\nabla_\kappa \cdot \boldsymbol{T}_\kappa(\boldsymbol{x}, \boldsymbol{I}) + \rho_\kappa(\boldsymbol{x})\boldsymbol{g} = 0, \tag{5-7}$$

$$\boldsymbol{n}_\kappa(\boldsymbol{x}) \cdot \boldsymbol{T}_\kappa(\boldsymbol{x}, \boldsymbol{I}) \cdot \big(\boldsymbol{I} - \boldsymbol{n}_\kappa(\boldsymbol{x}) \otimes \boldsymbol{n}_\kappa(\boldsymbol{x})\big)\big|_{\boldsymbol{x} \in \partial B} = 0. \tag{5-8}$$

Subtracting the equilibrium values of the quantities from their current values and linearizing the differences in $\delta \boldsymbol{u}(\boldsymbol{x}, t)$ and $\nabla_\kappa \otimes \delta \boldsymbol{u}(\boldsymbol{x}, t)$, we obtain

$$\delta \boldsymbol{T}_\kappa(\boldsymbol{x}, t) = \boldsymbol{T}_\kappa(\boldsymbol{x}, \boldsymbol{F}(\boldsymbol{x}, t)) - \boldsymbol{T}_\kappa(\boldsymbol{x}, \boldsymbol{I}) = \boldsymbol{C}_\kappa(\boldsymbol{x}, \boldsymbol{I}) : \nabla_\kappa \otimes \delta \boldsymbol{u}(\boldsymbol{x}, t), \tag{5-9}$$

$$\delta \boldsymbol{n}_\kappa(\boldsymbol{x}, t) = \boldsymbol{n}_\kappa(\boldsymbol{r}(\boldsymbol{x}, t)) - \boldsymbol{n}_\kappa(\boldsymbol{x}) = \delta \boldsymbol{u} \cdot \nabla_\kappa^\Sigma \otimes \boldsymbol{n}_\kappa(\boldsymbol{x}),$$

$$\delta \boldsymbol{n}_\kappa(\boldsymbol{x}, t) \cdot \boldsymbol{n}_\kappa(\boldsymbol{x}) = 0, \quad \delta(\boldsymbol{I} - \boldsymbol{n}_\kappa \otimes \boldsymbol{n}_\kappa) = -\delta \boldsymbol{n}_\kappa \otimes \boldsymbol{n}_\kappa - \boldsymbol{n}_\kappa \otimes \delta \boldsymbol{n}_\kappa. \tag{5-10}$$

The surface gradient $\nabla_\kappa^\Sigma \otimes \boldsymbol{n}_\kappa$ is specified here by the equality

$$\nabla_\kappa^\Sigma \otimes \boldsymbol{n}_\kappa = (\boldsymbol{I} - \boldsymbol{n}_\kappa \otimes \boldsymbol{n}_\kappa) \cdot \nabla_\kappa \otimes \boldsymbol{n}_\kappa. \tag{5-11}$$

It is not difficult to demonstrate that the surface gradient (5-11) is a symmetric TR(2) over the subspace tangent to ∂B at the points of smoothness.

Taking into account the equalities (5-6)–(5-11), we obtain the following linearized equations of motion and boundary conditions:

$$\rho_\kappa(\boldsymbol{x}) \cdot \delta \ddot{\boldsymbol{u}}(\boldsymbol{x}, t) = \nabla_\kappa \cdot \delta \boldsymbol{T}_\kappa(\boldsymbol{x}, \boldsymbol{I}) - \rho_\kappa(\boldsymbol{x}) \, \delta \boldsymbol{u}(\boldsymbol{x}, t) \cdot \nabla_\kappa \otimes \nabla_\kappa \, \varphi(\boldsymbol{x})$$
$$= \nabla_\kappa \cdot (\boldsymbol{C}_\kappa(\boldsymbol{x}, \boldsymbol{I}) : \nabla_\kappa \otimes \delta \boldsymbol{u}(\boldsymbol{x}, t)) - \rho_\kappa(\boldsymbol{x}) \, \delta \boldsymbol{u}(\boldsymbol{x}, t) \cdot \nabla_\kappa \otimes \nabla_\kappa \, \varphi(\boldsymbol{x}), \tag{5-12}$$

$$\delta \boldsymbol{u}(\boldsymbol{x}, t) \cdot \boldsymbol{n}_\kappa(\boldsymbol{x}) = 0, \quad \boldsymbol{x} \in \partial B, \tag{5-13}$$

$$(\boldsymbol{n}_\kappa(\boldsymbol{x}) \cdot \delta \boldsymbol{T}_\kappa(\boldsymbol{x}, \boldsymbol{I})) \cdot (\boldsymbol{I} - \boldsymbol{n}_\kappa(\boldsymbol{x}) \otimes \boldsymbol{n}_\kappa(\boldsymbol{x})) - (\boldsymbol{n}_\kappa(\boldsymbol{x}) \cdot \boldsymbol{T}_\kappa(\boldsymbol{x}, \boldsymbol{I}) \cdot \boldsymbol{n}_\kappa(\boldsymbol{x})) \, \delta \boldsymbol{u}(\boldsymbol{x}, t) \cdot \nabla_\kappa^\Sigma \otimes \boldsymbol{n}_\kappa(\boldsymbol{x}) = 0,$$
$$\boldsymbol{x} \in \partial B. \tag{5-14}$$

The solutions of the linearized equations of motion under linearized boundary conditions, having the form

$$\delta \boldsymbol{u}(\boldsymbol{x}, t) = \boldsymbol{u}(\boldsymbol{x}) \sin \omega t, \tag{5-15}$$

are called the free vibrations with frequency ω and mode $\boldsymbol{u}(\boldsymbol{x})$. Thus, for the modes the following equations and boundary conditions take place:

$$\omega^2 \rho_\kappa(\boldsymbol{x}) \, \boldsymbol{u}(\boldsymbol{x}) = -\nabla_\kappa \cdot (\boldsymbol{C}_\kappa(\boldsymbol{x}, \boldsymbol{I}) : \nabla_\kappa \otimes \boldsymbol{u}(\boldsymbol{x})) + \rho_\kappa(\boldsymbol{x}) \, \boldsymbol{u}(\boldsymbol{x}) \cdot \nabla_\kappa \otimes \nabla_\kappa \, \varphi(\boldsymbol{x}) =: \mathcal{A}(\boldsymbol{u}), \tag{5-16}$$

$$\boldsymbol{u}(\boldsymbol{x}) \cdot \boldsymbol{n}_\kappa(\boldsymbol{x}) = 0, \quad \boldsymbol{x} \in \partial B, \tag{5-17}$$

$$\boldsymbol{n}_\kappa(\boldsymbol{x}) \cdot (\boldsymbol{C}_\kappa(\boldsymbol{x}, \boldsymbol{I}) : \nabla_\kappa \otimes \boldsymbol{u}(\boldsymbol{x})) \cdot (\boldsymbol{I} - \boldsymbol{n}_\kappa(\boldsymbol{x}) \otimes \boldsymbol{n}_\kappa(\boldsymbol{x})) = (\boldsymbol{n}_\kappa(\boldsymbol{x}) \cdot \boldsymbol{T}_\kappa(\boldsymbol{x}, \boldsymbol{I}) \cdot \boldsymbol{n}_\kappa(\boldsymbol{x})) \, \boldsymbol{u}(\boldsymbol{x}) \cdot \nabla_\kappa^\Sigma \otimes \boldsymbol{n}_\kappa(\boldsymbol{x}),$$
$$\boldsymbol{x} \in \partial B. \tag{5-18}$$

In further calculations, the arguments of related quantities (which remain the same) will not be indicated so detailed.

we rewrite Equation (5-16) in the following operator form:

$$\lambda \rho_\kappa \boldsymbol{u} := \omega^2 \rho_\kappa \boldsymbol{u} = \mathcal{A}(\boldsymbol{u}). \tag{5-19}$$

Thus, the free vibration modes are the generalized eigenvectors of the linear differential operator $\mathcal{A}$, and the squared frequencies are the corresponding generalized eigenvalues (subsequently the term "generalized" will be omitted).

The mechanical system in hand has some fundamental distinctions from the elastic systems for which a rigorous mathematical theory of free vibrations (that is essentially a spectral theory for the corresponding operators under certain boundary conditions) does exist and is presented in the literature. For this reason, when constructing the spectral theory for the system under consideration, it is necessary to substantially modify the well-known fundamental theorems, preserving the general concept of the theory of free vibrations. Although in what follows the distinctions mentioned will be considered in detail, here we characterize them concisely:

(1) The operator $\mathcal{A}$ is *positive semidefinite*, the eigensubspace that corresponds to zero eigenvalue (so-called neutral perturbations not violating the equilibrium of the system) being *infinite-dimensional*.

(2) The boundary conditions are those of free sliding over a curved surface (that in particular, may have flat parts).

Let us derive an integral relationship for the free vibration frequencies and modes with regard for special features of the mechanical system in hand. To this end we multiply both sides of (5-16) by $\boldsymbol{u}(\boldsymbol{x})$ and after integrating over the region B, applying the Gauss theorem and making use of the boundary conditions (5-17), (5-18), we arrive at the equality

$$\omega^2 \langle \rho_\kappa \boldsymbol{u} \cdot \boldsymbol{u} \rangle_B = \langle \nabla_\kappa \otimes \boldsymbol{u} : \boldsymbol{C}_\kappa : \nabla_\kappa \otimes \boldsymbol{u} \rangle_B + \langle \rho_\kappa \boldsymbol{u} \cdot \nabla_\kappa \otimes \nabla_\kappa \varphi \cdot \boldsymbol{u} \rangle_B - \langle (\boldsymbol{n}_\kappa \cdot \boldsymbol{T}_\kappa \cdot \boldsymbol{n}_\kappa)(\boldsymbol{u} \cdot \nabla_\kappa^\Sigma \otimes \boldsymbol{n}_\kappa \cdot \boldsymbol{u}) \rangle_{\partial B}$$

$$= R\{\boldsymbol{u}\}. \tag{5-20}$$

Here the angular brackets denote the integral over the reference set indicated as the right subscript. We note that the quadratic functional

$$R\{\boldsymbol{u}\} := \langle \boldsymbol{u} \cdot \mathcal{A}(\boldsymbol{u}) \rangle_B, \tag{5-21}$$

is nothing but the second variation of total potential energy of the system on the kinematically admissible displacement fields (with regard for zero work of the boundary tractions). Thus, provided the free vibrations do exist, the following equality for corresponding frequencies and modes takes place:

$$\lambda = \omega^2 = \frac{R\{\boldsymbol{u}\}}{\langle \rho_\kappa \boldsymbol{u} \cdot \boldsymbol{u} \rangle_B} =: \Psi\{\boldsymbol{u}\}. \tag{5-22}$$

We note that the operator $\mathcal{A}$ is symmetric on the displacement fields satisfying boundary conditions (5-17), (5-18) in the sense that the bilinear functional $\langle \tilde{\boldsymbol{u}} \cdot \mathcal{A}(\boldsymbol{u}) \rangle_B$ is symmetric on such the fields. Indeed, we reason in exactly the same way as while deriving the equality (5-20), and obtain

$$\langle \tilde{\boldsymbol{u}} \cdot \mathcal{A}(\boldsymbol{u}) \rangle_B = \langle \nabla_\kappa \otimes \tilde{\boldsymbol{u}} : \boldsymbol{C}_\kappa : \nabla_\kappa \otimes \boldsymbol{u} \rangle_B + \langle \rho_\kappa \tilde{\boldsymbol{u}} \cdot \nabla_\kappa \otimes \nabla_\kappa \varphi \cdot \boldsymbol{u} \rangle_B - \langle (\boldsymbol{n}_\kappa \cdot \boldsymbol{T}_\kappa \cdot \boldsymbol{n}_\kappa)(\tilde{\boldsymbol{u}} \cdot \nabla_\kappa^\Sigma \otimes \boldsymbol{n}_\kappa \cdot \boldsymbol{u}) \rangle_{\partial B}$$

$$=: \mathcal{R}\{\tilde{\boldsymbol{u}}, \boldsymbol{u}\}, \tag{5-23}$$

whence, due to the symmetry of $\boldsymbol{C}_\kappa$ (the elastic moduli tensor for the Piola stress) and to the symmetry of TR(2) $\nabla_\kappa \otimes \nabla_\kappa \varphi$ and TR(2) $\nabla_\kappa^\Sigma \otimes \boldsymbol{n}_\kappa$, the symmetry of the bilinear functional $\mathcal{R}\{\tilde{\boldsymbol{u}}, \boldsymbol{u}\}$ follows:

$$\mathcal{R}\{\tilde{\boldsymbol{u}}, \boldsymbol{u}\} = \mathcal{R}\{\boldsymbol{u}, \tilde{\boldsymbol{u}}\}. \tag{5-24}$$

In what follows, the symmetric bilinear functional $\mathcal{R}\{\tilde{\boldsymbol{u}}, \boldsymbol{u}\}$ will be considered as the functional defined on a broader set, namely, on any kinematically admissible (i.e. tangential at the boundary) fields of small

displacements, as well as the quadratic functional

$$R\{u\} = \mathcal{R}\{u, u\}. \tag{5-25}$$

Kinematically admissible fields $u(x)$ form an infinite-dimensional linear space N which will be subsequently supplied with a scalar product that converts it into a Hilbert space.

From equations (5-19) and (5-24) it follows double orthogonality of the free vibration modes $u(x)$ and $\tilde{u}(x)$ corresponding to different eigenvalues λ and $\tilde{\lambda}$:

$$\left.\begin{array}{c} \lambda \rho_\kappa u = \mathcal{A}(u) \\ \tilde{\lambda} \rho_\kappa \tilde{u} = \mathcal{A}(\tilde{u}) \\ \lambda \neq \tilde{\lambda} \end{array}\right\} \implies \langle \rho_\kappa u \cdot \tilde{u} \rangle_B = \langle u \cdot \mathcal{A}(\tilde{u}) \rangle_B = 0. \tag{5-26}$$

From the expression (5-20) *for the functional $R\{u\}$ it is by no means obvious its positive semidefiniteness, but this is absolutely obvious from its canonical form derived by the authors for the bulk-elastic media in essentially more general assumptions* [Ryzhak et al. 2017]. As for the systems considered here, due to the assumption of constitutive homogeneity of a bulk-elastic medium, the canonical form of the functional is especially simple and reduces to the following:

$$R\{u\} = \left\langle K_\kappa \left(\nabla_\kappa \cdot u + \frac{\rho_\kappa}{K_\kappa} u \cdot g \right)^2 \right\rangle_B, \tag{5-27}$$

where $K_\kappa(x)$ and $\rho_\kappa(x)$ are the distributions of bulk modulus and density of a bulk-elastic medium in the reference equilibrium state. Taking into account that the constitutive relation for a bulk-elastic medium can be brought to the form

$$\rho = \rho(p), \tag{5-28}$$

its bulk modulus is specified by the equality

$$\frac{1}{K(\rho)} = \frac{1}{\rho(p)} \frac{d\rho}{dp}(p), \tag{5-29}$$

whereas the equilibrium pressure gradient obeys the equation

$$\nabla_\kappa p_\kappa = \rho_\kappa g, \tag{5-30}$$

we reduce $R\{u\}$ to the form

$$R\{u\} = \left\langle K_\kappa \left(\nabla_\kappa \cdot u + \frac{1}{\rho_\kappa} (u \cdot \nabla_\kappa \rho_\kappa) \right)^2 \right\rangle_B = \left\langle \frac{K_\kappa}{\rho_\kappa^2} \left((\nabla_\kappa \cdot (\rho_\kappa u))^2 \right) \right\rangle_B. \tag{5-31}$$

Further spectral analysis will be based on the properties of the functionals entering into (5-22).

From (5-31) it is obvious that positive semidefinite quadratic functional $R\{u\}$ vanishes on the infinite-dimensional subspace $N_0 \subset N$ formed by the fields $u_0(x)$ for which

$$\nabla_\kappa \cdot \left(\rho_\kappa(x) u_0(x) \right) = 0, \quad u_0 \cdot n_\kappa|_{\partial B} = 0. \tag{5-32}$$

These fields are the "neutral perturbations" that satisfy the linearized equilibrium equations and boundary conditions. In addition to the formal proof of this fact, which will be given in Appendix B, it can be justified also as follows: the fields $u_0(x)$ are the incremental displacements of such transformations

for which the spatial distribution of density remains unchanged, whence for a homogeneous bulk-elastic medium it follows that the spatial distribution of pressure does not change either.

Let us consider the subspace $N_0^\perp \subset N$ formed by the fields $\tilde{u}(x)$ orthogonal to N_0 in the sense of the scalar product $\langle \rho_\kappa u \cdot \tilde{u} \rangle_B$:

$$\tilde{u} \in N_0^\perp \iff \langle \rho_\kappa u_0 \cdot \tilde{u} \rangle_B = 0, \quad \forall u_0 \in N_0. \tag{5-33}$$

It is easy to demonstrate that the fields $\tilde{u} \in N_0^\perp$ are potential, i.e. they have the form

$$\tilde{u}(x) = \nabla_\kappa \gamma(x), \quad n_\kappa \cdot \nabla_\kappa \gamma|_{\partial B} = 0. \tag{5-34}$$

Moreover, any admissible field $u(x)$ can be represented in a unique way as the sum of $u_0(x)$ and $\tilde{u}(x)$:

$$u(x) = u_0(x) + \tilde{u}(x) \iff N = N_0 \oplus N_0^\perp, \tag{5-35}$$

meaning that N is the orthogonal direct sum of subspaces N_0 and $N_0^\perp$.

The space of admissible fields N supplied with the above-mentioned scalar product is a Hilbert space. We note that the norm generated by this scalar product, namely

$$\|u\| := (\langle \rho_\kappa u \cdot u \rangle_B)^{1/2}, \tag{5-36}$$

is equivalent to all the norms generated by scalar products of the type $\langle \beta(x) u(x) \cdot \tilde{u}(x) \rangle_B$ with weight functions $\beta(x)$ that are continuous and strictly positive in the closure of the domain B.

The subsets of the subspace $N_0^\perp$, bounded both in the value of the functional $R\{u\}$ and in the norm $\|u\|$ are compact in the sense of convergence with respect to this norm (and with respect to every norm equivalent to it). The presence of such a compactness is proved in Appendix A under additional supposition of piecewise convexity of the boundary ∂B, basing on classical Rellich's lemma together with a specific inequality of Korn's type, not occurred in the literature (cf. Horgan 1995).

Due to the presence of this compactness, a standard spectral theorem can be proved for the operator $\mathcal{A}$ on the subspace $N_0^\perp$, that implies that the standard properties of eigenvalues and eigenvectors (i.e. the free vibration modes) also take place.

We state the spectral theorem on a subspace $N_0^\perp$. An outline of its proof (containing some nonstandard elements resulting from the features of the mechanical system under consideration) is presented in Appendix B.

Spectral theorem. The linear operator $\mathcal{A}$ (5-16) under boundary conditions (5-17) on the subspace $N_0^\perp$ has a positive discrete spectrum $0 < \lambda_1 \le \lambda_2 \le \ldots$, $\lim_{m \to \infty} \lambda_m = +\infty$, with corresponding eigenvectors $u_m(x) \in N_0^\perp$ satisfying boundary conditions (5-18). Herein

$$\lambda_m = \inf_{\substack{u \ne 0 \\ u \in N_{m-1}^\perp}} \Psi\{u\} = \Psi\{u_m\}, \quad m = 1, 2, \ldots, \tag{5-37}$$

where the subspace $N_{m-1}^\perp$ for $m > 1$ is the orthogonal complement to $\text{span}(u_1, \ldots, u_{m-1}) =: N_{m-1}$ in the subspace $N_0^\perp$. Eigenvectors $u_m(x)$ are the extremals of the functional $\Psi\{u\}$ on subspaces $N_{m-1}^\perp$; they are mutually orthogonal and can be normalized. The corresponding orthonormal system of eigenvectors is complete in the sense of convergence in the norm (5-36) (and every norm equivalent to it).

A consequence of the spectral theorem in combination with certain fundamental properties of linear spaces is the comparison theorem for eigenvalues corresponding to different operators with different

weight functions and related different scalar products. The latter theorem is an effective tool for investigating the free vibration frequencies in the cases when it is impossible to obtain their exact values, since it allows one to obtain upper and lower bounds for them by finding the corresponding frequencies for suitable simple "comparison systems."

The statement and proof of the comparison theorem for the mechanical systems under consideration have a number of distinctions from those for the standard theorem.

Having in mind the comparison theorem, we reformulate in an equivalent way both the spectral problem and the spectral theorem in terms of a new unknown quantity $\boldsymbol{w}(\boldsymbol{x})$:

$$\boldsymbol{w}(\boldsymbol{x}) := \rho_\kappa(\boldsymbol{x})\,\boldsymbol{u}(\boldsymbol{x}) \quad \Longleftrightarrow \quad \boldsymbol{u}(\boldsymbol{x}) = \frac{1}{\rho_\kappa(\boldsymbol{x})}\boldsymbol{w}(\boldsymbol{x}), \quad \boldsymbol{w}(\boldsymbol{x})\cdot\boldsymbol{n}_\kappa(\boldsymbol{x}) = 0, \quad \boldsymbol{x}\in\partial B, \tag{5-38}$$

$$\widetilde{R}\{\boldsymbol{w}\} := R\left\{\frac{\boldsymbol{w}}{\rho_\kappa}\right\} = \left\langle \frac{K_\kappa}{\rho_\kappa^2}(\nabla_\kappa\cdot\boldsymbol{w})^2 \right\rangle_B,$$

$$\langle \rho_\kappa\boldsymbol{u}\cdot\boldsymbol{u}\rangle_B = \left\langle \frac{1}{\rho_\kappa}\boldsymbol{w}\cdot\boldsymbol{w} \right\rangle_B, \quad \widetilde{\Psi}\{\boldsymbol{w}\} := \Psi\left\{\frac{\boldsymbol{w}}{\rho_\kappa}\right\}, \quad \widetilde{\mathcal{A}}(\boldsymbol{w}) := \mathcal{A}\left(\frac{\boldsymbol{w}}{\rho_\kappa}\right). \tag{5-39}$$

The equalities (5-19) and (5-22) take the following form:

$$\lambda\boldsymbol{w} = \omega^2\boldsymbol{w} = \widetilde{\mathcal{A}}(\boldsymbol{w}), \tag{5-40}$$

$$\lambda = \omega^2 = \frac{\widetilde{R}\{\boldsymbol{w}\}}{\langle(1/\rho_\kappa)\boldsymbol{w}\cdot\boldsymbol{w}\rangle_B} =: \widetilde{\Psi}\{\boldsymbol{w}\}. \tag{5-41}$$

The space of all $\boldsymbol{w}(\boldsymbol{x})$ tangential at the boundary ∂B and supplied with a scalar product $\langle(1/\rho_\kappa)\boldsymbol{w}\cdot\boldsymbol{w}'\rangle_B$ is denoted $\widetilde{N}$, whereas the infinite-dimensional subspace of divergenceless fields $\boldsymbol{w}_0(\boldsymbol{x})$ corresponding to the zero eigenvalue, is denoted $\widetilde{N}_0$. We introduce also the subspaces into which the subspaces $N_0^\perp$, N_{m-1}, $N_{m-1}^\perp$ will be converted: $\widetilde{N}_0^\perp$ is the subspace orthogonal to $\widetilde{N}_0$ (in the sense of the scalar product of space $\widetilde{N}$); $\widetilde{N}_{m-1} = \mathrm{span}(\boldsymbol{w}_1,\ldots,\boldsymbol{w}_{m-1})$, where $\boldsymbol{w}_i =: \rho_\kappa\boldsymbol{u}_i$ is the eigenvector corresponding to the eigenvalue λ_i; $\widetilde{N}_{m-1}^\perp$ is the orthogonal complement to the subspace $\widetilde{N}_{m-1}$ in the subspace $\widetilde{N}_0^\perp$ (or, equivalently, the orthogonal complement to the subspace $\mathrm{span}(\widetilde{N}_0,\widetilde{N}_{m-1})$ in $\widetilde{N}$). It is obvious that $\widetilde{N}$ is the direct orthogonal sum of $\widetilde{N}_0$, $\widetilde{N}_{m-1}$, and $\widetilde{N}_{m-1}^\perp$:

$$\widetilde{N} = \widetilde{N}_0 \oplus \widetilde{N}_{m-1} \oplus \widetilde{N}_{m-1}^\perp. \tag{5-42}$$

The assertion of the spectral theorem remains the same except for the fact that equality (5-37) is converted into the following equality:

$$\lambda_m = \inf_{\boldsymbol{w}\neq 0,\ \boldsymbol{w}\in\widetilde{N}_{m-1}^\perp} \widetilde{\Psi}\{\boldsymbol{w}\} = \widetilde{\Psi}\{\boldsymbol{w}_m\}, \quad m = 1, 2, \ldots, \tag{5-43}$$

The eigenvectors $\boldsymbol{w}_m(\boldsymbol{x})$ are the extremals of functional $\widetilde{\Psi}\{\boldsymbol{w}\}$ on the subspaces $\widetilde{N}_{m-1}^\perp$, they are mutually orthogonal ($\langle(1/\rho_\kappa)\boldsymbol{w}_{m_1}\cdot\boldsymbol{w}_{m_2}\rangle_B = 0$, $m_1 \neq m_2$) and can be normalized with respect to the norm of space $\widetilde{N}$:

$$\||\boldsymbol{w}\|| := \sqrt{\left\langle \frac{1}{\rho_\kappa}\boldsymbol{w}\cdot\boldsymbol{w} \right\rangle_B}. \tag{5-44}$$

The corresponding orthonormal system of eigenvectors is complete in the sense of convergence in the norm (5-44) (and in every norm equivalent to it).

We now assume that there are two different continuous mechanical systems of a similar type occupying identical domains B with identical boundary conditions, but characterized by their own density distributions $\rho_\kappa^{(1)}(\boldsymbol{x})$, $\rho_\kappa^{(2)}(\boldsymbol{x})$ and bulk moduli distributions $K_\kappa^{(1)}(\boldsymbol{x})$, $K_\kappa^{(2)}(\boldsymbol{x})$, which allows one to define for these systems in a completely similar manner the functionals:

$$\widetilde{R}^{(j)}\{\boldsymbol{w}\}, \quad \left\langle \frac{1}{\rho_\kappa^{(j)}} \boldsymbol{w} \cdot \boldsymbol{w} \right\rangle_B, \quad \widetilde{\Psi}^{(j)}\{\boldsymbol{w}\}, \quad j = 1, 2.$$

It is obvious that for each of the systems there is its own set of eigenvalues $\lambda_0^{(j)} = 0$, $0 < \lambda_1^{(j)} \leq \lambda_2^{(j)} \leq \ldots$, $j = 1, 2$ and its own set of eigenvectors whose existence and properties result from the corresponding spectral theorem. Note that the subspaces $\widetilde{N}_0^{(1)}$, $\widetilde{N}_0^{(2)}$ (corresponding to the zero eigenvalue and being formed by the divergenceless fields $\boldsymbol{w}_0^{(j)}(\boldsymbol{x})$ tangential on ∂B) coincide with each other.

The Hilbert spaces $\widetilde{N}^{(j)}$ are characterized by different scalar products $\langle (1/\rho_\kappa^{(j)}) \boldsymbol{w} \cdot \boldsymbol{w}' \rangle_B$. Hence, the eigenvectors $\boldsymbol{w}_0^{(j)}(\boldsymbol{x})$, $\boldsymbol{w}_1^{(j)}(\boldsymbol{x})$, ... are mutually orthogonal in the sense of the corresponding scalar products, as well as the mutually orthogonal subspaces.

Now we state the comparison theorem.

Comparison theorem. Assume that the functional $\widetilde{\Psi}^{(2)}\{\boldsymbol{w}\}$ majorizes the functional $\widetilde{\Psi}^{(1)}\{\boldsymbol{w}\}$:

$$\widetilde{\Psi}^{(1)}\{\boldsymbol{w}\} \leq \widetilde{\Psi}^{(2)}\{\boldsymbol{w}\}, \quad \forall \boldsymbol{w} \in \widetilde{N}, \quad \boldsymbol{w} \neq \boldsymbol{0}. \tag{5-45}$$

Then for the corresponding eigenvalues (numbered in the order of nondecreasing) the following inequalities hold:

$$\lambda_m^{(1)} \leq \lambda_m^{(2)}, \quad m = 1, 2, \ldots . \tag{5-46}$$

The proof of the theorem, which differs from the standard proofs (due to the presence of an infinite-dimensional subspace corresponding to the zero eigenvalue) is presented in Appendix B.

The functionals $\widetilde{\Psi}^{(1)}\{\boldsymbol{w}\}$ and $\widetilde{\Psi}^{(2)}\{\boldsymbol{w}\}$ have a form that allows to obtain completely obvious minorizing and majorizing functionals with constant coefficients. To this end we introduce for each of the bulk-elastic media the fields of sound velocities $c_\kappa^{(1)}(\boldsymbol{x})$ and $c_\kappa^{(2)}(\boldsymbol{x})$:
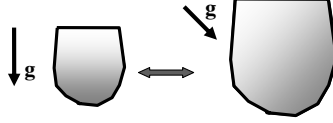
$$c_\kappa^{(1)}(\boldsymbol{x}) = \sqrt{\frac{K_\kappa^{(1)}}{\rho_\kappa^{(1)}}}, \quad c_\kappa^{(2)}(\boldsymbol{x}) = \sqrt{\frac{K_\kappa^{(2)}}{\rho_\kappa^{(2)}}}. \tag{5-47}$$

In addition, we introduce notations for the minimal (line below the symbol) and maximal (line above the symbol) values of a quantity. Then we have

$$\widetilde{\Psi}^{(1)}\{\boldsymbol{w}\} \leq (\bar{c}_\kappa^{(1)})^2 \frac{\bar{\rho}_\kappa^{(1)}}{\underline{\rho}_\kappa^{(1)}} \frac{\langle (\nabla_\kappa \cdot \boldsymbol{w})^2 \rangle_B}{\langle \boldsymbol{w} \cdot \boldsymbol{w} \rangle_B}, \quad (\underline{c}_\kappa^{(2)})^2 \frac{\underline{\rho}_\kappa^{(2)}}{\bar{\rho}_\kappa^{(2)}} \frac{\langle (\nabla_\kappa \cdot \boldsymbol{w})^2 \rangle_B}{\langle \boldsymbol{w} \cdot \boldsymbol{w} \rangle_B} \leq \widetilde{\Psi}^{(2)}\{\boldsymbol{w}\}. \tag{5-48}$$

If for two different bulk-elastic media occupying identical domains, the following inequality holds:

$$\sqrt{\frac{\bar{\rho}_\kappa^{(1)}}{\underline{\rho}_\kappa^{(1)}} \frac{\bar{\rho}_\kappa^{(2)}}{\underline{\rho}_\kappa^{(2)}}} \leq \frac{\underline{c}_\kappa^{(2)}}{\bar{c}_\kappa^{(1)}}, \tag{5-49}$$

Figure 2. Comparison of the free vibration frequencies for different media occupying similar domains in different fields.

then the functional $\widetilde{\Psi}^{(2)}\{\boldsymbol{w}\}$ obviously majorizes the functional $\widetilde{\Psi}^{(1)}\{\boldsymbol{w}\}$, from which it follows that each of the nonzero free vibration frequencies of the first medium does not exceed the corresponding frequency of the second medium:

$$\omega_m^{(1)} \leq \omega_m^{(2)}, \quad m = 1, 2, \ldots . \tag{5-50}$$

Remark. The relations obtained can easily be extended to the case when the domains occupied by different bulk-elastic media are similar (Figure 2).

In that case the functionals $\langle (\nabla_\kappa \cdot \boldsymbol{w})^2 \rangle_{B^{(j)}} / \langle \boldsymbol{w} \cdot \boldsymbol{w} \rangle_{B^{(j)}}$ entering into each of the inequalities (5-48), for different (similar) domains are to be reduced to one and the same domain B of some characteristic (unit) size. Then for the functionals mentioned it results in

$$\frac{\langle (\nabla_\kappa \cdot \boldsymbol{w})^2 \rangle_{B^{(j)}}}{\langle \boldsymbol{w} \cdot \boldsymbol{w} \rangle_{B^{(j)}}} = \frac{1}{(l^{(j)})^2} \frac{\langle (\nabla_\kappa \cdot \boldsymbol{w})^2 \rangle_{B}}{\langle \boldsymbol{w} \cdot \boldsymbol{w} \rangle_{B}}, \tag{5-51}$$

where $l^{(j)}$ is the characteristic size (say, the diameter) of the domain $B^{(j)}$. Hence, the inequality (5-49), from which the inequality for frequencies (5-50) follows, takes the following form:

$$\sqrt{\frac{\bar{\rho}_\kappa^{(1)}}{\underline{\rho}_\kappa^{(1)}} \frac{\bar{\rho}_\kappa^{(2)}}{\underline{\rho}_\kappa^{(2)}}} \leq \frac{c_\kappa^{(2)} / l^{(2)}}{\bar{c}_\kappa^{(1)} / l^{(1)}}. \tag{5-52}$$

6. Explicit bounds for the free vibration frequencies for domains of some special shapes

As for domains of arbitrary shape, the comparison theorem, in accordance with its statement, makes it possible only to compare the free vibration frequencies of different bulk-elastic media in the same (or similar) domains, but it fails to yield the explicit frequency bounds. However, for domains of the shape of a rectangular parallelepiped and for a certain set of other shapes the comparison theorem allows to obtain concrete analytical upper and lower bounds for the corresponding free vibration frequencies depending on the limit values of mechanical parameters of a medium and on the geometric parameters of a domain.

We note that the force field enters into the above bounds only via the quantities $\underline{\rho}_\kappa, \bar{\rho}_\kappa, \underline{c}_\kappa, \bar{c}_\kappa$. For this reason orientation of the domain with respect to the field can be absolutely arbitrary, and its influence on the resulting bounds for frequencies is related to its influence on the above-mentioned limit values of the mechanical parameters of a bulk-elastic medium that depend on the orientation.

The derivation of the bounds for frequencies is based on investigation of the functional

$$\Phi\{\boldsymbol{w}\} := \frac{\langle (\nabla_\kappa \cdot \boldsymbol{w})^2 \rangle_B}{\langle \boldsymbol{w} \cdot \boldsymbol{w} \rangle_B}, \tag{6-1}$$
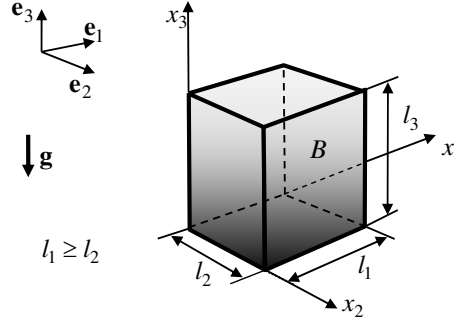
Figure 3. A domain B of the shape of a rectangular parallelepiped.

by means of expansion of the fields $\boldsymbol{w}(\boldsymbol{x})$ (previously converted into spatially periodic fields) into a spatial Fourier series. Various aspects of this method are presented in [Ryzhak 1993, 1994; 1997; 1999].

We consider first the domain B having the shape of a rectangular parallelepiped (Figure 3).

Let $(\boldsymbol{e}_1, \boldsymbol{e}_2, \boldsymbol{e}_3)$ be an orthonormal basis, and the corresponding Cartesian rectangular coordinates are specified by

$$\boldsymbol{x} = x_1 \boldsymbol{e}_1 + x_2 \boldsymbol{e}_2 + x_3 \boldsymbol{e}_3. \tag{6-2}$$

The rectangular parallelepiped B is specified by the following system of inequalities:

$$B = \{\boldsymbol{x} \mid 0 \le x_i \le l_i, \quad i = 1, 2, 3\}. \tag{6-3}$$

To convert the field $\boldsymbol{w}(\boldsymbol{x})$ tangential at the boundary ∂B into a spatially periodic field, we successively reflect the parallelepiped B together with the field defined on it with respect to the planes $x_1 = 0$, $x_2 = 0$, $x_3 = 0$. Thus the parallelepiped B is converted into the parallelepiped B':

$$B' = \{\boldsymbol{x} \mid -l_i \le x_i \le l_i, \quad i = 1, 2, 3\}, \tag{6-4}$$

whereas the field $\boldsymbol{w}(\boldsymbol{x})$ is converted into a spatially periodic field with three planes of symmetry in the B'. Using for the converted field the same notation $\boldsymbol{w}(\boldsymbol{x})$, we determine it by the following equalities:

$$\boldsymbol{w}(\boldsymbol{x} \cdot \boldsymbol{Q}_i) = \boldsymbol{w}(\boldsymbol{x}) \cdot \boldsymbol{Q}_i, \quad \boldsymbol{x} \in B', \quad i = 1, 2, 3, \tag{6-5}$$

where $\boldsymbol{Q}_i$ is the TR(2) specifying reflection with respect to the plane $x_i = 0$ (Figure 4, plane scheme).
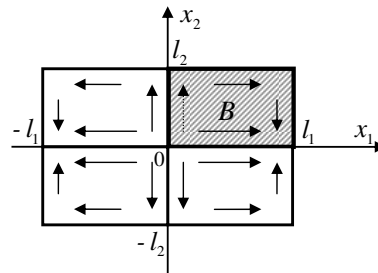
Figure 4. Conversion of the field into a periodic one by means of reflections.

We note that in mirror-symmetric points the following equalities take place:

$$|\boldsymbol{w}(\boldsymbol{x} \cdot \boldsymbol{Q}_i)| = |\boldsymbol{w}(\boldsymbol{x})|, \quad \nabla_\kappa \cdot \boldsymbol{w}(\boldsymbol{x} \cdot \boldsymbol{Q}_i) = \nabla_\kappa \cdot \boldsymbol{w}(\boldsymbol{x}). \tag{6-6}$$

For this reason

$$\langle (\nabla_\kappa \cdot \boldsymbol{w})^2 \rangle_{B'} = 8 \langle (\nabla_\kappa \cdot \boldsymbol{w})^2 \rangle_B, \quad \langle \boldsymbol{w} \cdot \boldsymbol{w} \rangle_{B'} = 8 \langle \boldsymbol{w} \cdot \boldsymbol{w} \rangle_B \tag{6-7}$$

$$\implies \quad \Phi\{\boldsymbol{w}\} = \frac{\langle (\nabla_\kappa \cdot \boldsymbol{w})^2 \rangle_{B'}}{\langle \boldsymbol{w} \cdot \boldsymbol{w} \rangle_{B'}}. \tag{6-8}$$

A well-known consequence of the spatial periodicity of the field $\boldsymbol{w}(\boldsymbol{x})$ is that the Fourier series for the field $\nabla_\kappa \otimes \boldsymbol{w}(\boldsymbol{x})$ is equal to the formally differentiated Fourier series for the field $\boldsymbol{w}(\boldsymbol{x})$. In combination with the Parseval theorem, this allows to replace the integrals in the numerator and denominator of expression (6-8) for the functional $\Phi\{\boldsymbol{w}\}$ by the sums of corresponding series (containing only the Fourier coefficients for the field $\boldsymbol{w}(\boldsymbol{x})$), and then investigate the ratio of the sums.

We introduce the notation for used hereinafter version of the triple Fourier series in the parallelepiped B'. The integer vectors $\boldsymbol{\mu}$ are specified by the following equalities and inequalities:

$$\boldsymbol{\mu} = \mu_1 \boldsymbol{e}_1 + \mu_2 \boldsymbol{e}_2 + \mu_3 \boldsymbol{e}_3, \quad \mu_i \text{ are integer,}$$
$$\mu_1 > 0, \quad \text{or} \quad \mu_1 = 0, \quad \mu_2 > 0, \quad \text{or} \quad \mu_1 = 0, \quad \mu_2 = 0, \quad \mu_3 > 0. \tag{6-9}$$

We define the discrete vectors $\boldsymbol{q}_\mu$:

$$\boldsymbol{q}_\mu = \sum_{i=1}^{3} \frac{\pi \mu_i}{l_i} \boldsymbol{e}_i, \tag{6-10}$$

and the following system of functions:

$$\varphi_0(\boldsymbol{x}) = (8 l_1 l_2 l_3)^{-1/2}, \quad \varphi_\mu(\boldsymbol{x}) = (4 l_1 l_2 l_3)^{-1/2} \cos \boldsymbol{q}_\mu \cdot \boldsymbol{x}, \quad \psi_\mu(\boldsymbol{x}) = (4 l_1 l_2 l_3)^{-1/2} \sin \boldsymbol{q}_\mu \cdot \boldsymbol{x}. \tag{6-11}$$

This system is complete and orthonormal in $L_2(B')$, the convergence in the norm of the corresponding space being independent of the order of summation, which allows to use triple summation (i.e. the summation over $\boldsymbol{\mu}$) without specifying the order of summation. We will use the symbol $\sim$ to denote the correspondence between the field and its Fourier series. Then for the fields $\boldsymbol{w}(\boldsymbol{x})$ and $\nabla_\kappa \otimes \boldsymbol{w}(\boldsymbol{x})$, as well as for $\nabla_\kappa \cdot \boldsymbol{w}(\boldsymbol{x})$ and $\nabla_\kappa \times \boldsymbol{w}(\boldsymbol{x})$, we have

$$\boldsymbol{w} \sim a_0 \varphi_0 + \sum_\mu (a_\mu \varphi_\mu + b_\mu \psi_\mu), \quad a_0 = 0, \tag{6-12}$$

$$\nabla_\kappa \otimes \boldsymbol{w} \sim \sum_\mu (\boldsymbol{q}_\mu \otimes b_\mu \varphi_\mu - \boldsymbol{q}_\mu \otimes a_\mu \psi_\mu),$$

$$\nabla_\kappa \cdot \boldsymbol{w} \sim \sum_\mu (\boldsymbol{q}_\mu \cdot b_\mu \varphi_\mu - \boldsymbol{q}_\mu \cdot a_\mu \psi_\mu), \tag{6-13}$$

$$\nabla_\kappa \times \boldsymbol{w} \sim \sum_\mu (\boldsymbol{q}_\mu \times b_\mu \varphi_\mu - \boldsymbol{q}_\mu \times a_\mu \psi_\mu).$$

Vanishing of the vector $\boldsymbol{a}_0$ is a consequence of symmetry of the field $\boldsymbol{w}(\boldsymbol{x})$, which is equivalent to tangentiality of the original field on the faces of original parallelepiped B. The presence of these symmetries results in the existence of certain relations between the Fourier coefficients corresponding to integer vectors $\boldsymbol{\mu}$ with the same values of μ_1 and of $|\mu_i|$, $i = 2, 3$. Specifically, basing on a vector $\boldsymbol{\mu}$ corresponding to positive μ_i, we form the remaining three vectors:

$$
\begin{aligned}
\boldsymbol{\mu}' &= \mu_1 \boldsymbol{e}_1 - \mu_2 \boldsymbol{e}_2 + \mu_3 \boldsymbol{e}_3 = \boldsymbol{\mu} \cdot \boldsymbol{Q}_2, \\
\boldsymbol{\mu}'' &= \mu_1 \boldsymbol{e}_1 + \mu_2 \boldsymbol{e}_2 - \mu_3 \boldsymbol{e}_3 = \boldsymbol{\mu} \cdot \boldsymbol{Q}_3, \\
\boldsymbol{\mu}''' &= \mu_1 \boldsymbol{e}_1 - \mu_2 \boldsymbol{e}_2 - \mu_3 \boldsymbol{e}_3 = -\boldsymbol{\mu} \cdot \boldsymbol{Q}_1 = \boldsymbol{\mu} \cdot \boldsymbol{Q}_2 \cdot \boldsymbol{Q}_3.
\end{aligned}
\tag{6-14}
$$

Then for the Fourier coefficients corresponding to vectors $\boldsymbol{\mu}'$, $\boldsymbol{\mu}''$, and $\boldsymbol{\mu}'''$, the following equalities hold:

$$
\begin{aligned}
\boldsymbol{a}_{\boldsymbol{\mu}} &= \boldsymbol{a}_{\boldsymbol{\mu}'} = \boldsymbol{a}_{\boldsymbol{\mu}''} = \boldsymbol{a}_{\boldsymbol{\mu}'''} = \boldsymbol{0}, \\
\boldsymbol{b}_{\boldsymbol{\mu}'} &= \boldsymbol{b}_{\boldsymbol{\mu}} \cdot \boldsymbol{Q}_2, \quad \boldsymbol{b}_{\boldsymbol{\mu}''} = \boldsymbol{b}_{\boldsymbol{\mu}} \cdot \boldsymbol{Q}_3, \quad \boldsymbol{b}_{\boldsymbol{\mu}'''} = -\boldsymbol{b}_{\boldsymbol{\mu}} \cdot \boldsymbol{Q}_1.
\end{aligned}
\tag{6-15}
$$

Note that in the Fourier expansion of the divergence for the divergenceless modes all the coefficients vanish, whence by virtue of (6-13) it follows that vectors $\boldsymbol{b}_{\boldsymbol{\mu}}$ are orthogonal to the corresponding vectors $\boldsymbol{q}_{\boldsymbol{\mu}}$:

$$
\boldsymbol{b}_{\boldsymbol{\mu}} \cdot \boldsymbol{q}_{\boldsymbol{\mu}} = 0, \quad \forall \boldsymbol{\mu}.
\tag{6-16}
$$

For the elements of the orthogonal subspace in hand, formed by the gradients of the scalar functions, their curls vanish, whence it follows that the vectors $\boldsymbol{b}_{\boldsymbol{\mu}}$ are collinear to the corresponding vectors $\boldsymbol{q}_{\boldsymbol{\mu}}$:

$$
\boldsymbol{b}_{\boldsymbol{\mu}} = \beta_{\boldsymbol{\mu}} \boldsymbol{q}_{\boldsymbol{\mu}}, \quad \forall \boldsymbol{\mu}.
\tag{6-17}
$$

Thus, in the above-mentioned subspace, by the Parseval theorem the following equalities hold:

$$
\Phi\{\boldsymbol{w}\} = \frac{\sum_{\boldsymbol{\mu}} (\boldsymbol{q}_{\boldsymbol{\mu}} \cdot \boldsymbol{b}_{\boldsymbol{\mu}})^2}{\sum_{\boldsymbol{\mu}} (\boldsymbol{b}_{\boldsymbol{\mu}} \cdot \boldsymbol{b}_{\boldsymbol{\mu}})} = \frac{\sum_{\boldsymbol{\mu}} \beta_{\boldsymbol{\mu}}^2 (\boldsymbol{q}_{\boldsymbol{\mu}} \cdot \boldsymbol{q}_{\boldsymbol{\mu}})^2}{\sum_{\boldsymbol{\mu}} \beta_{\boldsymbol{\mu}}^2 (\boldsymbol{q}_{\boldsymbol{\mu}} \cdot \boldsymbol{q}_{\boldsymbol{\mu}})} = \sum_{\boldsymbol{\mu}} \frac{\beta_{\boldsymbol{\mu}}^2 (\boldsymbol{q}_{\boldsymbol{\mu}} \cdot \boldsymbol{q}_{\boldsymbol{\mu}})}{\sum_{\tilde{\boldsymbol{\mu}}} \beta_{\tilde{\boldsymbol{\mu}}}^2 (\boldsymbol{q}_{\tilde{\boldsymbol{\mu}}} \cdot \boldsymbol{q}_{\tilde{\boldsymbol{\mu}}})} (\boldsymbol{q}_{\boldsymbol{\mu}} \cdot \boldsymbol{q}_{\boldsymbol{\mu}})
$$

$$
\geq \min_{\boldsymbol{\mu}} (\boldsymbol{q}_{\boldsymbol{\mu}} \cdot \boldsymbol{q}_{\boldsymbol{\mu}}) = (\boldsymbol{q}_{\boldsymbol{\mu}^1} \cdot \boldsymbol{q}_{\boldsymbol{\mu}^1})
\tag{6-18}
$$

$$
\implies \quad \theta_1 := \inf_{\boldsymbol{w} \in N_0^{\perp}} \Phi\{\boldsymbol{w}\} = \boldsymbol{q}_{\boldsymbol{\mu}^1} \cdot \boldsymbol{q}_{\boldsymbol{\mu}^1} = \Phi\{\boldsymbol{q}_{\boldsymbol{\mu}^1} \psi_{\boldsymbol{\mu}^1}\} > 0.
\tag{6-19}
$$

The value θ_1 defined by (6-19) is the smallest positive eigenvalue of the self-adjoint operator corresponding to the functional $\Phi\{\boldsymbol{w}\}$. In accordance with the spectral theorem, the next eigenvalue $\theta_2 \geq \theta_1$ is equal to the minimal value of the functional on the orthogonal complement of the "vector" $\boldsymbol{q}_{\boldsymbol{\mu}^1} \psi_{\boldsymbol{\mu}^1}$ in the subspace $N_0^{\perp}$. In the Fourier expansions for the elements of such an orthogonal complement the term $\boldsymbol{b}_{\boldsymbol{\mu}^1} \psi_{\boldsymbol{\mu}^1}$ is absent. Therefore on this orthogonal complement we have

$$
\Phi\{\boldsymbol{w}\} = \frac{\sum_{\boldsymbol{\mu} \neq \boldsymbol{\mu}^1} \beta_{\boldsymbol{\mu}}^2 (\boldsymbol{q}_{\boldsymbol{\mu}} \cdot \boldsymbol{q}_{\boldsymbol{\mu}})^2}{\sum_{\boldsymbol{\mu} \neq \boldsymbol{\mu}^1} \beta_{\boldsymbol{\mu}}^2 (\boldsymbol{q}_{\boldsymbol{\mu}} \cdot \boldsymbol{q}_{\boldsymbol{\mu}})} \geq \min_{\boldsymbol{\mu} \neq \boldsymbol{\mu}^1} (\boldsymbol{q}_{\boldsymbol{\mu}} \cdot \boldsymbol{q}_{\boldsymbol{\mu}}) = \boldsymbol{q}_{\boldsymbol{\mu}^2} \cdot \boldsymbol{q}_{\boldsymbol{\mu}^2}
\tag{6-20}
$$

$$
\implies \quad \theta_2 := \inf_{\substack{\boldsymbol{w} \in N_0^{\perp} \\ \boldsymbol{w} \perp \boldsymbol{q}_{\boldsymbol{\mu}^1} \psi_{\boldsymbol{\mu}^1}}} \Phi\{\boldsymbol{w}\} = \Phi\{\boldsymbol{q}_{\boldsymbol{\mu}^2} \psi_{\boldsymbol{\mu}^2}\} = \boldsymbol{q}_{\boldsymbol{\mu}^2} \cdot \boldsymbol{q}_{\boldsymbol{\mu}^2} \geq \theta_1.
\tag{6-21}
$$

It is obvious that the integer vectors $\boldsymbol{\mu}$ form a countable set; we number them in the order of nondecreasing of the absolute values of vectors $\boldsymbol{q}_{\boldsymbol{\mu}}$. Then, by induction

$$\theta_m = \Phi\{\boldsymbol{q}_{\boldsymbol{\mu}^m}\psi_{\boldsymbol{\mu}^m}\} = \boldsymbol{q}_{\boldsymbol{\mu}^m} \cdot \boldsymbol{q}_{\boldsymbol{\mu}^m} \geq \theta_{m-1}, \quad m = 1, 2, \ldots . \tag{6-22}$$

Thus, for a bulk-elastic medium in a domain having the shape and dimensions of the rectangular parallelepiped B, in accordance with inequalities (5-48), we obtain the following upper and lower bounds for the free vibration frequencies:

$$\underline{c}_\kappa \sqrt{\frac{\rho_\kappa}{\bar{\rho}_\kappa}} \sqrt{\theta_m} \leq \omega_m \leq \bar{c}_\kappa \sqrt{\frac{\bar{\rho}_\kappa}{\underline{\rho}_\kappa}} \sqrt{\theta_m}, \quad \sqrt{\theta_m} = |\boldsymbol{q}_{\boldsymbol{\mu}^m}| = \sqrt{\sum_{i=1}^{3} \frac{\pi^2}{l_i^2}(\mu_i^m)^2} . \tag{6-23}$$

The bounds for the first frequency are determined by the greatest edge length:

$$\sqrt{\theta_1} = |\boldsymbol{q}_{\boldsymbol{\mu}^1}| = \frac{\pi}{\max_i l_i} =: \frac{\pi}{\bar{l}}, \quad \sqrt{\frac{\rho_\kappa}{\bar{\rho}_\kappa}} \pi \frac{\underline{c}_\kappa}{\bar{l}} \leq \omega_1 \leq \sqrt{\frac{\bar{\rho}_\kappa}{\underline{\rho}_\kappa}} \pi \frac{\bar{c}_\kappa}{\bar{l}}. \tag{6-24}$$

The further order of nondecreasing in absolute value vectors $\boldsymbol{q}_{\boldsymbol{\mu}^m}$ and the corresponding eigenvalues θ_m depends on the "proportions" of the rectangular parallelepiped (i.e. on the ratios of the lengths of edges) and can vary greatly. As a simple example, we present the values of the first few eigenvalues θ_m for a cube with an edge l:

$$\begin{aligned} \theta_1 &= \theta_2 = \theta_3 = \frac{\pi^2}{l^2}, & \theta_4 &= \theta_5 = \theta_6 = \frac{2\pi^2}{l^2}, \\ \theta_7 &= \frac{3\pi^2}{l^2}, & \theta_8 &= \theta_9 = \theta_{10} = \frac{4\pi^2}{l^2}. \end{aligned} \tag{6-25}$$

Remark. In the absence of a force field, the equilibrium state of a bulk-elastic medium is uniform; consequently $\bar{\rho}_\kappa = \underline{\rho}_\kappa$, $\underline{c}_\kappa = \bar{c}_\kappa = c_\kappa$ and every pair of inequalities (6-24) converts into the equality

$$\omega_1 = \frac{\pi c_\kappa}{\bar{l}}.$$

In exactly the same way, the inequalities (6-23) convert into the following equalities:

$$\omega_m = c_\kappa \sqrt{\theta_m} = c_\kappa |\boldsymbol{q}_{\boldsymbol{\mu}^m}| = c_\kappa \sqrt{\sum_{i=1}^{3} \frac{\pi^2}{l_i^2}(\mu_i^m)^2} . \tag{6-26}$$

Thus, the bounds (6-23) and (6-24) give exact values of the free vibration frequencies in the case of a uniform equilibrium state and provide a good approximation in the case when the nonuniformity of the equilibrium state is not significant. The stated remark applies equally to other shapes of the domain considered below.

Remark. In the case of a significant value of the acceleration of gravity (or if the system under consideration moves with a high acceleration), and also in the case of a significant value of one of the dimensions of a system, the quantities entering into the upper and lower bounds (6-23), (6-24) for one and the same domain and the same bulk-elastic medium will be different for different orientations of the domain with respect to the direction of the force field.
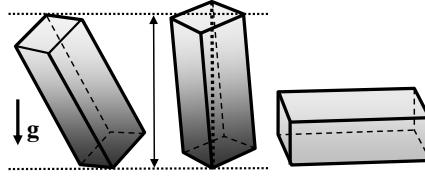
Figure 5. The influence of orientation with respect to the field direction.

Indeed, if the direction of the longest edge is close to the direction orthogonal to the field, and the dimension in the direction parallel to the field is small, then the values $\bar{\rho}_\kappa$, $\bar{c}_\kappa$ differ little from the values $\underline{\rho}_\kappa$, $\underline{c}_\kappa$. If, on the contrary, the greatest dimension corresponds to the direction parallel to the field, then these values differ greatly from each other (Figure 5). Obviously, this remark applies equally to any other shapes of the domain.

The above-described method is straightforward for a domain of the shape of a rectangular parallelepiped, but it can also be applied (in a somewhat more complicated way) to some other polyhedra. Let us consider three more shapes of the domain, which by means of similar techniques (reflection of the domain together with the vector field defined on it) can be converted into parallelepipeds with a spatially periodic vector field generated by the initial one.

The periodic field by construction will have a number of additional symmetries, which will affect the set of extremals of the functional $\Phi\{\boldsymbol{w}\}$ (i.e. eigenvectors of the corresponding operator): only a part of the eigenvectors for the parallelepiped (namely, those that possess the needed symmetries) will correspond to the eigenvectors for the original domain.

(a) A straight trihedral prism having a rectangular isosceles triangle as its base, which, when reflected with respect to the hypotenuse, turns into a square. Thus, the prism itself, when reflected with respect to the corresponding lateral face, is converted into a rectangular parallelepiped with a pair of square faces. Herewith the field $\boldsymbol{w}(\boldsymbol{x})$ reflected together with the original prism, is converted into a field in the rectangular parallelepiped, tangential at its boundary, but additionally possessing the symmetry with respect to one of the "diagonal" planes (Figure 6).

In what follows, as before, the parallelepiped together with the field $\boldsymbol{w}(\boldsymbol{x})$ is reflected with respect to the planes of faces. Finally we obtain a spatially periodic field for which the functional $\Phi\{\boldsymbol{w}\}$ takes the
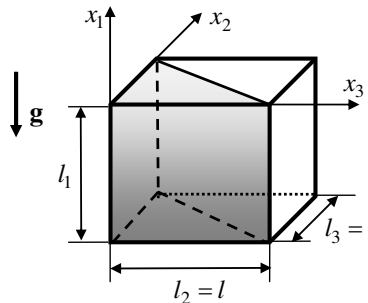
Figure 6. A straight trihedral prism with a rectangular isosceles triangle in the base.

same value as the original functional on the initial field $\boldsymbol{w}(\boldsymbol{x})$, whereas the Fourier series for $\nabla_\kappa \otimes \boldsymbol{w}(\boldsymbol{x})$ appears to be equal to formally differentiated Fourier series for $\boldsymbol{w}(\boldsymbol{x})$.

The presence of an additional symmetry of the field $\boldsymbol{w}(\boldsymbol{x})$ as compared to an arbitrary (tangential at the boundary) field in the rectangular parallelepiped results in certain additional properties of the Fourier coefficients in the expansion of the field $\boldsymbol{w}(\boldsymbol{x})$. Specifically, the pairs of terms of the Fourier series symmetric with respect to the diagonal plane should be equal in amplitude (while for the rectangular parallelepiped with square faces of one of the pairs, the amplitudes could be arbitrary). This results in less multiplicity of corresponding eigenvalues.

To describe the corresponding modes, we introduce some notation: the axis x_1 is the one directed along the edge orthogonal to the planes of the square faces, the axes x_2 and x_3 are directed along the catheti of an isosceles rectangular triangle, l_1 is the length of the edge directed along the axis x_1, $l = l_2 = l_3$ is the length of the edges directed along the axes x_2 and x_3, $\mu_1, \mu_2, \mu_3 \leq \mu_2$ are the nonnegative integers not equal to zero simultaneously. Then the mentioned pair of terms of the Fourier series has the following form (up to an arbitrary factor):

$$\boldsymbol{w}_{\mu_1\mu_2\mu_3}(\boldsymbol{x}) = \nabla_\kappa \left(\cos\left(\frac{\pi}{l_1}\mu_1 x_1\right) \cos\left(\frac{\pi}{l}\mu_2 x_2\right) \cos\left(\frac{\pi}{l}\mu_3 x_3\right) \right.$$
$$\left. + \cos\left(\frac{\pi}{l_1}\mu_1 x_1\right) \cos\left(\frac{\pi}{l}\mu_3 x_2\right) \cos\left(\pi\mu_2 \frac{x_3}{l}\right) \right). \quad (6\text{-}27)$$

The field (6-27) is one of the extremals of functional $\Phi\{\boldsymbol{w}\}$ for the considered triangle prism, i.e. the eigenvector of corresponding self-adjoint operator, with related eigenvalue

$$\theta_{\mu_1\mu_2\mu_3} = \pi^2\left(\frac{\mu_1^2}{l_1^2} + \frac{\mu_2^2 + \mu_3^2}{l^2}\right) = \boldsymbol{q}_\mu \cdot \boldsymbol{q}_\mu, \quad \boldsymbol{q}_\mu = \frac{\pi\mu_1}{l_1}\boldsymbol{e}_1 + \frac{\pi\mu_2}{l}\boldsymbol{e}_2 + \frac{\pi\mu_3}{l}\boldsymbol{e}_3. \quad (6\text{-}28)$$

Numbering the integer vectors $\boldsymbol{\mu} = \boldsymbol{\mu}^m$ in the order of nondecreasing of $|\boldsymbol{q}_{\boldsymbol{\mu}^m}|$, we obtain a nondecreasing sequence of eigenvalues:

$$\theta_{\boldsymbol{\mu}^m} = \boldsymbol{q}_{\boldsymbol{\mu}^m} \cdot \boldsymbol{q}_{\boldsymbol{\mu}^m}, \quad m = 1, 2, \dots . \quad (6\text{-}29)$$

It is obvious that

$$\theta_{\boldsymbol{\mu}^1} = \min_{\boldsymbol{\mu}} \boldsymbol{q}_\mu \cdot \boldsymbol{q}_\mu = \left(\frac{\pi}{\max(l_1, l)}\right)^2. \quad (6\text{-}30)$$

Bounds for the free vibration frequencies ω_m, as before, are given by inequalities (6-23).

(b) A triangular pyramid, the base of which is an isosceles rectangular triangle; the planes of the lateral faces passing through its catheti are orthogonal to the plane of the base, and the plane of lateral face passing through the hypotenuse makes with the plane of the base an angle equal to $\pi/4$ (Figure 7). Such a pyramid by a number of reflections with respect to the planes of the faces is converted into a cube.

Specifically, first, reflections are made with respect to the planes of the faces orthogonal to the base; hereby the original pyramid turns into a quadrangular pyramid, the base of which is a square with a side equal to the hypotenuse of the base of the original pyramid. Then the quadrangular pyramid is reflected with respect to the planes of the side faces and four quadrangular pyramids are formed with bases orthogonal to the base plane of the original pyramid and passing through the sides of the square mentioned. At the last stage, one (any) of the reflected pyramids is reflected with respect to one of its lateral faces in such a way that the plane of the base of reflected pyramid be parallel to the plane of the
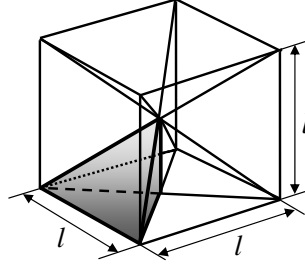
Figure 7. A triangular pyramid with rectangular isosceles triangle in the base.

base of the original pyramid. The totality of six quadrangular pyramids forms a cube with an edge equal to the hypotenuse of the base of the original triangular pyramid.

As for the vector field $\boldsymbol{w}(\boldsymbol{x})$ in the original pyramid, it also undergoes all the listed reflections and eventually turns into a field in the cube, which we still denote $\boldsymbol{w}(\boldsymbol{x})$. Although the cube is a particular case of the rectangular parallelepiped, considered in (a), in this case an important role in finding the extremals of functional $\Phi\{\boldsymbol{w}\}$ is played by the symmetries that the field $\boldsymbol{w}(\boldsymbol{x})$ gets by construction, namely: the resulting field $\boldsymbol{w}(\boldsymbol{x})$ is symmetric with respect to all diagonal planes of the cube (i.e. the planes orthogonal to the planes of a pair of faces and passing through the diagonals of the faces of this pair).

We introduce the Cartesian rectangular coordinates with the origin at one of vertices of the cube and axes directed along its edges. The edge length (the length of the hypotenuse of an isosceles triangle) will be denoted l. It can be shown that in the case under consideration the groups of terms of the Fourier series corresponding to the sets of integers μ_1, μ_2, μ_3, such that

$$0 \leq \mu_1 \leq \mu_2 \leq \mu_3, \quad \mu_3 > 0, \tag{6-31}$$

are given by the following equality:

$$\boldsymbol{w}_{\mu_1\mu_2\mu_3}(\boldsymbol{x}) = \sum_{(i,j,k)} \nabla_\kappa \left(\cos\left(\frac{\pi}{l}\mu_i x_1\right) \cos\left(\frac{\pi}{l}\mu_j x_2\right) \cos\left(\frac{\pi}{l}\mu_k x_3\right) \right), \tag{6-32}$$

where (i, j, k) are possible permutations of numbers $(1, 2, 3)$, and the numbers μ_1, μ_2, μ_3 additionally possess the property that the sum of any pair of them is an even number. The property is equivalent to that the numbers μ_i either all are odd, or all are even. The fields (6-32) are extremals of the functional $\Phi\{\boldsymbol{w}\}$, i.e. eigenvectors of the corresponding operator with eigenvalues

$$\theta_{\mu_1\mu_2\mu_3} = \frac{\pi^2}{l^2}(\mu_1^2 + \mu_2^2 + \mu_3^2) = \boldsymbol{q}_\mu \cdot \boldsymbol{q}_\mu, \quad \boldsymbol{q}_\mu = \frac{\pi}{l}(\mu_1 \boldsymbol{e}_1 + \mu_2 \boldsymbol{e}_2 + \mu_3 \boldsymbol{e}_3). \tag{6-33}$$

Numbering, as before, integer vectors $\boldsymbol{\mu} = \boldsymbol{\mu}^m$ in order of nondecreasing of $|\boldsymbol{q}_{\boldsymbol{\mu}^m}|$, we obtain a nondecreasing sequence of eigenvalues $\theta_{\boldsymbol{\mu}^m}$, where $m = 1, 2, 3, \ldots$. Obviously, the smallest eigenvalue corresponds to the triplet $(1, 1, 1)$:

$$\theta_{\boldsymbol{\mu}^1} = \min_{\boldsymbol{\mu}} \boldsymbol{q}_\mu \cdot \boldsymbol{q}_\mu = \frac{3\pi^2}{l^2}. \tag{6-34}$$
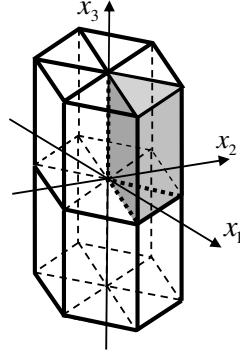
Figure 8. A straight trihedral prism with a regular triangle in the base. Conversion into a hexahedral prism.

It is also obvious that the second eigenvalue corresponds to the triplet $(0, 0, 2)$, and the third one corresponds to the triplet $(0, 2, 2)$:

$$\theta_{\mu^2} = \frac{4\pi^2}{l^2}, \quad \theta_{\mu^3} = \frac{8\pi^2}{l^2}. \tag{6-35}$$

In principle, it is not difficult to find any given number of the first eigenvalues. Bounds for the free vibration frequencies ω_m, as before, are given by inequalities (6-23).

(c) A straight trihedral prism with a height l_3, whose base is a regular triangle with the side l (and corresponding height $h = l\sqrt{3}/2$). We reflect the prism (as before, together with tangential at the boundary vector field defined in it) with respect to the two lateral faces, then the resulting quadrangular prism we reflect with respect to a larger lateral face; the resulting regular straight hexahedral prism is reflected with respect to the base (Figure 8).

As a result, we obtain a regular straight hexahedral prism of double height. Reflecting this hexahedral prism with respect to all the lateral faces, we obtain a polyhedron, the cross-section of which by a plane parallel to the base is shown in Figure 9, left. Continuing such reflections, we obtain a periodic vector field with a period $2h$ in the directions of axes x_1 and x_2 (parallel to the heights of regular triangle) and with a period $2l_3$ in the direction of axis x_3 (orthogonal to the base of the prism). Note that periodicity with a period $2h$ is also present in the direction parallel to the third height of regular triangle, but for the expansion of a vector field into a triple Fourier series only three directions of periodicity should be chosen from the four available; however, the presence of the fourth will result in the structure of terms of the Fourier series.

The elementary cell of periodicity here is an oblique parallelepiped with the edges $(2h, 2h, 2l_3)$, the cross-section of which by a plane parallel to the base of the original prism (that being a parallelogram) is also depicted in Figure 9, left. To represent the corresponding Fourier series taking into account the obliqueness of the coordinate system (x_1, x_2, x_3), we introduce the following notation: $\boldsymbol{e}_1, \boldsymbol{e}_2, \boldsymbol{e}_3$ are the unit basis vectors specifying the axes (x_1, x_2, x_3) (Figures 8 and 9)); the dual basis corresponding to the basis $(\boldsymbol{e}_1, \boldsymbol{e}_2, \boldsymbol{e}_3)$ is the basis $(\tilde{\boldsymbol{e}}_1, \tilde{\boldsymbol{e}}_2, \tilde{\boldsymbol{e}}_3 = \boldsymbol{e}_3)$ (Figure 9, right).

The system of basis functions (up to normalizing factors, which play a minor role in this problem) is
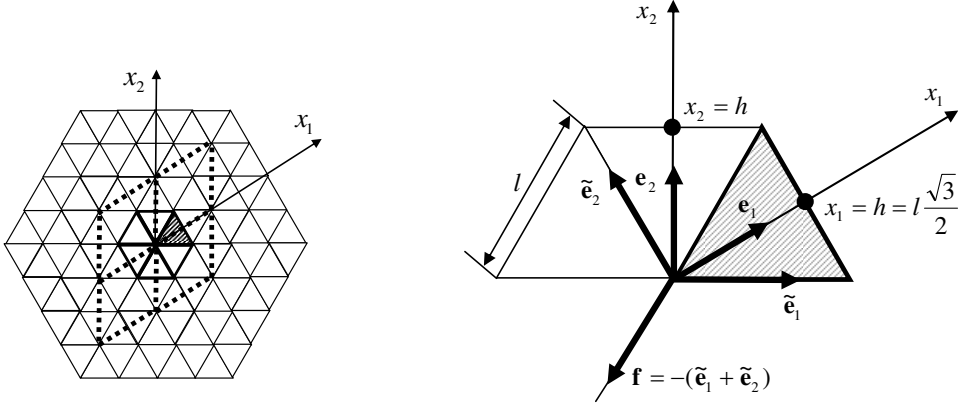
Figure 9. Left: Conversion of the field in the hexahedral prism into a periodic one by means of reflections. Right: Conventions for the Fourier series expansion in an oblique parallelepiped.

taken to be of the following form:

$$\sin(\boldsymbol{q}_\mu \cdot \boldsymbol{x}) \sin\!\Big(\frac{\pi}{l_3}\mu_3 x_3\Big), \quad \sin(\boldsymbol{q}_\mu \cdot \boldsymbol{x}) \cos\!\Big(\frac{\pi}{l_3}\mu_3 x_3\Big),$$

$$\cos(\boldsymbol{q}_\mu \cdot \boldsymbol{x}) \sin\!\Big(\frac{\pi}{l_3}\mu_3 x_3\Big), \quad \cos(\boldsymbol{q}_\mu \cdot \boldsymbol{x}) \cos\!\Big(\frac{\pi}{l_3}\mu_3 x_3\Big),$$

$$\boldsymbol{q}_\mu = \frac{\pi}{h}(\mu_1 \tilde{\boldsymbol{e}}_1 + \mu_2 \tilde{\boldsymbol{e}}_2), \tag{6-36}$$

$$\mu_3 \ge 0, \quad \mu_3 > 0 \Rightarrow \mu_1, \mu_2 = 0, \pm 1, \pm 2, \dots,$$

$$\mu_3 = 0 \Rightarrow \mu_1 \ge 0, \quad \mu_1 > 0 \Rightarrow \mu_2 = 0, \pm 1, \pm 2, \dots,$$

$$\mu_1 = 0 \Rightarrow \mu_2 = 1, 2, \dots .$$

Taking into account that the subspace of vector fields of interest is formed by the gradients of scalar fields, as well as the presence of symmetry with respect to the plane $x_3 = 0$, we arrive at the following expressions for two types of terms of the Fourier series corresponding to a set of integers (μ_1, μ_2, μ_3):

$$\boldsymbol{w}^c_{\mu_1\mu_2\mu_3} = \boldsymbol{q}_\mu \cos(\boldsymbol{q}_\mu \cdot \boldsymbol{x}) \cos\!\Big(\frac{\pi}{l_3}\mu_3 x_3\Big) - \frac{\pi}{l_3}\mu_3 \boldsymbol{e}_3 \sin(\boldsymbol{q}_\mu \cdot \boldsymbol{x}) \sin\!\Big(\frac{\pi}{l_3}\mu_3 x_3\Big),$$

$$\boldsymbol{w}^s_{\mu_1\mu_2\mu_3} = \boldsymbol{q}_\mu \sin(\boldsymbol{q}_\mu \cdot \boldsymbol{x}) \cos\!\Big(\frac{\pi}{l_3}\mu_3 x_3\Big) + \frac{\pi}{l_3}\mu_3 \boldsymbol{e}_3 \cos(\boldsymbol{q}_\mu \cdot \boldsymbol{x}) \sin\!\Big(\frac{\pi}{l_3}\mu_3 x_3\Big). \tag{6-37}$$

Each of the modes (6-37) would enter into an expansion with its own coefficient, these coefficients being arbitrary and independent, if not for the presence of symmetry of the vector field with respect to the planes of the lateral faces of original prism (due to sequence of reflections having led to periodicity): this results in definite relations between the coefficients. To specify these relations, we introduce, apart from the vectors $\tilde{\boldsymbol{e}}_1$ and $\tilde{\boldsymbol{e}}_2$, an additional vector $\boldsymbol{f}$ (Figure 9, right):

$$\boldsymbol{f} = -(\tilde{\boldsymbol{e}}_1 + \tilde{\boldsymbol{e}}_2). \tag{6-38}$$

The vectors $(\tilde{e}_1, \tilde{e}_2, f)$ under these reflections pass into each other and are equivalent to each other in the sense of the structure and symmetries of the constructed periodic field. The symmetry of a field, when the latter is expanded into the Fourier series, results in the symmetries of groups of its terms corresponding to the same value of μ_3 and the values of q_μ that pass into each other under the reflections. In general case, there are six such values, but in particular, they can coincide in pairs, and then there will be three of them.

We describe both cases. In the first case, we set $\mu_2 > 0$, $\mu_1 > \mu_2$. Then

$$
\boldsymbol{q}^{(1)}_{\mu_1\mu_2} := \frac{\pi}{h}(\mu_1\tilde{e}_1 + \mu_2\tilde{e}_2), \quad \boldsymbol{q}^{(2)}_{\mu_1\mu_2} := \frac{\pi}{h}(\mu_1\tilde{e}_2 + \mu_2\tilde{e}_1), \quad \boldsymbol{q}^{(3)}_{\mu_1\mu_2} := \frac{\pi}{h}(\mu_1\tilde{e}_2 + \mu_2 f),
$$
$$
\boldsymbol{q}^{(4)}_{\mu_1\mu_2} := \frac{\pi}{h}(\mu_1 f + \mu_2\tilde{e}_2), \quad \boldsymbol{q}^{(5)}_{\mu_1\mu_2} := \frac{\pi}{h}(\mu_1 f + \mu_2\tilde{e}_1), \quad \boldsymbol{q}^{(6)}_{\mu_1\mu_2} := \frac{\pi}{h}(\mu_1\tilde{e}_1 + \mu_2 f). \tag{6-39}
$$

In the second case, we set $\mu_2 = 0$, $\mu_1 > 0$. Then

$$
\boldsymbol{q}^{(1)}_{\mu_1} = \frac{\pi}{h}\mu_1\tilde{e}_1, \quad \boldsymbol{q}^{(2)}_{\mu_1} = \frac{\pi}{h}\mu_1\tilde{e}_2, \quad \boldsymbol{q}^{(3)}_{\mu_1} = \frac{\pi}{h}\mu_1 f. \tag{6-40}
$$

Modes of each type (i.e. $\boldsymbol{w}^c$ and $\boldsymbol{w}^s$), corresponding to the same set (6-40) or to the same set (6-39) of vectors $\boldsymbol{q}$, should have the same coefficients. It is almost obvious that when such vectors belong to the same set invariant with respect to reflections, that is equivalent to their absolute values being equal to each other.

Taking all the foregoing into account, we represent the Fourier series for the constructed periodic field $\boldsymbol{w}$, which possesses all the necessary symmetries, in the following form:

$$
\boldsymbol{w} \sim \sum_{\mu_3 > 0} a^s_{\mu_3} \frac{\pi}{l_3}\mu_3 \boldsymbol{e}_3 \sin\!\left(\frac{\pi}{l_3}\mu_3 x_3\right)
$$
$$
+ \sum_{\mu_1 > 0}\sum_{\mu_3 \geq 0}\sum_{i=1}^{3}\left(a^c_{\mu_1\mu_3}\left(\boldsymbol{q}^{(i)}_{\mu_1}\cos(\boldsymbol{q}^{(i)}_{\mu_1}\cdot\boldsymbol{x})\cos\!\left(\frac{\pi}{l_3}\mu_3 x_3\right) - \frac{\pi}{l_3}\mu_3 \boldsymbol{e}_3 \sin(\boldsymbol{q}^{(i)}_{\mu_1}\cdot\boldsymbol{x})\sin\!\left(\frac{\pi}{l_3}\mu_3 x_3\right)\right)\right.
$$
$$
\left. + a^s_{\mu_1\mu_3}\left(\boldsymbol{q}^{(i)}_{\mu_1}\sin(\boldsymbol{q}^{(i)}_{\mu_1}\cdot\boldsymbol{x})\cos\!\left(\frac{\pi}{l_3}\mu_3 x_3\right) + \frac{\pi}{l_3}\mu_3 \boldsymbol{e}_3 \cos(\boldsymbol{q}^{(i)}_{\mu_1}\cdot\boldsymbol{x})\sin\!\left(\frac{\pi}{l_3}\mu_3 x_3\right)\right)\right)
$$
$$
+ \sum_{\substack{\mu_2 > 0 \\ \mu_1 > \mu_2}}\sum_{\mu_3 \geq 0}\sum_{i=1}^{6}\left(a^c_{\mu_1\mu_2\mu_3}\left(\boldsymbol{q}^{(i)}_{\mu_1\mu_2}\cos(\boldsymbol{q}^{(i)}_{\mu_1\mu_2}\cdot\boldsymbol{x})\cos\!\left(\frac{\pi}{l_3}\mu_3 x_3\right) - \frac{\pi}{l_3}\mu_3 \boldsymbol{e}_3 \sin(\boldsymbol{q}^{(i)}_{\mu_1\mu_2}\cdot\boldsymbol{x})\sin\!\left(\frac{\pi}{l_3}\mu_3 x_3\right)\right)\right.
$$
$$
\left. + a^s_{\mu_1\mu_2\mu_3}\left(\boldsymbol{q}^{(i)}_{\mu_1\mu_2}\sin(\boldsymbol{q}^{(i)}_{\mu_1\mu_2}\cdot\boldsymbol{x})\cos\!\left(\frac{\pi}{l_3}\mu_3 x_3\right) + \frac{\pi}{l_3}\mu_3 \boldsymbol{e}_3 \cos(\boldsymbol{q}^{(i)}_{\mu_1\mu_2}\cdot\boldsymbol{x})\sin\!\left(\frac{\pi}{l_3}\mu_3 x_3\right)\right)\right). \tag{6-41}
$$

Due to periodicity of the "constructed" field $\boldsymbol{w}$, the Fourier expansions for $\nabla_\kappa \otimes \boldsymbol{w}$ and $\nabla_\kappa \cdot \boldsymbol{w} = \boldsymbol{I} : \nabla_\kappa \otimes \boldsymbol{w}$ are the result of applying of the corresponding operators to the terms of the Fourier series for the field itself. We note that multiplicity of the terms corresponding to $\mu_1 = \mu_2 = 0$, $\mu_3 > 0$ is equal to one, and multiplicity of the remaining terms is equal to two.

Each group of terms of the Fourier series forms either one-dimensional or two-dimensional subspace, these subspaces being mutually orthogonal both in the sense of the scalar product $\langle \boldsymbol{w} \cdot \tilde{\boldsymbol{w}}\rangle_{B'}$ corresponding to the denominator of the functional $\Phi\{\boldsymbol{w}\}$ (6-8) and in the sense of the bilinear functional $\langle(\nabla_\kappa \cdot \boldsymbol{w})(\nabla_\kappa \cdot \tilde{\boldsymbol{w}})\rangle_{B'}$ corresponding to its numerator (here the domain B' is an oblique parallelepiped specifying the cell of periodicity of the constructed field). By arguments almost coinciding with those in

derivation of (6-18)–(6-22), we obtain a set of values of the functional $\Phi\{\boldsymbol{w}\}$ on the Fourier series terms that correspond to all possible sets of numbers (μ_1, μ_2, μ_3):

$$\theta_{00\mu_3} = \left(\frac{\pi}{l_3}\right)^2 \mu_3^2,$$

$$\theta_{\mu_10\mu_3}^c = \theta_{\mu_10\mu_3}^s = \boldsymbol{q}_{\mu_1}^{(i)} \cdot \boldsymbol{q}_{\mu_1}^{(i)} + \left(\frac{\pi}{l_3}\right)^2 \mu_3^2 = \pi^2 \left(\frac{\mu_1^2}{(\frac{3}{4}l)^2} + \frac{\mu_3^2}{l_3^2}\right), \tag{6-42}$$

$$\theta_{\mu_1\mu_2\mu_3}^c = \theta_{\mu_1\mu_2\mu_3}^s = \boldsymbol{q}_{\mu_1\mu_21}^{(i)} \cdot \boldsymbol{q}_{\mu_1\mu_2}^{(i)} + \left(\frac{\pi}{l_3}\right)^2 \mu_3^2 = \pi^2 \left(\frac{\mu_1^2 + \mu_2^2 - \mu_1\mu_2}{(\frac{3}{4}l)^2} + \frac{\mu_3^2}{l_3^2}\right).$$

From the same arguments it follows that these are the eigenvalues of a self-adjoint operator corresponding to the functional $\Phi\{\boldsymbol{w}\}$. Numbering them in the order of nondecreasing and using the comparison theorem, we obtain upper and lower bounds for numbered in the same way the free vibration frequencies of the bulk-elastic medium in the domain of the shape under consideration:

$$\underline{c}_\kappa \sqrt{\frac{\rho_\kappa}{\bar{\rho}_\kappa}} \sqrt{\theta} \leq \omega \leq \bar{c}_\kappa \sqrt{\frac{\bar{\rho}_\kappa}{\underline{\rho}_\kappa}} \sqrt{\theta}. \tag{6-43}$$

In deriving the equalities (6-42), the following equations are used:

$$\tilde{\boldsymbol{e}}_1 \cdot \tilde{\boldsymbol{e}}_1 = \tilde{\boldsymbol{e}}_2 \cdot \tilde{\boldsymbol{e}}_2 = \boldsymbol{f} \cdot \boldsymbol{f} = \frac{4}{3}, \quad \tilde{\boldsymbol{e}}_1 \cdot \tilde{\boldsymbol{e}}_2 = \tilde{\boldsymbol{e}}_1 \cdot \boldsymbol{f} = \tilde{\boldsymbol{e}}_2 \cdot \boldsymbol{f} = -\frac{2}{3}. \tag{6-44}$$

From equalities (6-42) we obtain the value of the smallest eigenvalue:

$$\theta_{\min} = \left(\frac{\pi}{\max(\frac{3}{4}l, l_3)}\right)^2, \tag{6-45}$$

and the corresponding bounds (6-43) for the lowest frequency.

7. Examples of bilateral bounds for free vibration frequencies of the Mooney–Rivlin bulk-elastic media in rectangular parallelepipeds

The examples given below are based on the nonlinear bulk-elastic constitutive relation having some essential features of the well-known Mooney–Rivlin elastic solid. In what follows the former will be called the Mooney–Rivlin bulk-elastic medium. We remark that this type of constitutive relation is meaningful for any values of strain up to arbitrarily large values. This property is very important for the problems considered in the work. We remind that unlike the cases presented in the literature, in the problems investigated here the unperturbed state may be deformed greatly and nonuniformly with respect to the homogeneous unloaded configuration and this entails a great difference in possible methods of analysis.

In the cases presented in the literature, substantial restrictions are assumed regarding the unperturbed state of the medium, because the equations of motion with variable coefficients in general case cannot be solved analytically. In each particular case certain simplifications in the formulation of the problem are employed. For example, there may be equations of motion with variable coefficients of some specific type. In other cases, conditions of low compressibility of the medium are assumed, that allows at further analytical study to consider the equilibrium state of the medium as uniform. Sometimes nonuniformity

can be neglected due to a certain geometrical configuration of the system, for example, if the medium under consideration occupies a layer which is very thin in direction perpendicular to the direction of mass force field. All those assumptions allow to reduce the problem under consideration to an analytical study of equations with either constant coefficients or variable coefficients of some specific type, whereas further analysis is based on exact solutions of the equations.

As for our method, it is based on variational approach together with usage of some essential analytical findings of our own [Ryzhak et al. 2017; Ryzhak 1993; 1994; 1997], giving the opportunity of obtaining rigorous upper and lower bounds for the free vibration frequencies for a broad class of mechanical systems whose behavior is governed by equations with variable coefficients.

In the examples given below we demonstrate the bilateral bounds in the case of some mechanical systems with great nonuniformity of loaded configuration, and compare them with the well-known exact values for uniform systems.

For simplicity we assume that the domain occupied by the Mooney–Rivlin bulk-elastic medium is a rectangular parallelepiped. We first set the elastic potential of such a medium with respect to unit volume in the unloaded configuration $\tilde{\kappa}$:

$$
\begin{aligned}
\sigma_{\tilde{\kappa}}(\widetilde{\boldsymbol{F}}) &= \frac{K_0}{2}\left(\det\widetilde{\boldsymbol{F}} + \frac{1}{\det\widetilde{\boldsymbol{F}}}\right) \\
&= \frac{K_0}{2}\left(\frac{\rho_0}{\rho} + \frac{\rho}{\rho_0}\right),
\end{aligned}
\tag{7-1}
$$

where $\widetilde{\boldsymbol{F}}$ is the transformation gradient with respect to configuration $\tilde{\kappa}$, K_0, and ρ_0 are the bulk modulus and density in the unloaded state.

Let the medium occupying the rectangular parallelepiped be under the action of constant vertical gravity field $\boldsymbol{g}$. We assume that the largest edge of rectangular parallelepiped l_3 is the vertical one (see Figure 3). In this case it is not difficult to obtain the following analytical expressions for sound velocity, density, and bulk modulus as functions of the vertical coordinate x_3 measured from the bottom. On the upper face of parallelepiped, where $x_3 = l_3$, there are the minimal values of density $\rho(l_3) = \underline{\rho}$, bulk modulus $K(l_3) = \underline{K}$, and sound velocity $c(l_3) = \underline{c}$. Then we have

$$
\begin{aligned}
\rho(l_3 - x_3) &= \underline{\rho}\left(1 + \frac{\underline{\rho}}{\underline{K}}g(l_3 - x_3)\right) = \underline{\rho}\left(1 + \frac{g(l_3 - x_2)}{\underline{c}^2}\right), \\
K(l_3 - x_3) &= \underline{K}\left(1 + \frac{g(l_3 - x_3)}{\underline{c}^2}\right)^2, \\
c(l_3 - x_3) &= \sqrt{\frac{\underline{K}}{\underline{\rho}}\left(1 + \frac{g(l_3 - x_3)}{\underline{c}^2}\right)} = \underline{c}\sqrt{1 + \frac{g(l_3 - x_3)}{\underline{c}^2}}\,.
\end{aligned}
\tag{7-2}
$$

Maximal values of the quantities are attained at the bottom of parallelepiped, where $x_3 = 0$:

$$
\rho(l_3) = \bar{\rho} = \underline{\rho}\left(1 + \frac{gl_3}{\underline{c}^2}\right), \quad K(l_3) = \overline{K} = \underline{K}\left(1 + \frac{gl_3}{\underline{c}^2}\right)^2, \quad c(l_3) = \bar{c} = \underline{c}\sqrt{1 + \frac{gl_3}{\underline{c}^2}}\,.
\tag{7-3}
$$

Substituting the values (7-3) into inequalities (6-23), we obtain the following upper and lower bounds for the free vibration frequencies:

$$\frac{\underline{c}}{\sqrt{1+(gl_3/\underline{c}^2)}}\sqrt{\theta_m} \le \omega_m \le \underline{c}\left(1+\frac{gl_3}{\underline{c}^2}\right)\sqrt{\theta_m}\,,$$

$$\sqrt{\theta_m} = |\boldsymbol{q}_{\boldsymbol{\mu}^m}| = \sqrt{\sum_{i=1}^{3}\frac{\pi^2}{l_i^2}(\mu_i^m)^2}\,,$$

(7-4)

Introducing the dimensionless quantity

$$\tilde{\theta}_m := l_3^2\theta_m,$$

(7-5)

we rewrite inequalities (7-4) as follows:

$$\frac{\underline{c}}{l_3}\frac{\sqrt{\tilde{\theta}_m}}{\sqrt{1+(gl_3/\underline{c}^2)}} \le \omega_m \le \frac{\underline{c}}{l_3}\sqrt{\tilde{\theta}_m}\left(1+\frac{gl_3}{\underline{c}^2}\right).$$

(7-6)

In particular for the first frequency we obtain:

$$\sqrt{\theta_1} = |\boldsymbol{q}_{\boldsymbol{\mu}^1}| = \frac{\pi}{\max_i l_i} =: \frac{\pi}{l_3},\quad \frac{\underline{c}}{l_3}\frac{\pi}{\sqrt{1+(gl_3/\underline{c}^2)}} \le \omega_1 \le \frac{\underline{c}}{l_3}\pi\left(1+\frac{gl_3}{\underline{c}^2}\right).$$

(7-7)

From formulas (7-3) it follows that if the quantity $gl_3/\underline{c}^2$ is small enough, then

$$\rho(l_3-x_3) \approx \underline{\rho} \approx \bar{\rho},\quad K(l_3-x_3) \approx \underline{K} \approx \bar{K},\quad c(l_3-x_3) \approx \underline{c} \approx \bar{c},$$

and it is possible to consider the loaded unperturbed configuration of the medium as uniform or close to uniform. *In the case of uniform equilibrium state* (when $\underline{c} = \bar{c} = c$) every pair of inequalities (7-7) and (7-6) converts into the equalities and gives the *well-known exact values of free vibration frequencies*:

$$\omega_1 = \frac{\pi c}{l_3},\quad \omega_m = \frac{c}{l_3}\sqrt{\tilde{\theta}_m}\,.$$

(7-8)

In the case when the nonuniformity of the equilibrium state is not significant, the formulas (7-6) and (7-7) provide a good (and moreover, rigorous) approximation for free vibration frequencies. Clearly it will take place if:

(1) for given l_3 and $\underline{c}$ the mass force g is small enough,

(2) for given g and l_3 the minimal sound velocity $\underline{c}$ is great enough,

(3) for given g and $\underline{c}$ the vertical dimension l_3 is small enough.

  Let us now consider the case when the classical methods by no means give any results. For example we set

$$1+\frac{gl_3}{\underline{c}^2}=2.$$

Then

$$\bar{\rho} = \underline{\rho}\left(1+\frac{gl_3}{\underline{c}^2}\right) = 2\underline{\rho},\quad \bar{K} = \underline{K}\left(1+\frac{gl_3}{\underline{c}^2}\right)^2 = 4\underline{K},\quad \bar{c} = \underline{c}\sqrt{1+\frac{gl_3}{\underline{c}^2}} = \sqrt{2}\,\underline{c},$$

i.e. *the equilibrium state of the medium is strongly nonuniform.* Nevertheless our approach makes it possible to obtain the rigorous bilateral bounds for all free vibration frequencies:

$$\frac{c}{l_3}\frac{\sqrt{\tilde{\theta}_m}}{\sqrt{2}} \leq \omega_m \leq \frac{c}{l_3}\sqrt{\tilde{\theta}_m}, \qquad \frac{c}{l_3}\frac{\pi}{\sqrt{2}} \leq \omega_1 \leq \frac{c}{l_3}2\pi. \tag{7-9}$$

Conclusions

In the work the free vibrations of a homogeneous bulk-elastic medium occupying a closed domain with fixed and perfectly smooth boundary and subject to the action of a field of mass forces are investigated analytically by variational methods. The formulation of the problem is highly general: the nonlinear law of bulk elasticity is arbitrary, the shape of the domain is almost arbitrary (see Appendix A), the force field is an arbitrary potential field. Additionally the domains of a number of special shapes are considered.

For investigation of the problem under consideration it has become necessary to prove modifications of the fundamental theorems in the theory of free vibrations for elastic bodies. The main novel research tool is the use of the canonical form of second variation of total potential energy of the system [Ryzhak et al. 2017], which in this case assumes a particularly simple form, namely (5-27) and (5-31).

Proved in the work version of the comparison theorem for the free vibration frequencies results in the inequalities (5-49), (5-52). The inequalities obtained make it possible to compare with each other all the free vibration frequencies of two different bulk-elastic media in domains of identical or similar shapes and for different fields of mass forces as well as for the same field, but for different orientations of the domain with respect to it (Figure 5). The latter can be regarded as a special case of different fields. These results (expressing a certain combination of geometrical and mechanical similarity of the problems) find a number of applications, e.g. enable to model and investigate in laboratory the free vibrations of real large-scale systems (say, atmospheric layers).

Another important result of the work are the analytical bilateral bounds for all the free vibration frequencies of bulk-elastic media in domains of the following shapes: a rectangular parallelepiped with an arbitrary ratio of the lengths of edges, a straight trihedral prism (with either an isosceles rectangular triangle or regular triangle as the base), and a triangular pyramid with an isosceles rectangular triangle as the base, whose lateral faces passing through the catheti of the base are orthogonal to its plane, whereas a face passing through the hypotenuse of the base is inclined to its plane at a $\pi/4$ angle.

The above-mentioned analytical results are also valid for different fields of mass forces and for different orientations of the domains with respect to the same field, which obviously concerns the technical devices whose spatial position can be varied (see Figure 5). We note that the field itself enters into the obtained bilateral bounds indirectly, namely, via the maximal and minimal equilibrium values of the sound velocity in the medium in combination with the ratio of the maximal and minimal equilibrium density values. Obviously, in the absence of the force field, the equilibrium state of the medium is uniform, and hence, the upper and lower bounds coincide with each other and thus give the exact values of all frequencies of the spectrum not only for rectangular parallelepipeds (for which they could be obtained by the method of separation of variables), but also for other polyhedra (for which separation of variables cannot be applied).

If for a domain of some different shape (for example, a circular cylinder, a sphere or a spherical layer) the problem of free vibrations of a homogeneous bulk-elastic medium in the absence of the force field
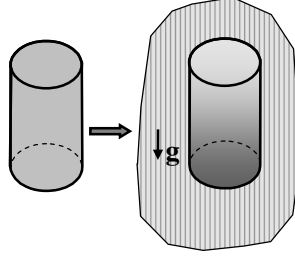
Figure 10. From exact values for the free vibration frequencies in the case of uniform equilibrium state to the bounds for them in the problem with stratification due to mass forces.

can be solved analytically and the values of all quantities θ_m are found, then the comparison theorem via inequalities (6-43) will give upper and lower bounds for all the frequencies ω_m of the medium in that domain with regard for the field and corresponding nonuniform distribution of density and velocity of sound (Figure 10). In the case when the values of quantities θ_m are found analytically only for a part of the free vibration modes in the absence of the field, then for the m-th frequency in the presence of the field only an upper bound will follow from the comparison theorem.

Appendix A. Proof of the compactness of subsets of subspace $N_0^\perp$ bounded both in the value of functional $R\{u\}$ and in the norm $\|u\|$

This compactness is a consequence of classical Rellich's lemma, the condition of which incorporates the boundedness both in the norm $(\langle u \cdot u \rangle_B)^{1/2}$ and in the value of the quadratic functional $\langle \nabla_\kappa \otimes u : \nabla_\kappa \otimes u \rangle_B$. Obviously, the norms $\|u\|$ and $(\langle u \cdot u \rangle_B)^{1/2}$ are equivalent to each other and to all norms of the same type with positive weights $\beta(x)$. Thus, it should be additionally proved that from boundedness of $R\{u\}$ and from boundedness of $\|u\|$ it follows the boundedness of $\langle \nabla_\kappa \otimes u : \nabla_\kappa \otimes u \rangle_B$. Since the fields $u(x)$ on the subspace $N_0^\perp$ are the gradients of scalar fields (5-34), we have

$$u(x) = \nabla_\kappa \gamma(x) \implies \nabla_\kappa \otimes u(x) = \nabla_\kappa \otimes \nabla_\kappa \gamma(x) = \left(\nabla_\kappa \otimes u(x) \right)^T. \tag{A-1}$$

Thus, the equivalent assertion is the boundedness of the functional

$$\langle \nabla_\kappa \otimes u^T : \nabla_\kappa \otimes u \rangle_B = \langle \nabla_\kappa \otimes u : \nabla_\kappa \otimes u \rangle_B. \tag{A-2}$$

We prove first of all that the integral of the square of divergence of $u(x)$ is bounded:

$$\nabla_\kappa \cdot u = (\nabla_\kappa \cdot u + u \cdot \nabla_\kappa \rho_\kappa / \rho_\kappa) - u \cdot \nabla_\kappa \rho_\kappa / \rho_\kappa$$
$$\implies (\nabla_\kappa \cdot u)^2 \le 2(\nabla_\kappa \cdot u + u \cdot \nabla_\kappa \rho_\kappa / \rho_\kappa)^2 + 2(u \cdot \nabla_\kappa \rho_\kappa / \rho_\kappa)^2$$
$$\le \frac{2}{\underline{K}_\kappa} K_\kappa (\nabla_\kappa \cdot u + u \cdot \nabla_\kappa \rho_\kappa / \rho_\kappa)^2 + 2(|\nabla_\kappa \rho_\kappa|^2 / \rho_\kappa^3) \rho_\kappa u \cdot u$$
$$\implies \langle (\nabla_\kappa \cdot u)^2 \rangle_B \le \frac{2}{\underline{K}_\kappa} R\{u\} + 2(|\nabla_\kappa \rho_\kappa|^2 / \rho_\kappa^3)_{\max} \|u\|^2. \tag{A-3}$$

Further we make use of some formulas of tensor analysis and calculations similar to those in deriving the well-known Kelvin formula:

$$\nabla_\kappa \cdot (\nabla_\kappa \otimes \boldsymbol{u}^T \cdot \boldsymbol{u}) = \nabla_\kappa \otimes \boldsymbol{u}^T : \nabla_\kappa \otimes \boldsymbol{u} + \boldsymbol{u} \cdot \left(\nabla_\kappa \cdot (\nabla_\kappa \otimes \boldsymbol{u}^T) \right)$$

$$= \nabla_\kappa \otimes \boldsymbol{u}^T : \nabla_\kappa \otimes \boldsymbol{u} + \boldsymbol{u} \cdot \nabla_\kappa (\nabla_\kappa \cdot \boldsymbol{u})$$

$$= \nabla_\kappa \otimes \boldsymbol{u}^T : \nabla_\kappa \otimes \boldsymbol{u} + \nabla_\kappa \cdot \left(\boldsymbol{u}(\nabla_\kappa \cdot \boldsymbol{u}) \right) - (\nabla_\kappa \cdot \boldsymbol{u})^2$$

$$\implies \langle \nabla_\kappa \otimes \boldsymbol{u}^T : \nabla_\kappa \otimes \boldsymbol{u} \rangle_B = \langle (\nabla_\kappa \cdot \boldsymbol{u})^2 \rangle_B + \langle \boldsymbol{n}_\kappa \cdot \nabla_\kappa \otimes \boldsymbol{u}^T \cdot \boldsymbol{u} \rangle_{\partial B} - \langle (\boldsymbol{n}_\kappa \cdot \boldsymbol{u}) \nabla_\kappa \cdot \boldsymbol{u} \rangle_{\partial B}$$

$$= \langle (\nabla_\kappa \cdot \boldsymbol{u})^2 \rangle_B + \langle \boldsymbol{u} \cdot \nabla_\kappa \otimes \boldsymbol{u} \cdot \boldsymbol{n}_\kappa \rangle_{\partial B}. \tag{A-4}$$

On smooth pieces of the boundary ∂B

$$\boldsymbol{u}(\boldsymbol{x}) \cdot \boldsymbol{n}_\kappa(\boldsymbol{x}) = 0 \implies d\boldsymbol{u} \cdot \boldsymbol{n}_\kappa + \boldsymbol{u} \cdot d\boldsymbol{n}_\kappa = 0. \tag{A-5}$$

Hence, for any tangential vector $\boldsymbol{y}$ the following equalities hold:

$$\boldsymbol{y} \cdot \nabla_\kappa \otimes \boldsymbol{u} \cdot \boldsymbol{n}_\kappa = -\boldsymbol{y} \cdot \nabla_\kappa^\Sigma \otimes \boldsymbol{n}_\kappa \cdot \boldsymbol{u}, \quad \boldsymbol{y} \perp \boldsymbol{n}_\kappa \implies \boldsymbol{u} \cdot \nabla_\kappa \otimes \boldsymbol{u} \cdot \boldsymbol{n}_\kappa = -\boldsymbol{u} \cdot \nabla_\kappa^\Sigma \otimes \boldsymbol{n}_\kappa \cdot \boldsymbol{u}. \tag{A-6}$$

Thus, taking into account the assumption of piecewise convexity of the boundary, we obtain

$$\langle \nabla_\kappa \otimes \boldsymbol{u}^T : \nabla_\kappa \otimes \boldsymbol{u} \rangle_B = \langle (\nabla_\kappa \cdot \boldsymbol{u})^2 \rangle_B - \langle \boldsymbol{u} \cdot \nabla_\kappa^\Sigma \otimes \boldsymbol{n}_\kappa \cdot \boldsymbol{u} \rangle_{\partial B} \leq \langle (\nabla_\kappa \cdot \boldsymbol{u})^2 \rangle_B, \tag{A-7}$$

that, with regard for equalities (A-1), (A-2) and inequality (A-3), proves the assertion.

We remark that condition of piecewise convexity here is only a sufficient condition, not a necessary one.

Appendix B. Outline of the proof of modified spectral theorem

In this appendix there will be stated in detail only the elements of the proof of formulated in the work modified spectral theorem, which differ significantly from the corresponding elements of the proof of classical spectral theorem for elastic bodies (see, for example, Gurtin 1972; Mikhlin 1964). These significant distinctions are related to the presence of an infinite-dimensional subspace of neutral perturbations N_0 (on which $\lambda = \omega^2 = 0$), and also to nonstandard boundary conditions (free sliding over a nonplane surface).

We consider first of all the variational problem of the infimum of functional $\Psi\{\boldsymbol{u}\}$ (5-22) on nonzero elements of the space N formed by all kinematically admissible fields $\boldsymbol{u}(\boldsymbol{x})$:

$$\boldsymbol{u}(\boldsymbol{x}) \in N \iff \boldsymbol{u}(\boldsymbol{x}) \cdot \boldsymbol{n}_\kappa(\boldsymbol{x})|_{\partial B} = 0. \tag{B-1}$$

From the canonical form (5-31) of the functional $R\{\boldsymbol{u}\}$ it is obvious that the infimum is equal to zero and is attained on nonzero fields $\boldsymbol{u}_0(\boldsymbol{x})$ forming the subspace N_0 (5-32). For what follows it should be proved that the fields $\boldsymbol{u}_0(\boldsymbol{x})$ are the solutions of linearized equilibrium equations (equations (5-16), (5-19) for $\lambda = \omega^2 = 0$ with boundary conditions (5-18)). We will analyze the inequality

$$R\{\boldsymbol{u}\} \geq R\{\boldsymbol{u}_0\} = 0, \quad \forall \boldsymbol{u} \in N, \tag{B-2}$$

not excluding $\boldsymbol{u} = \boldsymbol{0}$. We represent $\boldsymbol{u}$ as follows:

$$\boldsymbol{u} = \alpha \boldsymbol{u}_0 + \tilde{\boldsymbol{u}}, \quad -\infty < \alpha < \infty, \quad \tilde{\boldsymbol{u}} \in N, \tag{B-3}$$

$$R\{\alpha \boldsymbol{u}_0 + \tilde{\boldsymbol{u}}\} = \alpha^2 R\{\boldsymbol{u}_0\} + 2\alpha \mathcal{R}\{\tilde{\boldsymbol{u}}, \boldsymbol{u}_0\} + R\{\tilde{\boldsymbol{u}}\} = 2\alpha \mathcal{R}\{\tilde{\boldsymbol{u}}, \boldsymbol{u}_0\} + R\{\tilde{\boldsymbol{u}}\} \geq 0, \quad \forall \alpha$$

$$\implies \quad \mathcal{R}\{\tilde{\boldsymbol{u}}, \boldsymbol{u}_0\} = 0, \quad \forall \tilde{\boldsymbol{u}} \in N. \tag{B-4}$$

The initial equality (5-23) for the functional $\mathcal{R}\{\tilde{\boldsymbol{u}}, \boldsymbol{u}_0\}$ will be used:

$$\mathcal{R}\{\tilde{\boldsymbol{u}}, \boldsymbol{u}_0\} = \langle \nabla_\kappa \otimes \tilde{\boldsymbol{u}} : \boldsymbol{C}_\kappa : \nabla_\kappa \otimes \boldsymbol{u}_0 \rangle_B + \langle \rho_\kappa \tilde{\boldsymbol{u}} \cdot \nabla_\kappa \otimes \nabla_\kappa \varphi \cdot \boldsymbol{u}_0 \rangle_B - \langle (\boldsymbol{n}_\kappa \cdot \boldsymbol{T}_\kappa \cdot \boldsymbol{n}_\kappa) \tilde{\boldsymbol{u}} \cdot \nabla_\kappa^\Sigma \otimes \boldsymbol{n}_\kappa \cdot \boldsymbol{u}_0 \rangle_{\partial B}$$

$$= 0,$$

$$\nabla_\kappa \otimes \tilde{\boldsymbol{u}} : \boldsymbol{C}_\kappa : \nabla_\kappa \otimes \boldsymbol{u}_0 = \nabla_\kappa \cdot \left((\boldsymbol{C}_\kappa : \nabla_\kappa \otimes \boldsymbol{u}_0) \cdot \tilde{\boldsymbol{u}} \right) - \left(\nabla_\kappa \cdot (\boldsymbol{C}_\kappa : \nabla_\kappa \otimes \boldsymbol{u}_0) \right) \cdot \tilde{\boldsymbol{u}}$$

$$\implies \left\langle -\tilde{\boldsymbol{u}} \cdot \left(\nabla_\kappa \cdot (\boldsymbol{C}_\kappa : \nabla_\kappa \otimes \boldsymbol{u}_0) - \rho_\kappa \nabla_\kappa \otimes \nabla_\kappa \varphi \cdot \boldsymbol{u}_0 \right) \right\rangle_{\partial B}$$

$$+ \left\langle \left(\boldsymbol{n}_\kappa \cdot \boldsymbol{C}_\kappa : \nabla_\kappa \otimes \boldsymbol{u}_0 - (\boldsymbol{n}_\kappa \cdot \boldsymbol{T}_\kappa \cdot \boldsymbol{n}_\kappa) \nabla_\kappa^\Sigma \otimes \boldsymbol{n}_\kappa \cdot \boldsymbol{u}_0 \right) \cdot \tilde{\boldsymbol{u}} \right\rangle_{\partial B} = 0$$

$$\implies \mathcal{A}(\boldsymbol{u}_0) = \nabla_\kappa \cdot (\boldsymbol{C}_\kappa : \nabla_\kappa \otimes \boldsymbol{u}_0) - \rho_\kappa \nabla_\kappa \otimes \nabla_\kappa \varphi \cdot \boldsymbol{u}_0 = 0, \quad \boldsymbol{x} \in B,$$

$$(\boldsymbol{n}_\kappa \cdot \boldsymbol{C}_\kappa \cdot \nabla_\kappa \otimes \boldsymbol{u}_0) \cdot (\boldsymbol{I} - \boldsymbol{n}_\kappa \otimes \boldsymbol{n}_\kappa) - (\boldsymbol{n}_\kappa \cdot \boldsymbol{T}_\kappa \cdot \boldsymbol{n}_\kappa) \nabla_\kappa^\Sigma \otimes \boldsymbol{n}_\kappa \cdot \boldsymbol{u}_0 = 0, \quad \boldsymbol{x} \in \partial B.$$

Thus, the fulfillment of the linearized equations of equilibrium and boundary conditions on the subspace N_0 is proved (in other words, it is proved that the elements of the subspace N_0 are the neutral perturbations).

Now we pass to the problem of infimum of the functional $\Psi\{\boldsymbol{u}\}$ (5-22) on the subspace $N_0^\perp$ (5-33). From the canonical form of the functional $R\{\boldsymbol{u}\}$ (5-27), (5-31) it is obvious that the infimum does exist and is nonnegative. Moreover, from the compactness of the subsets of subspace $N_0^\perp$, bounded both in value of $R\{\boldsymbol{u}\}$ and in the norm $\|\boldsymbol{u}\|$ (5-36) (that is proved in Appendix A), it follows that it is attained at an extremal $\boldsymbol{u}_1(\boldsymbol{x}) \in N_0^\perp$:

$$\lambda_1 = \inf_{\substack{\boldsymbol{u} \neq \boldsymbol{0} \\ \boldsymbol{u} \in N_0^\perp}} \Psi\{\boldsymbol{u}\} = \Psi\{\boldsymbol{u}_1\} \geq 0. \tag{B-5}$$

Making use of the canonical form of $R\{\boldsymbol{u}\}$ together with existence of an extremal, it is not difficult to prove that

$$\lambda_1 > 0. \tag{B-6}$$

Indeed, assume that $\lambda_1 = 0$. Then it follows from (5-31) that

$$\nabla_\kappa \cdot (\rho_\kappa \boldsymbol{u}) = \nabla_\kappa \cdot (\rho_\kappa \nabla_\kappa \gamma) = 0, \quad \boldsymbol{n}_\kappa \cdot \nabla_\kappa \gamma |_{\partial B} = 0$$

$$\implies \nabla_\kappa \cdot (\gamma \rho_\kappa \nabla_\kappa \gamma) = \rho_\kappa \nabla_\kappa \gamma \cdot \nabla_\kappa \gamma$$

$$\implies \langle \rho_\kappa \nabla_\kappa \gamma \cdot \nabla_\kappa \gamma \rangle_B = \langle \gamma \rho_\kappa \boldsymbol{n}_\kappa \cdot \nabla_\kappa \gamma \rangle_{\partial B} = 0 \implies \nabla_\kappa \gamma \equiv 0. \tag{B-7}$$

The contradiction obtained proves the positivity of λ_1 (B-6).

Now it is to be proved that the field $\boldsymbol{u}_1(\boldsymbol{x})$ is a free vibration mode, i.e. an eigenvector of operator $\mathcal{A}$ with eigenvalue $\lambda_1 = \omega_1^2$, satisfying not only the kinematic boundary conditions of the tangentiality

at the boundary of the domain ∂B (5-17), but also the free sliding condition, whose linearized form is given by (5-18). In the proof, we again use the initial form of the functional $R\{u\}$ (5-20).

The condition for minimality of the functional $\Psi\{u\}$ (B-1) is equivalent to the following inequality:

$$R\{u\} \geq \lambda_1 \langle \rho_\kappa u \cdot u \rangle_B, \quad \forall u \in N_0^\perp, \tag{B-8}$$

the value $u = 0$ being not excluded. We represent u as follows:

$$u = \alpha u_1 + \tilde{u}, \quad -\infty < \alpha < \infty, \quad \tilde{u} \in N_0^\perp. \tag{B-9}$$

Substituting u (B-9) into (B-8), we obtain

$$\alpha^2(R\{u_1\} - \lambda_1 \langle \rho_\kappa u_1 \cdot u_1 \rangle_B) + 2\alpha(\mathcal{R}\{\tilde{u}, u_1\} - \lambda_1 \langle \rho_\kappa \tilde{u} \cdot u_1 \rangle_B) + R\{\tilde{u}\} - \lambda_1 \langle \rho_\kappa \tilde{u} \cdot \tilde{u} \rangle_B \geq 0,$$
$$\forall \tilde{u} \in N_0^\perp, \quad \forall \alpha. \tag{B-10}$$

It is obvious that the first term is equal to zero, the third term is nonnegative and does not depend on α. Hence, for satisfaction of the inequality (B-6) due to arbitrariness of α it is necessary and sufficient that the following equality be valid:

$$\mathcal{R}\{\tilde{u}, u_1\} - \lambda_1 \langle \rho_\kappa \tilde{u} \cdot u_1 \rangle_B = 0, \quad \forall \tilde{u} \in N_0^\perp.$$

Taking into account that (B-4) implies the equality

$$\mathcal{R}\{u_0, u_1\} = 0, \quad \forall u_0 \in N_0,$$

and also taking into account the orthogonality of the subspaces N_0 (5-32) and $N_0^\perp$ (5-33), we obtain a stronger equality:

$$\mathcal{R}\{\tilde{u}, u_1\} - \lambda_1 \langle \rho_\kappa \tilde{u} \cdot u_1 \rangle_B = 0, \quad \forall \tilde{u} \in N. \tag{B-11}$$

Repeating the calculations used earlier in the analysis of the equality (B-4), we obtain from (B-11) both the equality

$$\lambda_1 \rho_\kappa u_1 = \mathcal{A}(u_1), \quad x \in B, \tag{B-12}$$

and boundary conditions (5-18):

$$(n_\kappa \cdot C_\kappa : \nabla_\kappa \otimes u_1) \cdot (I - n_\kappa \otimes n_\kappa) - (n_\kappa \cdot T_\kappa \cdot n_\kappa)\nabla_\kappa^\Sigma \otimes n_\kappa \cdot u_1 = 0, \quad x \in \partial B,$$

which means the following: $u_1(x)$ is a free vibration mode of the system with the frequency $\omega_1 = \sqrt{\lambda_1}$. Subsequently, as in the standard proof of the spectral theorem in linear elasticity, it is assumed that the assertion of the spectral theorem is valid for the first $m - 1$ eigenvectors and it is proved (by means of the reasoning completely analogous to the preceding one) that the next extremal (with number m) on the subspace $N_{m-1}^\perp$ also satisfies the equality

$$\mathcal{R}\{\tilde{u}, u_m\} - \lambda_m \langle \rho_\kappa \tilde{u} \cdot u_m \rangle_B = 0, \quad \forall \tilde{u} \in N_{m-1}^\perp, \quad \lambda_m \geq \lambda_{m-1}, \quad u_m \in N_{m-1}^\perp. \tag{B-13}$$

From the preceding steps it followed that for each $k < m$

$$\mathcal{R}\{\tilde{u}, u_k\} - \lambda_k \langle \rho_\kappa \tilde{u} \cdot u_k \rangle_B = 0, \quad \forall \tilde{u} \in N,$$
$$\implies \mathcal{R}\{u_k, u_m\} - \lambda_k \langle \rho_\kappa u_k \cdot u_m \rangle_B = \mathcal{R}\{u_k, u_m\} = 0, \quad k = 0, 1, \ldots, m - 1, \tag{B-14}$$
$$\implies \mathcal{R}\{\tilde{u}, u_m\} - \lambda_m \langle \rho_\kappa \tilde{u} \cdot u_m \rangle_B = 0, \quad \forall \tilde{u} \in N.$$

From (B-14) follows the validity of both the equality

$$\lambda_m \rho_\kappa \boldsymbol{u}_m = \mathcal{A}(\boldsymbol{u}_m), \quad \boldsymbol{x} \in B, \tag{B-15}$$

and the boundary conditions (5-18)

$$(\boldsymbol{n}_\kappa \cdot \boldsymbol{C}_\kappa : \nabla_\kappa \otimes \boldsymbol{u}_m) \cdot (\boldsymbol{I} - \boldsymbol{n}_\kappa \otimes \boldsymbol{n}_\kappa) - (\boldsymbol{n}_\kappa \cdot \boldsymbol{T}_\kappa \cdot \boldsymbol{n}_\kappa) \nabla_\kappa^\Sigma \otimes \boldsymbol{n}_\kappa \cdot \boldsymbol{u}_m = 0, \quad \boldsymbol{x} \in \partial B. \tag{B-16}$$

Thus, $\boldsymbol{u}_m(\boldsymbol{x})$ is the free vibration mode with frequency $\omega_m = \sqrt{\lambda_m}$.

The proof of the remaining assertions of the spectral theorem reduces to standard reasoning (see, for example, Gurtin 1972; Mikhlin 1964) with the use of proved in Appendix A the compactness of subsets of space $N_0^\perp$ bounded both in values of $R\{\boldsymbol{u}\}$ and in the norm $\|\boldsymbol{u}\|$ (5-36).

Appendix C. Proof of the comparison theorem

We introduce the scalar products of two Hilbert spaces corresponding to two different bulk-elastic media occupying the identical domains (denoted by the same symbol B):

$$\widetilde{\mathcal{M}}^{(j)}\{\boldsymbol{w}, \boldsymbol{w}'\} := \left\langle \frac{1}{\rho^{(j)}} \boldsymbol{w} \cdot \boldsymbol{w}' \right\rangle_B, \quad j = 1, 2, \tag{C-1}$$

$$\widetilde{M}^{(j)}\{\boldsymbol{w}\} := \widetilde{\mathcal{M}}^{(j)}\{\boldsymbol{w}, \boldsymbol{w}\}, \tag{C-2}$$

$$\widetilde{\Psi}^{(j)}\{\boldsymbol{w}\} = \frac{\widetilde{R}^{(j)}\{\boldsymbol{w}\}}{\widetilde{M}^{(j)}\{\boldsymbol{w}\}}. \tag{C-3}$$

For each of the systems the divergenceless fields $\boldsymbol{w}(\boldsymbol{x})$ satisfying the kinematic boundary conditions $\boldsymbol{w} \cdot \boldsymbol{n}_\kappa|_{\partial B} = 0$ form a common infinite-dimensional subspace $\widetilde{N}_0$ on which $\widetilde{R}^{(j)}\{\boldsymbol{w}\} = 0$ and $\widetilde{\Psi}^{(j)}\{\boldsymbol{w}\} = 0$. From the spectral theorem for each of the systems it follows that on its own orthogonal complement to the subspace $\widetilde{N}_0$ there exists its own discrete set of eigenvectors orthogonal in the sense of its own scalar product $\widetilde{\mathcal{M}}^{(j)}\{\boldsymbol{w}, \boldsymbol{w}'\}$. We denote the orthogonal complements to the subspace $\widetilde{N}_0$ in the sense of scalar products $\widetilde{\mathcal{M}}^{(j)}$ as $(\widetilde{N}_0^{(j)})^\perp$, and the orthogonal complements in $(\widetilde{N}_0^{(j)})^\perp$ to the subspaces $\widetilde{N}_m^{(j)}$ spanned by the first m eigenvectors as $(\widetilde{N}_m^{(j)})^\perp$. The eigenvectors will be denoted $\boldsymbol{w}_k^{(j)}$. Then we have

$$\widetilde{N}_m^{(j)} = \mathrm{span}(\boldsymbol{w}_1^{(j)}, \ldots, \boldsymbol{w}_m^{(j)}), \tag{C-4}$$

$$\lambda_{m+1}^{(j)} = \inf_{\substack{\boldsymbol{w} \neq 0 \\ \boldsymbol{w} \in (\widetilde{N}_m^{(j)})^\perp}} \widetilde{\Psi}^{(j)}\{\boldsymbol{w}\} = \widetilde{\Psi}^{(j)}\{\boldsymbol{w}_{m+1}^{(j)}\}. \tag{C-5}$$

The space $\widetilde{N}$ of all kinematically admissible fields can be represented in two ways as a direct sum of subspaces:

$$\widetilde{N} = \widetilde{N}_0 \oplus \widetilde{N}_m^{(j)} \oplus (\widetilde{N}_m^{(j)})^\perp, \quad j = 1, 2, \tag{C-6}$$

where $\widetilde{N}_0$ and $(\widetilde{N}_m^{(j)})^\perp$ are infinite-dimensional subspaces, and $\widetilde{N}_m^{(j)}$ are finite-dimensional ones:

$$\dim \widetilde{N}_m^{(j)} = m. \tag{C-7}$$

Consider the values of the functional $\widetilde{\Psi}^{(2)}\{\boldsymbol{w}\}$ on the "alien" subspace $(\widetilde{N}_m^{(1)})^\perp$, having in mind to prove

that there exists a nonzero vector $\boldsymbol{v}$ in it for which

$$\widetilde{\Psi}^{(2)}\{\boldsymbol{v}\} \leq \lambda_{m+1}^{(2)}. \tag{C-8}$$

For this purpose we prove that there exists a nonzero vector $\boldsymbol{v}$ such that

$$\boldsymbol{v} \in (\widetilde{N}_m^{(1)})^\perp, \quad \boldsymbol{v} \in \mathrm{span}(\widetilde{N}_0, \widetilde{N}_{m+1}^{(2)}). \tag{C-9}$$

Consider a basis of the subspace $\widetilde{N}_{m+1}^{(2)}$ consisting of orthogonal (in the sense of $\widetilde{\mathcal{M}}^{(2)}$) eigenvectors $\boldsymbol{w}_1^{(2)}, \ldots, \boldsymbol{w}_{m+1}^{(2)}$. Normalizing them in the sense of the same scalar product, we denote the corresponding orthonormal basis $(\boldsymbol{e}_1, \ldots, \boldsymbol{e}_{m+1})$. Due to the expansion (C-6), each of the vectors $\boldsymbol{e}_i$ can be uniquely represented in the form of the following sum:

$$\boldsymbol{e}_i = \boldsymbol{g}_i + \boldsymbol{h}_i + \boldsymbol{f}_i = \boldsymbol{g}_i + \boldsymbol{g}_i', \quad i = 1, \ldots, m+1,$$
$$\boldsymbol{g}_i \in \widetilde{N}_0, \quad \boldsymbol{h}_i \in \widetilde{N}_m^{(1)}, \quad \boldsymbol{f}_i \in (\widetilde{N}_m^{(1)})^\perp. \tag{C-10}$$

In order to prove that the vectors $(\boldsymbol{g}_1', \ldots, \boldsymbol{g}_{m+1}')$ are linearly independent, we assume that their linear combination is equal to zero:

$$\alpha_1 \boldsymbol{g}_1' + \cdots + \alpha_{m+1} \boldsymbol{g}_{m+1}' = 0 \implies \alpha_1 \boldsymbol{e}_1 + \cdots + \alpha_{m+1} \boldsymbol{e}_{m+1} = \alpha_1 \boldsymbol{g}_1 + \cdots + \alpha_{m+1} \boldsymbol{g}_{m+1}$$
$$\implies \alpha_1 \boldsymbol{e}_1 + \cdots + \alpha_{m+1} \boldsymbol{e}_{m+1} = 0$$
$$\implies \alpha_i = 0, \quad i = 1, \ldots, m+1.$$

Thus, the linear independence of the vectors $(\boldsymbol{g}_1', \ldots, \boldsymbol{g}_{m+1}')$ is proved. Consider now once again their linear combination

$$\sum_{i=1}^{m+1} \alpha_i \boldsymbol{g}_i' = \sum_{i=1}^{m+1} \alpha_i \boldsymbol{h}_i + \sum_{i=1}^{m+1} \alpha_i \boldsymbol{f}_i. \tag{C-11}$$

Since $\boldsymbol{h}_i \in \widetilde{N}_m^{(1)}$, which is m-dimensional subspace, the vectors $(\boldsymbol{h}_1, \ldots, \boldsymbol{h}_{m+1})$ are linearly dependent; hence, there exists a set of numbers $(\alpha_1, \ldots, \alpha_{m+1})$, not all equal to zero, and such that

$$\sum_{i=1}^{m+1} \alpha_i \boldsymbol{h}_i = 0, \tag{C-12}$$

$$\implies \boldsymbol{v} := \sum_{i=1}^{m+1} \alpha_i \boldsymbol{g}_i' = \sum_{i=1}^{m+1} \alpha_i \boldsymbol{f}_i \neq 0, \tag{C-13}$$

$$\implies \sum_{i=1}^{m+1} \alpha_i \boldsymbol{e}_i - \sum_{i=1}^{m+1} \alpha_i \boldsymbol{g}_i = \sum_{i=1}^{m+1} \alpha_i \boldsymbol{f}_i,$$
$$-\boldsymbol{\gamma} := \sum_{i=1}^{m+1} \alpha_i \boldsymbol{g}_i \in \widetilde{N}_0, \quad \sum_{i=1}^{m+1} \alpha_i \boldsymbol{e}_i \in \widetilde{N}_{m+1}^{(2)}, \quad \sum_{i=1}^{m+1} \alpha_i \boldsymbol{f}_i \in (\widetilde{N}_m^{(1)})^\perp. \tag{C-14}$$

Thus, it is proved that there exists a nonzero vector $\boldsymbol{v} \in (\widetilde{N}_m^{(1)})^\perp$ such that

$$\boldsymbol{v} = \boldsymbol{\gamma} + \sum_{i=1}^{m+1} \alpha_i \boldsymbol{e}_i \tag{C-15}$$

$$\implies \widetilde{\Psi}^{(2)}\{\boldsymbol{v}\} = \frac{\widetilde{R}^{(2)}\big\{\boldsymbol{\gamma} + \sum_{i=1}^{m+1} \alpha_i \boldsymbol{e}_i\big\}}{\widetilde{M}^{(2)}\big\{\boldsymbol{\gamma} + \sum_{i=1}^{m+1} \alpha_i \boldsymbol{e}_i\big\}} = \frac{\sum_{i=1}^{m+1} \alpha_i^2 \lambda_i^{(2)}}{\widetilde{M}^{(2)}\{\boldsymbol{\gamma}\} + \sum_{i=1}^{m+1} \alpha_i^2} \le \lambda_{m+1}^{(2)}. \tag{C-16}$$

Due to the assumption regarding the functionals $\widetilde{\Psi}^{(i)}\{\boldsymbol{w}\}$ we have

$$\widetilde{\Psi}^{(1)}\{\boldsymbol{v}\} \le \widetilde{\Psi}^{(2)}\{\boldsymbol{v}\} \le \lambda_{m+1}^{(2)} \tag{C-17}$$

$$\implies \lambda_{m+1}^{(1)} = \inf_{\substack{\boldsymbol{w} \ne 0 \\ \boldsymbol{w} \in (\widetilde{N}_m^{(1)})^\perp}} \widetilde{\Psi}^{(1)}\{\boldsymbol{w}\} \le \widetilde{\Psi}^{(1)}\{\boldsymbol{v}\} \le \lambda_{m+1}^{(2)}. \tag{C-18}$$

which completes the proof.

References

[Gaziev and Kopachevsky 2013] E. L. Gaziev and N. D. Kopachevsky, "Small motions and eigenoscillations of a 'fluid-barotropic gas' hydrodynamic system", *Ukr. Mat. Visn.* **10**:1 (2013), 16–53. In Russian; translated in *J. Math. Sci.* **192**:4 (2013), 389–416.

[Gurtin 1972] M. E. Gurtin, "The linear theory of elasticity", pp. 1–295 in *Encyclopedia of physics*, vol. VI a/2, Springer, Berlin, 1972.

[Horgan 1995] C. O. Horgan, "Korn's inequalities and their applications in continuum mechanics", *SIAM Rev.* **37**:4 (1995), 491–511.

[Horgan and Chan 1999] C. O. Horgan and A. M. Chan, "Vibration of inhomogeneous strings, rods and membranes", *J. Sound Vib.* **225**:3 (1999), 503–513.

[Landau and Lifshitz 1987] L. D. Landau and E. M. Lifshitz, *Fluid mechanics*, Course of Theoretical Physics **6**, Butterworth-Heinemann, Oxford, 1987.

[Mikhlin 1964] S. G. Mikhlin, *Variational methods in mathematical physics*, Pergamon Press, Oxford, 1964.

[Ryzhak 1993] E. I. Ryzhak, "On stable deformation of 'unstable' materials in a rigid triaxial testing machine", *J. Mech. Phys. Solids* **41**:8 (1993), 1345–1356.

[Ryzhak 1994] E. I. Ryzhak, "On stability of homogeneous elastic bodies under boundary conditions weaker than displacement conditions", *Quart. J. Mech. Appl. Math.* **47** (1994), 663–672.

[Ryzhak 1997] E. I. Ryzhak, "Estimates for the frequencies of natural oscillations of homogeneous anisotropic bodies with a fixed boundary", *Prikl. Mat. Mekh.* **61**:4 (1997), 679–691. In Russian; translated in *J. Appl. Math. Mech.* **61**:4 (1997), 659-669.

[Ryzhak 1999] E. I. Ryzhak, "Korn's constant for a parallelepiped with a free face or pair of faces", *Math. Mech. Solids* **4**:1 (1999), 35–55.

[Ryzhak et al. 2017] E. I. Ryzhak, S. A. Mukhamediev, and S. V. Sinyukhina, "Conditions of stability and instability for a pair of arbitrarily stratified compressible fluids in an arbitrary non-uniform gravity field", *Int. J. Non-Linear Mech.* **96** (2017), 36–45.

[Truesdell 1972] C. Truesdell, *A first course in rational continuum mechanics*, Johns Hopkins University, Baltimore, 1972.

EUGENE I. RYZHAK: e_i_ryzhak@mail.ru
O. Schmidt Institute of Physics of the Earth, Russian Academy of Sciences, 10, B. Gruzinskaya St., Moscow, 123242, Russia

SVETLANA V. SINYUKHINA: sinyus@yandex.ru
O. Schmidt Institute of Physics of the Earth, Russian Academy of Sciences, 10, B. Gruzinskaya St., Moscow, 123242, Russia

■
■■msp

A MODIFIED SHEAR-LAG MODEL FOR PREDICTION OF
STRESS DISTRIBUTION IN UNIDIRECTIONAL FIBROUS COMPOSITES
CONSIDERING INTERPHASE

MOHAMMAD HASSAN ZARE AND MEHDI MONDALI

A modified shear-lag model is developed for unidirectional fibrous composites by considering the interphase region subjected to axial loading. A perfect bond at the fiber/interphase and interphase/matrix interfaces is assumed. The fiber, interphase, and matrix materials behave elastically during the analysis. The axial and shear stresses in fiber, interphase and matrix are analytically obtained as functions of the radial and axial directions using a micromechanical approach in a full-continuum model. The composite axial displacement and composite elastic modulus also are obtained. In order to consider the effect of inhomogeneity of the interphase in the three-phase micromechanics model, the elastic modulus of the interphase is assumed to vary with the radial coordinate. Two case studies, a carbon nanotube-reinforced polymer composite and an aramid fiber-reinforced rubber composite are used to validate the results of the model. The results predicted by the proposed analytical approach exhibited good agreement with the finite element results and available experimental measurements.

1. Introduction

The mechanical properties of composite materials are affected by geometrical factors and the structural behavior of the composite constituents [Fu et al. 2008; Lauke 2006]. In many composites reinforced by continuous or discontinuous fibers, there is also an interphase region which transmits the load between the matrix and fiber like a bridge. The interphase is an important constituent with significant effects on the performance of fiber-reinforced composites [Yang and Pitchumani 2004]. One concern during the modeling of the interphase region is its dimensional specifications and physical properties, which can be provided through experimental methods. Typical examples of composite materials having interphase regions are polymer composites reinforced with carbon nanotubes (CNTs) and hybrid fiber-reinforced rubber composites.

Several numerical studies have been conducted to investigate the effects of interphase mechanical properties on stress transfer of fiber-reinforced composites [Maligno et al. 2010; Wang et al. 2006; 2011]. Because of the importance of and wide applications for nanocomposites, numerical modeling using full-continuum or semicontinuum models has been the goal of many researchers. In full-continuum models, the material of the interphase region behaves as a continuum with constant or variable mechanical properties. In semicontinuum models, the interphase region consists of a regular set of spring elements which make the modeling and solution complicated and time-consuming [Wan et al. 2005; Needleman et al. 2010; Hernández-Pérez and Avilés 2010; Golestanian and Shojaie 2010; Kumar and Srinivas 2014; Rafiee and Pourazizi 2015]. Kumar and Srinivas [2014] used a three-phase finite element (FE) model to

analyze the effect of interphase properties on the elastic modulus of nanocomposites. The effect of CNT functionalization on the properties of interphase regions has been studied by Rafiee and Pourazizi [2015]. In their model, the interaction between CNTs and polymer in the interphase region was simulated using the semicontinuum approach.

Analytical methods can also be used to consider the effect of the interphase region in a unit cell. However, the complexity of the solution has meant that analytical studies have primarily been carried out without considering the interphase region [Muki and Sternberg 1970; Lawrence 1972; Takaku and Arridge 1973; Luk and Keer 1979; Budiansky et al. 1986; Kerans and Parthasarathy 1991; Abedian et al. 2007; Gao and Li 2005; Haque and Ramasetty 2005; Ang and Ahmed 2013]. The most well-known analytical model for describing the load transfer mechanism from matrix to reinforcement in fibrous composites is the shear-lag model presented by Cox [1952] and subsequently modified by others [Dow 1963; Rosen 1964; Nair and Kim 1992; Hsueh 1995]. In this theory, the load applied to the matrix is transferred to reinforcements through its cylindrical walls.

In comparison with models such as those by Tsai [Halpin 1984] and Eshelby [Taya and Arsenault 1987; Withers et al. 1989], the shear-lag model more comprehensively describes the load transfer mechanism from matrix to reinforcement; thus, researchers have tried to overcome the shortcomings of this model [Gao and Li 2005; Ang and Ahmed 2013; Nairn 1997; Zhao and Ji 1997; Beyerlein and Landis 1999; Zhang and He 2008]. Studies have also been conducted stress analysis of fibrous composites based on elasticity theory. Abedian et al. [2007] presented a micromechanics model to determine the elastic stress field in fiber-reinforced composites. In this model, the shear stress was obtained as a function of both radial and axial directions using the exact solution of the displacement fields in the matrix and reinforcement.

One shortcoming of the shear-lag model is its inability to consider the interphase region, but consideration of this region is required for improving the accuracy of analysis. Yao et al. [2013] investigated the effect of a graded interphase on the mechanism of stress transfer in a fiber reinforced composite using an improved shear-lag model with simple assumptions. The inhomogeneity of the interphase in their model was represented by the graded feature of the Young's modulus, which is graded according to a power law or a linear law in the radius direction.

Researchers have recently used the shear-lag model for CNT-reinforced polymer composites and hybrid fiber-reinforced rubber composites using the representative volume element [Gao and Li 2005; Haque and Ramasetty 2005; Liu and Chen 2003; Zhang et al. 2017]. Gao and Li [2005] developed a two-phase shear-lag model for CNT-reinforced polymer composites using a multiscale approach. Haque and Ramasetty [2005] analyzed a two-phase continuous fiber model of CNT-reinforced polymer composites to predict the interfacial axial and shear stresses.

The interface properties of CNT-reinforced composites were determined by Ang and Ahmed [2013] using an improved shear-lag model. The analytical results obtained by Ang and Ahmed were used to investigate the stress sustainability of CNT-reinforced polymer composites. Recently, a shear-lag model for stress analysis in hybrid fiber-reinforced rubber composites was presented by Zhang et al. [2017]; however, the model cannot determine the radial dependence of shear and axial stresses in the fiber and matrix.

The present study micromechanically analyzed unidirectional fibrous composites by considering the interphase region using a new modified shear-lag model. All stress components, including the shear and

axial stresses, in the fiber, interphase and matrix have been analytically obtained as functions of both the radial and axial directions. In order to consider the effect of inhomogeneity of the interphase, it was assumed that interphase properties such as elastic modulus will vary with the variation of the unit cell radius. To validate the results of the proposed model, two case studies on CNT-reinforced polymer composites and aramid fiber-reinforced rubber composites are presented to provide practical applications for this model.

The proposed model can also be applied for stress analysis of short fiber composites considering the interphase, which has not been addressed by other researchers thus far. The imaginary fiber technique was chosen to analyze the stress field in short fiber composites. In this method, the unit cell is divided into two regions (I and II) along the model length [Abedian et al. 2007; Hsueh 1988; 1990; 1992; 2000; Hsueh et al. 1997; Mondali and Abedian 2013]. Region I consists of the fiber and matrix and region II is the matrix material. The stress field in region I is determined first. The relations obtained for the stress field in region I can be used in region II if the mechanical properties of the fiber are replaced by the mechanical properties of the matrix in these relations. In fact, because the matrix along the fiber in region II is an "imaginary" fiber, this technique is known as the imaginary fiber technique.

The relation constants can be determined using appropriate continuity conditions on the common boundary of regions I and II. The significant difference and novelty of the present study with respect to the state-of-the-art is its ability to carry out stress analysis on the short fiber composites with interphase regions. It is necessary to note that application of the present model to short fiber composites and development of a modified imaginary fiber technique is currently being undertaken and the related articles will be published in the future.

2. Analytical method

2.1. *RVE modeling.* Analysis of the three-phase micromechanics unit cell was carried out using a full-continuum model. A continuous cylindrical fiber with radius r_f and length of $2l_f$ is surrounded by an interphase region with radius r_{ip} and thickness t_i. The interphase region is homogeneously and isotropically located between matrix and fiber, see Figure 1 (left).

The cylindrical polar coordinate system (r, θ, z) was used with the origin at the center of the unit cell. Geometrical symmetry, loading, and boundary conditions meant that analysis of three-phase model RVE could be performed only on the half length of l_m outside radius r_m in a 2D axisymmetric model of the unit cell, see Figure 1 (right). The following assumptions were made for the purpose of analysis:
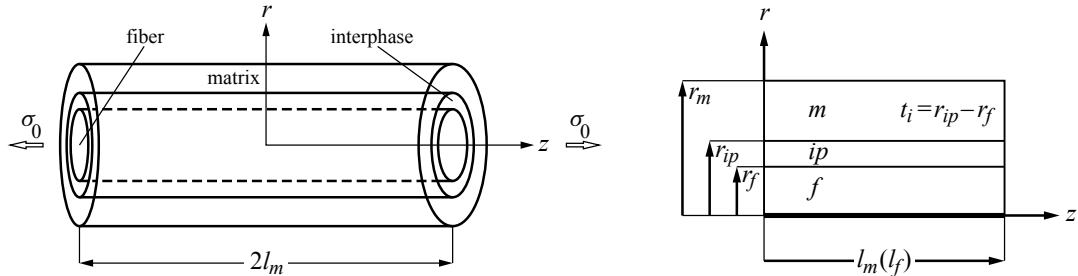
Figure 1. The three-phase model of RVE: 3D model (left) and 2D axisymmetric model (right).

(1) Interphase properties such as the elastic modulus vary with the unit cell radius.

(2) The fiber, matrix and interphase behave elastically.

(3) The analytical model is based on the shear-lag theory assuming a perfect bond at the fiber-interphase and interphase-matrix interfaces.

(4) Body and bonding forces are neglected in equilibrium equations.

(5) Partial derivatives of radial displacement relative to z are neglected [Gao and Li 2005; Yao et al. 2013].

2.2. *Governing equations and boundary conditions.* Governing equilibrium equations for axisymmetric problem in cylindrical coordinate are obtained as [Timoshenko and Goodier 1970]

$$\frac{\partial \sigma_{rr}^{\eta}}{\partial r} + \frac{\partial \tau_{rz}^{\eta}}{\partial z} + \frac{\sigma_{rr}^{\eta} - \sigma_{\theta\theta}^{\eta}}{r} = 0, \tag{1}$$

$$\frac{\partial \tau_{rz}^{\eta}}{\partial r} + \frac{\partial \sigma_{zz}^{\eta}}{\partial z} + \frac{\tau_{rz}^{\eta}}{r} = 0, \tag{2}$$

where superscript η is a variable that denotes the fiber, interphase, and matrix regions.

The constitutive equations of stress-strain for an isotropic material are

$$\varepsilon_{rr}^{\eta} = \frac{1}{E_{\eta}}[\sigma_{rr}^{\eta} - \nu_{\eta}(\sigma_{\theta\theta}^{\eta} + \sigma_{zz}^{\eta})], \tag{3}$$

$$\varepsilon_{\theta\theta}^{\eta} = \frac{1}{E_{\eta}}[\sigma_{\theta\theta}^{\eta} - \nu_{\eta}(\sigma_{rr}^{\eta} + \sigma_{zz}^{\eta})], \tag{4}$$

$$\varepsilon_{zz}^{\eta} = \frac{1}{E_{\eta}}[\sigma_{zz}^{\eta} - \nu_{\eta}(\sigma_{rr}^{\eta} + \sigma_{\theta\theta}^{\eta})], \tag{5}$$

$$\gamma_{rz}^{\eta} = \frac{\tau_{rz}^{\eta}}{G_{\eta}}. \tag{6}$$

Strain-displacement relations (geometrical equations) for axisymmetric problem are also given by

$$\varepsilon_{rr}^{\eta} = \frac{\partial u^{\eta}}{\partial r}, \tag{7}$$

$$\varepsilon_{\theta\theta}^{\eta} = \frac{u^{\eta}}{r}, \tag{8}$$

$$\varepsilon_{zz}^{\eta} = \frac{\partial w^{\eta}}{\partial z}, \tag{9}$$

$$\gamma_{rz}^{\eta} = \frac{\partial u^{\eta}}{\partial z} + \frac{\partial w^{\eta}}{\partial r}. \tag{10}$$

In the above relations, σ_{rr}^{η}, $\sigma_{\theta\theta}^{\eta}$, σ_{zz}^{η}, and τ_{rz}^{η} are the radial, circumferential, axial, and shear stresses, respectively. Also, ε_{rr}^{η}, $\varepsilon_{\theta\theta}^{\eta}$, ε_{zz}^{η}, and γ_{rz}^{η} are the radial, circumferential, axial, and shear strains components. Moreover, u^{η} and w^{η} are the radial and axial displacements and E_{η}, ν_{η}, and G_{η} are Young modulus, Poisson's ratio, and shear modulus of an isotropic material, respectively.

In such a problem, the applied boundary conditions are [Abedian et al. 2007]

$$\tau_{rz}^{f}(r_f) = \tau_{rz}^{ip}(r_f) = \tau_1, \tag{11}$$

$$\tau_{rz}^{ip}(r_{ip}) = \tau_{rz}^{m}(r_{ip}) = \tau_2, \tag{12}$$

$$\tau_{rz}^{m}(r_m) = 0, \tag{13}$$

$$\overline{\sigma_{zz}^{m}}(\pm l_m) = \sigma_0, \tag{14}$$

$$\sigma_{rr}^{m}(r_m) = 0, \tag{15}$$

$$\sigma_{rr}^{f}(r_f) = \sigma_{rr}^{ip}(r_f), \tag{16}$$

$$\sigma_{rr}^{ip}(r_{ip}) = \sigma_{rr}^{m}(r_{ip}). \tag{17}$$

2.3. *Obtaining the shear stresses in fiber, interphase, and matrix.* The shear-lag relation for fiber can be obtained by integration of equilibrium (2) with respect to r from 0 to r_f as [Gao and Li 2005]

$$\frac{\partial \overline{\sigma_{zz}^{f}}}{\partial z} = -\frac{2\tau_1}{r_f}, \tag{18}$$

where $\overline{\sigma_{zz}^{f}}$ is the average axial normal stress over the cross-section of the effective fiber and τ_1 is the fiber-interphase interface shear stress.

Because $\partial \sigma_{zz}^{f}/\partial z$ in (2) is a function of z, by applying (11), the fiber shear stress as a function of r can be obtained as [Abedian et al. 2007]

$$\tau_{rz}^{f} = \frac{r}{r_f}\tau_1. \tag{19}$$

Then the shear-lag relation of the interphase is obtained by integration of (2) with respect to r from r_f to r_{ip} as

$$\frac{\partial \overline{\sigma_{zz}^{ip}}}{\partial z} = -\frac{2}{(r_{ip}^2 - r_f^2)}(r_{ip}\tau_2 - r_f\tau_1), \tag{20}$$

where $\overline{\sigma_{zz}^{ip}}$ is the average axial normal stress over the cross-section of the interphase and τ_2 is the interphase-matrix interface shear stress.

Similarly taking into account that $\partial \sigma_{zz}^{ip}/\partial z$ in (2) is a function of z and applying (11) and (12), the interphase shear stress as a function of r can be obtained as

$$\tau_{rz}^{ip} = \frac{\tau_1 r_f(r_{ip}^2 - r^2) + \tau_2 r_{ip}(r^2 - r_f^2)}{r(r_{ip}^2 - r_f^2)}. \tag{21}$$

As stated, equations (12) and (13) can be used to obtain the matrix shear stress as a function of r as [Abedian et al. 2007]

$$\tau_{rz}^{m} = \frac{r_{ip}}{(r_m^2 - r_{ip}^2)}\left(\frac{r_m^2}{r} - r\right)\tau_2. \tag{22}$$

However, the interfacial shear stresses $\tau_1(z)$ and $\tau_2(z)$ in (19), (21), and (22) are still unknown functions of z. Therefore, substituting (22) into (6) and (10), and then integrating with respect to r from r_{ip}

to r_m will yield

$$\tau_2 = G_m \frac{(r_m^2 - r_{ip}^2)}{r_{ip}[r_m^2 \ln(r_m/r_{ip}) - \frac{1}{2}(r_m^2 - r_{ip}^2)]} (w_{r_m}^m - w_{r_{ip}}^m), \tag{23}$$

where $w_{r_{ip}}^m$ and $w_{r_m}^m$ are the matrix axial displacements at r_{ip} and r_m, respectively.

Also, by substituting (23) into (21) and then substituting the obtained equation into (6) and (10), τ_1 can be expressed by integrating with respect to r from r_f to r_{ip} as

$$\tau_1 = \frac{G_{ip}(r_{ip}^2 - r_f^2)}{r_f[r_{ip}^2 \ln(r_{ip}/r_f) - \frac{1}{2}(r_{ip}^2 - r_f^2)]} (w_{r_{ip}}^{ip} - w_{r_f}^{ip})$$
$$+ \left[\frac{G_m[r_f^2 \ln(r_{ip}/r_f) - \frac{1}{2}(r_{ip}^2 - r_f^2)]}{[r_m^2 \ln(r_m/r_{ip}) - \frac{1}{2}(r_m^2 - r_{ip}^2)]} \times \frac{(r_m^2 - r_{ip}^2)(w_{r_m}^m - w_{r_{ip}}^m)}{r_f[r_{ip}^2 \ln(r_{ip}/r_f) - \frac{1}{2}(r_{ip}^2 - r_f^2)]} \right], \tag{24}$$

where $w_{r_f}^{ip}$ and $w_{r_{ip}}^{ip}$ are the interphase axial displacements at r_f and r_{ip}, respectively.

In this case, the terms $\partial u^\eta / \partial z$ for the matrix and interphase are neglected according to the assumption that $\partial u^\eta / \partial z \ll \partial w^\eta / \partial r$, which is reasonable because of the tensile loading condition and the symmetry of the model.

Finally, substituting (23) into (22) gives the matrix shear stress as

$$\tau_{rz}^m = G_m \frac{(w_{r_m}^m - w_{r_{ip}}^m)}{[r_m^2 \ln(r_m/r_{ip}) - \frac{1}{2}(r_m^2 - r_{ip}^2)]} \left(\frac{r_m^2}{r} - r \right). \tag{25}$$

Also, substituting (23) and (24) into (21) gives the interphase shear stress as

$$\tau_{rz}^{ip} = \left(\frac{r_{ip}^2}{r} - r \right) [A(w_{r_{ip}}^{ip} - w_{r_f}^{ip}) + B(w_{r_m}^m - w_{r_{ip}}^m)] + C \left(r - \frac{r_f^2}{r} \right) (w_{r_m}^m - w_{r_{ip}}^m), \tag{26}$$

where the constants A, B, and C are given as

$$A = \frac{G_{ip}}{\left(r_{ip}^2 \ln(r_{ip}/r_f) - \frac{1}{2}(r_{ip}^2 - r_f^2) \right)},$$
$$B = \frac{G_m(r_m^2 - r_{ip}^2)\left(r_f^2 \ln(r_{ip}/r_f) - \frac{1}{2}(r_{ip}^2 - r_f^2) \right)}{(r_{ip}^2 - r_f^2)\left(r_{ip}^2 \ln(r_{ip}/r_f) - \frac{1}{2}(r_{ip}^2 - r_f^2) \right)\left(r_m^2 \ln(r_m/r_{ip}) - \frac{1}{2}(r_m^2 - r_{ip}^2) \right)}, \tag{27}$$
$$C = \frac{G_m(r_m^2 - r_{ip}^2)}{(r_{ip}^2 - r_f^2)\left(r_m^2 \ln(r_m/r_{ip}) - \frac{1}{2}(r_m^2 - r_{ip}^2) \right)}.$$

2.4. *Obtaining the axial stresses in matrix and interphase.* In this section, $w^m(r, z)$, the matrix axial displacement, is determined first. Substituting (25) into (6) and (10), and then integrating with respect to r from r_{ip} to r will yield

$$w^m(r, z) = w_{r_{ip}}^m + \frac{r_m^2 \ln(r/r_{ip}) - \frac{1}{2}(r^2 - r_{ip}^2)}{\left(r_m^2 \ln(r_m/r_{ip}) - \frac{1}{2}(r_m^2 - r_{ip}^2) \right)} (w_{r_m}^m - w_{r_{ip}}^m). \tag{28}$$

Next, assuming that the radial and circumferential stresses in the matrix are much smaller than the axial stress $[(\sigma_{rr}^{\eta} + \sigma_{\theta\theta}^{\eta}) \ll \sigma_{zz}^{\eta}]$, one can neglect the term $(\sigma_{rr}^{\eta} + \sigma_{\theta\theta}^{\eta})$ in comparison with σ_{zz}^{η} in (5). Therefore, substituting (28) into (9) and using (5) give the matrix axial stress as

$$\sigma_{zz}^m = \sigma_{r_{ip}}^m + \frac{r_m^2 \ln(r/r_{ip}) - \frac{1}{2}(r^2 - r_{ip}^2)}{\left(r_m^2 \ln(r_m/r_{ip}) - \frac{1}{2}(r_m^2 - r_{ip}^2)\right)} (\sigma_{r_m}^m - \sigma_{r_{ip}}^m), \tag{29}$$

where $\sigma_{r_{ip}}^m$ and $\sigma_{r_m}^m$ are the matrix axial stresses at r_{ip} and r_m, respectively.

Similarly, $w^{ip}(r, z)$, the interphase axial displacement, can be determined by substituting (26) into (6) and (10), and integrating with respect to r from r_f to r as

$$w^{ip}(r, z) = w_{r_f}^{ip} + \frac{\left(r_{ip}^2 \ln(r/r_f) - \frac{1}{2}(r^2 - r_f^2)\right)}{G_{ip}} \left(A(w_{r_{ip}}^{ip} - w_{r_f}^{ip}) + B(w_{r_m}^m - w_{r_{ip}}^m)\right)$$
$$+ \frac{C\left(\frac{1}{2}(r^2 - r_f^2) - r_f^2 \ln(r/r_f)\right)}{G_{ip}} (w_{r_m}^m - w_{r_{ip}}^m). \tag{30}$$

When E_{ip} is a constant, equation (30) reduces to the value reported by Zhang and He [2008]. Therefore, the average axial displacement of the interphase, $\overline{w^{ip}}(r, z)$, is

$$\overline{w^{ip}}(r, z) = w_{r_f}^{ip} + (w_{r_m}^m - w_{r_{ip}}^m) \frac{E_m(1 + \nu_{ip})}{E_{ip}(1 + \nu_m)} \left(\frac{\lambda_2\lambda_4 - \lambda_1\lambda_5}{\lambda_1\lambda_3}\right) + \frac{\lambda_4}{\lambda_1}(w_{r_{ip}}^{ip} - w_{r_f}^{ip}), \tag{31}$$

where

$$\lambda_1 = \frac{r_{ip}^2}{r_{ip}^2 - r_f^2} \ln\frac{r_{ip}}{r_f} - \frac{1}{2}, \qquad \lambda_2 = \frac{r_f^2}{r_{ip}^2 - r_f^2} \ln\frac{r_{ip}}{r_f} - \frac{1}{2}, \qquad \lambda_3 = \frac{r_m^2}{r_m^2 - r_{ip}^2} \ln\frac{r_m}{r_{ip}} - \frac{1}{2},$$

$$\lambda_4 = \frac{r_{ip}^4 \ln(r_{ip}/r_f) - \frac{1}{4}(3r_{ip}^2 - r_f^2)(r_{ip}^2 - r_f^2)}{(r_{ip}^2 - r_f^2)^2}, \qquad \lambda_5 = \frac{r_{ip}^2 r_f^2 \ln(r_{ip}/r_f) - \frac{1}{4}(r_{ip}^4 - r_f^4)}{(r_{ip}^2 - r_f^2)^2}. \tag{32}$$

Finally, substituting (30) into (9) and using (5) give the interphase axial stress as

$$\sigma_{zz}^{ip} = \sigma_{r_f}^{ip} + \frac{\left(r_{ip}^2 \ln(r/r_f) - \frac{1}{2}(r^2 - r_f^2)\right)}{G_{ip}} \left(A(\sigma_{r_{ip}}^{ip} - \sigma_{r_f}^{ip}) + B\frac{E_{ip}}{E_m}(\sigma_{r_m}^m - \sigma_{r_{ip}}^m)\right)$$
$$+ C\left(\frac{1}{2}(r^2 - r_f^2) - r_f^2 \ln(r/r_f)\right)\frac{2(1 + \nu_{ip})}{E_m}(\sigma_{r_m}^m - \sigma_{r_{ip}}^m), \tag{33}$$

where $\sigma_{r_f}^{ip}$ and $\sigma_{r_{ip}}^{ip}$ are the interphase axial stresses at r_f and r_{ip}, respectively.

2.5. *Obtaining the elastic modulus of the composite.* The effective Young's modulus of the composite, E_c, can be determined as

$$E_c = \frac{\sigma_0}{w/l_m}, \tag{34}$$

where w is the matrix axial displacement of the unit cell at $z = l_m$.

To determine w at $z = l_m$, the matrix axial displacement as a function of z must be determined. Here, using (6) and (10) and assuming that $\partial u^\eta / \partial z \ll \partial w^\eta / \partial r$ one can obtain

$$\tau_{rz}^m = G_m \frac{\partial w^m}{\partial r} \longrightarrow w^m = \frac{1}{G_m} \int \tau_{rz}^m \, dr. \tag{35}$$

Now, to determine τ_{rz}^m as a function of z, the average axial stress in the fiber and interphase as functions of z should be obtained first. Hence, substituting (24) into shear-lag equation, (18), and differentiating the resultant equation using (5) and (9) with respect to z yields

$$\frac{d^2(\overline{\sigma_{zz}^f})}{dz^2} - \lambda^2 \overline{\sigma_{zz}^f} = \alpha \, \overline{\sigma_{zz}^{ip}} + \beta \sigma_0. \tag{36}$$

Similarly, substituting (23) and (24) into (20) and differentiating the resultant equation with respect to z yield

$$\frac{d^2 \overline{\sigma_{zz}^{ip}}}{dz^2} - \bar{\lambda}^2 \overline{\sigma_{zz}^{ip}} = \bar{\alpha} \, \overline{\sigma_{zz}^f} + \bar{\beta} \sigma_0, \tag{37}$$

where

$$\alpha = -2 \left(\frac{r_{ip}^2}{r_f^2} - 1 \right) \left(\frac{A}{E_{ip}} - \frac{B}{E_m} \chi_1 \chi_2 \right), \qquad \bar{\alpha} = \frac{2(C-B)}{E_m} r_f^2 \chi_1 - \frac{2A}{E_f},$$

$$\beta = -2 \left(\frac{r_{ip}^2}{r_f^2} - 1 \right) \frac{B}{E_m} r_m^2 \chi_1, \qquad \bar{\beta} = -\frac{2(C-B)}{E_m} r_m^2 \chi_1, \tag{38}$$

$$\lambda = \left[2 \left(\frac{r_{ip}^2}{r_f^2} - 1 \right) \left(\frac{A}{E_f} + \frac{B}{E_m} r_f^2 \chi_1 \right) \right]^{1/2}, \qquad \bar{\lambda} = \left(\frac{2(C-B)}{E_m} \chi_1 \chi_2 + \frac{2A}{E_{ip}} \right)^{1/2},$$

in terms of the parameters

$$\chi_1 = \frac{\left(r_m^2 \ln(r_m/r_{ip}) - \frac{1}{2}(r_m^2 - r_{ip}^2) \right)}{\left(r_m^4 \ln(r_m/r_{ip}) - \frac{1}{4}(r_m^2 - r_{ip}^2)(3r_m^2 - r_{ip}^2) \right)}, \qquad \chi_2 = r_{ip}^2 - r_f^2 + \frac{E_m}{E_{ip}} (r_m^2 - r_{ip}^2). \tag{39}$$

It should be noted that when the interphase layer thickness is set to zero, i.e. $r_{ip} - r_f = 0$, substituting (24) into (18) and differentiating with respect to z reduce (36) and (37) to (40) which is the same as that of Gao and Li [2005]:

$$\frac{d^2 \overline{\sigma_{zz}^f}}{dz^2} - \lambda^2 \overline{\sigma_{zz}^f} = -\lambda^2 \frac{r_m^2}{r_f^2 + \frac{E_m}{E_f}(r_m^2 - r_f^2)} \sigma_0. \tag{40}$$

In this equation, the average axial stress in fiber $\overline{\sigma_{zz}^f}$ and interfacial shear stress τ_1 can be obtained with the same form as those given by Gao and Li [2005].

Using (36) and (37), one can obtain a fourth-order characteristic equation as

$$m^4 - (\lambda^2 + \bar{\lambda}^2) m^2 + (\lambda^2 \bar{\lambda}^2 - \alpha \bar{\alpha}) = 0. \tag{41}$$

In order to obtain the shear and axial stresses in all three phases, the roots of the characteristic equation should be obtained first. The characteristic equation has four distinct real roots for which negative values are not feasible. The positive values of the roots can be calculated as follows:

$$m_1 = \sqrt{\frac{(\lambda^2 + \bar{\lambda}^2) + \sqrt{(\lambda^2 - \bar{\lambda}^2)^2 + 4\alpha\bar{\alpha}}}{2}}, \qquad m_2 = \sqrt{\frac{(\lambda^2 + \bar{\lambda}^2) - \sqrt{(\lambda^2 - \bar{\lambda}^2)^2 + 4\alpha\bar{\alpha}}}{2}}. \qquad (42)$$

Solve (36) and (37) for fiber and interphase average axial stresses:

$$\overline{\sigma_{zz}^f} = c_1 e^{m_1 z} + c_2 e^{-m_1 z} + c_3 e^{m_2 z} + c_4 e^{-m_2 z} + \frac{\bar{\beta}\alpha - \bar{\lambda}^2\beta}{\lambda^2\bar{\lambda}^2 - \alpha\bar{\alpha}}\sigma_0, \qquad (43)$$

$$\overline{\sigma_{zz}^{ip}} = \frac{m_1^2 - \lambda^2}{\alpha}(c_1 e^{m_1 z} + c_2 e^{-m_1 z}) + \frac{m_2^2 - \lambda^2}{\alpha}(c_3 e^{m_2 z} + c_4 e^{-m_2 z}) - \frac{\bar{\beta}\lambda^2 - \beta\bar{\alpha}}{\lambda^2\bar{\lambda}^2 - \alpha\bar{\alpha}}\sigma_0. \qquad (44)$$

Substitute (43) into (18) to obtain the shear stress at the interface between the fiber and interphase as

$$\tau_1 = -\frac{r_f}{2}\left(m_1(c_1 e^{m_1 z} - c_2 e^{-m_1 z}) + m_2(c_3 e^{m_2 z} - c_4 e^{-m_2 z})\right). \qquad (45)$$

Also, substituting (44) and (45) into (20) gives the shear stress at the interface between interphase and matrix as

$$\tau_2 = -\frac{m_1}{2r_{ip}\alpha}\left((r_{ip}^2 - r_f^2)(m_1^2 - \lambda^2) + \alpha r_f^2\right)(c_1 e^{m_1 z} - c_2 e^{-m_1 z})$$
$$-\frac{m_2}{2r_{ip}\alpha}\left((r_{ip}^2 - r_f^2)(m_2^2 - \lambda^2) + \alpha r_f^2\right)(c_3 e^{m_2 z} - c_4 e^{-m_2 z}). \qquad (46)$$

Next, the shear stresses in fiber, interphase, and matrix are obtained by substituting (45) and (46) into (19), (21), and (22), respectively:

$$\tau_{rz}^f(r, z) = -\frac{r}{2}\left(m_1(c_1 e^{m_1 z} - c_2 e^{-m_1 z}) + m_2(c_3 e^{m_2 z} - c_4 e^{-m_2 z})\right), \qquad (47)$$

$$\tau_{rz}^{ip}(r, z) = -\frac{(c_1 e^{m_1 z} - c_2 e^{-m_1 z})}{2(r_{ip}^2 - r_f^2)\alpha}\left[m_1\left(r - \frac{r_f^2}{2}\right)\left((r_{ip}^2 - r_f^2)(m_1^2 - \lambda^2) + \alpha r_f^2\right) + m_1 r_f^2 \alpha\left(\frac{r_{ip}^2}{r} - r\right)\right]$$
$$-\frac{(c_3 e^{m_2 z} - c_4 e^{-m_2 z})}{2(r_{ip}^2 - r_f^2)\alpha}\left[m_2\left(r - \frac{r_f^2}{r}\right)\left((r_{ip}^2 - r_f^2)(m_2^2 - \lambda^2) + \alpha r_f^2\right) + m_2 r_f^2 \alpha\left(\frac{r_{ip}^2}{r} - r\right)\right], \qquad (48)$$

$$\tau_{rz}^m(r, z) = -\frac{(r_m^2/r - r)}{2\alpha(r_m^2 - r_{ip}^2)}\left[m_1(c_1 e^{m_1 z} - c_2 e^{-m_1 z})\left((r_{ip}^2 - r_f^2)(m_1^2 - \lambda^2) + \alpha r_f^2\right)\right.$$
$$\left. + m_2(c_3 e^{m_2 z} - c_4 e^{-m_2 z})\left((r_{ip}^2 - r_f^2)(m_2^2 - \lambda^2) + \alpha r_f^2\right)\right]. \qquad (49)$$

Because the average axial stresses of the fiber, matrix and interphase at $z = l_m$ are equal to applied stress σ_0 and interfacial shear stresses τ_1 and τ_2 are equal to zero at the center of the unit cell ($z = 0$),

Material	Young's modulus (GPa)	Poisson's ratio
Carbon nanotube	1000	0.28
Polymer matrix	2.5	0.3
Interphase	10	0.3

Table 1. Mechanical properties of the materials used in the model [Kumar and Srinivas 2014].

the constants c_1 to c_4 can be determined as

$$c_1 = c_2 = \frac{\frac{m_2^2 - \lambda^2}{\alpha}\left(1 - \frac{\bar{\beta}\alpha - \bar{\lambda}^2\beta}{\lambda^2\bar{\lambda}^2 - \alpha\bar{\alpha}}\right) - \frac{\bar{\beta}\lambda^2 - \beta\bar{\alpha}}{\lambda^2\bar{\lambda}^2 - \alpha\bar{\alpha}} - 1}{(e^{m_1 l_m} + e^{-m_1 l_m})\frac{m_2^2 - m_1^2}{\alpha}}\, \sigma_0, \tag{50}$$

$$c_3 = c_4 = \frac{1 - \frac{m_1^2 - \lambda^2}{\alpha}\left(1 - \frac{\bar{\beta}\alpha - \bar{\lambda}^2\beta}{\lambda^2\bar{\lambda}^2 - \alpha\bar{\alpha}}\right) + \frac{\bar{\beta}\lambda^2 - \beta\bar{\alpha}}{\lambda^2\bar{\lambda}^2 - \alpha\bar{\alpha}}}{(e^{m_2 l_m} + e^{-m_2 l_m})\frac{m_2^2 - m_1^2}{\alpha}}\, \sigma_0. \tag{51}$$

Finally, substituting (49) into (35) and integrating with respect to r from r_{ip} to r_m, gives the matrix axial displacement. Its value at $z = l_m$ is

$$w = \frac{r_m^2 \ln r_{ip} - r_{ip}^2/2}{2\alpha G_m (r_m^2 - r_{ip}^2)}\big[m_1 c_1 (e^{m_1 l_m} - e^{-m_1 l_m})\big((r_{ip}^2 - r_f^2)(m_1^2 - \lambda^2) + \alpha r_f^2\big)$$
$$+ m_2 c_3 (e^{m_2 l_m} - e^{-m_2 l_m})\big((r_{ip}^2 - r_f^2)(m_2^2 - \lambda^2) + \alpha r_f^2\big)\big]. \tag{52}$$

3. Results and discussion

Two case studies of composite materials having interphase regions were considered to examine the validity of the present analytical model. The composite materials were CNT-reinforced polymer composites (CNTRC) and aramid fiber reinforced rubber composites (AFRC). The results obtained using the proposed analytical modeling was compared with available experimental studies and with the results of the FE model in ABAQUS software. Moreover, the effect of the geometrical factors and mechanical properties of the constituents were investigated for each case study.

3.1. *Case study 1 (CNTRC).* In this case study, capped nanotube is replaced by a solid cylindrical fiber with flat ends [Gao and Li 2005]. The elastic modulus of CNT is $E_{\mathrm{CNT}} = 1000\,\mathrm{GPa}$ while the effective elastic modulus of fiber is determined as $E_f = 1006\,\mathrm{GPa}$ [Gao and Li 2005; Ang and Ahmed 2013]. The dimensions of RVE are taken to be $r_f = 0.471\,\mathrm{nm}$ and $r_m = 5r_f$ where r_f and r_m are the fiber and matrix radii, respectively [Gao and Li 2005]. Also, the nanotube thickness is $t_{\mathrm{CNT}} = 0.34\,\mathrm{nm}$ though the interphase thickness can be determined versus nanotube thickness as $t_i/t_{\mathrm{CNT}} = 1$ [Hernández-Pérez and Avilés 2010]. Other required mechanical specifications are represented in Table 1.

3.1.1. *Analytical model validation.* The analytical results were validated by FE simulation of a full-continuum three-phase model as shown in Figure 1. The analytical and FE results of the normalized average axial stress in the fiber and matrix and normalized shear stress at the interface between the fiber and interphase versus the normalized length of the fiber are presented in Figures 2 and 3. Good
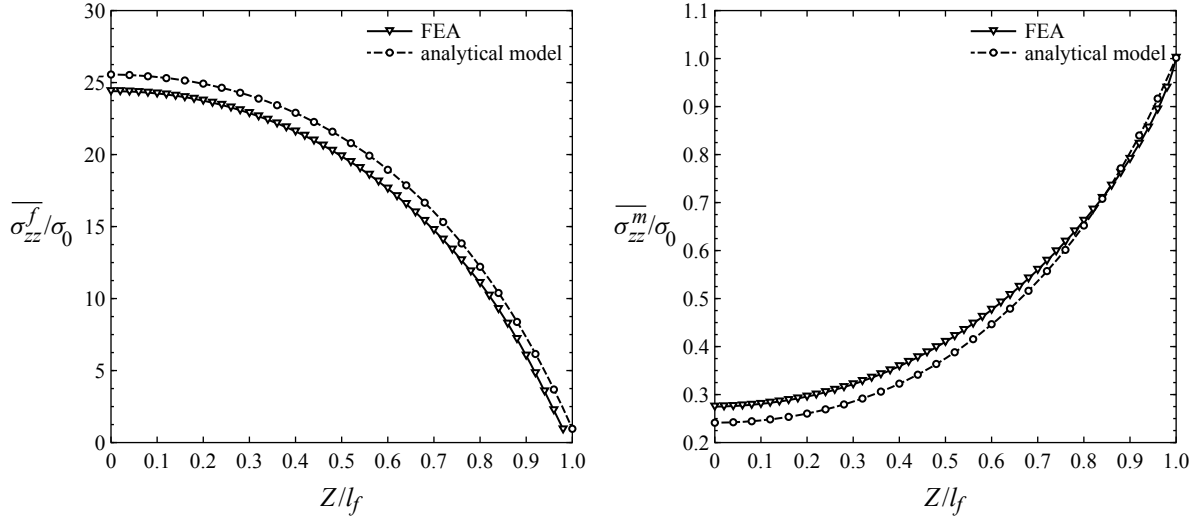
Figure 2. Analytical and FEA results of normalized average axial stress in fiber (left) and matrix (right) versus normalized fiber length.
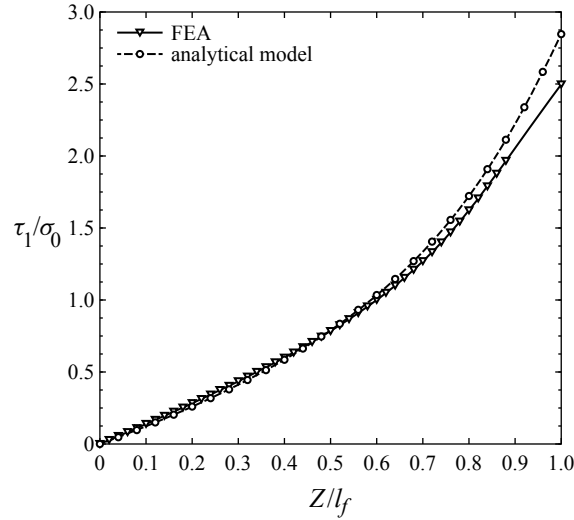
Figure 3. Analytical and FEA results of normalized shear stress at the interface between fiber and interphase versus normalized length of fiber.

agreement was found between the analytical and numerical predictions for these stress components, which demonstrates the capability of the proposed analytical model.

Validation was also done by calculating the axial elastic modulus of the composite normalized by the matrix elastic modulus and comparing it with the results presented by Hernández-Pérez and Avilés [2010]. Figure 4 shows the influence of interphase thickness on the elastic modulus of the composite. As seen, the modulus of the CNTRC strongly depends on the thickness of the interphase. The maximum
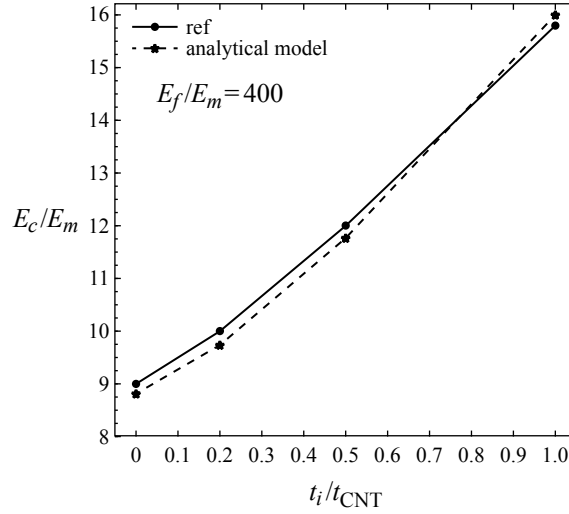
Figure 4. Axial elastic modulus of composite versus interphase thickness. The reference curve (solid) is from [Kumar and Srinivas 2014].

value for the CNTRC elastic modulus was obtained at a thickness ratio equal to one, i.e. $t_i/t_{\text{CNT}} = 1$. This result has been confirmed by other researchers [Wan et al. 2005].

Now, the influence of effective parameters such as fiber aspect ratio, matrix-to-nanotube modulus ratio and inhomogeneity of the interphase are investigated to determine the analytical modeling accuracy.

3.1.2. *Effect of fiber aspect ratio.* The average axial stresses of fiber and interphase normalized by the applied stress σ_0 in four different aspect ratios along the fiber length are presented in Figure 5.
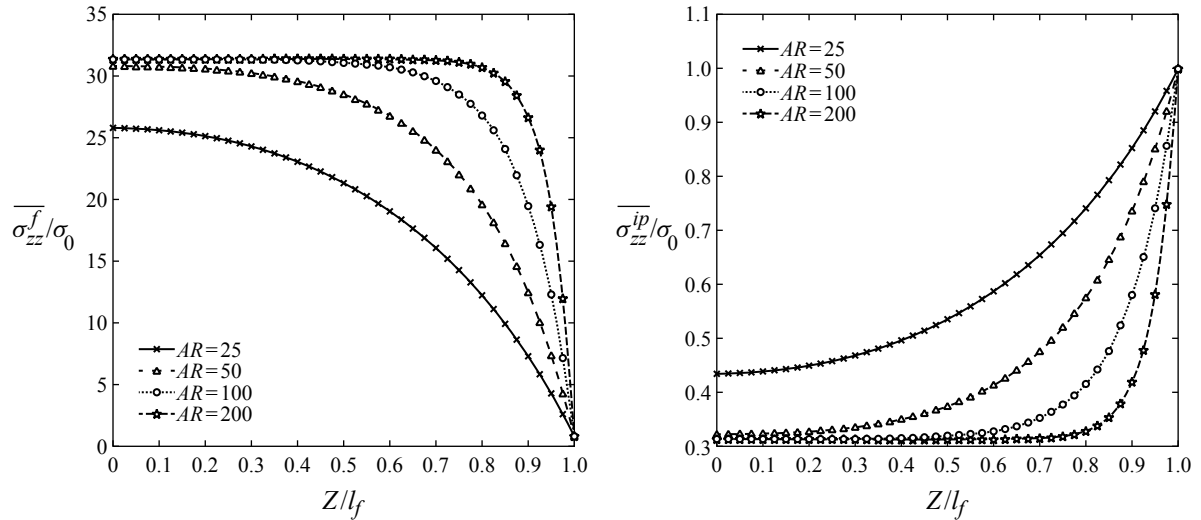
Figure 5. Normalized axial stress in fiber (left) and in interphase (right) versus normalized length of fiber for various aspect ratios.
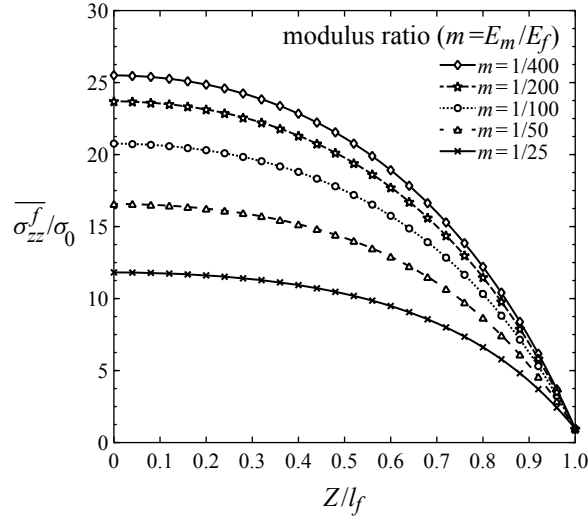
Figure 6. Normalized average axial stress of CNT along the fiber length in five different ratios of matrix to fiber elastic modulus.

As shown, the axial stress in the fiber increased as the aspect ratio increased and the axial stress in interphase decreased as aspect ratio increased. It can be concluded that more loads are transmitted to the fiber at high aspect ratios.

3.1.3. *Effects of the ratio of matrix to fiber elastic modulus.* The average axial stress of the fiber and the interfacial shear stress of the fiber-interphase along the fiber length are presented for five ratios of matrix to fiber elastic modulus, $m = E_m/E_f$. Figure 6 shows the average axial stress of the fiber normalized by applied stress σ_0 along the fiber length.

The figure shows that a decrease in the modulus ratio will increase the axial stress of the CNTs, which indicates that more loads have been transmitted to the fiber. The interfacial shear stress of the fiber-interphase normalized by applied stress σ_0 along the fiber length is shown in Figure 7.

As mentioned, based on shear-lag theory, the interfacial shear stress of fiber-interphase τ_1 increase with a decrease in the modulus ratio. Hence, the CNTs will be stronger at lower values of m and the load capacity will increase. There are no significant differences between the results of the axial and shear stresses of CNTs for values of m smaller than 1/200. In addition, if the elastic modulus of the fiber and matrix are equal ($m \approx 1$), the axial stress of the fiber will be equal to applied stress σ_0, which suggests that reinforcement has no effect on composite strength.

3.1.4. *Effect of inhomogeneous interphase.* In order to investigate the effect of an inhomogeneous interphase on the stress transfer mechanism in a three-phase micromechanics model, the interphase Young's modulus was considered to be an exponential function of r as

$$E_{ip}(r) = Pe^{-Qr}, \tag{53}$$

where P and Q are material constants obtained by applying the continuity condition of the modulus at
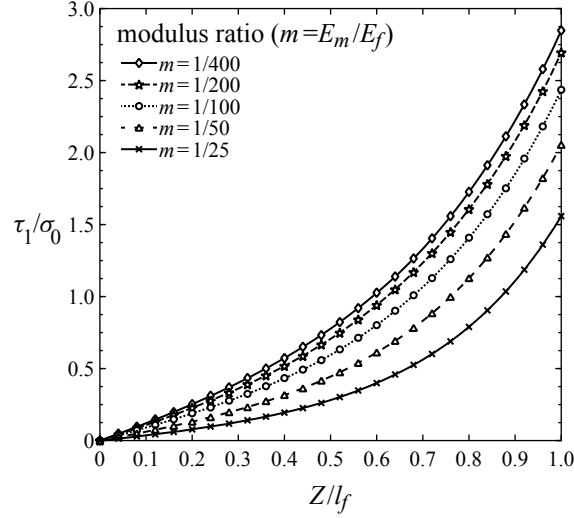
Figure 7. Normalized interfacial shear stress of fiber-interphase along the fiber length in five different ratios of matrix to fiber elastic modulus.

the interfaces:

$$Q = \frac{1}{t_1} \ln \frac{E_f}{E_m}, \qquad P = E_m e^{Q(r_f + t_i)}. \tag{54}$$

The variation in the interphase Young's modulus E_{ip} along the normalized RVE radius at four ratios of interphase thickness is shown in Figure 8. Because the Young's modulus of the fiber was considerably higher than that of the matrix, E_{ip} decreased with an increase in r from r_f to r_{ip} because of the continuity of the Young's modulus over the interfaces.
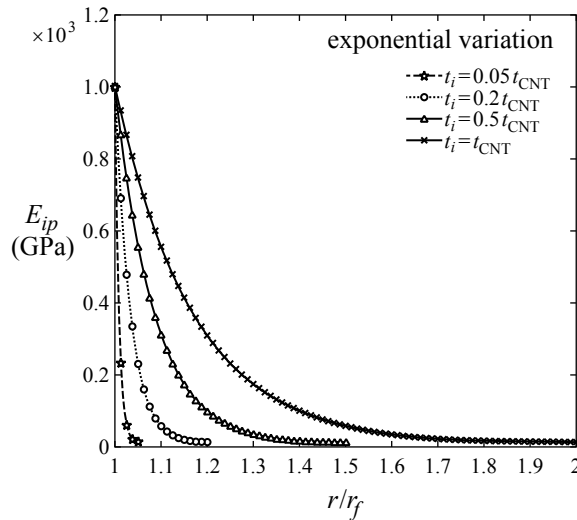
Figure 8. Interphase Young modulus (E_{ip}) along the normalized RVE radius in four different ratios of interphase thickness.
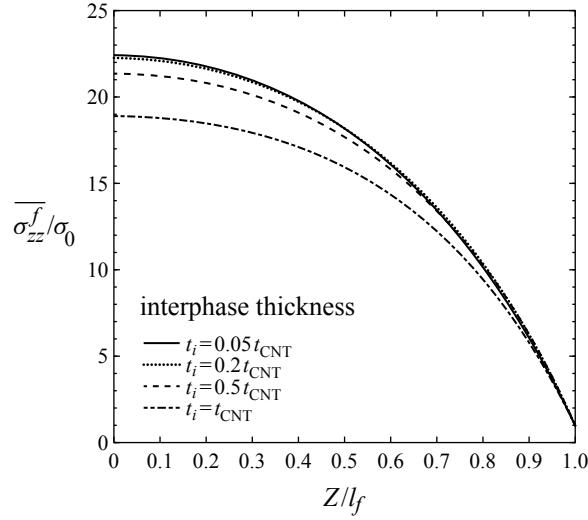
Figure 9. Normalized average axial stress of CNT along the fiber length in four different ratios of interphase thickness.

Figure 9 shows the average axial stress of CNTs normalized by applied stress σ_0 along the fiber length at four ratios of interphase thickness. As seen, the average axial stress in the fiber decreased with an increase in the interphase thickness. Consequently, the volume fraction of the interphase increased while the volume fraction of matrix decreased, which suggests that the contribution of the fiber for bearing the applied load decreased substantially.

The interfacial shear stresses of the fiber-interphase and interphase-matrix, τ_1 and τ_2, normalized by applied stress σ_0 along the fiber length at four ratios of interphase thickness are shown in Figure 10. Both interfacial shear stresses τ_1 and τ_2 increased with a decrease in the interphase thickness.

3.2. *Case study 2 (AFRC).* The material used in this case study was AFRC, the mechanical properties of which are given in Table 2.

The RVE radius was $r_m = 5r_f$ and the dimensions of the fiber were $r_f = 6\,\mu\text{m}$ and $l_f = 15r_f$ where r_f is the fiber radius and l_f is the half length of the RVE [Yu et al. 2015]. The interphase thickness varied from 0 to 1 μm, which is in accordance with the suggestions made by Papanicolaou et al. [2007]. For the composite used here, the interphase elastic modulus and Poisson's ratio were assumed to be functions of r_f as presented in (55) as suggested by Shen and Li [2003]:

$$Z_{ip}(r) = Z_m \left[1 - \frac{P}{t_i^Q} (r_{ip} - r)^Q \right]. \tag{55}$$

Material	Young's modulus	Poisson's ratio
Fiber	136 GPa	0.2
Matrix	128 MPa	0.3

Table 2. Mechanical properties of aramid fiber reinforced composite [Coffey et al. 2007].
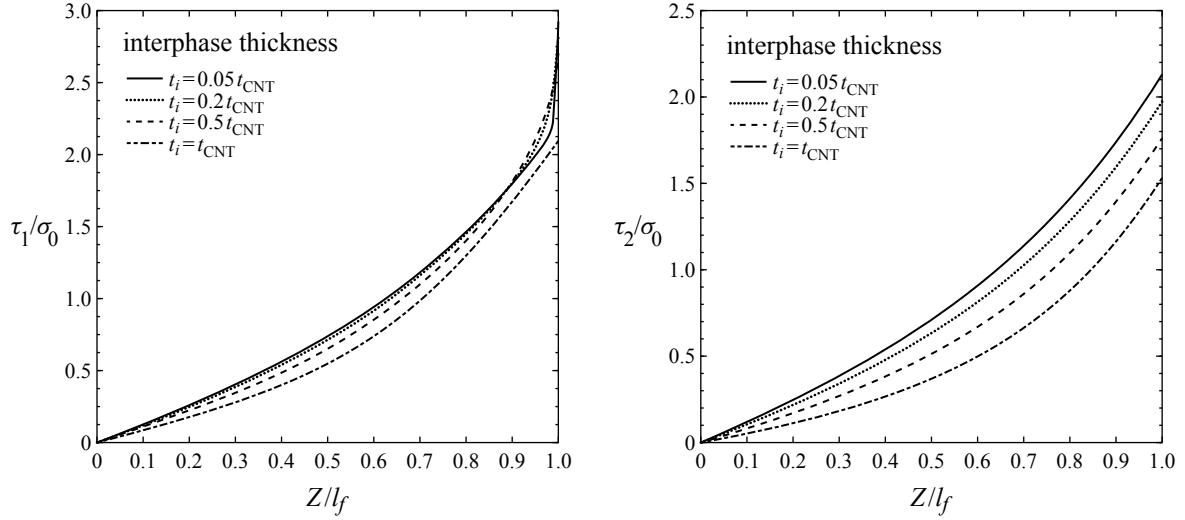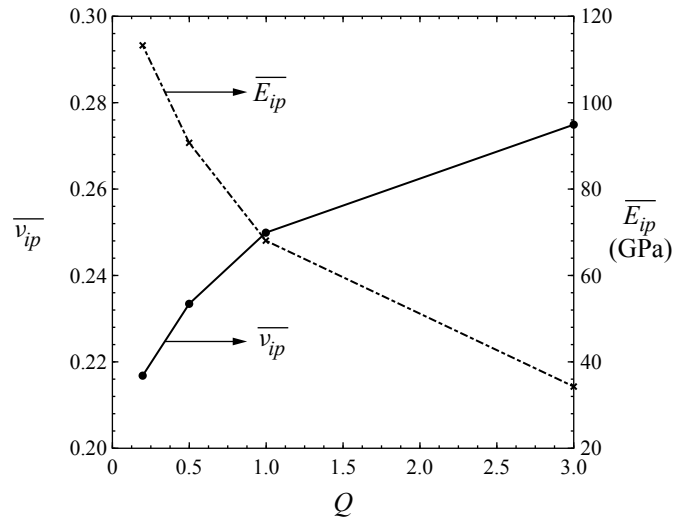
Figure 10. Normalized interfacial shear stress of fiber-interphase (left) and interphase-matrix (right) along fiber length in four different ratios of interphase thickness.

The symbol Z in (55) denotes both the elastic modulus and the Poisson's ratio. The constant Q varies from 0.2 to 3 and the constant P can be given as
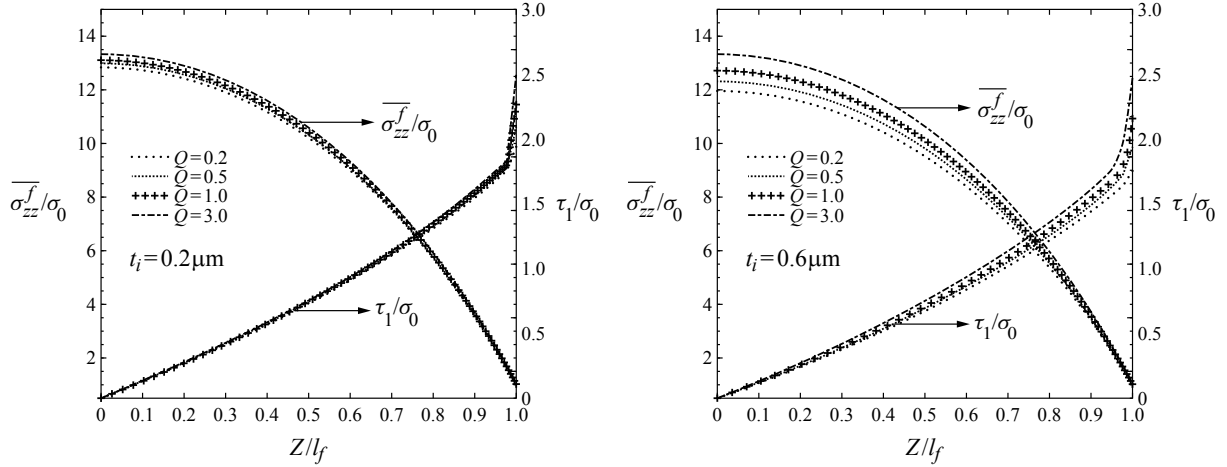
$$P = \frac{Z_m - Z_{ip}(r_f)}{Z_m}. \tag{56}$$

Figure 11 shows the predicted values of the average elastic modulus and Poisson's ratio of the interphase versus Q. The Poisson's ratio increased with Q, going from 0.216 to 0.275. The average elastic modulus decreased with an increase in Q, varying from 134 GPa to 113 GPa.

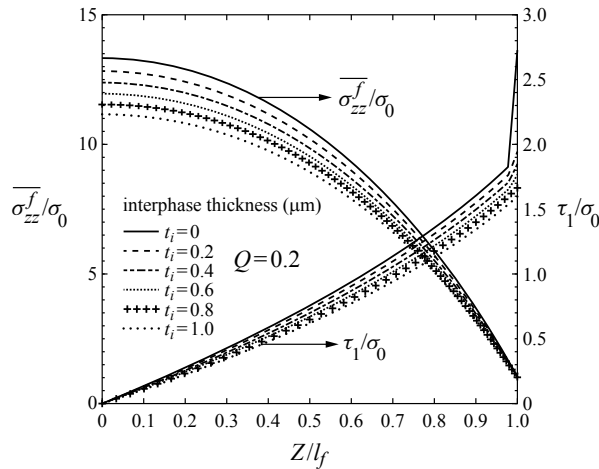**Figure 11.** Average elastic modulus and Poisson's ratio of the interphase versus Q.

Figure 12. Average stress of fiber and interfacial shear stress of fiber-interphase along the fiber length at four different values of Q for $t_i = 0.2\,\mu$m (left) and for $t_i = 0.6\,\mu$m (right).

The normalized average stress of the fiber and the normalized interfacial shear stress of the fiber-interphase along the fiber length at four values of Q were obtained for interphase thicknesses of $t_i = 0.2\,\mu$m and $t_i = 0.6\,\mu$m as depicted in Figure 12.

As is clear from the figures, both the average axial stress of the fiber and interfacial shear stress τ_1 increased with an increase in Q because the elastic modulus of the interphase decreased with an increase in Q. Also, the dependence of the fiber axial and interfacial stresses on Q was noticeably at higher interphase thicknesses, which is in accordance with the results obtained by Kiritsi and Anifantis [2001].

Figure 13 shows the normalized average stress of the fiber and the normalized interfacial shear stress

Figure 13. Average stress of fiber and interfacial shear stress of fiber-interphase along the fiber length in six different thicknesses of interphase for $Q = 0.2$.

| Q	$\overline{\sigma^f_{\max}}/\sigma_0$		$\tau_{\max}/\sigma_0$	
	$\nu_{ip}=cte$	$\nu_{ip}(r)$	$\nu_{ip}=cte$	$\nu_{ip}(r)$
0.2	11.9464	11.947	1.758	1.7653
0.6	13.3192	13.3194	2.4671	2.4745

Table 3. Effect of radial dependency of interphase Poisson's ratio on the average stress of fiber and interfacial shear stress of fiber-interphase for $t_i = 0.6\,\mu\text{m}$.

of the fiber-interphase along the fiber length at $Q = 0.2$ at six interphase thicknesses from 0 to $1\,\mu\text{m}$. As seen, the stresses decreased as the interphase thickness increased; thus, at $t_i = 0$ without considering the interphase region, the average axial stress of the fiber and interfacial shear stress τ_1 reach their maximum values.

It is noted that the radial dependence for the interphase Poisson's ratio had no significant effect on the average stress of the fiber and the interfacial shear stress of the fiber-interphase. The normalized maximum average stress of the fiber and the normalized maximum interfacial shear stress of the fiber-interphase at $t_i = 0.6\,\mu\text{m}$ with and without radial dependence on the interphase Poisson's ratio are given in Table 3.

As shown, radial variation of the interphase Poisson's ratio had a slight effect on the maximum average stress of the fiber and maximum interfacial shear stress of the fiber-interphase. This may be due to the fact that the difference between the Poisson's ratios of the fiber and matrix was small. Thus, the radial variation of the Poisson's ratio of the interphase can be neglected.

Finally, the analytical model was validated by comparison of the results with those obtained from available experimental measurements. Comparison of the analytical model predictions and Raman spectroscopy experimental data [Coffey et al. 2007] of the fiber axial stress obtained for applied stress
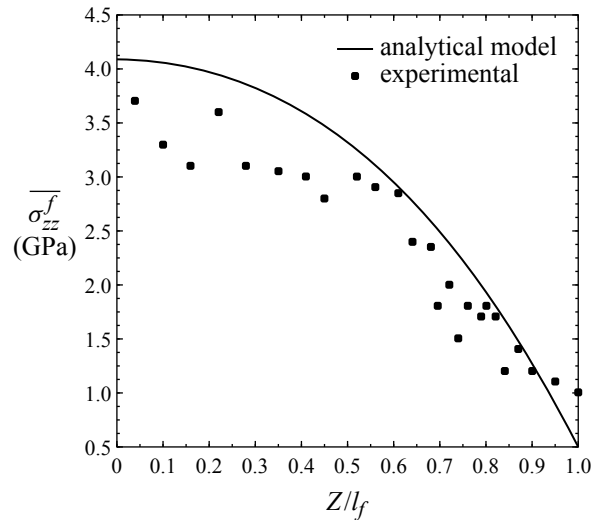
Figure 14. Comparison of analytical model prediction with experimental data of fiber axial stress for applied stress $\sigma_0 = 10\,\text{MPa}$ [Coffey et al. 2007].

$\sigma_0 = 10$ MPa is shown in Figure 14. More information on the experimental measurements of the average axial stress of the fiber can be found in [Coffey et al. 2007].

Figure 14 shows that the average axial stress of the fiber is in good agreement with the experimental measurements, especially for $Z/l_f > 0.5$. Therefore, the accuracy of the proposed analytical model and the results of this research has been validated as well.

4. Conclusion

A three-phase shear-lag model was developed to investigate the effects of an inhomogeneous interphase on the mechanism of stress transfer in unidirectional fibrous composites. Considering the results of two case studies on composite materials having interphase regions, CNTRC and AFRC, the following conclusions were made.

- The thickness of the interphase strongly influenced the elastic modulus of the CNTRC, such that the maximum value of the composite elastic modulus occurred at an interphase thickness which was equal to the radius of the fiber.

- The average axial stress in fiber decreased with an increase in the interphase thickness and interfacial shear stresses τ_1 and τ_2 increased with a decrease in the interphase thickness.

- The average axial stress of the fiber and the interfacial shear stress of the fiber-interphase increased with a decrease in the modulus ratio, which indicates that the fiber was stronger at lower modulus ratios and, consequently, its load capacity increased.

- When the difference between the Poisson's ratio of the fiber and matrix was small, the radial variation of the interphase Poisson's ratio could be neglected.

- Finally, the results obtained by the proposed analytical model were in good agreement with the results of FE analysis and the available experimental measurements, which demonstrates the capability of the model.

References

[Abedian et al. 2007] A. Abedian, M. Mondali, and M. Pahlavanpour, "Basic modifications in 3D micromechanical modeling of short fiber composites with bonded and debonded fiber end", *Comput. Mater. Sci.* **40**:3 (2007), 421–433.

[Ang and Ahmed 2013] K. K. Ang and K. S. Ahmed, "An improved shear-lag model for carbon nanotube reinforced polymer composites", *Compos. B Eng.* **50** (2013), 7–14.

[Beyerlein and Landis 1999] I. J. Beyerlein and C. M. Landis, "Shear-lag model for failure simulations of unidirectional fiber composites including matrix stiffness", *Mech. Mater.* **31**:5 (1999), 331–350.

[Budiansky et al. 1986] B. Budiansky, J. W. Hutchinson, and A. G. Evans, "Matrix fracture in fiber-reinforced ceramics", *J. Mech. Phys. Solids* **34**:2 (1986), 167–189.

[Coffey et al. 2007] A. B. Coffey, C. M. O'Bradaigh, and R. J. Young, "Interfacial stress transfer in an aramid reinforced thermoplastic elastomer", *J. Mater. Sci.* **42**:19 (2007), 8053–8061.

[Cox 1952] H. L. Cox, "The elasticity and strength of paper and other fibrous materials", *Br. J. Appl. Phys.* **3**:3 (1952), 72–79.

[Dow 1963] N. Dow, "Study of stress near a discontinuity in a filament-reinforced composite metal", in *Space SciLab Missile and Space Division*, General Electric Co Tech., Report, 1963.

[Fu et al. 2008] S.-Y. Fu, X.-Q. Feng, B. Lauke, and Y.-W. Mai, "Effects of particle size, particle/matrix interface adhesion and particle loading on mechanical properties of particulate-polymer composites", *Compos. Part B-Eng.* **39**:6 (2008), 933–961.

[Gao and Li 2005] X.-L. Gao and K. Li, "A shear-lag model for carbon nanotube-reinforced polymer composites", *Int. J. Solids Struct.* **42**:5-6 (2005), 1649–1667.

[Golestanian and Shojaie 2010] H. Golestanian and M. Shojaie, "Numerical characterization of CNT-based polymer composites considering interface effects", *Comput. Mater. Sci.* **50**:2 (2010), 731–736.

[Halpin 1984] J. C. Halpin, *Primer on composite materials: analysis*, Technomic, Lancaster (PA), 1984.

[Haque and Ramasetty 2005] A. Haque and A. Ramasetty, "Theoretical study of stress transfer in carbon nanotube reinforced polymer matrix compositesj", *Compos. Struct.* **71**:1 (2005), 68–77.

[Hernández-Pérez and Avilés 2010] A. Hernández-Pérez and F. Avilés, "Modeling the influence of interphase on the elastic properties of carbon nanotube composites", *Comput. Mater. Sci.* **47**:4 (2010), 926–933.

[Hsueh 1988] C.-H. Hsueh, "Analytical evaluation of interfacial shear strength for fiber-reinforced ceramic composites", *J. Am. Ceram. Soc.* **71**:6 (1988), 490–493.

[Hsueh 1990] C.-H. Hsueh, "Interfacial debonding and fiber pull-out stresses of fiber-reinforced composites", *Mater. Sci. Eng. A* **123**:1 (1990), 1–11.

[Hsueh 1992] C.-H. Hsueh, "Interfacial debonding and fiber pull-out stresses of fiber-reinforced composites VII: improved analyses for bonded interfaces", *Mater. Sci. Eng. A* **154**:2 (1992), 125–132.

[Hsueh 1995] C.-H. Hsueh, "A modified analysis for stress transfer in fibre reinforced composites with bonded fibre ends", *J. Mater. Sci.* **30**:1 (1995), 219–224.

[Hsueh 2000] C.-H. Hsueh, "Young's modulus of unidirectional discontinuous-fibre composites", *Compos. Sci. Technol.* **60**:14 (2000), 2671–2680.

[Hsueh et al. 1997] C. H. Hsueh, R. J. Young, X. Yang, and P. F. Becher, "Stress transfer in a model composite containing a single embedded fiber", *Acta Mater.* **45**:4 (1997), 1469–1476.

[Kerans and Parthasarathy 1991] R. J. Kerans and T. A. Parthasarathy, "Theoretical analysis of the fiber pullout and pushout tests", *J. Am. Ceram. Soc.* **74**:7 (1991), 1585–1596.

[Kiritsi and Anifantis 2001] C. C. Kiritsi and N. K. Anifantis, "Load carrying characteristics of short fiber composites containing a heterogeneous interphase region", *Comput. Mater. Sci.* **20**:1 (2001), 86–97.

[Kumar and Srinivas 2014] P. Kumar and J. Srinivas, "Numerical evaluation of effective elastic properties of CNT-reinforced polymers for interphase effects", *Comput. Mater. Sci.* **88** (2014), 139–144.

[Lauke 2006] B. Lauke, "Determination of adhesion strength between a coated particle and polymer matrix", *Compos. Sci. Technol.* **66**:16 (2006), 3153–3160.

[Lawrence 1972] P. Lawrence, "Some theoretical consideration of fiber pull-out from an elastic matrix", *J. Mater. Sci.* **7**:1 (1972), 1–6.

[Liu and Chen 2003] Y. J. Liu and X. L. Chen, "Continuum models of carbon nanotube-based composites using the boundary element method", *Electron. J. Boundary Element.* **1**:2 (2003), 316–335.

[Luk and Keer 1979] V. K. Luk and L. M. Keer, "Stress analysis for an elastic half space containing an axially-loaded rigid cylindrical rod", *Int. J. Solids Struct.* **15**:10 (1979), 805–827.

[Maligno et al. 2010] A. R. Maligno, N. A. Warrior, and A. C. Long, "Effects of interphase material properties in unidirectional fibre reinforced composites", *Compos. Sci. Technol.* **70**:1 (2010), 36–44.

[Mondali and Abedian 2013] M. Mondali and A. Abedian, "An analytical model for stress analysis of short fiber composites in power law creep matrix", *Int. J. Non-Linear Mech.* **57** (2013), 39–49.

[Muki and Sternberg 1970] R. Muki and E. Sternberg, "Elastostatic load-transfer to a half-space from a partially embedded axially loaded rod", *Int. J. Solids Struct.* **6**:1 (1970), 69–90.

[Nair and Kim 1992] S. V. Nair and H. G. Kim, "Modification of the shear lag analysis for determination of elastic modulus of short-fiber (or Whisker) reinforced metal matrix composites", *J. Appl. Mech.* (*ASME*) **59**:2S (1992), 176–182.

[Nairn 1997] J. A. Nairn, "On the use of shear-lag methods for analysis of stress transfer in unidirectional composites", *Mech. Mater.* **26**:2 (1997), 63–80.

[Needleman et al. 2010] A. Needleman, T. L. Borders, L. C. Brinson, V. M. Flores, and L. S. Schadler, "Effect of an interphase region on debonding of a CNT reinforced polymer composite", *Compos. Sci. Technol.* **70**:15 (2010), 2207–2215.

[Papanicolaou et al. 2007] G. C. Papanicolaou, N. K. Anifantis, L. K. Keppas, and T. V. Kosmidou, "Stress analysis of short fiber-reinforced polymers incorporating a hybrid interphase region", *Compos. Interface.* **14**:2 (2007), 131–152.

[Rafiee and Pourazizi 2015] R. Rafiee and R. Pourazizi, "Influence of CNT functionalization on the interphase region between CNT and polymer", *Comput. Mater. Sci.* **96** (2015), 573–578.

[Rosen 1964] B. W. Rosen, "Tensile failure of fibrous composites", *AIAA J.* **2**:11 (1964), 1985–1991.

[Shen and Li 2003] L. Shen and J. Li, "Effective elastic moduli of composites reinforced by particle or fiber with an inhomogeneous interphase", *Int. J. Solids Struct.* **40**:6 (2003), 1393–1409.

[Takaku and Arridge 1973] A. Takaku and R. G. C. Arridge, "The effect of interfacial radial and shear stress on fiber pull-out in composite materials", *J. Phys. D* **6**:17 (1973), 2038–2047.

[Taya and Arsenault 1987] M. Taya and R. J. Arsenault, "A comparison between a shear-lag type model and an Eshelby type model in predicting the mechanical properties of a short fiber composite", *Scr. Metall.* **21**:3 (1987), 349–354.

[Timoshenko and Goodier 1970] S. P. Timoshenko and J. N. Goodier, *Theory of elasticity*, 3rd ed. ed., McGraw-Hill, New York, 1970.

[Wan et al. 2005] H. Wan, F. Delale, and L. Shen, "Effect of CNT length and CNT-matrix interphase in carbon nanotube (CNT) reinforced composites", *Mech. Res. Commun.* **32**:5 (2005), 481–489.

[Wang et al. 2006] J. Wang, S. L. Crouch, and S. G. Mogilevskaya, "Numerical modeling of the elastic behavior of fiber-reinforced composites with inhomogeneous interphases", *Compos. Sci. Technol.* **66**:1 (2006), 1–18.

[Wang et al. 2011] X. Wang, J. Zhang, Z. Wang, S. Zhou, and X. Sun, "Effects of interphase properties in unidirectional fiber reinforced composite materials", *Mater. Des.* **32**:6 (2011), 3486–3492.

[Withers et al. 1989] P. J. Withers, W. M. Stobbs, and O. B. Pederson, "The application of the eshelby method of internal stress determination to short fibre metal matrix composites", *Acta Metall.* **37**:11 (1989), 3061–3084.

[Yang and Pitchumani 2004] F. Yang and R. Pitchumani, "Effects of interphase formation on the modulus and stress concentration factor of fiber-reinforced thermosetting-matrix composites", *Compos. Sci. Technol.* **64**:10-11 (2004), 1437–1452.

[Yao et al. 2013] Y. Yao, S. Chen, and P. Chen, "The effect of a graded interphase on the mechanism of stress transfer in a fiber-reinforced composite", *Mech. Mater.* **58** (2013), 35–54.

[Yu et al. 2015] X. Yu, B. Gu, and B. Zhang, "Effects of short fiber tip geometry and inhomogeneous interphase on the stress distribution of rubber matrix sealing composites", *J. Appl. Polym. Sci.* **132**:1-8 (2015), 41638.

[Zhang and He 2008] J. Zhang and C. He, "A three-phase cylindrical shear-lag model for carbon nanotube composites", *Acta Mech.* **196**:1-2 (2008), 33–54.

[Zhang et al. 2017] B. Zhang, X. Yu, and B. Gu, "An improved shear lag model for predicting stress distribution in hybrid fiber reinforced rubber composites", *Fiber. Polym.* **18**:2 (2017), 349–356.

[Zhao and Ji 1997] P. Zhao and S. Ji, "Refinements of the shear-lag model and its applications", *Tectonophys.* **279**:1-4 (1997), 37–53.

MOHAMMAD HASSAN ZARE: `zare_mhz@yahoo.com`
Department of Mechanical Engineering, Science and Research Branch, Islamic Azad University, Tehran, Iran

MEHDI MONDALI: `mondali@srbiau.ac.ir`
Department of Mechanical Engineering, Science and Research Branch, Islamic Azad University, Tehran, Iran

msp

■■msp

NONLINEAR FREE VIBRATION OF NANOBEAMS BASED ON NONLOCAL STRAIN GRADIENT THEORY WITH THE CONSIDERATION OF THICKNESS-DEPENDENT SIZE EFFECT

WEI CHEN, LIN WANG AND HU-LIANG DAI

Although the strain gradient and stress gradient parameters have been widely considered in the frame of nonlocal strain gradient theory, the literature concerned with the additional effect of slender ratio parameter in nonlocal strain gradient beam models is limited. In this paper, a nonlinear dynamical model for nonlocal strain gradient beams is developed and its nonlinear free vibration is analyzed. In the proposed dynamical model, the size-dependent properties associated not only with the nonlocal strain gradient and nonlocal stress gradient parameters but also with the slender ratio parameter are discussed. The effect of slender ratio parameter, which may be also interpreted as the thickness-dependent size effect, is caused by the stress on account of the thickness-direction strain gradient. Based on nonlocal strain gradient theory, the nonlinear governing equation of boundary conditions of the nanobeam are derived first. Then the nonlinear governing equation is simplified for special symmetric boundary conditions and external loadings. In the nonlinear free vibration analysis, an analytical solution for predicting the nonlinear free vibration frequencies is derived via the homotopy analysis method. It is shown that the nonlinear frequencies of the nanobeam display significant size-dependent phenomena for large values of slender ratio parameter and either stiffness-softening or stiffness-hardening behavior may occur. Our results also demonstrate that, besides conventional strain gradient and stress gradient effects, the thickness-dependent size effect can be significant for slender nanobeams and cannot be ignored in many cases.

1. Introduction

In the past years, nanoscience and nanotechnology have developed rapidly. Many nano- and micro-sized devices and structures have been applied in advanced technology, such as biosensors [Pei et al. 2004], nanosensors [Anker et al. 2008; Cui et al. 2001; Patolsky and Lieber 2005], nanoactuators [Shi et al. 2010; Sul and Yang 2009], atomic force microscopy (AFM) [Eaton and West 2010; Eom et al. 2011; Farokhi et al. 2016; Pereira 2001], and nano-/micro-electromechanical systems (NEMS/MEMS) [Li et al. 2003; Li et al. 2007]. In these engineering applications, beams, plates and shells in nano-size are the basic components and have been used widely [Pei et al. 2004; Ç. Demir and Civalek 2017].

For the purpose of better guidance to nanotechnology, more extensive studies of the statics and dynamics of nanobeams, nanoplates and nanoshells are requisite. It has been reported that nano-/micro-scale materials/structures have the properties of size effects observed by both experiments [Lam et al. 2003; McFarland et al. 2005; Kulkarni et al. 2005] and numerical simulations [Agrawal et al. 2008; Duan and Wang 2007]. Some results showed that structures in nano-size may behave either stiffness-hardening or

stiffness-softening (see, e.g., Li et al. 2015a; Li et al. 2015b; Li 2014). Because of the time-consuming of molecular (atom) dynamics simulations and the difficulties of controlling experiments at micro/nano-scale, many nonclassical continuum theories have been proposed to explain and predict the size effects of structures at small sizes. Among various nonclassical continuum theories, the nonlocal elasticity theory is one of the most popular ones for static and dynamic analysis of nanostructures.

The nonlocal elasticity theory developed by Eringen [2002] thinks that the nonlocal stress at a reference point is influenced by the strain at all points of the body. From this point of view, the nonlocal elasticity theory is quite different from the point-to-point stress-strain relationship in the classical local elasticity theory. According to the nonlocal elasticity theory, by means of an integral with a nonlocal kernel function over the body, the long-range interactions between the atoms are incorporated. Eringen [2002] suggested that the integral constitutive law may be simplified to the form of differential equations when considering specified kind of kernel function. Based on nonlocal elasticity theory, there were a large number of studies on the static and dynamic responses of nanorods [Huang 2012; Lembo 2016; Narendar and Gopalakrishnan 2010; Wang et al. 2006], nanobeams [Aydogdu 2009; Dai et al. 2018; Reddy 2007; Thai 2012; Tuna and Kirca 2016], nanoplates [Assadi and Farshi 2011; Reddy 2010; Murmu and Adhikari 2011; Wang and Zhang 2018] and nanoshells [Shen 2010; Khademolhosseini et al. 2010; Hu et al. 2008; Ghavanloo and Fazelzadeh 2013a]. In many early studies on nonlocal elastic models, it was reported that the nonlocal natural frequency is generally lower than the local one, showing a stiffness-softening effects. For more details on nonlocal elastic models, the interested reader is referred to the comprehensive review by Eltaher et al. [2016].

Other than the nonlocal elastic models, the stiffness-softening effect of which was frequently reported, a stiffness-hardening effect may occur in the strain gradient elasticity theory [Aifantis 1992]. Based on the assumption that small-scale effect is associated with high-order deformation mechanism, additional strain gradient terms were suggested to be considered in the strain gradient elasticity theory. Recently, based on strain gradient elasticity theory, the significant strain gradient effects have been investigated in many studies when considering the static and dynamic behaviors of rods [Rahaeifard 2015], beams [Akgöz and Civalek 2011; Kong et al. 2009; Lazopoulos 2012; Xu and Deng 2016; Wang et al. 2018], plates [Ansari et al. 2015; Movassagh and Mahmoodi 2013; Ieşan 2014; Wang et al. 2011; Zhang et al. 2015], and shells [Ghavanloo and Fazelzadeh 2013b; Zeighampour and Beni 2014; Papargyri-Beskou et al. 2012] in nano-size.

In order to capture both size-dependent stiffness-softening and stiffness-hardening phenomena, Lim et al. [2015] developed a "nonlocal strain gradient theory" and investigated the wave propagation based on nonlocal strain beam models. This theory may be viewed as a combination of nonlocal elasticity theory and strain gradient theory. Because of its more generalized feature, there were fruitful studies on nonlocal strain gradient rods [Li et al. 2016a; Xu et al. 2017b; Zhu and Li 2017], beams [Li et al. 2015c; Li et al. 2016b; Xu et al. 2017a] and plates [Ebrahimi et al. 2016]. It is noted that the boundary conditions in nonlocal strain gradient models are complex due to the high-order stress. In this regard, Xu et al. [2017b] have recommended a weighted residual approach to derive the expressions of high-order forces and boundary conditions.

The aforementioned nonlocal strain gradient beam models assumed that the size effect in the beam's thickness direction of nanobeams may be neglected for simplification, i.e., the Laplacian operator was supposed to be $\nabla^2 = \partial^2/\partial x^2$ for various beam models. Very recently, however, it was shown by Li et al.

[2018] that the size effect of strain gradient in the thickness direction ($\varepsilon_{xx,z}$) may be important for statics analysis and should be accounted for. Although there were several previous studies on the nonlinear vibration of nonlocal strain gradient beams (see, e.g., Li et al. 2016b; Şimşek 2016), these studies have not considered the strain gradient in the beam's thickness direction. In this work, we initiate to investigate the nonlinear free vibration of nonlocal strain gradient beams incorporating the strain gradient effect in the beam's thickness direction. It will be shown that the thickness-dependent size effect associated with the nanobeam's slender ratio on the nonlinear free vibration of nanobeams may be remarkable.

2. Nonlocal strain gradient theory

According to the nonlocal strain gradient theory developed by Lim et al. [2015], the total stress tensor accounts for not only the nonlocal stress tensor but also the strain gradient stress tensor, i.e.

$$t_{ij} = \sigma_{ij} - \nabla \sigma_{ijm}^{(1)}, \tag{1}$$

where ∇ is the Laplacian operator, and the nonlocal stress tensor σ_{ij} and the higher-order nonlocal stress tensor $\sigma_{ijm}^{(1)}$ are defined by

$$\sigma_{ij} = C_{ijkl} \int_V \alpha_0(|\chi' - \chi|, e_0 a) \, \varepsilon'_{kl} \, dV, \tag{2}$$

$$\sigma_{ijm}^{(1)} = l^2 C_{ijkl} \int_V \alpha_1(|\chi' - \chi|, e_1 a) \, \varepsilon'_{kl,m} \, dV, \tag{3}$$

where ε_{kl} is the classical strain tensor, $\varepsilon_{kl,m}$ is the strain gradient tensor, C_{ijkl} is the fourth-order elasticity tensor, l is the material length scale parameter introduced to consider the significance of strain gradient stress field, $e_0 a$ and $e_1 a$, which are nonlocal parameters, are introduced to consider the significance of nonlocal elastic stress field.

As solving the integral constitutive equations of (1) is very difficult, a simplified form of differential equations will be used in this study. Let $\alpha_0(\chi', \chi, e_0 a)$ and $\alpha_1(\chi', \chi, e_1 a)$ be the nonlocal functions for the classical stress tensor and the strain gradient stress tensor, respectively. We suppose that α_0 and α_1 can satisfy the conditions given by Eringen [1983]. The linear nonlocal differential operator is used in the nonlocal functions, i.e., $\mathcal{L}_i = 1 - (e_i a)^2 \nabla^2$ for $i = 0, 1$. Furthermore, it is assumed that $e = e_0 = e_1$; thus one obtains
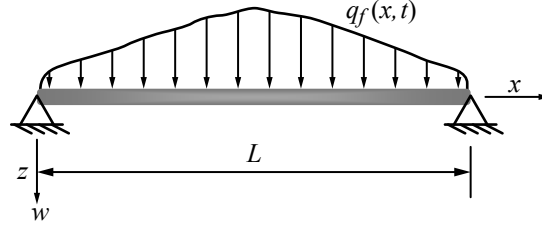
$$\left(1 - (ea)^2 \nabla^2\right) \sigma_{ij} = C_{ijkl} \, \varepsilon_{kl}, \tag{4}$$

$$\left(1 - (ea)^2 \nabla^2\right) \sigma_{ijm}^{(1)} = l^2 C_{ijkl} \, \varepsilon_{kl,m}. \tag{5}$$

The general constitutive equations for size-dependent beams can be simplified as [Lim et al. 2015]

$$[1 - (ea)^2 \nabla^2] \, t_{ij} = C_{ijkl} \, \varepsilon_{kl} - l^2 \nabla^2 C_{ijkl} \, \varepsilon_{kl}, \tag{6}$$

where ea is a stress-gradient parameter introduced to involve stress gradient effect, while l is a strain-gradient parameter introduced to involve strain gradient effect.

Figure 1. Schematic of a nanobeam.

For an Euler–Bernoulli beam-type structure, the size-dependent behavior may be neglected in the width directions. Thus, the general constitutive relation can be further simplified to [Li et al. 2018]

$$\left[1 - (ea)^2 \frac{\partial^2}{\partial x^2}\right] t_{xx} = \left[1 - l^2 \left(\frac{\partial^2}{\partial x^2} + \frac{\partial^2}{\partial z^2}\right)\right] E \varepsilon_{xx}, \tag{7}$$

where E denotes the elasticity modulus, t_{xx} denotes the axial normal stress, and ε_{xx} denotes the axial strain. It should be noted that the formulations for the nonlocal elasticity theory [Eringen 1983] or the strain gradient theory [Aifantis 1992; Mindlin 1965; Aifantis and Willis 2005; Polizzotto 2012] can be obtained by setting $ea = 0$ or $l = 0$.

3. Formulation

The system under consideration consists of a nanobeam of length L between two immovable supports, internal cross-sectional area A, mass density ρ, and flexural rigidity EI, as shown in Figure 1. The beam is uniform along its length and the cross-section is symmetric. In this section, we will derive the equations of motion based on the nonlocal strain gradient theory by accounting for the geometric nonlinearity associated with the axial extension of the beam.

3.1. *General governing equations.* The displacements (u_1, u_2, u_3) of an Euler–Bernoulli beam along the (x, z) coordinate directions are given by

$$u_1(x, z) = u(x) - zw', \quad u_2(x, z) = 0, \quad u_3(x, z) = w(x), \tag{8}$$

where u is the longitudinal displacement, w is the transverse displacement of the mid-plane, and $(\ )' = \partial/\partial x$.

According to the von-kármán nonlinear strain expression, the nonzero strain for a beam under large displacements can be written as

$$\varepsilon_{xx} = u' + \tfrac{1}{2} w'^2 - z w'', \tag{9}$$

where ε_{xx} is the axial strain.

We will derive the nonlinear equations of motion and boundary conditions by utilizing Hamilton's principle. Based on the nonlocal strain gradient theory, the virtual work of the strain energy is given by

[Li et al. 2018]

$$\delta U = \int_V \left(\sigma_{xx} \delta\varepsilon_{xx} + \sigma_{xxx}^{(1)} \delta\varepsilon_{xx,x} + \sigma_{xxz}^{(1)} \delta\varepsilon_{xx,z} \right) dV$$

$$= \int_0^L \int_A \left[\sigma_{xx} \delta\left(u' + \tfrac{1}{2}w'^2 - zw''\right) + \sigma_{xxx}^{(1)} \delta\left(u'' + w'w'' - zw'''\right) + \sigma_{xxz}^{(1)} \delta(-w'') \right] dA\, dx$$

$$= \int_0^L N^{(0)} \delta\left(u' + \tfrac{1}{2}w'^2\right) dx - \int_0^L M^{(0)} \delta w'' dx + \int_0^L N_x^{(1)} \delta\left(u'' + w'w''\right) dx$$

$$\qquad\qquad\qquad - \int_0^L M_x^{(1)} \delta w''' \, dx + \int_0^L N_z^{(1)} \delta(-w'') \, dx$$

$$= \int_0^L \left(N_x^{(1)''} - N^{(0)'} \right) \delta u \, dx$$

$$\quad + \int_0^L \left[-(N^{(0)} w')' - (N_x^{(1)} w'')' + (N_x^{(1)} w')'' + M_x^{(1)'''} - M^{(0)''} - N_z^{(1)''} \right] \delta w \, dx$$

$$\quad + \left(N^{(0)} - N_x^{(1)'} \right) \delta u \big|_0^L + N_x^{(1)} \delta u' \big|_0^L$$

$$\quad + \left(N^{(0)} w' + N_x^{(1)} w'' + M^{(0)'} + N_z^{(1)'} - (N_x^{(1)} w')' - M_x^{(1)''} \right) \delta w \big|_0^L$$

$$\quad + \left(-M^{(0)} + N_x^{(1)} w' + M_x^{(1)'} - N_z^{(1)} \right) \delta w' \big|_0^L - M_x^{(1)} \delta w'' \big|_0^L. \tag{10}$$

In (10), $N^{(0)}$ and $M^{(0)}$ are the lower-order force and moment for axial and transverse directions, respectively; $N_x^{(1)}$ and $N_z^{(1)}$ are the high-order axial forces due to strain gradient in the axial and thickness directions, respectively; $M_x^{(1)}$ is the high-order moment. These resultants are defined by

$$N^{(0)} = \int_A \sigma_{xx} \, dA, \tag{11a}$$

$$N_x^{(1)} = \int_A \sigma_{xxx}^{(1)} \, dA, \tag{11b}$$

$$N_z^{(1)} = \int_A \sigma_{xxz}^{(1)} \, dA, \tag{11c}$$

$$M^{(0)} = \int_A z\sigma_{xx} \, dA, \tag{11d}$$

$$M_x^{(1)} = \int_A z\sigma_{xxx}^{(1)} \, dA. \tag{11e}$$

The stress resultants can be given by

$$(1 - \mu^2\nabla^2)\, N^{(0)} = EA\left(u' + \tfrac{1}{2}w'^2\right), \tag{12a}$$

$$(1 - \mu^2\nabla)^2\, N_x^{(1)} = l^2 EA(u'' + w'w''), \tag{12b}$$

$$(1 - \mu^2\nabla^2)\, M^{(0)} = -EIw'', \tag{12c}$$

$$(1 - \mu^2\nabla^2)\, M_x^{(1)} = -l^2 EIw''', \tag{12d}$$

$$(1 - \mu^2\nabla^2)\, N_z^{(1)} = -l^2 EAw''. \tag{12e}$$

If body force, body couple and externally imposed tension are either absent or neglected, the virtual work done by an external transverse force q_f can be written as

$$\delta W = -\int_0^L q_f \, \delta w \, dx. \tag{13}$$

Since the considered beam is supported at both ends, the longitudinal displacement and velocity are relatively small. Hence, the kinetic energy of the nanobeam may be approximated as

$$K = \frac{1}{2}\int_0^L \rho A \left(\frac{\partial w}{\partial t}\right)^2 dx. \tag{14}$$

In the frame of Hamilton's principle, the dynamic governing equation and boundary conditions of this beam can be derived based on the following variational equation:

$$\delta \int_{t_1}^{t_2} (K - U + W) \, dt = 0. \tag{15}$$

Substituting (10), (13), and (14) into (15), one obtains the equations of motion as

$$\delta u : \left(N^{(0)} - N_x^{(1)'}\right)' = 0, \tag{16a}$$

$$\delta w : \rho A \ddot{w} - (N^{(0)} w')' - (N_x^{(1)} w'')' + (N_x^{(1)} w')'' + M_x^{(1)'''} - M^{(0)''} - N_z^{(1)''} + q_f = 0, \tag{16b}$$

and the boundary conditions as

$$\delta u : N^{(0)} - N_x^{(1)'} = 0 \qquad\qquad \text{or} \quad u = 0, \tag{17a}$$

$$\delta u' : N_x^{(1)} = 0 \qquad\qquad \text{or} \quad u' = 0, \tag{17b}$$

$$\delta w : N^{(0)} w' + N_x^{(1)} w'' + M^{(0)'} + N_z^{(1)'} - (N_x^{(1)} w')' - M_x^{(1)''} = 0 \quad \text{or} \quad w = 0, \tag{17c}$$

$$\delta w' : -M^{(0)} + N_x^{(1)} w' + M_x^{(1)'} - N_z^{(1)} = 0 \qquad\qquad \text{or} \quad w' = 0, \tag{17d}$$

$$\delta w'' : M_x^{(1)} = 0 \qquad\qquad \text{or} \quad w'' = 0, \tag{17e}$$

where the dot above w denotes the time differentiation with respect to t. By defining

$$N_{0x} = N^{(0)} - N_x^{(1)'}, \tag{18}$$

and combining (12a), (12b), and (17a), we have

$$N_{0x} = EA\left(u' + \tfrac{1}{2}w'^2\right) - EIl^2(u''' + w'w''' + w''^2) = \text{constant}. \tag{19}$$

Hence (16b) can be rewritten as

$$\rho A \ddot{w} - N_{0x} w'' + \left(M_x^{(1)'} - M^{(0)} - N_z^{(1)}\right)'' + q_f = 0. \tag{20}$$

Upon combining (12c)–(12e), we have

$$(1 - \mu^2 \nabla^2)\left(M_x^{(1)'} - M^{(0)} - N_z^{(1)}\right) = -l^2 EI w^{(IV)} + EI w'' + l^2 EA w'', \tag{21}$$

where $^{(IV)}$ denotes the fourth derivative. With the help of (20) and (21), the final governing equation of the nanobeam can be obtained as

$$\rho A \left(1 - \mu^2 \frac{\partial}{\partial x^2}\right) \ddot{w} - N_{0x} \left(1 - \mu^2 \frac{\partial}{\partial x^2}\right) w'' + \left(EI - EI\, l^2 \frac{\partial}{\partial x^2} + l^2 EA\right) w^{(IV)} + \left(1 - \mu^2 \frac{\partial}{\partial x^2}\right) q_f = 0. \quad (22)$$

3.2. _Governing equations for special boundary conditions._ In Section 3.1, we have obtained the general equation of motion, equation (22). This governing equation can be finalized once N_{0x} is given. Nevertheless, N_{0x} may have different forms for different boundary conditions. In this subsection, we will discuss the N_{0x} expression for several typical boundary conditions, and then finalize the governing equations.

For free-free boundary conditions, since $N_{0x}(0) = N_{0x}(L) = 0$, it is clear that $N_{0x} = 0$ based on (19). In this work, the system under consideration is a beam assumed supported at two axially immobile supports, i.e., $u(0) = u(L) = 0$. Hence, there are three possible types of boundary conditions for the longitudinal displacement to determine the N_{0x} expression. These three types of boundary conditions are

$$\text{case } 1 : u(0) = 0, \quad u(L) = 0, \quad N_x^{(1)}(0) = 0, \quad N_x^{(1)}(L) = 0, \quad (23a)$$

$$\text{case } 2 : u(0) = 0, \quad u(L) = 0, \quad u'(0) = 0, \quad N_x^{(1)}(L) = 0, \quad (23b)$$

$$\text{case } 3 : u(0) = 0, \quad u(L) = 0, \quad u'(0) = 0, \quad u'(L) = 0. \quad (23c)$$

Based on the weighted residual approaches, the high-order axial forces due to strain gradient in the axial direction is given by Xu et al. [2017b]

$$N_x^{(1)} = EAl^2 (u'' + w'w''). \quad (24)$$

For pinned-pinned or clamped-clamped supports, case 1 and case 2 can be rewritten as

$$\text{case } 1 : u(0) = 0, \quad u(L) = 0, \quad u''(0) = 0, \quad u''(L) = 0, \quad (25a)$$

$$\text{case } 2 : u(0) = 0, \quad u(L) = 0, \quad u'(0) = 0, \quad u''(L) = 0. \quad (25b)$$

3.2.1. _Determination of N_{0x} for Case 1._ With the help of (25a), integrating (19) over the beam length results in

$$N_{0x} = \frac{EA}{2L} \int_0^L w'^2 dx - \frac{l^2 EA}{L} [w'(L)\, w''(L) - w'(0)\, w''(0)]. \quad (26)$$

For pinned-pinned or clamped-clamped supports, we have

$$N_{0x} = \frac{EA}{2L} \int_0^L w'^2 dx. \quad (27)$$

Now the governing equation of the nanobeam can be obtained as

$$\rho A(1 - \mu^2 \partial/\partial x^2) \ddot{w} - \frac{EA}{2L} \left(\int_0^L w'^2 dx\right) (1 - \mu^2 \partial/\partial x^2) w'' + EI(1 - l^2 \partial/\partial x^2) w^{(IV)}$$
$$+ l^2 EA w^{(IV)} + (1 - \mu^2 \partial/\partial x^2) q_f = 0. \quad (28)$$

3.2.2. *Determination of N_{0x} for Case 2 and Case 3.* For case 2 or case 3, N_{0x} cannot be obtained using a similar treatment as that proposed in Section 3.2.1. A more general method is required to obtain the expression of u in the form of w and its derivatives. We rewrite (19) as

$$u' - l^2 u''' = f(x), \tag{29}$$

where

$$f(x) = -\frac{1}{2}w'^2 + l^2(w''w'' + w'w''') + \frac{N_{0x}}{EA}. \tag{30}$$

The general solution of the homogeneous part of (29) is

$$u_0(x) = C_1 + C_2\, e^{x/l} + C_3\, e^{-x/l}, \tag{31}$$

where C_1, C_2, and C_3 are constants to be determined by using boundary conditions. By rewriting (29) as

$$\boldsymbol{Y}' = \boldsymbol{AY} + \boldsymbol{B}(x), \tag{32}$$

where

$$\boldsymbol{Y} = \begin{bmatrix} u'' \\ u' \end{bmatrix}, \quad \boldsymbol{A} = \begin{bmatrix} 0 & 1/l^2 \\ 1 & 0 \end{bmatrix}, \quad \boldsymbol{B} = \begin{bmatrix} -f/l^2 \\ 0 \end{bmatrix}, \tag{33}$$

and setting

$$\boldsymbol{Y}(x) = \boldsymbol{P}(x)\,\boldsymbol{Q}(x). \tag{34}$$

Equation (33) can be written as

$$(\boldsymbol{P}' - \boldsymbol{AP})\boldsymbol{Q} + \boldsymbol{P}\boldsymbol{Q}' = \boldsymbol{B}. \tag{35}$$

By using the condition

$$\boldsymbol{P}' - \boldsymbol{AP} = 0, \tag{36}$$

Equation (35) leads to

$$\boldsymbol{Q} = \int \boldsymbol{P}^{-1}\boldsymbol{B}\, dx. \tag{37}$$

By solving (36) we have

$$\boldsymbol{P} = \begin{bmatrix} \dfrac{1}{l}\, e^{x/l} & -\dfrac{1}{l}\, e^{-x/l} \\ e^{x/l} & e^{-x/l} \end{bmatrix}. \tag{38}$$

Upon combining (33), (34), (37), and (38), a particular solution of (29) can be found, i.e.,

$$u_1(x) = -\frac{1}{2l}\int\left(e^{x/l}\int f e^{-x/l}dx\right)dx + \frac{1}{2l}\int\left(e^{-x/l}\int f e^{x/l}dx\right)dx. \tag{39}$$

Therefore, the general solution of (29) is finally given by

$$u(x) = C_1 + C_2\, e^{x/l} + C_3\, e^{-x/l} - \frac{1}{2l}\int\left(e^{x/l}\int f e^{-x/l}dx\right)dx + \frac{1}{2l}\int\left(e^{-x/l}\int f e^{x/l}dx\right)dx. \tag{40}$$

The four undetermined constants C_1, C_2, C_3, and N_{0x} in the u expression of (40) can be determined for a set of given boundary conditions. However, the solving process for C_1, C_2, C_3, and N_{0x} may be complicated.

3.2.3. *Final governing equations for symmetric boundary conditions.* In Section 3.2.1, we have given the explicit expression of N_{0x} for boundary conditions of case 1. As discussed in Section 3.2.2, however, the general expression of N_{0x} is difficult to obtain for case 2 and case 3. It is also noted that the beam of case 3 has the same longitudinal constraints at both ends. For case 3, actually, the expression of N_{0x} can be obtained only for some special situations.

As a result, when the nanobeam with both ends subjected to the same boundary conditions for either longitudinal or transverse motions (i.e., the equations for boundary conditions at both ends are identical), the explicit expression of N_{0x} can be obtained and hence the governing equations finalized. Now we consider the following possible special type of symmetric boundary conditions:

$$u''(0) = u''(L), \quad w'(0) = w'(L), \quad w''(0) = w''(L). \tag{41}$$

Based on (41), integrating (19) over the beam length yields

$$N_{0x} = \frac{EA}{2L} \int_0^L w'^2 \, dx. \tag{42}$$

Since the expression in (42) is identical to the result of (27) for case 1, the governing equation (28) is still valid for the considered symmetric boundary conditions. For asymmetric boundary conditions, equation (28) is not applicable.

3.3. *Nondimensionalization.* In order to simplify the form of the governing equation and to reduce the number of parameters, we introduce the following dimensionless quantities:

$$\bar{x} = \frac{x}{L}, \quad \bar{w} = \frac{w}{r}, \quad t = \bar{t}\sqrt{\frac{\rho A L^4}{EI}}, \quad \eta = \frac{L}{r}, \quad \tau = \frac{ea}{L}, \quad \zeta = \frac{l}{L}, \quad \bar{q}_f = \frac{q_f L^4}{EIr}, \tag{43}$$

where

$$r = \sqrt{I/A}, \tag{44}$$

is the turning radius of the nanobeam's cross section, and η is the slenderness ratio of the nanobeam.

With the aid of (43), the dimensionless governing equation of the system is written as

$$\left(1 - \tau^2 \frac{\partial^2}{\partial \bar{x}^2}\right)\frac{\partial^2 \bar{w}}{\partial \bar{t}^2} - \frac{1}{2}\left[\int_0^1 \left(\frac{\partial^2 \bar{w}}{\partial \bar{x}^2}\right)^2 dx\right]\left(1 - \tau^2 \frac{\partial^2}{\partial \bar{x}^2}\right)\frac{\partial^2 \bar{w}}{\partial \bar{x}^2}$$
$$+ \left(1 - \zeta^2 \frac{\partial^2}{\partial \bar{x}^2}\right)\frac{\partial^4 \bar{w}}{\partial \bar{x}^4} + \zeta^2 \eta^2 \frac{\partial^4 \bar{w}}{\partial \bar{x}^4} + \left(1 - \tau^2 \frac{\partial^2}{\partial \bar{x}^2}\right)\bar{q}_f = 0. \tag{45}$$

Since (45) is represented in dimensionless form, it is more convenient for us to further investigate the free vibrations of the nanobeam in a more general sense.

Equation (45) is the dimensionless equation of motion considering geometric nonlinearities and the strain gradient in the lateral direction. Upon dropping the time varying terms and transverse loading $\bar{q}$,

equation (45) may be reduced to the equation developed by Li et al. [2018] for static problems. Further, if the terms associated with the thickness-direction strain gradient and geometric nonlinearities are either neglected or absent, we can obtain the same equation given by Lu et al. [2017]. A new term, $\zeta^2\eta^2\,\partial^4\overline{w}/\partial\bar{x}^4$, has been added in (45) if compared with the mathematical model proposed by Şimşek [2016]. This new term represents the thickness-dependent size effect. It must be noted that the value of slenderness ratio η is always large (the order of 10^1 or more). Therefore, the thickness-dependent size effect can be remarkable in many cases and needs to be considered in the dynamic analysis of nanobeams. It should also be mentioned that (45) is valid when (i) the longitudinal constraints satisfy (25a) of case 1 and the transverse constraints at both ends are either pinned or clamped, or (ii) the longitudinal constraints satisfy case 3 and the transverse constraints at both ends are identical with $\bar{q}_f(\bar{x}) = \bar{q}_{f0}(1 - \bar{x})$ when $0 \leq \bar{x} \leq 1$.

4. Solutions

In this section, the nonlinear free vibration of a nanobeam governed by (45) will be studied. The external transverse loading $q_f(x, t)$ is assumed to be absent. Thus, we have

$$\left(1 - \tau^2\frac{\partial^2}{\partial\bar{x}^2}\right)\frac{\partial^2\overline{w}}{\partial\bar{t}^2} - \frac{1}{2}\left[\int_0^1\left(\frac{\partial^2\overline{w}}{\partial\bar{x}^2}\right)^2 dx\right]\left(1 - \tau^2\frac{\partial^2}{\partial\bar{x}^2}\right)\frac{\partial^2\overline{w}}{\partial\bar{x}^2} + \left(1 - \zeta^2\frac{\partial^2}{\partial\bar{x}^2}\right)\frac{\partial^4\overline{w}}{\partial\bar{x}^4} + \zeta^2\eta^2\frac{\partial^4\overline{w}}{\partial\bar{x}^4} = 0. \quad (46)$$

Based on the Galerkin's approach, equation (46) can be solved analytically by using a single-mode discretization or numerically by using a multi-mode discretization.

4.1. *Analytical solution based on the homotopy analysis method.* According to the Galerkin's approach, the approximate expression of $\overline{w}(\bar{x}, \bar{t})$ is assumed as

$$\overline{w}(\bar{x}, \bar{t}) = \phi(\bar{x})\,q(\bar{t}), \quad (47)$$

where $\phi(\bar{x})$ is the characteristic mode for a set of given boundary conditions, and $q(\bar{t})$ is the corresponding time-dependent generalized coordinate. The substitution of (47) into (46) yields

$$\frac{\partial^2 q}{\partial\bar{t}^2} + (D_{L1} + D_{L2} + D_{L3})\,q + (D_{N1} + D_{N2})\,q^3 = 0, \quad (48)$$

where

$$D_{L1} = \frac{\int_0^1\phi\phi^{(IV)}d\bar{x}}{S}, \quad D_{L2} = \frac{-\zeta^2\int_0^1\phi\phi^{(VI)}d\bar{x}}{S}, \quad D_{L3} = \frac{\zeta^2\eta^2\int_0^1\phi\phi^{(IV)}d\bar{x}}{S}, \quad (49)$$

where

$$D_{N1} = \frac{-\frac{1}{2}\int_0^1\phi\phi''d\bar{x}\int_0^1\phi'\phi'd\bar{x}}{S}, \quad D_{N2} = \frac{\frac{1}{2}\tau^2\int_0^1\phi\phi^{(IV)}d\bar{x}\int_0^1\phi'\phi'd\bar{x}}{S}. \quad (50)$$

where

$$S = \int_0^1\phi\phi\,d\bar{x} - \tau^2\int_0^1\phi\phi''d\bar{x}.$$

For pinned-pinned nanobeams, the characteristic modes can be defined as follows [Li et al. 2016b; Şimşek 2016]:

$$\phi_n(\bar{x}) = \sin(n\pi\bar{x}) \quad (n = 1, 2, 3, \ldots). \quad (51)$$

By combining (48)–(51), one obtains

$$\frac{\partial^2 q}{\partial \bar{t}^2} + \frac{(1 + \zeta^2\eta^2 + n^2\pi^2\zeta^2)\, n^4\pi^4}{1 + n^2\pi^2\tau^2} q + \frac{n^4\pi^4}{2} q^3 = 0. \tag{52}$$

One may rewrite (52) as

$$\frac{\partial^2 q}{\partial \hat{t}^2} + q + \gamma q^3 = 0, \tag{53}$$

where $\hat{t} = \omega\bar{t}$, and

$$\omega = n^2\pi^2\sqrt{\frac{1 + \zeta^2\eta^2 + n^2\pi^2\zeta^2}{1 + n^2\pi^2\tau^2}}, \quad \gamma = \frac{1 + n^2\pi^2\tau^2}{2(1 + \zeta^2\eta^2 + n^2\pi^2\zeta^2)}. \tag{54}$$

Equation $(54)_1$ is the expression of linear natural frequencies for nonlocal strain gradient beams. It is noted that the thickness-dependent effect is associated with the term of $\zeta^2\eta^2$. If the term of $\zeta^2\eta^2$ in $(54)_2$ is neglected, equation $(54)_2$ can be reduced to the expression obtained by Li et al. [2016b]. For calculation purpose, the initial conditions of the nanobeam considered are assumed to be

$$q(0) = a, \quad \dot{q}(0) = 0. \tag{55}$$

The second-order approximate frequency of (53) in the frame of homotopy analysis method can be obtained as [Liao 2003]

$$\Omega \approx \frac{131072 + 393216\gamma a^2 + 440832\gamma^2 a^4 + 218880\gamma^3 a^6 + 40599\gamma^4 a^8}{1024(4 + 3\gamma a^2)^{7/2}}. \tag{56}$$

Hence the nonlinear free vibration frequency is given by

$$\omega_{NL} = \omega_L\Omega = \frac{n^2\pi^2}{\sqrt{2\gamma}} \frac{131072 + 393216\gamma a^2 + 440832\gamma^2 a^4 + 218880\gamma^3 a^6 + 40599\gamma^4 a^8}{1024(4 + 3\gamma a^2)^{7/2}}. \tag{57}$$

4.2. Numerical results based on Galerkin's approach using a multi-mode approximation.

In Section 4.1, we have obtained the analytical solution of (57) via the homotopy analysis method based on a single-mode discretization. To demonstrate the validity of expression (57), we will numerically solve the governing equation (46) by using a multi-mode discretization. Based on the Galerkin's approach, $\bar{w}$ can be expressed as

$$\bar{w}(\bar{x}, \bar{t}) = \sum_{j=1}^{N} \phi_j(\bar{x})\, q_j(\bar{t}). \tag{58}$$

Substituting (58) into (46), multiplying by $\phi_i(\bar{x})$ and integrating over $\bar{x}$ from 0 to 1 further lead to

$$m_{ij}\frac{\partial^2 q_j}{\partial \bar{t}^2} + k_{ij}q_j + \alpha_{ijkl}\, q_j\, q_k\, q_l = 0, \tag{59}$$

where

$$m_{ij} = \int_0^1 \phi_i\phi_j d\bar{x} - \tau^2\int_0^1 \phi_1\phi_j'' d\bar{x}, \quad k_{ij} = (1 + \zeta^2\eta^2)\int_0^1 \phi_1\phi_j^{(IV)} d\bar{x} - \zeta^2\int_0^1 \phi_1\phi_j^{(VI)} d\bar{x},$$

$$\alpha_{ijkl} = -\frac{1}{2}\int_0^1 \phi_i\phi_j''\int_0^1 \phi_k'\phi_l'\, d\bar{x}\, d\bar{x} + \frac{1}{2}\tau^2\int_0^1 \phi_i\phi_j^{(IV)}\int_0^1 \phi_k'\phi_l'\, d\bar{x}\, d\bar{x}. \tag{60}$$

For the purpose of numerical calculations, equation (59) is rewritten as its first-order state form, i.e.,

$$\dot{z} = Az + G(z), \tag{61}$$

where

$$p = \frac{\partial p}{\partial \bar{t}}, \quad z = [q; p] \quad \text{and} \quad A = \begin{bmatrix} 0 & I \\ -M^{-1}K & 0 \end{bmatrix}, \quad G = \begin{bmatrix} 0 \\ -M^{-1}g \end{bmatrix}. \tag{62}$$

The initial conditions of the beam are assumed to be defined by (55) as well.

Equation (62) is then solved by employing a fourth-order Runge–Kutta integration method with variable step sizes. Hence we can obtain the displacement responses for given values of initial conditions, strain-gradient parameter ζ, stress-gradient parameter τ and slenderness ratio η. Typical results are shown in Figure 2.

Numerical results of nonlinear free vibration frequencies are compared in Figure 3 with the analytical solutions, for various truncated mode number N, strain-gradient and stress-gradient parameters. That
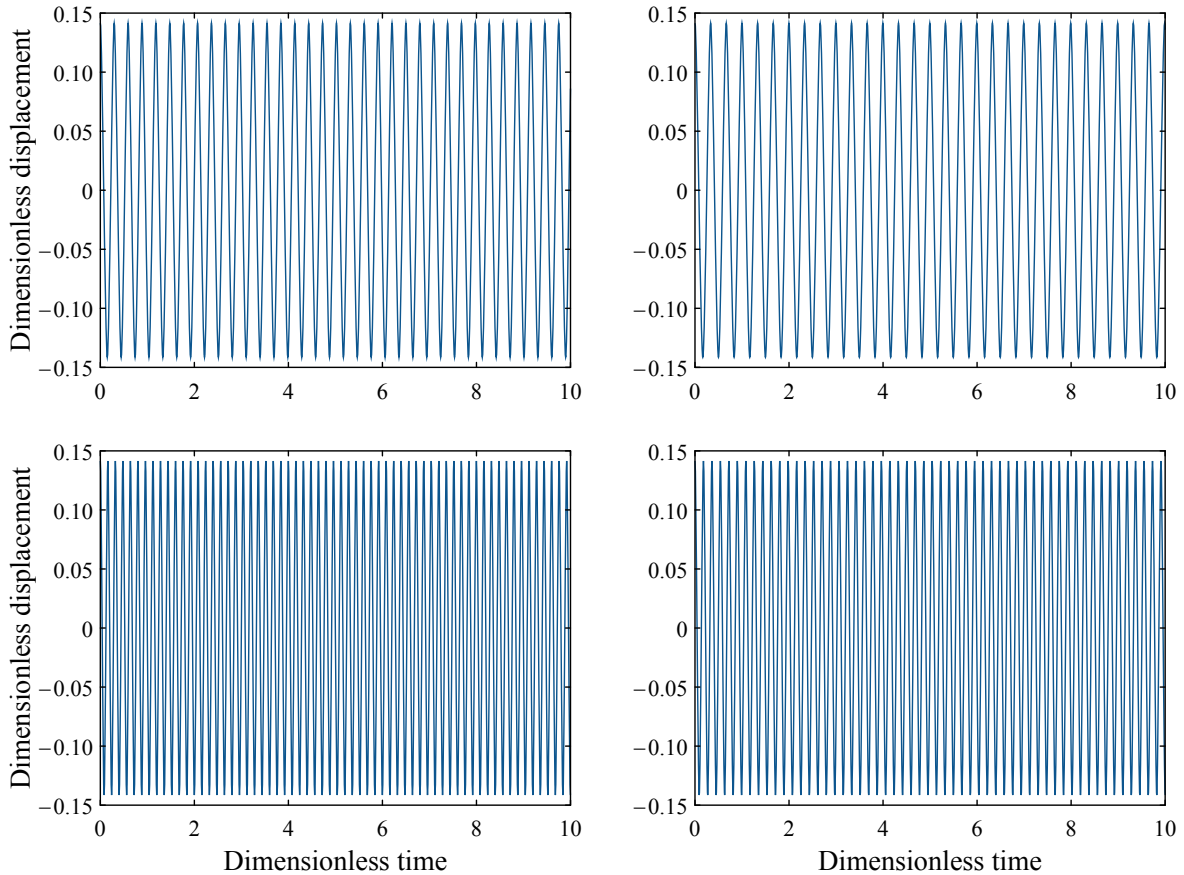

Figure 2. Displacement responses based on high-dimensional Galerkin discretization model. $N = 3$; $a = 0.1$; $\eta = 20$; $\zeta = 0.1$ (top) or $\zeta = 0.2$ (bottom); $\tau = 0.1$ (left) or $\tau = 0.2$ (right).
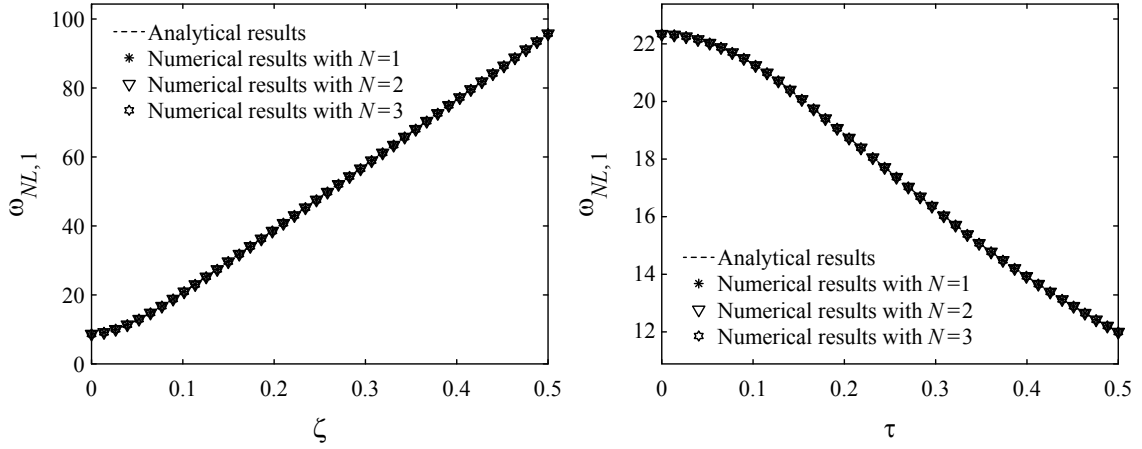
Figure 3. The nonlinear fundamental frequencies $\omega_{NL,1}$ predicted by analytical and numerical methods ($\eta = 20$, $a = 0.1$); $\tau = 0.1$ (left) and $\zeta = 0.1$ (right).

figure suggests that the single-mode analytical results agree well with the high-dimensional numerical ones. Since the single-mode-based analytical result has high precision, we will utilize the analytical expression of (57) to investigate the nonlinear free vibrations of the nanobeam in the following analysis.

4.3. *Parameter analysis.* Based on (57), the ratios of nonlinear nonclassical fundamental frequencies $\omega_{NL,1}$ to the linear nonclassical fundamental frequencies $\omega_{L,1}$ are obtained for various γa^2. Typical results are shown in Figure 4 (left). It is seen that the nonlinear frequency ratio increases as the initial amplitude a increases, which is known as a nonlinear "hardening spring" behavior. This is because that the increase of initial amplitude can increase the axial stretching, yielding larger nonlinear frequencies. The size-dependent effects of ζ, τ, and η on the nonlinear frequencies of the nanobeam may be implicit in the nonlinear parameter γ. Thus, there is a "hardening spring" behavior of size effects when γ is larger than the classic one of $\gamma = 0.5$ and a "softening spring" behavior when $\gamma < 0.5$.
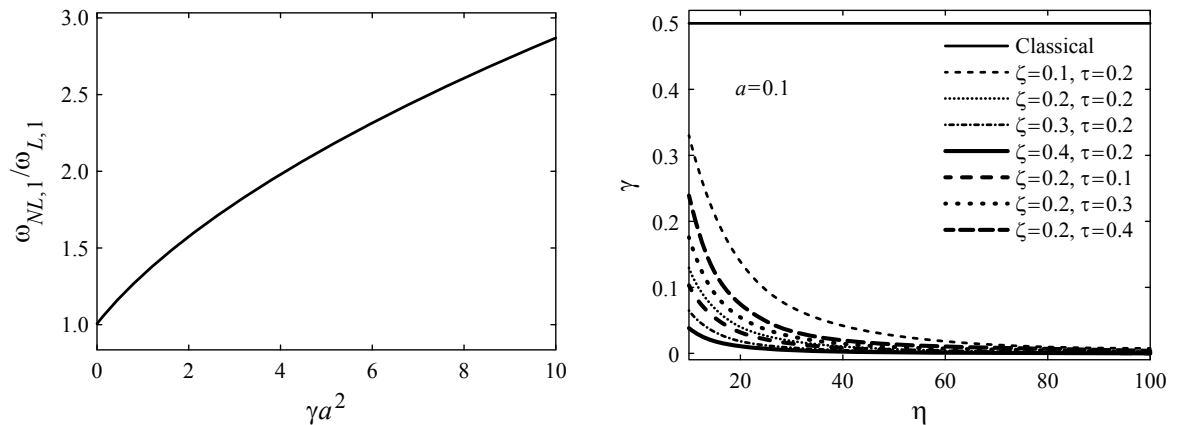
Figure 4. Left: fundamental frequencies ratios $\omega_{NL,1}/\omega_{L,1}$ versus γa^2. Right: nonlinear parameter γ versus slenderness ratio η.
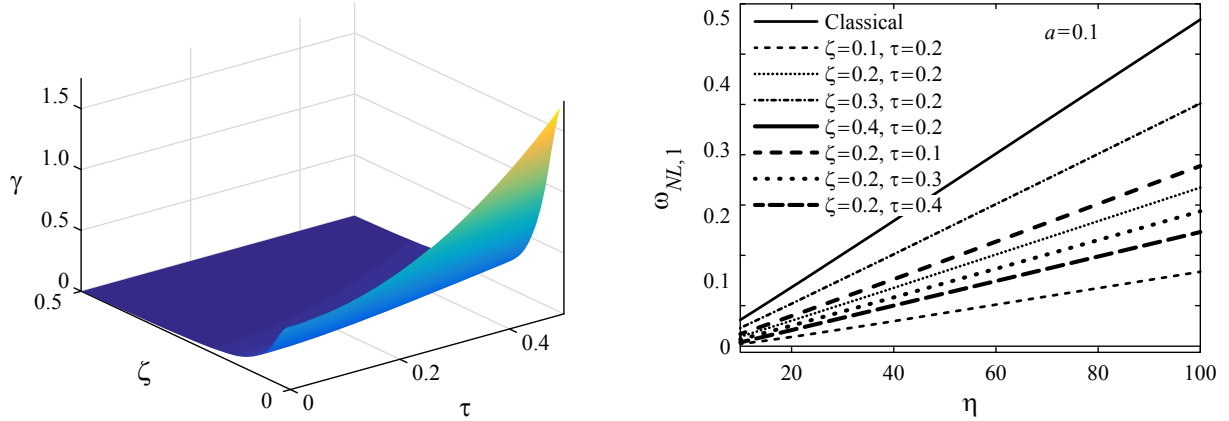
Figure 5. Left: nonlinear parameter γ for various ζ and τ when $a = 0.1$ and $\eta = 20$. Right: the effect of slenderness ratio η on $\omega_{NL,1}$.

Unlike the size-dependent effect of ζ, τ, and η on linear frequencies, the evolution of which shows a trend of monotonous increase (see expression $(54)_1$) when any one of these three key parameters is increased, the evolution of the size-dependent effect of ζ, τ, and η on nonlinear frequencies is quite different. It is observed from Figure 4 (right) and Figure 5 (left) that the parameter γ increases with increasing τ and decreases with increasing ζ and η. This implies that the two key parameters of ζ and η can reduce the size-dependent effect on nonlinear frequencies when considering the geometric nonlinearities quantized by γ. As shown in Figure 5 (left), for $\zeta = 0$ and $\tau = 0$, the value of γ corresponds to the case of a classical beam. Interestingly, the nonlocal strain gradient beams can produce either a lager or a smaller nonlinear frequency ratio than the classical one.

More importantly, the slenderness ratio η has a significant effect on the nonlinearity of the nanobeam, as shown in Figure 4 (right). It is not surprising, therefore, that the influence of η on the nonlinear frequencies is remarkable (see Figure 5, right). It is noted that the nonlinear frequencies increase nearly linearly with increasing slenderness ratio η.

The results shown in Figure 6 indicate that the nonlinear fundamental frequencies $\omega_{NL,1}$ with consideration of the thickness-dependent size effect is much larger than those without that consideration. Indeed, the underlying reason for the thickness-dependent size effect (stiffness-hardening) is associated with the nanobeam's oscillations. During oscillations, the cross section of the nanobeam and the corresponding turning radius become smaller while the slenderness ratio is increased. In this case, the strain gradient in the thickness direction will become larger and the effect of the corresponding high-order stress is amplified, resulting in an added remarkable positive stiffness.

5. Conclusions

We proposed a nonlinear nonlocal strain gradient Euler–Bernoulli beam model for dynamic analysis of nanobeams with two immovable supports and used it to study the nonlinear free vibration of nanobeams. In particular, the effect of strain gradient in the thickness direction, which was usually neglected before, has been accounted for in the current dynamic analysis. The governing equation is derived for all possible boundary conditions and is further simplified for symmetric boundary conditions and lateral loads.
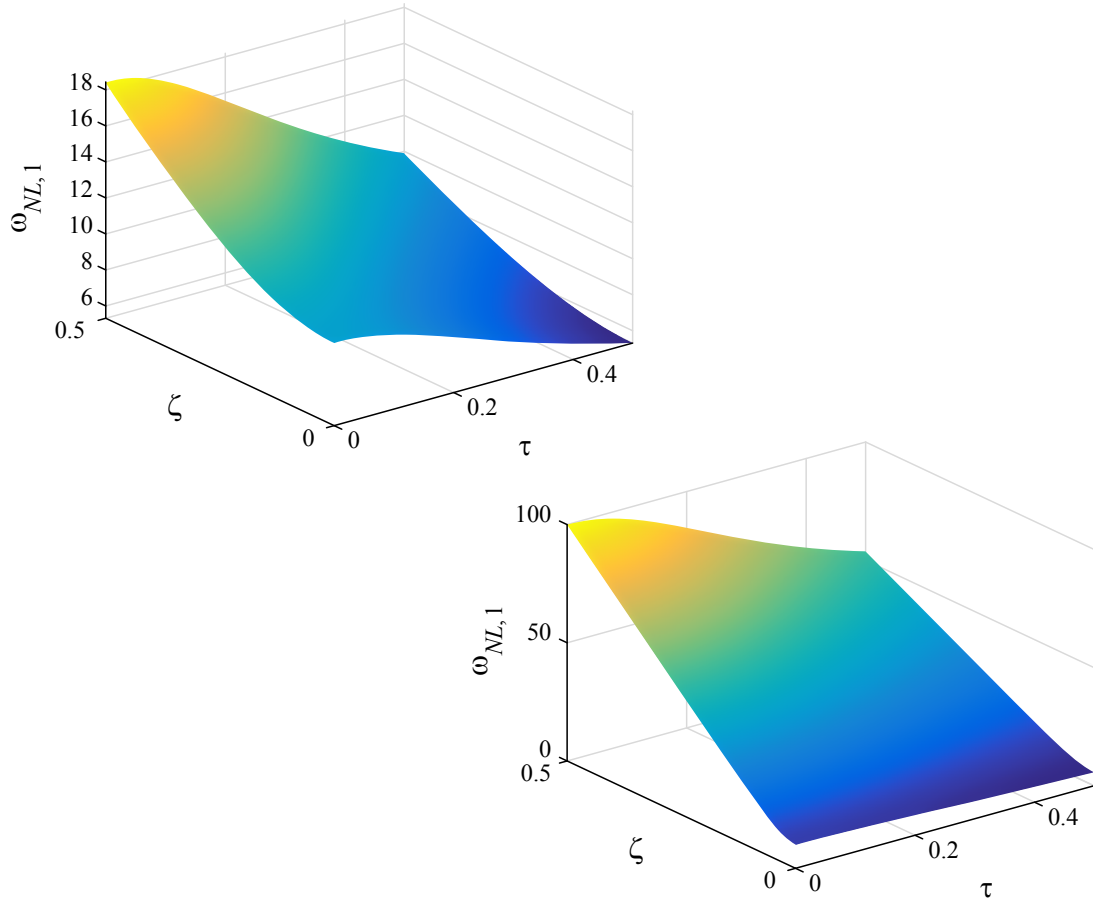
Figure 6. The nonlinear fundamental frequencies $\omega_{NL,1}$ with and without strain gradient effect in the thickness direction: $\eta = 20$, without $\varepsilon_{xx,z}$ effect (left) and $\eta = 20$, with $\varepsilon_{xx,z}$ effect (right).

Using a one-mode Galerkin's discretization, the governing equation is analytically solved using the homotopy analysis method, yielding an approximate analytical formulation of the nonlinear frequencies for pinned-pinned boundary conditions. The governing equation is further numerically solved via a Galerkin approach with a multi-mode discretization. It is found that the numerical results agree well with the analytical one. Our results showed that the thickness-dependent size effect on the nonlinear free vibration of nanobeams may be remarkable, highlighting the importance of thickness-dependent size effects in the design of nanoscale devices and systems.

In this study, we have finalized the nonlinear governing equation for symmetric boundary conditions by deriving the explicit expression of axial stretching forces (N_{0x}). For asymmetric boundary conditions and some other cases with complex kinds of lateral loads, how to determine the expression of N_{0x} is still a challenging question and needs further investigations.

The thickness-dependent size effect is also a kind of strain gradient one. However, some previous studies focused on the strain gradient effect in the lengthwise direction (x direction) only by neglecting

the strain gradient effect in the thickness direction (z direction). In this work, we found that the strain gradient in the thickness direction can be very important for slender nanobeams. As can be expected, when a three-dimensional nanobeam is considered, the strain gradient effects in all the x, y, and z directions need to be considered.

Acknowledgement

References

[Agrawal et al. 2008] R. Agrawal, B. Peng, E. E. Gdoutos, and H. D. Espinosa, "Elasticity size effects in ZnO nanowires — a combined experimental-computational approach", *Nano Lett.* **8**:11 (2008), 3668–3674.

[Aifantis 1992] E. C. Aifantis, "On the role of gradients in the localization of deformation and fracture", *Int. J. Eng. Sci.* **30**:10 (1992), 1279–1299.

[Aifantis and Willis 2005] K. E. Aifantis and J. R. Willis, "The role of interfaces in enhancing the yield strength of composites and polycrystals", *J. Mech. Phys. Solids* **53**:5 (2005), 1047–1070.

[Akgöz and Civalek 2011] B. Akgöz and Ö. Civalek, "Strain gradient elasticity and modified couple stress models for buckling analysis of axially loaded micro-scaled beams", *Int. J. Eng. Sci.* **49**:11 (2011), 1268–1280.

[Anker et al. 2008] J. N. Anker, W. P. Hall, O. Lyanders, N. C. Shah, J. Zhao, and R. P. V. Duyne, "Biosensing with plasmonic nanosensors", *Nat. Mater.* **7** (2008), 422–453.

[Ansari et al. 2015] R. Ansari, R. Gholami, M. F. Shojaei, V. Mohammadi, and S. Sahmani, "Bending, buckling and free vibration analysis of size-dependent functionally graded circular/annular microplates based on the modified strain gradient elasticity theory", *Eur. J. Mech. A-Solid.* **49** (2015), 251–267.

[Assadi and Farshi 2011] A. Assadi and B. Farshi, "Stability analysis of graphene based laminated composite sheets under non-uniform inplane loading by nonlocal elasticity", *Appl. Math. Model.* **35**:9 (2011), 4541–4549.

[Aydogdu 2009] M. Aydogdu, "A general nonlocal beam theory: its application to nanobeam bending, buckling and vibration", *Physica E* **41**:9 (2009), 1651–1655.

[Şimşek 2016] M. Şimşek, "Nonlinear free vibration of a functionally graded nanobeam using nonlocal strain gradient theory and a novel Hamiltonian approach", *Int. J. Eng. Sci.* **105** (2016), 12–27.

[Cui et al. 2001] Y. Cui, Q. Wei, H. Park, and C. M. Lieber, "Nanowire nanosensors for highly sensitive and selective detection of biological and chemical species", *Science* **293**:5533 (2001), 1289–1292.

[Dai et al. 2018] H. L. Dai, S. Ceballes, A. Sbdelkefi, Y. Z. Hong, and L. Wang, "Exact modes for post-buckling characteristics of nonlocal nanobeams in longitudinal magnetic field", *Appl. Math. Model.* **55** (2018), 758–775.

[Ç. Demir and Civalek 2017] Ç. Demir and Ö. Civalek, "On the analysis of microbeams", *Int. J. Eng. Sci.* **121** (2017), 14–33.

[Duan and Wang 2007] W. H. Duan and C. M. Wang, "Exact solutions for axisymmetric bending of micro/nanoscale circular plates based on nonlocal plate theory", *Nanotechnology* **18**:38 (2007), 385704.

[Eaton and West 2010] P. Eaton and P. West, *Atomic force microscopy*, Oxford University Press, 2010.

[Ebrahimi et al. 2016] F. Ebrahimi, M. R. Barati, and A. Dabbagh, "A nonlocal strain gradient theory for wave propagation analysis in temperature-dependent inhomogeneous nanoplates", *Int. J. Eng. Sci.* **107** (2016), 169–182.

[Eltaher et al. 2016] M. A. Eltaher, M. E. Khater, and S. A. Emam, "A review on nonlocal elastic models for bending, buckling, vibrations, and wave propagation of nanoscale beams", *Appl. Math. Model.* **40**:5-6 (2016), 4109–4128.

[Eom et al. 2011] K. Eom, H. S. Park, D. S. Yoon, and T. Kwon, "Nanomechanical resonators and their applications in biological/chemical detection: nanomechanics principles", *Phys. Rep.* **503**:4-5 (2011), 115–163.

[Eringen 1983] A. C. Eringen, "On differential equations of nonlocal elasticity and solutions of screw dislocation and surface waves", *J. Appl. Phys.* **54**:9 (1983), 4703–4710.

[Eringen 2002] A. C. Eringen, *Nonlocal continuum field theories*, Springer, 2002.

[Farokhi et al. 2016] H. Farokhi, M. P. Païdoussis, and A. K. Misra, "A new nonlinear model for analyzing the behaviour of carbon nanotube-based resonators", *J. Sound Vib.* **378** (2016), 56–75.

[Ghavanloo and Fazelzadeh 2013a] E. Ghavanloo and S. A. Fazelzadeh, "Radial vibration of free anisotropic nanoparticles based on nonlocal continuum mechanics", *Nanotechnology* **24**:7 (2013), 075702.

[Ghavanloo and Fazelzadeh 2013b] E. Ghavanloo and S. A. Fazelzadeh, "Free vibration analysis of orthotropic doubly-curved shallow shells based on the gradient elasticity", *Compos. B Eng.* **45**:1 (2013), 1448–1457.

[Hu et al. 2008] Y.-G. Hu, K. M. Liew, Q. Wang, X. Q. He, and B. I. Yakobson, "Nonlocal shell model for elastic wave propagation in single- and double-walled carbon nanotubes", *J. Mech. Phys. Solids* **56**:12 (2008), 3475–3485.

[Huang 2012] Z. Huang, "Nonlocal effects of longitudinal vibration in nanorod with internal long-range interactions", *Int. J. Solids Struct.* **49**:15-16 (2012), 2150–2154.

[Ieşan 2014] D. Ieşan, "Deformation of thin chiral plates in strain gradient elasticity", *Eur. J. Mech. A-Solid.* **44** (2014), 212–221.

[Khademolhosseini et al. 2010] F. Khademolhosseini, R. K. N. D. Rajapakse, and A. Nojeh, "Torsional buckling of carbon nanotubes based on nonlocal elasticity shell models", *Comput. Mater. Sci.* **48**:4 (2010), 736–742.

[Kong et al. 2009] S. Kong, S. Zhou, Z. Nie, and K. Wang, "Static and dynamic analysis of micro beams based on strain gradient elasticity theory", *Int. J. Eng. Sci.* **47**:4 (2009), 487–498.

[Kulkarni et al. 2005] A. J. Kulkarni, M. Zhou, and F. J. Ke, "Orientation and size dependence of the elastic properties of zinc oxide nanobelts", *Nanotechnology* **16**:12 (2005), 2749–2756.

[Lam et al. 2003] D. C. C. Lam, F. Yang, A. C. M. Chong, J. Wang, and P. Tong, "Experiments and theory in strain gradient elasticity", *J. Mech. Phys. Solids* **51**:8 (2003), 1477–508.

[Lazopoulos 2012] A. K. Lazopoulos, "Dynamic response of thin strain gradient elastic beams", *Int. J. Mech. Sci.* **58**:1 (2012), 27–33.

[Lembo 2016] M. Lembo, "On nonlinear deformations of nonlocal elastic rods", *Int. J. Solids Struct.* **90** (2016), 215–227.

[Li 2014] C. Li, "Torsional vibration of carbon nanotubes: comparison of two nonlocal models and a semi-continuum model", *Int. J. Mech. Sci.* **82** (2014), 25–31.

[Li et al. 2003] X. Li, B. Bhushan, K. Takashima, C.-W. Baek, and Y.-K. Kim, "Mechanical characterization of micro/nanoscale structures for MEMS/NEMS applications using nanoindentation techniques", *Ultramicroscopy* **97**:1-4 (2003), 481–494.

[Li et al. 2007] M. Li, H. X. Tang, and M. L.Roukes, "Ultra-sensitive NEMS-based cantilevers for sensing, scanned probe and very high-frequency applications", *Nat. Nanotechnol.* **2** (2007), 114–120.

[Li et al. 2015a] C. Li, S. Li, L. Yao, and Z. Zhu, "Nonlocal theoretical approaches and atomistic simulations for longitudinal free vibration of nanorods/nanotubes and verification of different nonlocal models", *Appl. Math. Model.* **39**:15 (2015), 4570–4585.

[Li et al. 2015b] C. Li, L. Yao, W. Chen, and S. Li, "Comments on nonlocal effects in nano-cantilever beams", *Int. J. Eng. Sci.* **87** (2015), 47–57.

[Li et al. 2015c] L. Li, Y. Hu, and L. Ling, "Flexural wave propagation in small-scaled functionally graded beams via a nonlocal strain gradient theory", *Compos. Struct.* **133** (2015), 1079–1092.

[Li et al. 2016a] L. Li, Y. Hu, and X. Li, "Longitudinal vibration of size-dependent rods via nonlocal strain gradient theory", *Int. J. Mech. Sci.* **115-116** (2016), 135–144.

[Li et al. 2016b] L. Li, X. Li, and Y. Hu, "Free vibration analysis of nonlocal strain gradient beams made of functionally graded material", *Int. J. Eng. Sci.* **102** (2016), 77–92.

[Li et al. 2018] L. Li, H. Tang, and Y. Hu, "The effect of thickness on the mechanics of nanobeams", *Int. J. Eng. Sci.* **123** (2018), 81–89.

[Liao 2003] S. Liao, *Beyond perturbation: introduction to the homotopy analysis method*, Chapman & Hall/CRC Press, 2003.

[Lim et al. 2015] C. W. Lim, G. Zhang, and J. N. Reddy, "A higher-order nonlocal elasticity and strain gradient theory and its applications in wave propagation", *J. Mech. Phys. Solids* **78** (2015), 298–313.

[Lu et al. 2017] L. Lu, X. Guo, and J. Zhao, "A unified nonlocal strain gradient model for nanobeams and the importance of higher order terms", *Int. J. Eng. Sci.* **119** (2017), 265–277.

[McFarland et al. 2005] A. W. McFarland, M. A. Poggi, M. J. Doyle, L. A. Bottomley, and J. S. Colton, "Influence of surface stress on the resonance behavior of microcantilevers", *Appl. Phys. Lett.* **87**:5 (2005), 053505.

[Mindlin 1965] R. D. Mindlin, "Second gradient of strain and surface-tension in linear elasticity", *Int. J. Solids Struct.* **1**:4 (1965), 417–428.

[Movassagh and Mahmoodi 2013] A. A. Movassagh and M. J. Mahmoodi, "A micro-scale modeling of Kirchhoff plate based on modified strain-gradient elasticity theory", *Eur. J. Mech. A-Solid.* **40** (2013), 50–59.

[Murmu and Adhikari 2011] T. Murmu and S. Adhikari, "Nonlocal vibration of bonded double-nanoplate-systems", *Compos. B Eng.* **42**:7 (2011), 1901–1911.

[Narendar and Gopalakrishnan 2010] S. Narendar and S. Gopalakrishnan, "Ultrasonic wave characteristics of nanorods via nonlocal strain gradient models", *J. Appl. Phys.* **107** (2010), 084312.

[Papargyri-Beskou et al. 2012] S. Papargyri-Beskou, S. V. Tsinopoulos, and D. E. Beskos, "Wave propagation in and free vibrations of gradient elastic circular cylindrical shells", *Acta Mech.* **223**:8 (2012), 1789–1807.

[Patolsky and Lieber 2005] F. Patolsky and C. M. Lieber, "Nanowire nanosensors", *Mater. Today* **8**:5 (2005), 20–28.

[Pei et al. 2004] J. Pei, F. Tian, and T. Thundat, "Glucose biosensor based on the microcantilever", *Anal. Chem.* **76**:2 (2004), 292–297.

[Pereira 2001] R. S. Pereira, "Atomic force microscopy as a novel pharmacological tool", *Biochem. Pharmacol.* **62**:8 (2001), 975–983.

[Polizzotto 2012] C. Polizzotto, "A gradient elasticity theory for second-grade materials and higher order inertia", *Int. J. Solids Struct.* **49**:15-16 (2012), 2121–2137.

[Rahaeifard 2015] M. Rahaeifard, "Size-dependent torsion of functionally graded bars", *Compos. B Eng.* **82** (2015), 205–211.

[Reddy 2007] J. N. Reddy, "Nonlocal theories for bending, buckling and vibration of beams", *Int. J. Eng. Sci.* **45**:2-8 (2007), 288–307.

[Reddy 2010] J. N. Reddy, "Nonlocal nonlinear formulations for bending of classical and shear deformation theories of beams and plates", *Int. J. Eng. Sci.* **48**:11 (2010), 1507–1518.

[Shen 2010] H.-S. Shen, "Nonlocal shear deformable shell model for bending buckling of microtubules embedded in an elastic medium", *Phys. Lett. A* **374**:39 (2010), 4030–4039.

[Shi et al. 2010] X. Shi, Y. Cheng, N. M. Pugno, and H. Gao, "A translational nanoactuator based on carbon nanoscrolls on substrates", *Appl. Phys. Lett.* **96**:5 (2010), 053115.

[Sul and Yang 2009] O. Sul and E. H. Yang, "A multi-walled carbon nanotube-aluminum bimorph nanoactuator", *Nanotechnol.* **20**:9 (2009), 095502.

[Thai 2012] H.-T. Thai, "A nonlocal beam theory for bending, buckling, and vibration of nanobeams", *Int. J. Eng. Sci.* **52** (2012), 56–64.

[Tuna and Kirca 2016] M. Tuna and M. Kirca, "Exact solution of Eringen's nonlocal integral model for bending of Euler–Bernoulli and Timoshenko beams", *Int. J. Eng. Sci.* **105** (2016), 80–92.

[Wang and Zhang 2018] Y. Wang and Z. Zhang, "Non-local buckling analysis of functionally graded nanoporous metal foam nanoplates", *Coatings* **8**:11 (2018), 389.

[Wang et al. 2006] C. M. Wang, Y. Y. Zhang, S. S. Ramesh, and S. Kitipornchai, "Buckling analysis of micro- and nano-rods/tubes based on nonlocal Timoshenko beam theory", *J. Phys. D Appl. Phys.* **39**:17 (2006), 3904–3909.

[Wang et al. 2011] B. Wang, S. Zhou, J. Zhao, and X. Chen, "A size-dependent Kirchhoff micro-plate model based on strain gradient elasticity theory", *Eur. J. Mech. A-Solid.* **30**:4 (2011), 517–524.

[Wang et al. 2018] Y. Q. Wang, H. L. Zhao, C. Ye, and J. W. Zu, "A porous microbeam model for bending and vibration analysis based on the sinusoidal beam theory and modified strain gradient theory", *Int. J. Appl. Mech.* **10**:5 (2018), 1850059.

[Xu and Deng 2016] X.-J. Xu and Z.-C. Deng, "Closed-form frequency solutions for simplified strain gradient beams with higher-order inertia", *Eur. J. Mech. A-Solid.* **56** (2016), 59–72.

[Xu et al. 2017a] X.-J. Xu, X.-C. Wang, M.-L. Zheng, and Z. Ma, "Bending and buckling of nonlocal strain gradient elastic beams", *Compos. Struct.* **160** (2017), 366–377.

[Xu et al. 2017b] X.-J. Xu, M.-L. Zheng, and X.-C. Wang, "On vibrations of nonlocal rods: Boundary conditions, exact solutions and their asymptotics", *Int. J. Eng. Sci.* **119** (2017), 217–231.

[Zeighampour and Beni 2014] H. Zeighampour and Y. T. Beni, "Cylindrical thin-shell model based on modified strain gradient theory", *Int. J. Eng. Sci.* **78** (2014), 27–47.

[Zhang et al. 2015] B. Zhang, Y. He, D. Liu, L. Shen, and J. Lei, "An efficient size-dependent plate theory for bending, buckling and free vibration analyses of functionally graded microplates resting on elastic foundation", *Appl. Math. Model.* **39**:13 (2015), 3814–3845.

[Zhu and Li 2017] X. Zhu and L. Li, "On longitudinal dynamics of nanorods", *Int. J. Eng. Sci.* **120** (2017), 129–145.

WEI CHEN: `w_chen@hust.edu.cn`
Department of Mechanics, Huazhong University of Science and Technology, Wuhan, China

and

Hubei Key Laboratory for Engineering Structural Analysis and Safety Assessment, Wuhan, China

LIN WANG: `wanglindds@hust.edu.cn`
Department of Mechanics, Huazhong University of Science and Technology, Wuhan, China

and

Hubei Key Laboratory for Engineering Structural Analysis and Safety Assessment, Wuhan, China

HU-LIANG DAI: `daihulianglx@hust.edu.cn`
Department of Mechanics, Huazhong University of Science and Technology, Wuhan, China

and

Hubei Key Laboratory for Engineering Structural Analysis and Safety Assessment, Wuhan, China

■msp

ENERGY-MAXIMIZING HOLES IN AN ELASTIC PLATE
UNDER REMOTE LOADING

SHMUEL VIGDERGAUZ AND ISAAC ELISHAKOFF

A single hole in an infinite elastic plate is used as the simplest setup to find the hole shape which induces the maximum energy increment in a homogeneous stress field given at infinity. In order to avoid the energy unboundedness trivially caused by jagged shapes with an arbitrarily large number of sharp notches, we restrict our attention to only fully concave shapes with everywhere negative curvature. It goes in parallel with the well-known fact that the energy-minimizing hole shapes are invariably convex. Though rather empirical, this easily verified condition allows us to obtain finite and stable energy maxima at moderate computation cost using the same flexible scheme as in the first author's previous research on optimal shaping of the single energy-minimizing hole. The scheme combines a standard genetic algorithm optimization with an efficient semianalytic direct solver and with an economic shape parametrization, both formulated in complex-variable terms. The results obtained are detailed in tables and graphs. They may stimulate further studies in both theoretical and practical directions.

1. Background and motivation

Thin and flat perforated construction elements are widely employed in engineering design. Fulfilling technological functions, holes weaken the structure and hence may substantially reduce its mechanical performance. This happens due to high stresses and energy local concentration induced by the holes in an applied external field σ^∞ with the components

$$\sigma_{xx}^\infty = P, \quad \sigma_{yy}^\infty = Q, \quad \sigma_{xy}^\infty = 0. \tag{1-1}$$

The resultant stress state of the structure depends on the holes' shapes, areas, and mutual arrangement. Of these geometrical factors, the shapes are less important and less determined. On the one hand, they can be chosen to achieve a more favorable construction stress state which, on the other hand, may be adversely affected by technologically inevitable shape uncertainties, even relatively small ones (in the intuitive sense).

Mathematically, such situations fall either in optimization, i.e., looking for the most favorable solutions, or antioptimization, i.e., searching for the least favorable solutions (with regard to the same certain criterion). Interested readers may consult with [Elishakoff and Ohsaki 2010; Hlaváček et al. 2004; Banichuk and Neittaanmäki 2010]. This paper also adopts the worst-case scenario approach.

Quantitatively, the stress state is assessed by either of two interrelated criteria, each having its own field of application:

(A) The stress concentration factor (SCF), that is, the maximum of the von Mises stresses along the hole shapes.

(B) The energy increment brought by the holes into a given outer stress field. For definiteness purposes, the increment is taken at unit load and normalized by the area of the hole.

Extremization of either (A) or (B) gives some extremal (the "best" or the "worst") properties of the perforated plate.

The SCF (criterion (A)) is most generally employed when the holes' shapes are treated deterministically and is found by solving the direct in-plane problem of elastostatics with no optimization involved. One can refer to [Pilkey and Pilkey 2008; Savruk and Kazberuk 2017; Murakami 2017], as well as the review paper [Hardy and Malik 1992].

Shape uncertainties were dealt with probabilistically by Pal'mov [1963] and Sheinin [1972] who developed a probabilistic risk measure. These and other researches were summarized in [Khusu et al. 1975; Vitenberg 1971]. This approach has a drawback which consists in the difficulty of obtaining the needed probabilistic characteristics of the random shapes. Recognizing this difficulty, Givoli and Elishakoff [1992] resorted to an alternative approach where they characterized uncertainty via some integral bounds and correctly exemplified a hypocycloid as the simplest "worst" hole shape. The possible disadvantage of such an approach consists in the possibility that the integral inequality is satisfied and still the shape of the form might possess a very sharp, even if very small, notch with an arbitrarily large SCF. In other words, this criterion, due to its local nature, is unbounded above and so is unsuitable for antioptimization.

At the same time, such a single notch produces only a finite energy increment, even in the limiting case of a needle shape. By this reason, more promising is the stress-averaging energy criterion (B), which can deal with some sort of extremal forms over a wide variety of the holes' shapes. For examples, the reader may consult [Cherkaev et al. 1998; Vigdergauz 2006; Pedersen et al. 1992; Pedersen 2013]. To the authors' best knowledge, the only published attempt to analyze the energy-*maximizing* ("worst") shape was made by Vigdergauz [2006] for the simplest case of a single square symmetric hole in a plate under remote shear by exploiting the semianalytical optimization scheme specially developed for identifying the energy-*minimizing* shapes. As the shape's design variables, this accepts the first n nonzero terms of the Laurent series of the conformal mapping of the shape sought onto a circle. Expectedly, with increasing n the antioptimized hole shape tends to form a rapidly growing number of small sharp notches (manifested themselves as shape curvature oscillations) whose overall energy increment also grows and actually turns unbounded. By contrast, the energy-*minimizing* process is highly stable even for $n = 4 \div 6$ as shown numerically in [Cherkaev et al. 1998; Vigdergauz 2006].

Remarkably, the resultant optimal holes' shapes are convex (or, equivalently, have a nonnegative curvature) everywhere, although this was not required *a priori* in the solving procedure. As if reversing the situation, we propose to confine our further antioptimization analysis to only concave shapes with nonpositive curvature and hence avoid generating multiple notches. Computations performed under this restriction show fast convergence (again at $n = 4 \div 6$) to stable finite maxima. These, combined with the previously obtained minimum values, comprise the attainable two-sided bounds on the energy increment for any hole shape of a constant-signed curvature.

Our contribution is therefore three-fold:

- First, the integral-type energy increment is proposed as a new antioptimization criterion instead of the local SCF, which is trivially unbounded in the deterministic (nonprobabilistic) risk maximization.

- Second, the obvious necessity of avoiding the uncontrolled appearance of multiple edge notches is transformed to a rather "natural" and easily verified condition of a nonpositive shape curvature.

- Finally, using the previously developed global optimization scheme, the detailed numerical results are obtained for a single energy-maximizing hole with various degrees p of rotational symmetry under biaxial tension and pure shear. The resultant shapes are close to p-cusped hypocycloids with the energy maximum decreasing at increasing p. Recently, similar curves have been considered by Shahzad et al. [2017] in the related context of out-of-plane elasticity.

The rest of the paper is structured as follows. Section 2 formalizes the problem in terms of the relevant analytical background. Section 3 details the proposed three-component algorithm which provides a stable numerical solution of the antioptimization problem at hand. The results obtained are presented and discussed in Section 4. Our findings are summarized in Section 5. Some new analytical derivations are placed in the Appendix.

2. Proposed model and basic equations

Locate an isotropic and linearly elastic infinite plate in the plane of a complex variable $z = x + iy$. Let the plate contain a single traction-free hole with a piecewise smooth boundary L enclosing the origin of the Cartesian system xOy. Let also the contour L be composed of p convex or concave identical smooth arcs λ_j, $j = \overline{1, p}$ sequentially rotated around the origin. They form p connection points, possibly irregular, as exemplified in Figure 1 for $p = 4$. In what follows, we denote these shapes as L_p, $p = 2, 3, \ldots$, retaining the notation L for general closed curves. The assumption of the constant-signed arcs' curvature will be shown to be crucial for the optimization analysis performed in the next sections.

To facilitate further general derivations, we parameterize a shape L with a real angular variable θ along the unit circle γ:

$$L : t = \omega(\xi), \quad \xi = \exp i\theta \in \gamma, \quad \bar{\xi} = \xi^{-1}, \quad |\xi| = 1, \tag{2-1}$$

where $\omega(\zeta)$ is the univalent analytic function informally mapping the exterior $\Sigma : |\zeta| \geq 1$ of γ onto the considered elastic domain S:
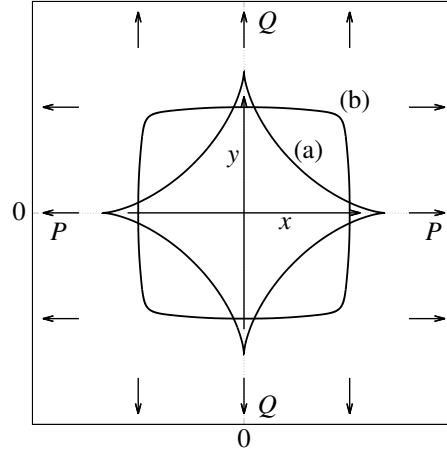
$$\Sigma + \gamma \xrightarrow[\omega(\zeta)]{} S + L, \quad \omega(\zeta) = \zeta + \sum_{k=1}^{\infty} d_k \zeta^{-k}. \tag{2-2}$$

Without loss of generality, say L is placed symmetrically with respect to the x-axis and, hence, the coefficients $\{d_k\}$ are pure real.

The traction-free condition along the hole boundary reads

$$\sigma_{\rho\rho}(t), \ \sigma_{\rho\tau}(t) \equiv 0, \quad t \in L, \tag{2-3}$$

where $\sigma(t) = \{\sigma_{\rho\rho}, \sigma_{\tau\tau}, \sigma_{\rho\tau}\}$ stands for the stress tensor in a local system of curvilinear orthogonal coordinates (ρ, τ) at a point $t \in L$.

Figure 1. The problem schematic: an infinite plate with a traction-free hole under uniform stresses. The cases $P = Q$ and $P = -Q$ correspond to remote bulk and shear, respectively. The piecewise smooth hole boundary possesses a certain rotational symmetry and is either concave (a) or convex (b) everywhere except possibly at a finite number of angular points.

Under a given remote load (1-1), the plate is in plain strain or plain stress, so displacements or gradients in the out-of-plain direction may be omitted from consideration. Then the resultant state of stress in the auxiliary domain $\Sigma + \gamma$ can be effectively described by a pair of the Kolosov–Muskhelishvili (KM) potentials [Muskhelishvili 1963], which are complex-valued analytic functions in Σ and continuously extendible to γ, with far-field asymptotics (1-1):

$$\Phi_0(\zeta) = B + \Phi(\zeta), \quad \Psi_0(\zeta) = \Gamma + \Psi(\zeta), \ \zeta \in \Sigma, \quad \Phi(\zeta), \ \Psi(\zeta) = O(|\zeta|^{-2}); \qquad \text{(2-4a)}$$

$$4B = \text{Tr}\{\sigma^\infty\} = Q + P, \quad 2\Gamma = \text{Dev}\{\sigma^\infty\} = Q - P, \quad \text{Im } B, \ \text{Im } \Gamma = 0, \qquad \text{(2-4b)}$$

and convergent series expansions

$$\Phi(\zeta) = \sum_{k=2}^{\infty} a_k \zeta^{-k}, \quad \Psi(\zeta) = \sum_{k=2}^{\infty} b_k \zeta^{-k}, \quad \zeta \in \Sigma + \gamma. \qquad \text{(2-5)}$$

The local stresses are related to $\Phi_0(\zeta)$, $\Psi_0(\zeta)$ through the commonly known formulae which are not displayed here to save room. The first order items $\sim \zeta^{-1}$ must be zero to match the static state conditions [Muskhelishvili 1963].

Substituting (2-4a) into (2-3) yields the boundary condition for the KM potentials $\Phi(\zeta)$, $\Psi(\zeta)$ vanishing at infinity:

$$-\frac{2}{\xi^2}\overline{\omega'(\xi)}[\text{Re } \Phi_0(\xi) + B] + \overline{\omega(\xi)}\Phi_0'(\xi) + \Gamma\omega'(\xi) = -\omega'(\xi)\Psi_0(\xi), \quad \xi \in l. \qquad \text{(2-6)}$$

The terms in (2-6) are rearranged specifically for later use.

By integrating (2-6) over γ, one gets the hole-induced energy increment δW as a linear combination of the leading coefficients a_2, b_2 (see, for instance, [Vigdergauz 2001]):

$$\delta W = 2\pi f^{-1}(2\Gamma a_2 + B b_2), \tag{2-7}$$

where f signifies the hole area, by which δW is normalized.

For dimensional reasons, a_2, b_2 are proportional to f [Muskhelishvili 1963]:

$$a_2 = \alpha_2 f, \quad b_2 = \beta_2 f, \tag{2-8}$$

and hence, equivalently,

$$\delta W = 2\pi (2\Gamma \alpha_2 + B\beta_2). \tag{2-9}$$

So, in fact, (2-7) and (2-9) present the energy density that is the hole-induced energy stored in the plate and taken per hole area unit. At given remote loading this quantity depends only on the hole shape. In particular, for a circle ($t \in L$, $|t|^2 = R^2$, $\omega(\xi) = \xi$), one has [Muskhelishvili 1963]

$$\Phi(\xi) = \frac{\Gamma R^2}{\xi^2}, \quad \Psi(\xi) = \frac{2B R^2}{\xi^2} + 3\frac{\Gamma R^4}{\xi^4}, \quad \alpha_2 = \frac{\Gamma}{\pi}, \quad \beta_2 = \frac{2B}{\pi}, \tag{2-10}$$

and therefore,

$$\delta W = 4(\Gamma^2 + B^2). \tag{2-11}$$

By the residues theorem [Ahlfors 1953], the hole area f is expressed in current terms as

$$f = \frac{1}{2i} \int_L \bar{t}\, dt = \frac{1}{2i} \int_\gamma \overline{\omega(\xi)}\omega'(\xi)\, d\xi = \pi \left(1 - \sum_{k=1}^{\infty} k|d_k|^2 \right). \tag{2-12}$$

Similarly, some other useful integrals are (where $\delta_{n,0}$ is the Kronecker delta)

$$\frac{1}{2\pi i} \int_L t^n\, dt = 0, \quad \frac{1}{2\pi i} \int_L \frac{dt}{t^n} = \delta_{n,1}, \quad n = 0, 1, \ldots, \quad t \in L, \tag{2-13}$$

and [Muskhelishvili 1963]

$$2\pi i B + 2Im \int_\gamma \overline{\phi(\xi)}\omega'(\xi)\, d\xi = -\int_\gamma \psi(\xi)\omega'(\xi)\, d\xi = 2\pi i b_2, \tag{2-14}$$

where

$$\phi'(\xi) = \omega'(\xi)\Phi(\xi), \quad \psi'(\xi) = \omega'(\xi)\Psi(\xi). \tag{2-15}$$

3. Problem formulation and solution scheme

We are now in a position to quantitatively rephrase the 2-D shape antioptimization problem at hand in complex-variable terms.

Given a far stress field (B, Γ) find a p-cusped hole boundary L_p which maximizes the normalized increment (2-9):

$$\delta W(B, \Gamma, L_p) \xrightarrow[\{L_p\}]{} \max(B, \Gamma, p). \tag{3-1}$$

Recall that L_p is defined in Section 1 as composed of p identical arcs with constant-signed curvature κ. Pure geometrical considerations give [Pólya and Szegő 1972, part 3, problem 108]

$$\kappa(t) \equiv \frac{1}{\rho(t)} = \frac{1 + \mathrm{Re}(\tau \omega''(\tau)/\omega'(\tau))}{|\tau \omega'(\tau)|}, \quad t = \omega(\tau) \in L, \quad \tau \in \gamma, \tag{3-2}$$

where $\rho(t)$ is the radius of curvature (reciprocal of curvature) at a point $t \in L$.

Since the denominator in the right-hand side of (3-2) is always nonnegative, the hole boundary is nonconvex (nonconcave) everywhere if and only if the numerator is nonpositive (nonnegative), respectively, along the basic arc λ_1:

$$\mathrm{Re}\left(\tau \frac{\omega''(\tau)}{\omega'(\tau)}\right) \xrightarrow[\forall \tau \in \lambda_1]{} \begin{cases} \text{concave if } \leq -1, \\ \text{convex if } \geq -1. \end{cases} \tag{3-3}$$

This easily verified condition effectively restricts the optimization process to target only the L_p-type shapes as required.

In general, (3-1) cannot be performed analytically, except in some simple but nontrivial cases described below, though numerically this is a rather standard problem. Its solution is conveniently obtained by an iterative loop over successively modified shapes while computing the criterion (fitness function) of each feasible candidate selected from the predefined pool $\{L_p\}$. For this purpose, a specially tailored approach was developed and validated in the first author's previous papers (see, for instance, [Vigdergauz 2006]). It includes three main ingredients:

- an efficient and adaptive shape parametrization scheme,

- an enhanced direct solver to evaluate the energy increment for an arbitrarily given shape, and

- a genetic algorithm (GA) approach as the antioptimum search engine.

Their peculiarities are briefly outlined in the next subsections for reader's convenience.

3.1. *Shape parametrization scheme.* For numerical purposes, the infinite Laurent expansion (2-2) is commonly truncated to the first M terms. In the current context, it is justified *a posteriori* by the fact that with increasing M the GA approximations do converge rapidly to a stable solution under the restriction (3-3). Geometrically, higher coefficients in (2-2) are responsible for quickly changing local elements of the mapped shape which inevitably violate the constant signed curvature requirement. Otherwise, the antioptimized shape tends to form acute-angled cusps and teeth resulting in unbounded growth of the energy increment as compared at the top right of Figure 4 in Section 4.

Independently of (3-3), coefficients $\{d_j\}$ must fall into the successfully narrowing intervals

$$-1/\sqrt{k} \leq d_k \leq 1/\sqrt{k}, \quad k = 1, 2, \ldots \tag{3-4}$$

to provide one-to-one mapping between L and γ [Ahlfors 1953]. This allows us to treat these intervals as linear constraints in the maximization problem (3-1) and hence encode the pool $\{L_p\}$ of shapes through an ordered M-length string of real numbers ($b_k, k = \overline{1, M}$) which form an M-dimensional hyper-rectangle Π_M where any shape is presented with a point specified by its coordinates. This scheme is used to perform numerical single-objective global maximization of the energy increment over a wide range of design variables $\{d_k\}$ subject to the nonstrict inequality constraint (3-3).

Remark. Inequalities (3-4) are necessary, but are on no account sufficient conditions for the mapping uniqueness. However, in numerical practice it is desirable to accelerate the computations by narrowing these intervals. To our best knowledge, it can be done only for the one-term mapping

$$\omega(\xi) = \xi + d_k/\xi^k, \quad |d_k| \leq 1/k, \quad k \geq 1, \tag{3-5}$$

where the right inequality is necessary and sufficient to prevent self-crossing of L. However, simple geometrical arguments show that for any shape the constant-signed curvature (3-3) is a more restrictive requirement than the mapping uniqueness which, therefore, has no need to be checked separately. The case of an ellipse ($k = 1$) is excluded as impractical for the current problem since its limiting one-to-one map degenerates in a straight slit with zero area $f = 0$. Otherwise this limit corresponds to a p-cusped hypocycloid ($k = p - 1$, $d_k = \pm(p - 1)$) with $f = 1 - 1/(p - 1)$ and the negative curvature

$$\kappa(\theta) = -\frac{p-2}{4} \csc\left(\tfrac{1}{2}p\theta\right), \quad 0 \leq \theta \leq 2\pi, \quad p = 3, 4, \dots \tag{3-6}$$

Here and henceforth, the opposite signs in d_k indicate rotation through the angle π/p.

In the next subsection this L_p shape is proven to solve the antioptimization problem with only one of the two orientations corresponding to the global energy maximum.

3.2. *Direct solver.* Equation (2-6) states that its left side is the boundary value of a function holomorphic outside the unit circle γ and vanishing at infinity, which thus has no nonnegative powers of ζ as actually taken in the Laurent series (2-5) for $\Psi(\xi)$. However, substitution of the first expansion from (2-5) and (2-2) into (2-6) does produce these powers with the coefficients composed of a_k, d_k, and integers. The reason is the conjugation operation over $\zeta : \overline{\xi^k} = \xi^{-k}, k = \pm 1, \pm 2, \dots$ By equating them to zero, Kalandiya [1975] gets an infinite system of linear algebraic equations in the unknowns $\{a_k\}$ only:

$$a_{m+2} - \sum_{k=1}^{m}(m - k + 1)\bar{d}_{m-k+1}a_k - (m + 1)\sum_{k=1}^{\infty}\bar{d}_{m+k+1}\bar{a}_k = A_m, \quad m = 0, 1, \dots; \tag{3-7a}$$

$$A_0 = 2B - \Gamma, \quad A_1 = 0, \quad A_m = -2B(m + 1)\bar{d}_{m+1}, \quad m \geq 2, \tag{3-7b}$$

with no coefficients of $\Psi(\xi)$. These can be simply restored afterwards through (2-6) and (2-13), when needed. The first sum in (3-7a) is omitted for $m = 0, 1$.

Remarkably, for any M-term finite mapping ($d_k = 0, \forall k > M$), the system (3-7) also shrinks to the first M equations in the unknowns $a_k, k = \overline{1, M}$ while the infinite remainder of them in the unknowns $a_k, k > M$ is next solved analytically by a finite differences technique [Vigdergauz 2006].

As applied to $\omega(\zeta)$, the p-fold symmetry states that only $d_{pl-1}, l = 1, 2, \dots,$ differ from zero so that $M = np - 1$, where n is a new truncation parameter which also governs the solution, though in a different way. While M appears implicitly in the resolving system (3-7), n serves as the number of design variables in the optimization encoding/decoding scheme (see the next subsection).

For better clarity, two basic loadings of different rotational symmetry and analytical peculiarities are considered separately, those of square-antisymmetric pure shear ($B = 0$, $\Gamma = 1$) and isotropic bulk loading ($2B = 1$, $\Gamma = 0$). In either case, the coefficients $\{a_k\}$ could also partially vanish due to adopted p-fold symmetry of the hole shape, thus further diminishing the system size from M to $N < M$ in nonzero unknowns $a_k, k = 1, 2, \dots, N$.

3.2.1. *Pure shear.* Here the coefficient β_2 disappears in the energy increment expression $\delta W = 4\alpha\Gamma^2$, which can be obtained by taking directly from the solution of the $(N \times N)$ truncated system (3-7). This case has been studied in detail previously [Vigdergauz 2006] though the energy maxima were not considered there. Particularly, for only one nonzero mapping term ($n = 1$) we have:

- A triangular symmetry ($p = 3$, $M = 2$, $N = 1$):

$$a_2 = 1, \quad \delta W_2 = \frac{4}{(1 - 2d_2^2)}, \quad \min_{d_2} \delta W_2 = \delta W_2^{(\mathrm{min})} = 4, \quad d_2^{(\mathrm{min})} = 0, \tag{3-8a}$$

$$\max_{d_2} \delta W_2 = \delta W_2^{(\mathrm{max})} = 8, \quad d_2^{(\mathrm{max})} = \pm\tfrac{1}{2}. \tag{3-8b}$$

- A square symmetry ($p = 4$, $M = 3$, $N = 1$):

$$a_2 = \frac{1}{1 - d_3}, \quad \delta W_3 = \frac{4}{(1 - d_3)(1 - 3d_3^2)} \tag{3-9a}$$

$$\delta W_3^{(\mathrm{min})} = \frac{9}{\sqrt{2} + 1}, \quad d_3^{(\mathrm{min})} = \frac{1 - \sqrt{2}}{3}, \tag{3-9b}$$

$$\delta W_3^{(\mathrm{max})} = 9, \quad d_3^{(\mathrm{max})} = \tfrac{1}{3}. \tag{3-9c}$$

- A more-fold symmetry ($p \geq 5$, $M = p - 1$, $N = 2$):

$$a_2 = \frac{1}{1 - (M - 1)d_M^2}, \quad \delta W_p = \frac{4}{(1 - (M - 1)d_M^2)(1 - Md_M^2)}, \tag{3-10a}$$

$$\delta W_p^{(\mathrm{min})} = 4, \quad d_M^{(\mathrm{min})} = 0, \tag{3-10b}$$

$$\delta W_p^{(\mathrm{max})} = \frac{4M^3}{(M^2 - M + 2)(M - 1)}, \quad d_M^{(\mathrm{max})} = \pm\frac{1}{M}. \tag{3-10c}$$

We note that only the case $p = 4$ is sensitive to the hypocycloid angular position as given by the sign of d_3. It produces the global energy maximum (3-9c) when aligned with the main stresses directions $\left(d_3 = \tfrac{1}{3}\right)$ and the halved value $\delta W = 4.5$ otherwise.

3.2.2. *Bulk loading.* With solved a_k, $k = \overline{1, M}$, the Ψ-related coefficient b_2 is arrived at analytically by a little algebra as detailed in the Appendix. Again, as before, the case $n = 1$ takes a simple closed form ($M = p - 1$):

$$\delta W(d_M) = 4B^2 \frac{1 + Md_M^2}{1 - Md_M^2}, \quad \delta W_M^{(\mathrm{max})} = \frac{4(M + 1)}{M - 1}, \quad d_M^{(\mathrm{max})} = \pm\frac{1}{M}. \tag{3-11}$$

The above formulas suggest two analytical conclusions for $n = 1$:

(A) for any $p > 2$ and either loading the energy-maximizing hole shape with constant-signed curvature is an everywhere concave p-cusped hypocycloid, or

(B) the associated energy maximum monotonically decreases with increasing p.

In the general case of $n > 1$ these are numerically extended in the next section.

The subsection is concluded with the following summarizing observation. It is a matter of direct verification to prove that a hypocycloid is the only fully concave one-term mapping (3-5). All smaller

values of $|d_k|$ give raise to convex zones gradually expanding from the vertices. Put it differently, under the concavity requirement, the searching space $\{L_p\}$ is nontrivially populated only for $n > 1$

3.3. *The global optimization scheme.* The design variables ($a_k, k = \overline{1, M}$) must meet the constant-signed curvature condition (3-3), otherwise they are free to vary in large intervals (3-4). Due to the nature of the objective function δW, the maximization problem (3-1) may have many local maxima even though the number M of design variables is small (at most six in our numerical simulations). This circumstance precludes the use of exhaustive search or traditional descent methods.

An effective alternative is provided by an evolutionary-type genetic algorithm (GA). Devised by Holland [1975], it has become well-accepted in the last several decades (see, for instance, [Goldberg and Sastry 2007]). This heuristic approach performs a gradientless optimization in a large search space by mimicking the Darwinian process of natural selection over successive generations through blind crossover and mutation operations. The major advantage of the GA is that it explores the solution space by testing parameter combinations simultaneously to avoid local extrema of the objective function, and requires no derivative information [Goldberg and Sastry 2007].

The GA operates by constructing a population of M-strings and finds δW for each string. These are encoded using a discrete 16-bit procedure where each design variable is represented only by $2^{16} - 1$ separate values in the continuous search space. In view of (3-4), this representation is decoded from a randomly generated integer (or gene) $v \in [-I; I]$, $I = 2^{15}$ as $d_k = v/I \sqrt{k}$, $k = \overline{1, M}$. The genes for different coefficients are concatenated into an ordered $16N$ binary set, or chromosome, that encodes a set of design variables. The chromosome's fitness value is obtained by solving the corresponding direct problem of finding δW while checking the restriction (3-3) at 100 points equally spaced in the irreducible interval $\theta \in [0; \pi/p]$. Once a randomly generated set's population has been evaluated, bitwise crossover and mutations are next applied to the chromosomes with a certain probability level, thus producing the next generation. Then the process is successively repeated to gradually increase the species' fitness δW in the long run. In view of this, wherever (3-3) is violated, the corresponding set obtains a penalty as its fitness, and the GA process takes the next candidate. The idea is to make the set noncompetitive by assigning the penalty, as the squared violation is multiplied by a very large negative constant. The optimization is stopped after some N_{iter} iterations — in belief that the process really converges. Practically, N_{iter} is chosen in such a way that the optimization criterion remains unchanged in successive iterations well in advance of termination.

For the reader's convenience, Table 1 summarizes the above-introduced governing parameters.

After adjusting the heuristic probability levels of the GA operations, this scheme was used to obtain the numerical results presented in the next section. In order to prevent the GA process against possibly being "stuck" quite far from the global maximum, multiple runs are carried out in the current work for each separate problem at the given number n of nonzero mapping terms. Motivated by the proposed optimization strategy, we form a sequence of approximations in ascending order of n, which converges rapidly to a stable hole shape.

4. Numerical results

4.1. *Pure shear* ($Q = -P : B = 0$, $\Gamma = 1$). For illustration purposes, the number p of the contour cusps is chosen here as a power of two to better match the square antisymmetry of loading.

GA parameter	parameter value(s)
gene	integer $[-2^{31}; 2^{31}]$
individual	interface shape
degree of the shape's rotational symmetry (p)	integer $3 \div 128$
population size	$20000 \div 50000$ (depending on the parameter p)
number of genes (n)	up to 6
number of nonzero mapping terms	depending on parameter p
truncation size of the conformal mapping (M)	$pn - 1$
resolving system size (N)	$\leq M$
initial population	$20000 \div 50000$ random individuals
selection	tournament
elitism	four best individuals
crossover	1-point
crossover rate	0.99
creep mutation	by randomly changing a bit
creep mutation rate	0.35
jump mutation	by adding a random integer value typically $[-2^9; 2^9]$
jump mutation rate	0.35
stopping criterion (N_{iter})	after $100 \div 150$ iterations

Table 1. GA operator types, their probability rates, and related parameters typically used in further optimizations.

n	M	d_3	d_7	d_{11}	d_{15}	d_{19}	d_{23}	$\delta W_4^{(\text{max})}$
1	3	0.33333						9.000
2	7	0.39461	-0.02626					11.967
3	11	0.43363	-0.05303	0.00648				15.613
4	15	0.43504	-0.06192	0.01431	-0.00194			16.069
5	19	0.43644	-0.06037	0.01212	-0.00164	0.00024		16.172
6	23	0.43785	-0.05794	0.01009	-0.00164	0.00024	$4.45 \cdot 10^{-5}$	16.259

Table 2. Pure shear. A single square symmetric ($p = 4$) hole: the antioptimal mapping coefficients and the global criterion $\delta W_4^{(\text{max})}$ for different values of n and $M = 4n - 1$.

Table 2 confirms the expected fast convergence of the GA approximations to the steady state solution after the few first values of n, which is typical for any p. Figure 3 shows the evolution of the antioptimal holes from the single ($n = 1$) to multiterm stable ($n = 4 \div 6$) shape.
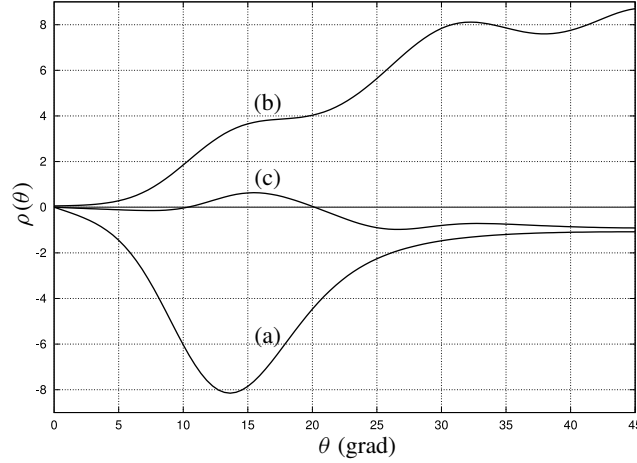
Figure 2. Pure shear. The curvature radii $\rho(\theta)$ for the energy-extremal holes with square symmetry ($p = 4$).

p	$\delta W_p^{(\max)}$	$\delta W_p^{(\min)}$	$\delta W_p^{(\max)}/\delta W_p^{(\min)}$
4	16.259	3.71449	4.377
8	6.975	4.0	1.744
16	5.289	4.0	1.322
32	4.571	4.0	1.143
64	4.141	4.0	1.035
128	4.067	4.0	1.017

Table 3. Pure shear. The energy extrema attained at the maximizing and minimizing hole shapes with different degrees p of rotational symmetry and constant-signed curvature. The value $\delta W_p^{(\min)}$ at $p = 4$ is obtained by GA optimization in [Vigdergauz 2006].

Table 3 displays the stable values of $\delta W_p^{(\max)}$ and $\delta W_p^{(\min)}$ numerically computed at $n = 4 \div 6$ for shapes of constant negative and constant positive curvature, respectively. The allowed energy interval $\Delta W_p \equiv [\delta W_p^{(\min)}; \delta W_p^{(\max)}]$ is seen to shrink gradually to the point $\delta W_p^{(\max)} = \delta W_p^{(\min)} = 4$ with increasing p and

$$\max_p \Delta W_p^{(\text{shear})} = \Delta W_4^{(\text{shear})} = [3.714; 16.259]; \quad \lim_{p \to \infty} \Delta W_p^{(\text{shear})} \to [4; 4]. \quad (4\text{-}1)$$

The subsection is concluded with Figure 2 outlining how the signed curvatures radii $\rho(\theta)$ of different extremal shapes (indicated in the previous figure by the same letters) relate to each other. For easier comparison, the energy minimizing shape (b) is first rotated through 45° to be oriented like the two others. In the absence of restriction (3-3), the resultant shape (c) is seen to form zones of high curvature with alternating sign located near the vertices and is associated with unlimited growth of the energy increment [Vigdergauz 2006].
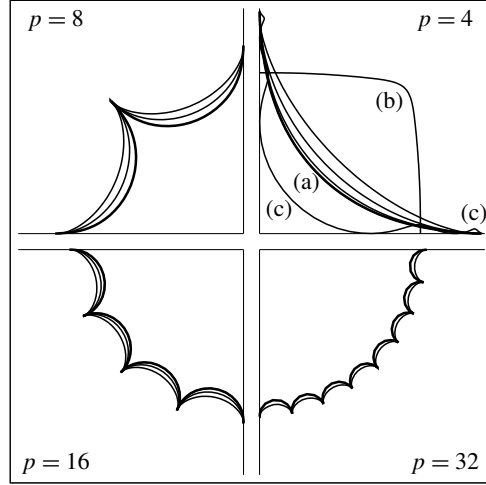
Figure 3. Pure shear. Evolution of the energy-maximizing p-cusped concave hole shapes with increasing number N of the conformal mapping terms to the limiting (boldfaced) curves. The energy-*minimizing* (b) and the extremal cross-like (c) contours [Vigdergauz 2006] at $n = 23$ are also added for contrast.

n	M	d_2	d_5	d_8	d_{11}	d_{14}	$\delta W_3^{(\max)}$
1	2	0.5					3.000
2	5	0.55786	-0.02315				4.188
3	8	0.60657	-0.05161	0.00561			6.448
4	11	0.61837	-0.06120	0.00988	-0.00089		7.616
5	14	0.62062	-0.06233	0.01026	-0.00112	$4.89E-05$	7.753

Table 4. Bulk loading. A single symmetric triangular ($p = 3$) hole: the antioptimal mapping coefficients and the global criterion $\delta W_3^{(\max)}$ for different values of n and $M = 3n - 1$.

4.2. *Bulk loading* ($Q = P : 2B = 1$, $\Gamma = 0$).

Since this load is isotropic, the problem's rotational symmetry is determined only by parameter p, which is chosen here as a multiple of 3.

The results are organized like in the previous subsection. Table 4 exemplifies the GA convergence process for $p = 3$. Figure 4 presents the L_p shape's evolution to the steady state form with increasing parameter n.

Other computational findings (not displayed here to save space but available from the authors) indicate that with increasing p the stable values of $\delta W_p^{(\max)}$ expectedly decrease to the commonly known p-independent global minimum $W_p^{(\min)} = 4$ invariably achieved at a circle. Here,

$$\max_p \Delta W_p^{(\text{bulk})} = \Delta W_3^{(\text{bulk})} = [1; 7.753]; \quad \lim_{p \to \infty} \Delta W_p^{(\text{bulk})} \to [1; 1]. \tag{4-2}$$

A close inspection of Tables 2 and 4 suggests the following general observations, providing a deeper understanding of how the proposed maximization criterion (2-9) works:
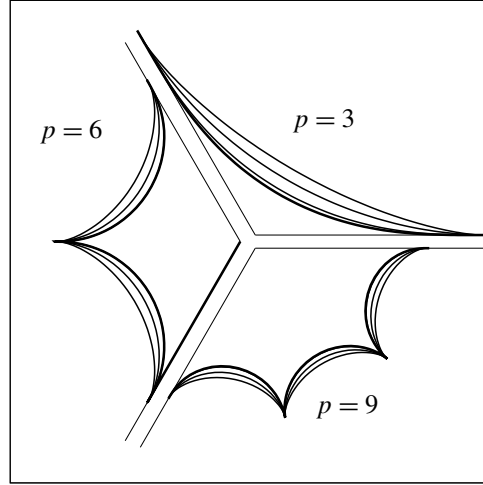
Figure 4. The bulk loading case. Evolution of the energy-maximizing p-cusped concave hole shapes with increasing number N of the conformal mapping terms to the limiting (boldfaced) curves.

- At given n, each table row forms a sequence of rapidly vanishing mapping coefficients. It seems like each next coefficient tends to correct the previous one with aim to increase the shape-induced energy while preserving the arc concavity. Then the coefficients' alternative signs implicitly indicate a good numerical stability of the antioptimization process.

- The resultant leading coefficient d_{p-1} lies outside the empirical interval (3-5) — though, of course, within the wider necessity bounds (3-4):

$$\frac{1}{p-1} \le |d_{p-1}| \le \frac{1}{\sqrt{p-1}}, \quad p = 3, 4, \ldots \tag{4-3}$$

With increasing p, this interval monotonously shrinks to the zero-point, thus giving no room for antioptimization under the imposed concavity assumption. That is just the reason why with growing p, the energy maximum also shrinks to the limiting value attained at zero mapping coefficients $\{d_k\}$ (a circular hole).

A separate remark is necessary about the case ($p = 4$). For both loadings, the GA-obtained energy *maximizing* shapes (shown in upper right of Figure 3) are practically the same (if not identical), unlike the energy-*minimizing* ones which differ markedly from each other.

5. Conclusions

In concluding we summarize the basic assumptions under which the considered optimization problem has been effectively solved by the simplest GA scheme combined with the semianalytical direct solver:

- The chosen energy increment is the antioptimization criterion of an averaging rather than local nature. It allows the avoidance of the "epsilon technique" used, say, in [Givoli and Elishakoff 1992; Pal'mov 1963] for upper prebounding the hoop stresses.

- Instead, the global nonparametric restriction of constant-signed curvature is imposed to form a practically representative searching pool of the energy-maximizing holes' shapes with a finite increment. This restriction is easily verified numerically by conformal mapping technique within the simple, robust, and computationally efficient direct solver.

As a result it turns out that the energy increments possess a high but stable sensitivity to random disturbances of the fully concave/convex hole shapes, and hence can be accurately evaluated with moderate computing effort.

The results numerically obtained here complement those for the energy-*minimizing* shapes in [Vigdergauz 2006]. Taken together, they provide new two-sided bounds on the hole-induced energy increment, which are exact within the constant-signed curvature constraint Their widest gaps over parameter p for the basic load cases are given in (4-1) and (4-2).

Appendix: An analytical solution of the master system (3-7) for remote bulk load

Though the unknowns a_k, $k > M$ are outside the scope of the energy increment expression (2-7), they are needed to restore the first KM potential, and hence to evaluate the boundary hoop stresses [Muskhelishvili 1963]

$$\sigma_{\theta\theta}(\xi) = 4\,\mathrm{Re}\,\Phi_0(\xi) = 4B + 4\sum_{k=2}^{\infty} a_k \cos(k\theta), \quad \xi \in L. \tag{A-1}$$

For pure shear ($B = 0 \rightarrow A_m = 0, \forall m > 2$) the above Fourier series can also be summed up analytically [Vigdergauz 2006] by applying the standard finite differences technique [Levi and Lessman 1992] to the infinite homogeneous system with the load-independent constant coefficients $1, 0, -d_1, -2d_2, \ldots, -Md_M$ of the actual bandwidth n resulted from (3-7) for $m > M - 1$ when the second sum apparently disappears:

$$a_{m+2} - \sum_{k=1}^{M} k d_k a_{m-k+1} = 0, \quad m = M, M+1, \ldots \tag{A-2}$$

$\Phi_0(\xi)$ is then expressed as

$$\Phi_0(\xi) = \frac{R_M(\bar{\xi})}{\xi \omega'(\xi)}, \tag{A-3}$$

where $R_M(\xi)$ is a polynomial of degree M in ξ, given as

$$R_M(\zeta) = r_M \zeta^M + r_{M-1} z^{M-1} + \cdots + r_0, \tag{A-4}$$

with the coefficients

$$r_0 = a_1 = 0, \quad r_1 = a_2, \quad r_m = a_{m+1} - \sum_{k=2}^{m} (-1)^k (k) d_k a_{m+k+1}, \quad m \geq 2, \tag{A-5}$$

which may partially vanish owing to the rotational symmetry.

Remarkably, the solution (A-3) is valid also for the bulk loading case corresponding to the same homogeneous ($D_m = 0, \rightarrow A_m = 0, m = M, m = M+1, \ldots$) system (A-2). Then, from (2-15) it follows

that

$$\phi'(\xi) = \frac{R_n(\bar{\xi})}{\xi} = \sum_{m=1}^{M} \frac{r_m}{\xi^{m+1}}; \quad \phi(\xi) = -\sum_{m=1}^{M} \frac{r_m}{m\xi^m}. \tag{A-6}$$

Finally, substitution of (A-6) into (2-15) gives, while making use of (2-13),

$$b_2 = 2\left(B + \sum_{m=1}^{M} d_m r_m\right). \tag{A-7}$$

Particularly, for $n = 1$ the above expressions are simplified to

$$r_M = BMd_M, \quad b_2 = 2B(1 + Md_M^2), \quad \beta_2 = \frac{b_2}{f} = 2B\frac{1 + Md_M^2}{\pi(1 - Md_M^2)}, \tag{A-8}$$

thus arriving at (3-11).

References

[Ahlfors 1953] L. V. Ahlfors, *Complex analysis*, McGraw-Hill, New York, 1953.

[Banichuk and Neittaanmäki 2010] N. V. Banichuk and P. J. Neittaanmäki, *Structural optimization with uncertainties*, Solid Mech. Appl. **162**, Springer, 2010.

[Cherkaev et al. 1998] A. V. Cherkaev, Y. Grabovsky, A. B. Movchan, and S. K. Serkov, "The cavity of the optimal shape under the shear stresses", *Int. J. Solids Struct.* **35**:33 (1998), 4391–4410.

[Elishakoff and Ohsaki 2010] I. Elishakoff and M. Ohsaki, *Optimization and anti-optimization of structures under uncertainty*, Imperial College Press, London, 2010.

[Givoli and Elishakoff 1992] D. Givoli and I. Elishakoff, "Stress concentration at a nearly circular hole with uncertain irregularities", *J. Appl. Mech. (ASME)* **59**:2S (1992), S65–S71.

[Goldberg and Sastry 2007] D. E. Goldberg and K. Sastry, *Genetic algorithms: the design of innovation*, 2nd ed., Springer, 2007.

[Hardy and Malik 1992] S. J. Hardy and N. H. Malik, "A survey of post-Peterson stress concentration factor data", *Int. J. Fatigue* **14**:3 (1992), 147–153.

[Hlaváček et al. 2004] I. Hlaváček, J. Chleboun, and I. Babuška, *Uncertain input data problems and the worst scenario method*, North-Holland Series Appl. Math. Mech. **46**, Elsevier, Amsterdam, 2004.

[Holland 1975] J. H. Holland, *Adaptation in natural and artificial systems*, Univ. Michigan Press, Ann Arbor, 1975.

[Kalandiya 1975] A. I. Kalandiya, *Mathematical methods of two-dimensional elasticity*, Mir, Moscow, 1975.

[Khusu et al. 1975] A. P. Khusu, Y. R. Vitenberg, and V. A. Pal'mov, Шероховатость поверхностей, Izdat. "Nauka", Moscow, 1975.

[Levi and Lessman 1992] H. Levi and F. Lessman, *Finite difference equations*, Dover, New York, 1992.

[Murakami 2017] Y. Murakami, *Theory of elasticity and stress concentration*, Wiley, Chichester, 2017.

[Muskhelishvili 1963] N. I. Muskhelishvili, *Some basic problems of the mathematical theory of elasticity*, Noordhoff, Groningen, 1963.

[Pal'mov 1963] V. A. Pal'mov, "State of stress in the neighborhood of a rough surface of elastic bodies", *Prikl. Mat. Mekh.* **27**:5 (1963), 963–969. In Russian; translated in *J. Appl. Math. Mech.* **27**:5 (1963), 1479–1489.

[Pedersen 2013] N. L. Pedersen, "Optimization of bolt thread stress concentrations", *Arch. Appl. Mech.* **83**:1 (2013), 1–14.

[Pedersen et al. 1992] P. Pedersen, L. Tobiesen, and S. H. Jensen, "Shapes of orthotropic plates for minimum energy concentration", *J. Struct. Mech.* **20**:4 (1992), 499–514.

[Pilkey and Pilkey 2008] W. D. Pilkey and D. F. Pilkey, *Peterson's stress concentration factors*, 3rd ed., Wiley, New York, 2008.

[Pólya and Szegő 1972] G. Pólya and G. Szegő, *Problems and theorems in analysis, I: Series, integral calculus, theory of functions*, Grundlehren der Math. Wissenschaften **193**, Springer, 1972.

[Savruk and Kazberuk 2017] M. P. Savruk and A. Kazberuk, *Stress concentration at notches*, Springer, 2017.

[Shahzad et al. 2017] S. Shahzad, F. Dal Corso, and D. Bigoni, "Hypocycloidal inclusions in nonuniform out-of-plane elasticity: stress singularity vs. stress reduction", *J. Elasticity* **126**:2 (2017), 215–229.

[Sheinin 1972] V. I. Sheinin, "On asymptotic method of calculation of stresses near the rough surface of elastic bodies", *Izv. Akad. Nauk SSSR Mekh. Tverd. Tela* **2** (1972), 94–102. In Russian; translated in *Mech. Solids* **2** (1972).

[Vigdergauz 2001] S. Vigdergauz, "Genetic algorithm perspective to identify energy optimizing inclusions in an elastic plate", *Int. J. Solids Struct.* **38**:38 (2001), 6851–6867.

[Vigdergauz 2006] S. Vigdergauz, "The stress-minimizing hole in an elastic plate under remote shear", *J. Mech. Mater. Struct.* **1**:2 (2006), 387–406.

[Vitenberg 1971] Y. P. Vitenberg, Шероховатость поверхности и методы ее оценки, Sudostroenie, Moscow, 1971.

SHMUEL VIGDERGAUZ: shmuelvigdergauz@gmail.com
R&D Division, The Israel Electric Corp. Ltd., Haifa, Israel

ISAAC ELISHAKOFF: elishako@fau.edu
Department of Ocean and Mechanical Engineering, Florida Atlantic University, Boca Raton, FL, United States

msp

ANISOTROPIC MULTIMATERIAL LATTICES AS THERMAL ADAPTERS

Marina M. Toropova

Design concepts for anisotropic adaptive lattices compounded of triangular multimaterial cells are considered. The lattices connect two parts of a structure (referred here as the substrates) made of materials with different coefficients of thermal expansion (CTEs) and subject to large variation of temperature. They are designed to eliminate mismatched thermal expansion and provide constant independent of temperature distance between the substrates. Because all connections with the substrates and within the lattice are made with pins, the whole structure is free of bending and thermal expansion mismatch stresses. The designed lattices are scale independent. Relationships between cell geometry (triangle angles and height) and the CTEs of selected lattice materials are obtained. Two-cell and three-cell one-row and five-cell two-row planar lattices are designed. Furthermore, axisymmetric adaptive lattice assembly is considered. Such a lattice can have cylindrical or conical shape and may be compounded of several rows. Cell members in all designed lattices are made of conventional materials. Lattice materials providing the largest structural efficiency are recommended.

1. Introduction

Multimaterial adaptive lattices are used as connectors between two parts of a structure that are made of materials with different CTEs. If the structure experiences cyclic temperature variations, thermal expansion mismatch stresses may lead to deformations and damages [Edeson et al. 2010]. Various approaches are used to eliminate or mitigate the stresses. The first approach relates to thermal expansion mismatch adapters made of layered composite materials with graded CTE. For example, in [Yousefiani et al. 2009a; Yousefiani et al. 2009b], the authors proposed this type of adapter for a composite plate with contoured profile layers and for a layered injector-chamber attachment components in rocket engines. [Dang 2006] used composite adapters with graded CTE as components of a precision optical assembly to prevent lens misalignment. However, layered composite thermal adapters tend to accumulate residual stresses arising between the layers due to differences in the CTEs. Cyclic thermal variation amplifies the stresses and causes nonrecoverable deformations. Another approach to accommodate differential thermal expansion relates to compliant connections with low stiffness, e.g., Du et al. [2016; 2017] used flexible connections to mitigate thermal expansion mismatch deformations between a satellite platform and supporting composite rods, but this strategy reduces the overall stiffness. Multimaterial lattices do not have these drawbacks and are perfect in structures for which low weight is desirable. They are stiff and do not generate thermal expansion mismatch stresses. The lattices are compound of conventional materials and are designed in such a way that on the edges connected to the substrates, the lattice CTEs coincide with the CTEs of the corresponding substrate materials. Various thermally adaptive lattices are presented

in [Toropova and Steeves 2014; 2015; 2016]. In these papers, the lattices are comprised of hexagonal cells with pin-joined members; three hexagon vertices are connected to an internal triangle made of a material with the CTE that differs from the hexagon material CTE. Each cell is anisotropic with three CTEs along the sides of the virtual base triangle upon which the cell is built. Such cells provide a wide range of the CTEs, but are noticeably sensitive to manufacturing imperfections in pin joints. However, the lattice design methodology elaborated in these works can be used in the design of adaptive lattices compounded of planar triangular cells that can be considered as a particular case of the hexagonal cells with zero skew angles. The triangular cells have much simpler configuration with only three pin joints, may be easily manufactured, and are much less sensitive to manufacturing imperfections compared to hexagonal cells. Three linear cell members may be made of materials with different CTEs, and the angles adjacent to the triangle base may also be different. Such cells are similar to the triangular cells used in [Grima et al. 2007a; 2007b; Miller et al. 2008; Wei et al. 2016; 2017], but have a higher degree of anisotropy, which is needed for thermal adapters. The lattices comprised of the cells are nonperiodic and the cells are nonidentical, which differs from [Sigmund and Torquato 1996; 1997; Lakes 1996; 2007; Ha et al. 2017; Gibiansky and Torquato 1997; Jefferson et al. 2009; Steeves et al. 2007; Berger et al. 2011; Berger and McMeeking 2018; Lehman and Lakes 2013; Gdoutos et al. 2013; Hopkins et al. 2013; Xu and Pasini 2016; Wei et al. 2018a]. Despite the cell's simple structure, the lattices composed of the triangular cells are able to eliminate or mitigate stresses due to different CTEs in the substrate materials.

In this paper, one-row and two-row planar lattices and multirow nonplanar axisymmetric cylindrical and conical adaptive lattices are designed. The lattices have straight-line members with pin connections to the substrates, between and within cells. Because of this, the lattices accommodate thermal deformations of the substrates without generating thermal stresses. Also, the designed lattices provide a constant temperature-independent distance between the substrates. The planar adaptive lattices may be used in multifunctional sandwich panels when they operate under variable thermal conditions, while the multirow axisymmetric adaptive lattices are used in various artificial Earth satellites as interface adapters that are not intended to bear large loads but must have optimal structural efficiency [Vasiliev et al. 2012], for example, as connectors and parts of platforms for antennas, mirrors, and other optical systems. Such nonplanar one-row axisymmetric lattices consisting of planar hexagonal cells and adapting or tuning the CTEs of two cylindrical substrates were suggested in [Toropova and Steeves 2015; 2016]. Later, the design of nonplanar lattices compounded of planar cells was developed in [Wei et al. 2018b], where planar triangular and square cells were used in lattice cylindrical shells with tailorable thermal expansion. Thermal tuning and morphing of anisotropic composite lattice shells (anisogrids) formed by clockwise and counterclockwise helical and circumferential tubular members were investigated in [Phoenix and Tarazaga 2017; 2018; Phoenix et al. 2018]. In the present work, multirow axisymmetric lattices comprised of planar triangular cells with members made of conventional materials are designed to serve as thermal adapters. The lattices can be comprised of the desirable number of cylindrical and conical rows; the cells in different rows can have different geometry and be made of different materials. However, there are no thermal expansion mismatch stresses between the rows. Relationships linking cell geometry with the CTEs of lattice cells are obtained. In contrast with conventional anisogrids, the lattices are free of bending and thermal stresses.

For all lattices presented here, the structural efficiency defined as stiffness per mass is calculated. Cell materials that provide the largest structural efficiency are indicated. The lattices are scale independent

and may be used at macro- and microscales. They do not accumulate residual stresses or display material hysteresis [Steeves et al. 2009]. Strength problems related to the lattices are not studied in the paper.

## 2. Formulation of the problem

Consider a structure subject to cyclic variations of temperature and consisting of two adjacent parts (referred here as the substrate one and the substrate two) made of materials with different CTEs A_1 and A_2, respectively. If the parts are connected to each other directly, temperature variations cause mechanical stresses due to thermal expansion mismatch that can lead to nonrecoverable deformations. An anisotropic adaptive lattice that connects the two substrates and has the CTE A_1 on the edge adjacent to the substrate one and the CTE A_2 on the edge connected to the substrate two eliminates thermal expansion mismatch stresses (Figure 1).

Lattice cells have triangular shape with straight-line members that can have different lengths and be made of materials with different CTEs. Because all joints with the substrates, between cells and cell members are made with pins, the cell members can rotate and accommodate thermal expansions. The design of the adaptive lattice consists of finding angles in all cells if cell member materials are selected. Design requirements define candidates for cell materials. Then, equations linking cell geometry with material CTEs must be derived accounting for the number of rows and the number of cells in every row. The equations can be satisfied for different CTE combinations of materials-candidates providing multiple solutions to the problem. The cell member materials for which the structural efficiency is maximal are indicated.

3. Triangular anisotropic cell

In an arbitrary triangular cell, the members AB, BC, and AC (Figure 2) are made of conventional materials with Young's modulus E_i, density ρ_i, and CTE α_i, $i = 1, 2, 3$, respectively. Cell angles a and b can be different providing different member lengths $AB = L_1$, $BC = L_2$, and $AC = L_3$.

If the three member CTEs α_i, $i = 1, 2, 3$, are known, the cell geometry, i.e., the angles a and b, can be found from the conditions that the CTE along the height h is zero, the CTE along the line AB is A_1, and the CTE along the connection line to the second substrate, which passes through the vertex C, is A_2. Therefore, the cell geometry depends on A_1, A_2, and three-cell CTEs α_i, $i = 1, 2, 3$, which are
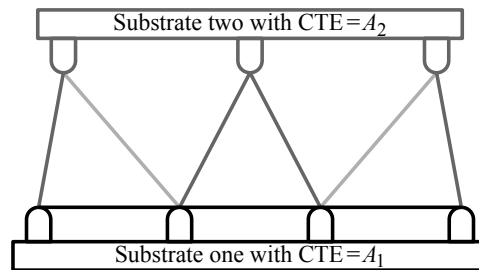
Figure 1. An example of an adaptive lattice eliminating thermal mismatch stresses between substrates with different CTEs. Lattice cell members with different CTEs are depicted with different shade of gray.
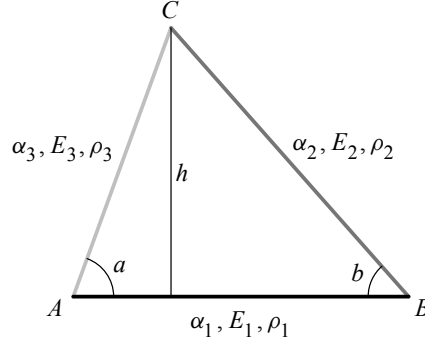
Figure 2. A lattice cell ABC with angles a and b. The members AB, BC, and AC are made of materials with CTE α_i, Young's modulus E_i, and density ρ_i, $i = 1, 2, 3$, respectively.

equal to the CTEs of selected member materials. In this work, we do not account for thermal expansion of the substrates in the vertical direction. This problem was considered in [Toropova and Steeves 2016]. Because different choices of member materials for given A_1, A_2 determines different cell geometry, it is important to select the cell materials that provide the largest structural efficiency, i.e., stiffness per mass. For anisotropic cells compound of external hexagons and internal triangles, the structural efficiency under uniaxial loading was found in [Toropova and Steeves 2015]. A similar approach is used here to find the structural efficiency of the triangular cell under a vertical force N applied to the vertex C. The forces in the members AB, BC, AC are equal, respectively:

$$F_1 = N\frac{\cos a \cos b}{\sin(a+b)}, \quad F_2 = -N\frac{\cos a}{\sin(a+b)}, \quad F_3 = -N\frac{\cos b}{\sin(a+b)}.$$

The vertical deflection of the cell in vertex C where the force N is applied is

$$\delta = \frac{N}{\sin^2(a+b)}\left[\frac{L_1}{\Lambda_1 E_1}\cos^2 a \cos^2 b + \frac{L_2}{\Lambda_2 E_2}\cos^2 a + \frac{L_3}{\Lambda_3 E_3}\cos^2 b\right],$$

where Λ_i, $i = 1, 2, 3$, are cross-sectional areas of the members AB, BC, AC, respectively. The structural stiffness S_u under uniaxial loading can be expressed as

$$S_u = \frac{Nh}{\delta L_1}.$$

Then, the nondimensional structural efficiency P is equal to

$$P = \frac{\rho_1}{E_1}\frac{S_u}{M} = \frac{\rho_1}{E_1}\frac{h\sin^2(a+b)}{L_1\left[\dfrac{L_1}{\Lambda_1 E_1}\cos^2 a \cos^2 b + \dfrac{L_2}{\Lambda_2 E_2}\cos^2 a + \dfrac{L_3}{\Lambda_3 E_3}\cos^2 b\right]M}, \tag{3-1}$$

where the mass M per unit area of the lattice is

$$M = \frac{\rho_1 \Lambda_1 L_1 + \rho_2 \Lambda_2 L_2 + \rho_3 \Lambda_3 L_3}{L_1 h}. \tag{3-2}$$

Taking into account (3-2), Equation (3-1) can be rewritten as

$$P = \left(\frac{h}{L_1}\right)^2 \frac{\sin^4(a+b)}{D},$$ (3-3)

where

$$D = [\sin(a+b) + Q_1 \sin a + Q_2 \sin b][\sin(a+b) \cos^2 a \cos^2 b + Q_3 \cos^2 a \sin a + Q_4 \cos^2 b \sin b],$$

$$Q_1 = \frac{\rho_2}{\rho_1} \frac{\Lambda_2}{\Lambda_1}, \quad Q_2 = \frac{\rho_3}{\rho_1} \frac{\Lambda_3}{\Lambda_1}, \quad Q_3 = \frac{E_1}{E_2} \frac{\Lambda_1}{\Lambda_2}, \quad Q_4 = \frac{E_1}{E_3} \frac{\Lambda_1}{\Lambda_3}.$$

From (3-3), we see that P increases when $a \to \frac{1}{2}\pi$ or $b \to \frac{1}{2}\pi$ and decreases when $a \to 0$ or $b \to 0$; the structural efficiency reduces when coefficients Q_i, $i = \overline{1,4}$, containing physical constants of member materials increase. In a particular case, when the angles $a = b$ and all members have the same cross-sectional areas and are made of the same material, the nondimensional structural efficiency is equal to

$$P = \frac{\sin^4 a}{(\cos a + 1)(\cos^3 a + 1)}.$$

If, for example, $a = b = 60°$, then $P = \frac{1}{3}$, which is identical with the maximal structural efficiency for the triangular lattice with equilateral cells found in [Steeves et al. 2007]. If $a = b = 70°$, $P = 0.5587$; for $a = b = 80°$, $P = 0.7973$. Thus, cells with larger angles a and b are preferable in terms of structural efficiency.

4. Planar lattices

In this section, stretch dominated two-cell and three-cell one-row lattices and a five-cell two-row lattice compounded of triangular cells are considered. All the lattices have a vertical line of symmetry. For two-cell and three-cell lattices the relationships connecting cell angles with member material CTEs are derived using the condition of constant, temperature-independent lattice height and kinematic conditions on the lattice edges connected to the substrates. Then, it is shown how the relationships are modified if these two lattices are combined into a five-cell two-row lattice. For lattices of more complicated shape or lattices without the vertical line of symmetry, the relationships between cell geometry and material CTEs can be derived in similar way. Lattice design starts with the selection of cell lateral side materials, and then cell angles are found. In all cells, the triangle base side material coincides with the first substrate material to exclude thermal expansion mismatch.

4A. *Two-cell lattices.* Let a two-cell lattice (Figure 3) be connected to the first substrate with the CTE A_1 along the line AB and to the second substrate with the CTE A_2 along the line CE, and α_{AD}, α_{DB}, and α_h denote the CTEs along AD, DB, and the height h, respectively. Because $\alpha_h = 0$,

$$\alpha_{AD} = \frac{\alpha_3}{\cos^2 a}, \quad \alpha_{DB} = \frac{\alpha_2}{\cos^2 b}.$$

The distance CE between the vertex C and the lattice line of symmetry must thermally expand with the CTE A_2, hence

$$\cos b = \sqrt{\alpha_2/A_2}$$ (4-1)
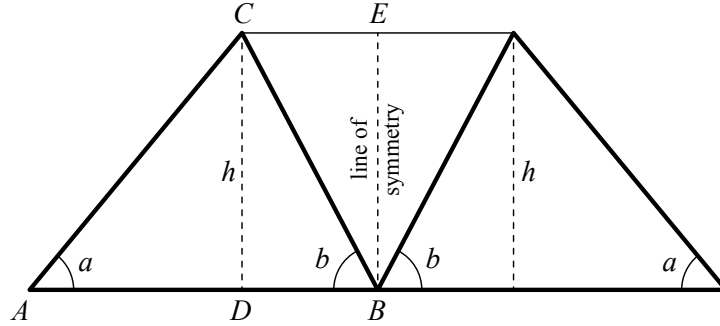
Figure 3. Two-cell lattice with a line of symmetry and a distance h between substrates.

and $\alpha_2 < A_2$. The distance between vertices A and B must expand with CTE A_1, so

$$\frac{\alpha_3}{\sin a \cos a} - A_1 \cot a = (A_1 - A_2) \cot b. \tag{4-2}$$

The angles a and b can be found from (4-1) and (4-2) as

$$a = \frac{1}{2}\left[\arccos\left(\frac{2\alpha_3 - A_1}{w_1}\right) + \phi_1\right], \quad b = \arccos\sqrt{\alpha_2/A_2}, \tag{4-3}$$

where

$$w_1 = \sqrt{A_1^2 + \frac{\alpha_2}{A_2 - \alpha_2}(A_1 - A_2)^2}, \quad \phi_1 = \arccos\frac{A_1}{w_1}. \tag{4-4}$$

The second equation in (4-3) shows that the angle b rises when α_2 decreases and A_2 increases. From (4-2), it is seen that the angle a depends on the angle b and the CTE α_3. Therefore, the first equation in (4-3) shows that if the angle b is found, then the angle a is greater for a greater difference $A_1 - 2\alpha_3$, i.e., for a smaller CTE α_3.

4B. *Three-cell lattices.* Let a three-cell lattice (Figure 4) be connected to the first substrate with the CTE A_1 along the line AD and to the second substrate with the CTE A_2 along the line CE. The lattice has a vertical line of symmetry so that the angles in the middle cell $a_2 = b_2$ (Figure 4). To define lattice geometry, we have to find relationships between cell angles a_1, b_1 (related to the left cell), the angles $a_2 = b_2$ and the material CTEs A_1, A_2, α_{1i}, $i = 1, 2, 3$, and α_{2j}, $j = 1, 2, 3$, where α_{11}, α_{12}, α_{13} are the material CTEs of the members AB, BC, AC, respectively, and α_{21}, α_{22}, α_{23} are the material CTEs of the members BD, DE, and BE, respectively.

Repeating the procedure applied in the subsection above, we find

$$\cos^2 a_2 = \frac{\alpha_{23}}{A_1},$$

$$\frac{\alpha_{12}}{\sin b_1 \cos b_1} - A_2 \cot b_1 = (A_2 - A_1) \cot a_2,$$

$$\frac{\alpha_{13}}{\sin a_1 \cos a_1} - A_1 \cot a_1 = \left(A_1 - \frac{\alpha_{12}}{\cos^2 b_1}\right) \cot b_1. \tag{4-5}$$
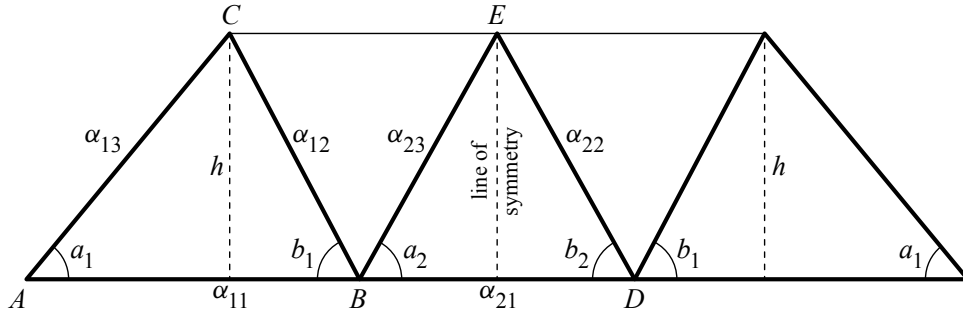
Figure 4. Designation of CTEs in a three-cell lattice with a line of symmetry and a distance h between substrates.

The solutions to the equations (4-5) can be presented as

$$a_2 = b_2 = \arccos \sqrt{\frac{\alpha_{23}}{A_1}},$$

$$b_1 = \frac{1}{2}\left[\arccos \frac{2\alpha_{12} - A_2}{w_2} + \phi_2 \right], \qquad (4\text{-}6)$$

$$a_1 = \frac{1}{2}\left[\arccos \frac{2\alpha_{13} - A_1}{w_3} + \phi_3 \right],$$

where $\alpha_{23} < A_1$ and

$$w_2 = \sqrt{A_2^2 + \frac{\alpha_{23}}{A_1 - \alpha_{23}}(A_1 - A_2)^2}, \qquad \phi_2 = \arccos \frac{A_2}{w_2}, \qquad (4\text{-}7)$$

$$w_3 = \sqrt{A_1^2 + \cot^2 b_1 \left(A_1 - \frac{\alpha_{12}}{\cos^2 b_1} \right)^2}, \qquad \phi_3 = \arccos \frac{A_1}{w_3}. \qquad (4\text{-}8)$$

Equations (4-5) show that the angle b_1 depends on the angle a_2, and the angle a_1 depends on the angle b_1. From (4-6)–(4-8) it follows that smaller values of α_{23} lead to larger values of the angle a_2. When a_2 is found, the angle b_1 is larger for a smaller α_{12}, and for the found values of a_2 and b_1 the angle a_1 is larger for a smaller α_{13}.

4C. *Five-cell two-row lattice.* The lower row in a five-cell two-row lattice is designed as if it connects two substrates with the same CTE A_1 (Figure 5).

In this case, (4-6) are transformed into

$$a_1 = \arccos \sqrt{\frac{\alpha_{13}}{A_1}}, \quad b_1 = \arccos \sqrt{\frac{\alpha_{12}}{A_1}}, \quad a_2 = b_2 = \arccos \sqrt{\frac{\alpha_{23}}{A_1}}, \qquad (4\text{-}9)$$

where $\alpha_{1i} < A_1$, $i = 2, 3$, and $\alpha_{11} = A_1$, α_{12}, α_{13} are the CTEs pertaining to the left cell in the lower row and the CTEs $\alpha_{21} = A_1$, $\alpha_{22} = \alpha_{23}$ relate to the middle cell in the lower row. For the angles in the upper

Figure 5. Designation of CTEs in a two-row five-cell lattice with a line of symmetry; the height of the first row is h_1 and the height of the second row is h_2.

row cells, (4-3) can be rewritten as

$$c = \frac{1}{2}\left[\arccos\left(\frac{2\beta_{13} - A_1}{w_1}\right) + \phi_1\right], \quad d = \arccos\sqrt{\frac{\beta_{12}}{A_2}},$$

$$w_1 = \sqrt{A_1^2 + \frac{\beta_{12}}{A_2 - \beta_{12}}(A_1 - A_2)^2}, \quad \phi_1 = \arccos\frac{A_1}{w_1}, \tag{4-10}$$

where the angles c, d, and the CTEs $\beta_{11} = A_1$, β_{12}, and β_{13} relate to the left cell in the upper row, and $\beta_{12} < A_2$. Note, that in a two-row lattice, the rows can have different heights $h_1 \neq h_2$, which are independent of temperature changes.

Expressions (4-3), (4-6), (4-9), and (4-10) obtained in this section are scale independent and present the cell angles as functions of A_1, A_2, and the CTEs of the cell member materials.

5. Examples of lattice design

In the examples considered in this paper, the first substrate is made of aluminum (CTE $= 22.2$ ppm/°C, Young's modulus $E = 70$ GPa, density $\rho = 2.7$ kg/m^3), while the second substrate is made of titanium (CTE $= 8.6$ ppm/°C, Young's modulus $E = 116$ GPa, density $\rho = 4.5$ kg/m^3). For lattice design, we have to select cell member materials and then find cell geometry. Because the first substrate is made of aluminum, the cell base members are also made of aluminum. Let possible candidates for the cell lateral member materials be titanium, Kovar (CTE $= 5.5$ ppm/°C, Young's modulus $E = 138$ GPa, density $\rho = 8.0$ kg/m^3), and Invar (CTE $= 1.2$ ppm/°C, Young's modulus $E = 140$ GPa, density $\rho = 8.1$ kg/m^3). These materials are selected because they are conventional in aerospace applications. In other design problems, different materials can be considered. Having the relationships (4-3), (4-6), (4-9), and (4-10) derived in the previous section, we can find cell geometry for two-cell and three-cell one-row lattices and five-cell two-row lattices. Here, the cell angles are found for different combinations of titanium, Kovar, and Invar for cell members. The structural efficiency calculated under uniaxial loading using (3-3)

line #	α_2 (ppm/°C)	α_3 (ppm/°C)	a	b	P
1	1.2	8.6	58.2°	68.1°	0.3631
2	1.2	5.5	66.6°	68.1°	0.3842
3	1.2	1.2	81.9°	68.1°	0.4453
4	5.5	8.6	69.7°	36.9°	0.1697
5	5.5	5.5	76.2°	36.9°	0.2010

Table 1. Angles and structural efficiency of cells in two-cell lattices connecting aluminum and titanium substrates; lateral cell members are made of different combinations of titanium, Kovar, and Invar materials.

depends on the cell angles, which depend on the cell material CTEs. The coefficients Q_i, $i = 1, 2, 3, 4$, reflecting the cell material physical properties, act as parameters. The structural efficiency of the whole lattice is equal to the minimum structural efficiency among all cells.

5A. *Two-cell lattice.* The structural efficiency and the angles in two-cell lattices calculated by (4-3) and (4-4) for member materials with CTEs α_2 and α_3 are shown in Table 1. It is seen that the lattice with cells made of Invar lateral and aluminum base sides and the angles $a = 81.9°$, $b = 68.1°$ (line 3) has the largest structural efficiency $P = 0.4453$. The presence of smaller angles b (lines 4, 5) noticeably reduces the structural efficiency.

5B. *Three-cell lattice.* Let P_1 and P_2 denote the structural efficiency of the left and the middle lattice cells (Figure 4), respectively. According to Table 2, the left cell made of the left titanium and the right Invar lateral sides has the structural efficiency $P_1 = 0.2947$, and the middle cell with Invar lateral sides has the structural efficiency $P_2 = 0.5401$ (line 3). Hence, the structural efficiency of the whole lattice is $P = 0.2947$, which is the largest among all other three-cell lattices with different combinations of cell member materials (lines 1, 2, 4, 5, 6) but significantly lower than the structural efficiency of the two-cell lattice connecting substrates made of the same materials. In general, analysis shows that the more cells the adaptive lattice comprises, the more the cells differ from isosceles triangles and as a result the total lattice structural efficiency reduces. In all lines of Table 2, $P_2 > P_1$, this is because the geometry of the middle cell in the designed lattice does not depend on A_2. Therefore, a lattice connecting two substrates with the same CTEs has the maximum structural efficiency.

5C. *Five-cell two-row lattice.* It is possible to increase the structural efficiency of a three-cell lattice by transforming it into a five-cell two-row lattice with an additional upper row consisting of two cells. In this case, the first row of the five-cell two-row lattice is designed as if it connects two substrates with the same CTE and the lateral members are made of the same material. Hence, the triangular cells in the first row have the same angles $a_i = b_i$, $i = 1, 2$. Table 3 contains the cell angles $a_i = b_i = a$ and the structural efficiency of the cells calculated for lateral member materials with CTEs $\alpha_{12} = \alpha_{13} = \alpha_{23}$. It is seen that cells with Invar lateral sides have the largest structural efficiency $P = 0.5401$.

The upper row of the lattice coincides with the two-cell lattice designed earlier. Table 1 shows that cells with Invar lateral sides and aluminum base side have the largest structural efficiency $P = 0.4453$, which is less than 0.5401. Hence, the total lattice structural efficiency, which is identical with the structural

line #	α_{12} (ppm/°C)	α_{13} (ppm/°C)	α_{23} (ppm/°C)	a_1	b_1	a_2	P_1	P_2
1	1.2	8.6	8.6	76.4°	32.6°	51.5°	0.1751	0.1943
2	1.2	8.6	5.5	73.0°	40.0°	60.2°	0.2099	0.2593
3	1.2	8.6	1.2	65.3°	55.9°	76.6°	0.2947	0.5401
4	5.5	8.6	8.6	82.6°	14.3°	51.5°	0.0830	0.1911
5	5.5	8.6	5.5	80.6°	17.9°	60.2°	0.0995	0.2593
6	5.5	8.6	1.2	75.5°	27.1°	76.6°	0.1357	0.5401

Table 2. Angles and structural efficiency of cells in three-cell lattices connecting aluminum and titanium substrates; lateral cell members are made of different combinations of titanium, Kovar, and Invar materials.

line #	$\alpha_{12} = \alpha_{13} = \alpha_{23}$ (ppm/°C)	$a_1 = b_1 = a_2 = a$	P
1	8.6	51.5°	0.1943
2	5.5	60.2°	0.2593
3	1.2	76.6°	0.5401

Table 3. Angles and structural efficiency of cells in the first row of five-cell two-row lattices; lateral cell members are made of titanium, Kovar, and Invar materials as if they connect two aluminum substrates.

efficiency of the two-cell lattice, is attained if the cell lateral sides in both rows are made of Invar and the base sides of aluminum. A sketch of the kinematics of the lattice is shown in Figure 6 where the lattice edges connected to the aluminum and titanium substrates thermally expand with the CTE of aluminum and titanium, respectively.

Three examples presented in this section demonstrate that cell lateral sides made of materials with smaller CTEs lead to larger angles adjacent to the triangle base side, and the cells with the larger angles have the larger structural efficiency even if the lateral side materials have a larger density. Note that if $A_1 > A_2$, hexagonal cells [Toropova and Steeves 2014; 2015] cannot be used in planar thermally adaptive lattices because in this case the range of their CTEs [Toropova and Steeves 2016] is not wide enough for adapting purposes.

6. Axisymmetric lattices

In this section, we consider cylindrical and conical axisymmetric lattices. Such lattices can be used in satellite structures as connectors between the main satellite body and an outboard platform. Here, the two substrates are simulated as circular disks with radii R_1 and R_2, respectively. The lattices may consist of one or more rows of different heights, so that a desirable total distance between the substrates can be attained by combination of different rows (Figure 7).

We assume that every row has a lower and an upper circular boundary, which are virtual, so that the cells in every row are connected to the virtual lower circle with radius r_i and to the virtual upper circle with radius r_{i+1}, and $r_1 = R_1$, $r_{m+1} = R_2$ where m is the total number of rows. To form a smooth
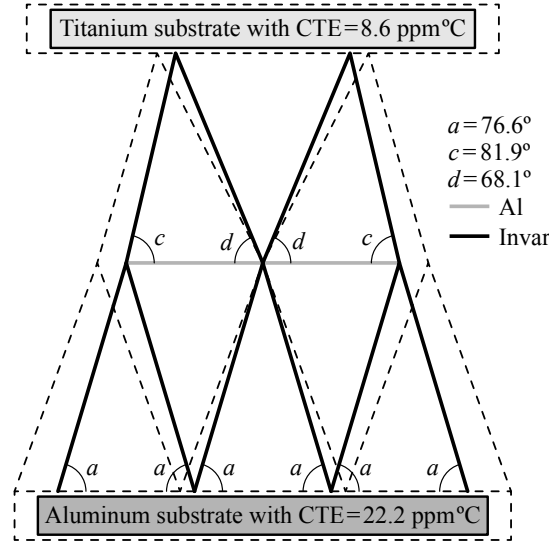
Figure 6. Sketch of the kinematics of the thermal expansion of the two-row five-cell lattice with aluminum cell base sides and Invar lateral sides. The cells with the angles $a = 76.6^o$, $c = 81.9^o$, $d = 68.1^o$ provide the largest structural efficiency of the lattice $P = 0.4453$ for the selected materials. The solid lines show the initial positions of the lattice, while the dashed lines show the lattice configuration and substrates after thermal changes. Note that the height of every row does not change with temperature.
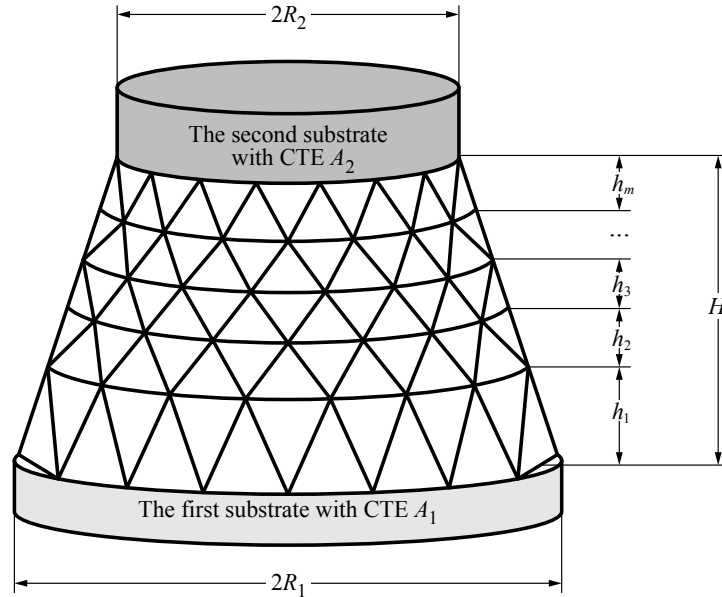
Figure 7. An example of an axisymmetric adaptive lattice consisting of m rows and connecting two circular disks with CTEs A_1 and A_2 and radii R_1 and R_2, respectively. The distance between the substrates is H, while the height of every row is h_i, $i = \overline{1, m}$.
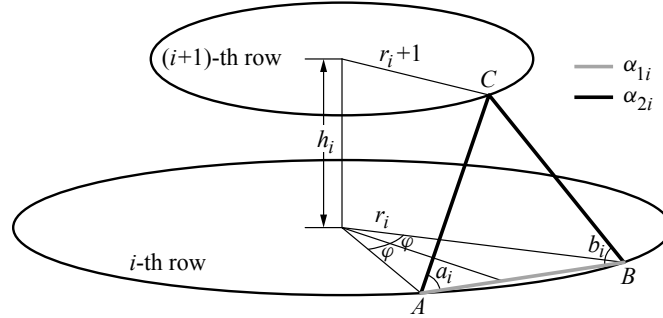
Figure 8. An axisymmetric lattice cell ABC in the i_{th} row. r_i and r_{i+1} are the radii of the lower and the upper row boundaries, respectively; h_i is the row height; the angle $\phi = \pi/n$, where n is a number of cells in every row. The base side AB is made of a material with the CTE α_{1i}, while the lateral sides AC and BC are made of a material with CTE α_{2i}. The cell angles at the base triangle side are equal to each other $a_i = b_i$.

cylindrical or conical surface, all rows have the same slope: $(r_i - r_{i+1})/h_i = \text{constant} = \gamma$, $i = \overline{1, m}$. In every row, there are the same number of cells and all cells have the same geometry and combination of materials that may differ from the cells in other rows. Different rows can have different heights, which remain independent of temperature, and the total distance $H = h_1 + h_2 + \cdots + h_m$ between the two substrates (Figure 7) also stays independent of temperature changes. Each cell in the i-th row is a planar straight-side triangle with the base side AB made of a material with the CTEs α_{1i}, and the lateral sides BC and AC made of materials with the CTEs α_{2i} and α_{3i}, $i = \overline{1, m}$, respectively (Figure 8). It is assumed that the cell angles a_i and b_i are equal to each other and the lateral cell sides are made of the same material, so $\alpha_{2i} = \alpha_{3i}$. Therefore, the adaptive lattice is axisymmetric. In every row, we need to know two CTEs on its lower and upper boundaries, which are denoted as B_i and B_{i+1}, respectively. Two types of lattice arrangement can be used. In the first-type lattice, the first row is designed as if it connects substrates with the CTEs A_1 and A_2, i.e., $B_1 = A_1$ and $B_2 = A_2$ and all other rows connect substrates with the CTEs A_2 and A_2, i.e., $B_2 = B_i = A_2$, $i = \overline{3, m+1}$. In the second-type lattice, all rows except the last one are designed as if they connect substrates with the CTEs A_1 and A_1, i.e., $B_i = B_{i+1} = A_1$, $i = \overline{1, m-1}$ and the last row connects substrates with the CTEs A_1 and A_2, i.e., $B_m = A_1$ and $B_{m+1} = A_2$. In every row, the height h_i and the angles $a_i = b_i$ depend on B_i, B_{i+1}, and the CTE $\alpha_{2i} = \alpha_{3i}$. Before starting lattice design, we have to specify a number n of cells in every row and a lattice slope γ. The rows are designed sequentially starting with the first row. In every row, we have to select cell materials and then find the cell angles and the row height. In conical lattices, the slope differs from zero, so in every row, a radius of the upper circle r_{i+1} must be found to be used in the design of the next row. When the rows are designed, they are arranged into a whole lattice. Among all solutions to the problem, we select the combination of lattice materials that provide the largest structural efficiency.

7. One-row design

Consider a separate row of the axisymmetric lattice. It consists of n cells that connect a lower circle with radius r_i and the CTE B_i and an upper circle with radius r_{i+1} and the CTE B_{i+1}. Repeating the

procedure described in [Toropova and Steeves 2015; 2016], the CTE of the material of the cell lateral sides can be presented in the form

$$\alpha_{2i} = \alpha_{3i} = \frac{r_i^2 B_i - r_i r_{i+1} \cos\phi(B_i + B_{i+1}) + r_{i+1}^2 B_{i+1}}{r_i^2 + r_{i+1}^2 - 2r_i r_{i+1} \cos\phi + h_i^2}, \tag{7-1}$$

where $\phi = \pi/n$. The normalized height of every row can be expressed from (7-1) as

$$\eta_i = \frac{h_i}{R_1} = \sqrt{\frac{B_i - \alpha_{2i} + q_i^2(B_{i+1} - \alpha_{2i}) - q_i \cos\phi(B_i + B_{i+1} - 2\alpha_{2i})}{\alpha_{2i}}}, \tag{7-2}$$

where $q_i = r_{i+1}/r_i$. The angles $a_i = b_i$ between the base and the lateral sides in the cell are

$$a_i = b_i = \arccos\frac{\sin\phi}{\sqrt{1 + q_i^2 - 2q_i \cos\phi + \eta_i^2}}. \tag{7-3}$$

Now, we need to specify the CTEs B_i and B_{i+1}. Because aluminum and titanium are conventional materials for a satellite and its outboard platform, the triangle base sides in the first-row cells are made of aluminum and $\alpha_{11} = B_1$ is equal to the CTE of aluminum. For B_i and B_{i+1}, $i = \overline{2, m}$, there are three possibilities: both B_i and B_{i+1} are equal to the CTE of aluminum, both B_i and B_{i+1} are equal to the CTE of titanium, and B_i is equal to the CTE of aluminum, while B_{i+1} is equal to the CTE of titanium. The normalized height of a lattice row and the angles between the base and the lateral cell sides are found from (7-2), (7-3), which are scale independent, and shown in Figures 9–11 for $0.5 \le q_i \le 1$, $n = 16$. Cylindrical lattices have $q_i = 1$, while for conical lattices $q_i < 1$. The curves in the plots correspond to three possible materials of the cell lateral sides: titanium, Kovar, and Invar. The intersections of these curves with the vertical line $q_i = 1$ in left sides of Figures 9, 10, and 11 provide the values of the row heights if the lateral cell sides in the cylindrical lattice are made of titanium, Kovar, and Invar, respectively. The intersections of these curves with the vertical line $q_i = 1$ in the right sides of Figures 9, 10, and 11 provide the values of the angles at the cell base sides if the lateral cell sides are made of the same set of materials. Figure 9 relates to aluminum and titanium row boundaries, Figure 10 to both titanium row boundaries, and Figure 11 to both aluminum row boundaries.

In conical lattices, $\eta_i = -q_i/\gamma + 1/\gamma$. Hence, the intersections of the straight lines in Figures 9, 10, 11 with the curves indicate the values of the row normalized height η_i and the normalized radius q_i of the row upper boundary if the cell lateral sides are made of titanium, Kovar or Invar, respectively. These values of q_i are marked with an asterisk. In this work, all plots are built for $\gamma = 0.25$. The cell angles $a_i = b_i$ can be found in Figures 9, 10, 11 when q_i are equal to the values marked with an asterisk. It is seen (Figures 9, 11) that for $\gamma = 0.25$, the straight line does not cross the Invar curves, hence, the conic lattice rows connecting aluminum and titanium substrates or both aluminum substrates can have the cell lateral sides made of titanium or Kovar but not of Invar. In a conic lattice with a smaller slope γ, cell lateral sides made of Invar may be possible. The plots in Figure 10 contain only two curves because cells with all sides made of titanium cannot provide zero CTE along the row height.

All plots show that the smaller the CTE of the lateral-side material is, cells with larger angles $a_i = b_i$ and heights η_i are needed to adapt thermal expansion. In all plots, the curves related to Invar lateral sides lie noticeably higher than the curves related to Kovar or titanium lateral members. The influence of the cell geometry on the structural efficiency is considered in the next section.
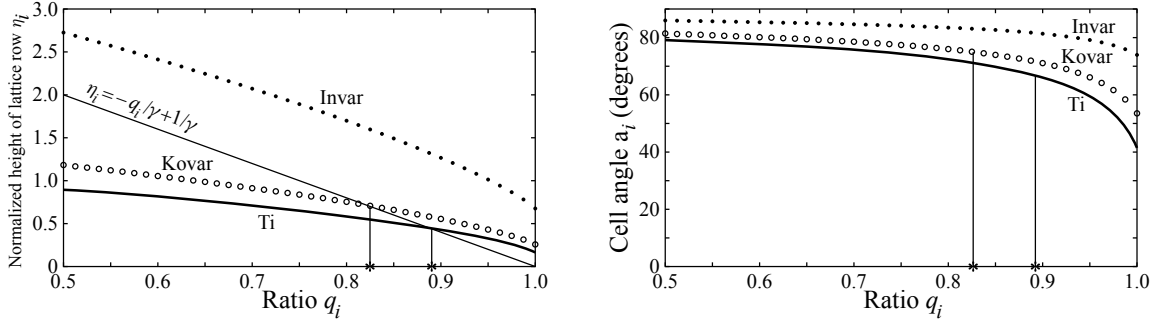
Figure 9. Normalized row height (left) and angle between the base and the lateral cell sides (right) for $B_i = 22.2\,\text{ppm/}^\circ\text{C}$, $B_{i+1} = 8.6\,\text{ppm/}^\circ\text{C}$, $n = 16$. Lateral cell side are made of Invar, Kovar, or titanium. Values of q_i with asterisks relate to conical lattices with the slope $\gamma = 0.25$.
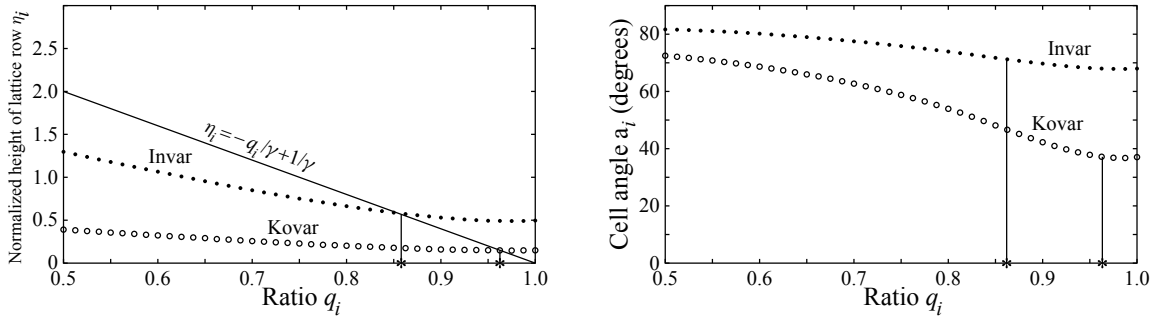

Figure 10. Normalized row height (left) and angle between the base and the cell lateral sides (right) for $B_i = B_{i+1} = 8.6\,\text{ppm/}^\circ\text{C}$, $n = 16$. Lateral cell sides are made of Invar, Kovar, or titanium. Values of q_i with asterisks relate to conical lattices with the slope $\gamma = 0.25$.
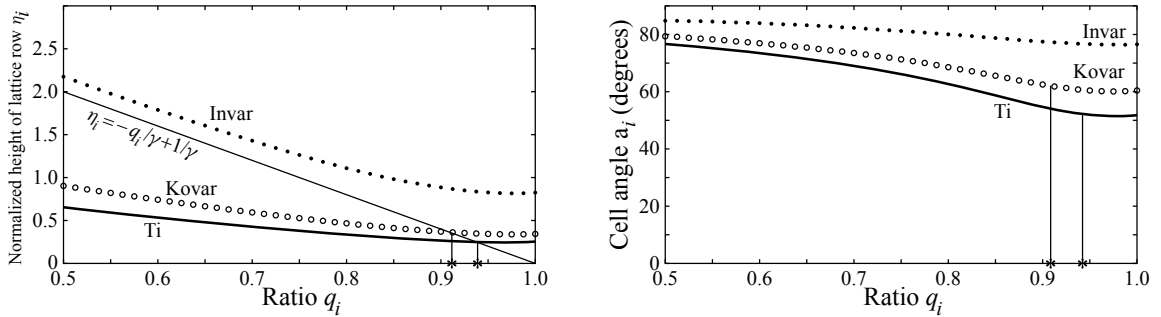
Figure 11. Normalized row height (left) and angle between the base and the cell lateral sides (right) for $B_i = B_{i+1} = 22.2\,\text{ppm/}^\circ\text{C}$, $n = 16$. Lateral cell sides are made of Invar, Kovar, or titanium. Values of q_i with asterisks relate to conical lattices with the slope $\gamma = 0.25$.
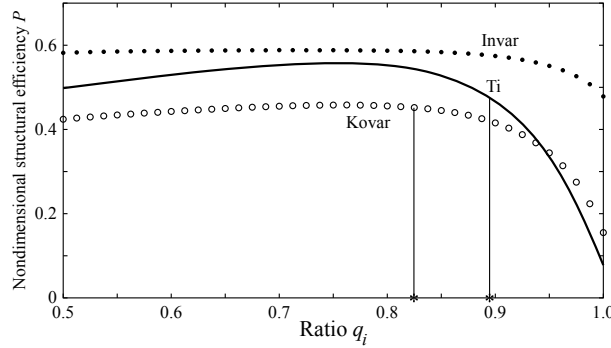
Figure 12. Nondimensional structural efficiency of a cell in axisymmetric lattice under uniaxial loading with Invar, Kovar, and titanium lateral sides for $B_i = 22.2$ ppm/°C, $B_{i+1} = 8.6$ ppm/°C, $n = 16$, $\Lambda_{1i} = \Lambda_{2i}$.

8. Structural efficiency of a cell in the axisymmetric lattice

If a cell in the axisymmetric lattice is in equilibrium when the force N is applied to its upper vertex C (Figure 8), the forces in the base and the lateral triangle sides are

$$F_1 = \tfrac{1}{2} N \cot a, \quad F_2 = F_3 = -\frac{N}{2 \sin a}.$$

Equation (3-3) for nondimensional structural efficiency of a cell in the axisymmetric lattice can be transformed into

$$P = \frac{\eta_i^4}{(\sin \phi + Q_1 l)(\sin^3 \phi + Q_2 l^3)},$$

where

$$l = \sqrt{1 + q_i^2 - 2q_i \cos \phi + \eta_i^2}, \quad Q_1 = \frac{\rho_{2i} \Lambda_{2i}}{\rho_{1i} \Lambda_{1i}}, \quad Q_2 = \frac{\Lambda_{1i} E_{1i}}{\Lambda_{2i} E_{2i}},$$

and Λ_{1i}, Λ_{2i}, E_{1i}, E_{2i}, ρ_{1i}, and ρ_{2i} are cross-sectional area, Young's modulus, and density of the materials of the base and the lateral cell sides, respectively. The curves describing the structural efficiency of the lattice cell with the lateral sides made of titanium, Kovar, or Invar are shown in Figures 12–14 for aluminum and titanium, both titanium, and both aluminum row boundaries, respectively. The intersections of these curves with the vertical line $q_i = 1$ provide the values of the structural efficiency of the cell in the one-row cylindrical lattice. The structural efficiency of the cell in the one-row conical lattice can be found in these figures when q_i takes the values marked with an asterisk; they coincide with the corresponding q_i marked with an asterisk in Figures 9, 10, 11. The plots are built for $\Lambda_{1i} = \Lambda_{2i}$.

The plots show that the structural efficiency depends of cell geometry, which depends on cell material CTEs. Note that the number of cells n in each row insignificantly affects the cell angles $a_i = b_i$ and the structural efficiency P, although they both slightly decrease when n increases.
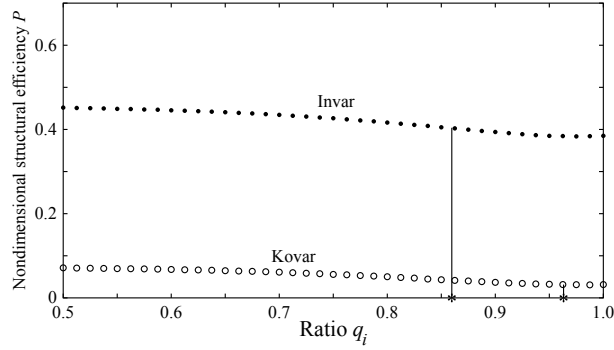
Figure 13. Nondimensional structural efficiency of a cell in axisymmetric lattice under uniaxial loading with Invar and Kovar lateral sides for $B_i = B_{i+1} = 8.6$ ppm/°C, $n = 16$, $\Lambda_{1i} = \Lambda_{2i}$.
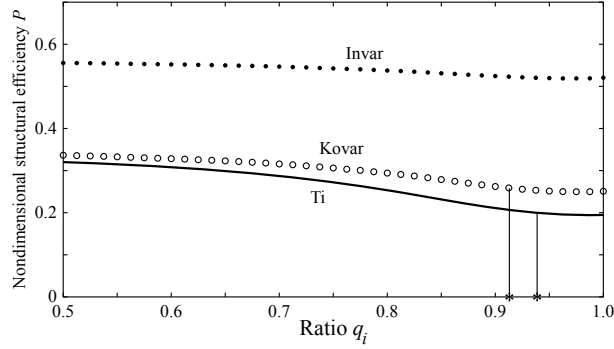
Figure 14. Nondimensional structural efficiency of a cell in axisymmetric lattice under uniaxial loading with Invar, Kovar, and titanium lateral sides for $B_i = B_{i+1} = 22.2$ ppm/°C, $n = 16$, $\Lambda_{1i} = \Lambda_{2i}$.

9. Cylindrical lattices

In cylindrical lattices $R_1 = R_2 = R$, and all lattice rows also have the same radius R. Equations (7-1)–(7-2) can be rewritten as

$$\alpha_{2i} = \alpha_{3i} = \frac{2\sin^2\left(\frac{1}{2}\phi\right)(B_i + B_{i+1})}{4R^2 \sin^2\left(\frac{1}{2}\phi\right) + h_i^2},$$

$$\eta_i = \sin\left(\tfrac{1}{2}\phi\right)\sqrt{\frac{2B_i + 2B_{i+1} - 4\alpha_{2i}}{\alpha_{2i}}}. \tag{9-1}$$

Cell angles $a_i = b_i$ can be found as

$$a_i = b_i = \arccos\frac{\cos\left(\frac{1}{2}\phi\right)\sqrt{2\alpha_{2i}}}{\sqrt{B_i + B_{i+1}}}. \tag{9-2}$$

line #	B_i (ppm/°C)	B_{i+1} (ppm/°C)	$\alpha_{2i} = \alpha_{3i}$ (ppm/°C)	η_i	$a_1 = b_1$	P
1	22.2	8.6	1.2	0.67	73.9°	0.4788
2	22.2	8.6	5.5	0.26	53.5°	0.1562
3	22.2	8.6	8.6	0.17	42.0°	0.0798
4	22.2	22.2	1.2	0.82	76.6°	0.5198
5	22.2	22.2	5.5	0.34	60.3°	0.2508
6	22.2	22.2	8.6	0.25	51.7°	0.1954
7	8.6	8.6	1.2	0.49	68.2°	0.3841
8	8.6	8.6	5.5	0.15	37.3°	0.0364

Table 4. Normalized row height, cell angles, and structural efficiency in 16-cell one-row cylindrical lattices connecting two substrates with CTEs B_i and B_{i+1} corresponding to aluminum or titanium. Lines 1–3 relate to Figures 9 and 12; lines 4–6 to Figures 11 and 14; and lines 7, 8 to Figures 10 and 13; $q_i = 1$. Lateral cell sides are made of titanium, Kovar, or Invar materials.

The cylindrical lattice is assembled row by row. The total number of lattice rows depends on a desirable lattice height. Every row is designed as if it connects two circles so that the second circle material in a row and the first circle material in the next row must have the same CTE. Because A_1 and A_2 relate to aluminum and titanium, respectively, the row circle materials may be aluminum or titanium. Hence the base cell sides can be made of aluminum or titanium. Figures 9, 10, 11 show that titanium, Kovar, and Invar can be selected as cell lateral side materials if the lower and the upper circles are made of aluminum and titanium, respectively, or if the both circles are made of aluminum. For both titanium row circle boundaries, Invar and Kovar lateral cell sides are possible. Cell geometry (the angles and the normalized height) and the nondimensional cell structural efficiency under uniaxial loading obtained from (9-1) and (9-2) are shown in Table 4.

Table 4 demonstrates that cell lateral sides made of Invar provide the largest structural efficiency compared to Kovar and titanium lateral sides, which is in agreement with the data in Figures 12–14. Hence, we consider the design of the first- and the second-type adaptive lattices with Invar cell lateral sides connecting aluminum and titanium substrates, which are shown in Figures 15 and 16, respectively. Only four rows are depicted.

First-type lattice. The normalized height of the lattice's first row (line 1 in Table 4) is 0.67 and the cell base side is made of aluminum while the lateral sides are made of Invar; the cell angles are 73.9° and the structural efficiency is 0.4788. All other rows have the normalized height 0.49 (line 7 in Table 4) and are made of titanium for the base and Invar for the lateral sides; the cell angles are 68.2° and the structural efficiency is 0.3841. Hence, the lattice structural efficiency is 0.3841 and the total height is $[0.67 + (m-1)0.49]R$ (Figure 15).

Second-type lattice. The normalized height of the lattice's first $m-1$ rows is 0.82 (line 4 in Table 4), the cell base side is made of aluminum, while the lateral sides are made of Invar; the cell angles are 76.6° and the structural efficiency is 0.5198. The last row has a normalized height 0.67 (line 1 in Table 4) with aluminum base and Invar lateral cell sides, the cell angles are 73.9° and the structural efficiency is
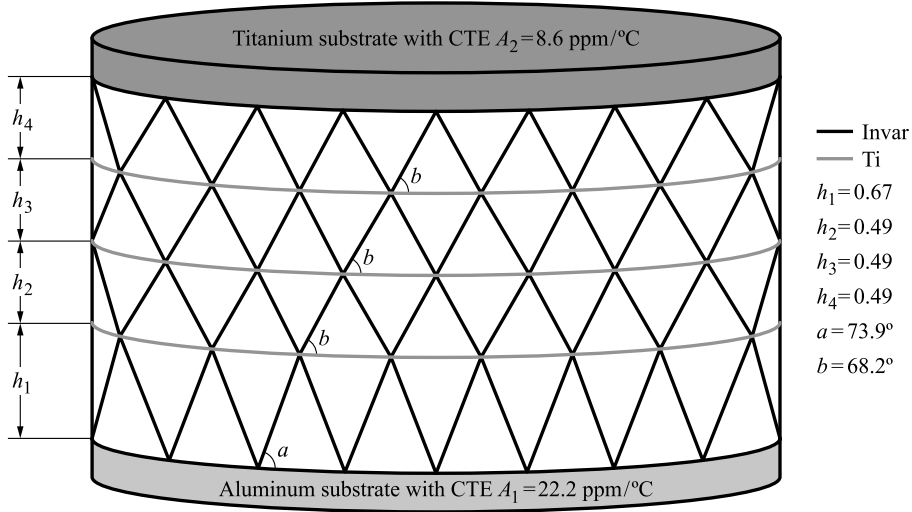
Figure 15. First-type cylindrical adaptive lattice connecting aluminum and titanium circular disks. The cell lateral members are made of Invar. In the first row, the angle at the triangle base side is $a = 73.9^o$ and the base members are made of aluminum, while in all other rows the angle at the triangle base side is $b = 68.2^o$ and the base members are made of titanium. The lattice structural efficiency is $P = 0.3841$.

0.4788. Hence, the lattice structural efficiency is 0.4788 and the total height is $[0.82(m-1) + 0.67]R$ (Figure 16), which are larger than in the first-type lattice.

It is possible to design other adaptive cylindrical lattices connecting aluminum and titanium substrates composed of cells made of Kovar or titanium lateral sides, but their structural efficiency is significantly smaller. For example, in the second-type cylindrical lattice with Kovar cell lateral sides the cell angles in the first $m-1$ rows are $60.3°$ (line 5 in Table 4), the heights of the rows are equal to 0.34, and the structural efficiency is 0.2508. In the last row, the angles are $53.5°$ (line 2 in Table 4), the height is 0.26, and the structural efficiency is 0.1562. The total structural efficiency is min $\{0.2508, 0.1562\} = 0.1562$ and the total height is $[0.34(m-1) + 0.26]R$. Also, a first-type lattice with Kovar lateral sides is possible, but its structural efficiency is extremely low (line 8 in Table 4). A second-type lattice with all titanium lateral cell sides (line 6 and 3 in Table 4) has very small structural efficiency min $\{0.1954, 0.0798\} = 0.0798$.

10. Conical lattices

A truncated conical lattice consists of several rows. If the lattice slope and the CTEs of the row boundaries B_i, B_{i+1} are predetermined and the lateral cell side CTEs $\alpha_{2i} = \alpha_{3i}$ are selected, the normalized radius of the upper-row circle can be expressed from (7-2) as

$$q_i = \frac{2\alpha_{2i} - w(s_{1i} + s_{2i})\gamma^2 - \sqrt{(2\alpha_{2i} - w(s_{1i} + s_{2i})\gamma^2)^2 - 4(\alpha_{2i} - s_{2i}\gamma^2)(\alpha_{2i} - s_{1i}\gamma^2)}}{2(\alpha_{2i} - s_{2i}\gamma^2)},$$
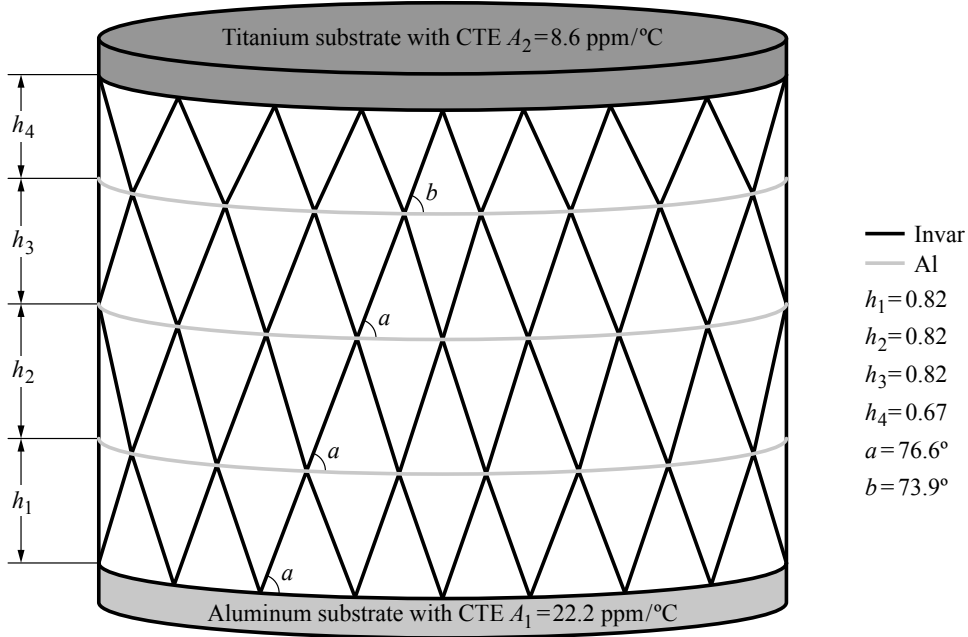
Figure 16. Second-type cylindrical adaptive lattice connecting aluminum and titanium circular disks. The cell lateral members are made of Invar, while the base members are made of aluminum. In the last row, the angle at the triangle base side is $b = 73.9^o$ and in all other rows the angle at the triangle base side is $a = 76.6^o$. Lattice structural efficiency is $P = 0.4788$.

where $s_{1i} = B_i - \alpha_{2i}$, $s_{2i} = B_{i+1} - \alpha_{2i}$, $w = \cos\phi$. The cell angles in the i-th row are

$$a_i = b_i = \arccos \frac{\sin\phi\sqrt{\alpha_{2i}}}{\sqrt{B_i + q_i^2 B_{i+1} - q_i \cos\phi(B_i + B_{i+1})}}.$$

Because the lattices designed in this work are scale independent, let $R_1 = 1$.

First-type lattices. Here, we design two first-type lattices. If $\gamma = 0.25$, then the first row of the conical lattice can have titanium or Kovar cell lateral sides (Section 8). In the next rows connecting two virtual titanium circles the cell lateral sides may be made of Kovar or Invar, but Invar is preferable because it provides larger structural efficiency. In the first row of the first lattice, the lateral and the base cell sides are made of titanium and aluminum, respectively, while in the first row of the second lattice the lateral and the base cell sides are made of Kovar and aluminum, respectively. In both lattices, starting from the second row, the cells have Invar lateral and titanium base sides. Tables 5 and 6 contain the values of the row height, the cell angles and the structural efficiency in the two first-type lattices. Both lattices can have as many rows as it is necessary for design purposes; in all following rows the cell materials and the angles will be the same as in the lines 2, 3, 4 of Tables 5 and 6. The minimum structural efficiency in both tables is the same $P = 0.3914$ but their total heights are different: $H = 178$ in the first lattice

row #	B_i (ppm/°C)	B_{i+1} (ppm/°C)	$\alpha_{2i} = \alpha_{3i}$ (ppm/°C)	h_i	$a_i = b_i$	q_i	P
1	22.2	8.6	8.6	0.46	67.2°	0.89	0.4892
2	8.6	8.6	1.2	0.51	71.6°	0.86	0.3914
3	8.6	8.6	1.2	0.44	71.6°	0.86	0.3914
4	8.6	8.6	1.2	0.37	71.6°	0.86	0.3914

Table 5. Cell angles, structural efficiency, and row heights in the first-type conical lattice consisting of four rows and connecting aluminum and titanium substrates. The cell lateral sides in the first row are made of titanium, while in other rows of Invar.

row #	B_i (ppm/°C)	B_{i+1} (ppm/°C)	$\alpha_{2i} = \alpha_{3i}$ (ppm/°C)	h_i	$a_i = b_i$	q_i	P
1	22.2	8.6	5.5	0.72	75.2°	0.82	0.4523
2	8.6	8.6	1.2	0.47	71.6°	0.86	0.3914
3	8.6	8.6	1.2	0.40	71.6°	0.86	0.3914
4	8.6	8.6	1.2	0.35	71.6°	0.86	0.3914

Table 6. Cell angles, structural efficiency, and row heights in the first-type conical lattice consisting of four rows and connecting aluminum and titanium substrates. The cell lateral sides in the first row are made of Kovar, while in other rows of Invar.

row #	B_i (ppm/°C)	B_{i+1} (ppm/°C)	$\alpha_{2i} = \alpha_{3i}$ (ppm/°C)	h_i	$a_i = b_i$	q_i	P
1	22.2	22.2	8.6	0.25	52.6°	0.94	0.1996
2	22.2	22.2	8.6	0.24	52.6°	0.94	0.1996
3	22.2	22.2	8.6	0.22	52.6°	0.94	0.1996
4	22.2	8.6	8.6	0.37	67.2°	0.89	0.4892

Table 7. Cell angles, structural efficiency, and row heights in the second-type conical lattice consisting of four rows and connecting aluminum and titanium substrates. The cell lateral sides are made of titanium.

(Figure 17) and $H = 194$ in the second lattice. Note that in conical lattices neighboring rows can have the same cell angles but row heights are different.

Second-type lattices. Two second-type conical lattices are designed here; their geometric data and the structural efficiency are shown in Tables 7 and 8, respectively. In both lattices, the base cell sides in all rows are made of aluminum. As it was shown in Section 8, second-type conical lattices cannot have cell lateral sides made of Invar. Hence, the cell lateral sides in the first lattice are made of titanium with the total structural efficiency $P = 0.1996$ and the total height $H = 108$, while the lateral sides in the second lattice are made of Kovar with the total structural efficiency $P = 0.2608$ and the total heights $H = 153$, which is noticeably smaller than for two first-type conical lattices designed earlier.

Cylindrical and conical lattice rows designed in this work can be combined in any desirable way. For example, a lattice in Figure 18 consists of a one-row cylindrical lattice and a four-row conical lattice. Both

row #	B_i (ppm/°C)	B_{i+1} (ppm/°C)	$\alpha_{2i} = \alpha_{3i}$ (ppm/°C)	h_i	$a_i = b_i$	q_i	P
1	22.2	22.2	5.5	0.36	62.13°	0.91	0.2608
2	22.2	22.2	5.5	0.33	62.13°	0.91	0.2608
3	22.2	22.2	5.5	0.30	62.13°	0.91	0.2608
4	22.2	8.6	5.5	0.54	75.23°	0.82	0.4523

Table 8. Cell angles, structural efficiency, and row heights in the second-type conical lattice consisting of four rows and connecting aluminum and titanium substrates. The cell lateral sides are made of Kovar.
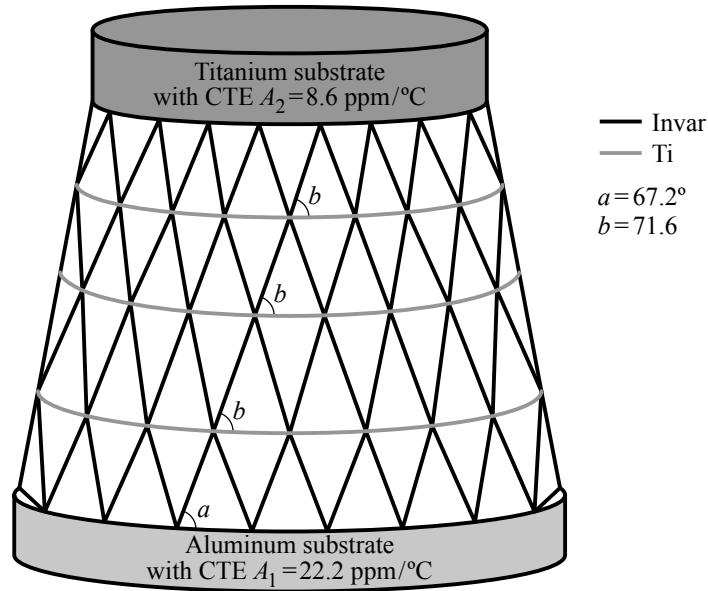
Figure 17. First-type conical adaptive lattice with Invar lateral cell members connecting aluminum and titanium circular disks. In the first row, the angle at the triangle base side is $a = 67.2^o$ and the base members are made of aluminum, while in all other rows the angle at the triangle base side is $b = 71.6^o$ and the base members are made of titanium. Lattice structural efficiency is $P = 0.3914$.

lattices in Figures 17, 18 have the same structural efficiency $P = 0.3914$. The design of axisymmetric lattices performed here demonstrates that both types of lattice arrangement can provide large structural efficiency. For example, the first row in Figure 18 belongs to the first-type, while the other rows to the second-type of lattice arrangement.

11. Conclusions

The research shows that planar triangular cells can form planar or 3-D axisymmetric cylindrical or conical anisotropic adaptive lattices connecting two substrates with different CTEs. Such lattices do not accumulate thermal stresses, provide temperature independent-distance and have high ability to eliminate
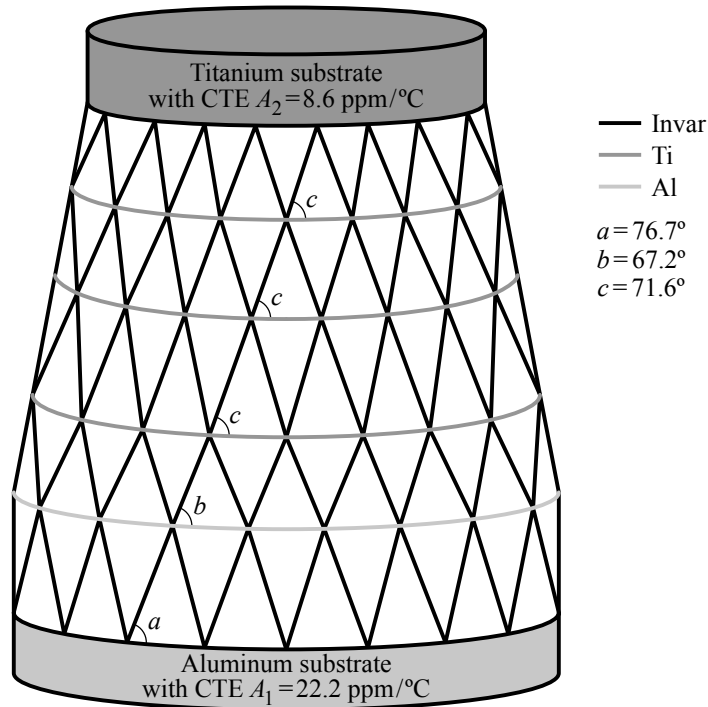
Figure 18. Five-row axisymmetric adaptive lattice combined of a one-row cylindrical lattice and a four-row conical lattice and connecting aluminum and titanium circular disks. Cell lateral sides are made of Invar. The cells in the first two rows have aluminum base sides and in all other rows - titanium base sides. The angle at the triangle base side in the first row is $a = 73.9^o$, in the second row is $b = 67.2^o$, and in all other rows $c = 71.6^o$. Lattice structural efficiency is $P = 0.3914$.

thermal expansion mismatch stresses between the substrates. Lattice cells are straight line triangles with different angles at the cell base sides; three-cell members are made of conventional materials with different CTEs. Nonidentical cells can be arranged in several rows of different heights. To design such a lattice, the equations linking the cell angles to the CTEs of member materials must be obtained from the kinematic constraints imposed on the lattice; their solutions are scale independent. Materials desirable for the design task with CTEs that provide the existence of a solution to these equations are considered in order to select a combination yielding the maximum structural efficiency of the lattice. The cell angles are found from the equations as functions of two substrate CTEs and the CTEs of cell materials. It is noticed that materials with smaller CTEs lead to cells with larger angles at the cell base sides, which results in larger structural efficiency of the cells under uniaxial loading. The lattices with triangular cells can connect substrates with both ratios of their CTEs $A_1 < A_2$ or $A_1 > A_2$, which is different from planar lattices with hexagonal cells (used in previous works) that can serve as adapters only when $A_1 < A_2$. Compared to the lattices with hexagonal cells the presented lattices can be easily manufactured and are more stable to manufacturing imperfections because each cell has only three joints.

References

[Berger and McMeeking 2018] J. B. Berger and R. M. McMeeking, "Mechanical characterization of a bonded tailorable coefficient of thermal expansion lattice with near optimal performance", *J. Mater. Res.* **33**:20 (2018), 3383–3397.

[Berger et al. 2011] J. Berger, C. Mercer, R. M. McMeeking, and A. G. Evans, "The design of bonded bimaterial lattices that combine low thermal expansion with high stiffness", *J. Am. Ceram. Soc.* **94**:S1 (2011), S42–S54.

[Dang 2006] C. H. Dang, "Coefficient of thermal expansion adaptor", US patent application US20080160274A1, 2006, https://tinyurl.com/pat0274a1.

[Du et al. 2016] Z. Du, M. Zhu, Z. Wang, and J. Yang, "Design and application of composite platform with extreme low thermal deformation for satellite", *Compos. Struct.* **152** (2016), 693–703.

[Du et al. 2017] Z.-C. Du, H.-F. Hou, Z.-G. Wang, and J.-G. Yang, "Thermal deformation isolation for satellite platforms via flexible connections", *Int. J. Precis. Eng. Manuf.* **18**:12 (2017), 1821–1832.

[Edeson et al. 2010] R. Edeson, G. S. Aglietti, and A. R. L. Tatnall, "Conventional stable structures for space optics: the state of the art", *Acta Astronaut.* **66**:1-2 (2010), 13–32.

[Gdoutos et al. 2013] E. Gdoutos, A. A. Shapiro, and C. Daraio, "Thin and thermally stable periodic metastructures", *Exp. Mech.* **53**:9 (2013), 1735–1742.

[Gibiansky and Torquato 1997] L. V. Gibiansky and S. Torquato, "Thermal expansion of isotropic multiphase composites and polycrystals", *J. Mech. Phys. Solids* **45**:7 (1997), 1223–1252.

[Grima et al. 2007a] J. N. Grima, P.-S. Farrugia, R. Gatt, and V. Zammit, "Connected triangles exhibiting negative Poisson's ratios and negative thermal expansion", *J. Phys. Soc. Jpn.* **76**:2 (2007), art. id. 025001.

[Grima et al. 2007b] J. N. Grima, P. S. Farrugia, R. Gatt, and V. Zammit, "A system with adjustable positive or negative thermal expansion", *Proc. R. Soc. Lond. A* **463**:2082 (2007), 1585–1596.

[Ha et al. 2017] C. S. Ha, M. E. Plesha, and R. S. Lakes, "Simulations of thermoelastic triangular cell lattices with bonded joints by finite element analysis", *Extreme Mech. Lett.* **12** (2017), 101–107.

[Hopkins et al. 2013] J. B. Hopkins, K. J. Lange, and C. M. Spadaccini, "Designing microstructural architectures with thermally actuated properties using freedom, actuation, and constraint topologies", *J. Mech. Des. (ASME)* **135**:6 (2013), art. id. 061004.

[Jefferson et al. 2009] G. Jefferson, T. A. Parthasarathy, and R. J. Kerans, "Tailorable thermal expansion hybrid structures", *Int. J. Solids Struct.* **46**:11-12 (2009), 2372–2387.

[Lakes 1996] R. Lakes, "Cellular solid structures with unbounded thermal expansion", *J. Mater. Sci. Lett.* **15**:6 (1996), 475–477.

[Lakes 2007] R. Lakes, "Cellular solids with tunable positive or negative thermal expansion of unbounded magnitude", *Appl. Phys. Lett.* **90**:22 (2007), art. id. 221905.

[Lehman and Lakes 2013] J. Lehman and R. Lakes, "Stiff lattices with zero thermal expansion and enhanced stiffness via rib cross section optimization", *Int. J. Mech. Mater. Des.* **9**:3 (2013), 213–225.

[Miller et al. 2008] W. Miller, D. S. Mackenzie, S. W. Smith, and K. E. Evans, "A generalised scale-independent mechanism for tailoring of thermal expansivity: positive and negative", *Mech. Mater.* **40**:4-5 (2008), 351–361.

[Phoenix and Tarazaga 2017] A. A. Phoenix and P. A. Tarazaga, "Dynamic model reduction using data-driven Loewner-framework applied to thermally morphing structures", *J. Sound Vib.* **396** (2017), 274–288.

[Phoenix and Tarazaga 2018] A. A. Phoenix and P. A. Tarazaga, "Thermal morphing anisogrid smart space structures, I: Introduction, modeling, and performance of the novel smart structural application", *J. Vib. Control* **24**:13 (2018), 2853–2872.

[Phoenix et al. 2018] A. A. Phoenix, J. Borggaard, and P. A. Tarazaga, "Thermal morphing anisogrid smart space structures, II: Ranking of geometric parameter importance, trust region optimization, and performance evaluation", *J. Vib. Control* **24**:13 (2018), 2873–2893.

[Sigmund and Torquato 1996] O. Sigmund and S. Torquato, "Composites with extremal thermal expansion coefficients", *Appl. Phys. Lett.* **69**:21 (1996), 3203–3205.

[Sigmund and Torquato 1997] O. Sigmund and S. Torquato, "Design of materials with extreme thermal expansion using a three-phase topology optimization method", *J. Mech. Phys. Solids* **45**:6 (1997), 1037–1067.

[Steeves et al. 2007] C. A. Steeves, S. L. dos Santos e Lucato, M. He, E. Antinucci, J. W. Hutchinson, and A. G. Evans, "Concepts for structurally robust materials that combine low thermal expansion with high stiffness", *J. Mech. Phys. Solids* **55**:9 (2007), 1803–1822.

[Steeves et al. 2009] C. A. Steeves, C. Mercer, E. Antinucci, M. Y. He, and A. G. Evans, "Experimental investigation of the thermal properties of tailored expansion lattices", *Int. J. Mech. Mater. Des.* **5**:2 (2009), 195–202.

[Toropova and Steeves 2014] M. M. Toropova and C. A. Steeves, "Bimaterial lattices with anisotropic thermal expansion", *J. Mech. Mater. Struct.* **9**:2 (2014), 227–244.

[Toropova and Steeves 2015] M. M. Toropova and C. A. Steeves, "Adaptive bimaterial lattices to mitigate thermal expansion mismatch stresses in satellite structures", *Acta Astronaut.* **113** (2015), 132–141.

[Toropova and Steeves 2016] M. M. Toropova and C. A. Steeves, "Bimaterial lattices as thermal adapters and actuators", *Smart Mater. Struct.* **25**:11 (2016), art. id. 115030.

[Vasiliev et al. 2012] V. V. Vasiliev, V. A. Barynin, and A. F. Razin, "Anisogrid composite lattice structures: development and aerospace applications", *Compos. Struct.* **94**:3 (2012), 1117–1127.

[Wei et al. 2016] K. Wei, H. Chen, Y. Pei, and D. Fang, "Planar lattices with tailorable coefficient of thermal expansion and high stiffness based on dual-material triangle unit", *J. Mech. Phys. Solids* **86** (2016), 173–191.

[Wei et al. 2017] K. Wei, Y. Peng, W. Wen, Y. Pei, and D. Fang, "Tailorable thermal expansion of lightweight and robust dual-constituent triangular lattice material", *J. Appl. Mech.* (*ASME*) **84**:10 (2017), art. id. 101006.

[Wei et al. 2018a] K. Wei, Y. Peng, K. Wang, S. Duan, X. Yang, and W. Wen, "Three dimensional lightweight lattice structures with large positive, zero and negative thermal expansion", *Compos. Struct.* **188** (2018), 287–296.

[Wei et al. 2018b] K. Wei, Q. Yang, B. Ling, Z. Qu, Y. Pei, and D. Fang, "Design and analysis of lattice cylindrical shells with tailorable axial and radial thermal expansion", *Extreme Mech. Lett.* **20** (2018), 51–58.

[Xu and Pasini 2016] H. Xu and D. Pasini, "Structurally efficient three-dimensional metamaterials with controllable thermal expansion", *Sci. Rep.* **6** (2016), art. id. 34924.

[Yousefiani et al. 2009a] A. Yousefiani, J. M. Comfort, J. G. Vollmer, and M. L. Hand, "Joined composite structures with a graded coefficient of thermal expansion for extreme environment applications", US Patent application US20090266870A1, Boeing, 2009, https://tinyurl.com/yb7bsgm2.

[Yousefiani et al. 2009b] A. Yousefiani, J. G. Vollmer, M. L. Hand, and J. M. Comfort, "Built-up composite structures with a graded coefficient of thermal expansion for extreme environment applications", US Patent application US20090269497A1, Boeing, 2009, https://patents.google.com/patent/US20090269497.

MARINA M. TOROPOVA: marina.toropova@mtmedi.com
MT Medi Corp, Toronto, ON, Canada

■msp

THERMAL STRESS AROUND AN ELLIPTIC HOLE WEAKENED BY ELECTRIC CURRENT IN AN INFINITE THERMOELECTRIC PLATE

KUN SONG, HAO-PENG SONG, PETER SCHIAVONE AND CUN-FA GAO

We propose effective strategies to manage thermal stress around an elliptic hole induced by electric current and heat flux in a thermoelectric material. Our results indicate that the thermal stress can be reduced dramatically, with little influence on conversion efficiency, by simply adjusting the value of the electric current. In fact, we find that additional electric current in the vertical direction can totally neutralize the thermal stress at a particular point, including the thermal stress singularity at a crack tip.

1. Introduction

Thermoelectric materials have the ability to convert heat directly into electric power and vice versa. Such materials are particularly advantageous in that they are noiseless, have no mechanical moving parts, and create no pollution. The use of thermoelectric materials has been pervasive in many different applications [Zhao and Tan 2014; Riffat and Ma 2003; Tritt and Subramanian 2006] but their lower thermal-electric conversion efficiency precludes their use as alternatives to traditional engines.

Much effort has been devoted to the optimization of the performance of thermoelectric materials; for example, the incorporation of nanoinclusions [Kim et al. 2006; Pei et al. 2011] and the continual development of manufacturing processes [Okamura et al. 2010; Kim and Chun 2007] as well as to the optimization of thermoelectric devices [Xuan 2002; Göktun 36; Omer and Infield 1998]. A crucial part of this ongoing progress is the simultaneous development of mathematical models and theoretical analyses required to support and guide overall progress in this area. For example, Callen [1960] has proposed the governing equations of a thermoelectric medium; Liu [2012] has developed a continuum theory for thermoelectric bodies in the framework of continuum mechanics while adhering to the general principles of thermodynamics; effective thermoelectric behavior of layered heterogeneous media has been studied by Yang et al. [2012]; Song et al. [2017] have discussed the overall macroperformance of a multilayered thermoelectric medium. These studies have led to dramatic improvements in the performance of thermoelectric devices as well as rapid recent developments in both their design and application.

Reliability and lifespan are also important factors to be considered in thermoelectric devices since most thermoelectric materials have relatively inferior mechanical properties. It has been shown that even in the absence of mechanical restraints, temperature gradients in thermoelectric materials create complex mechanical stress distributions, which are particularly severe in high performance media and difficult to counteract via free deformation [Choi et al. 2011; Yu et al. 2012]. In contrast to classical materials, simply connected thermoelectric media also suffer from the induction of thermal stresses, leading to,

for example, a (thermal stress) singularity of order $r^{-1/2}$ at the tip of an impermeable crack [Song et al. 2015]. Research into the suppression of thermal stress in thermoelectric systems, however, remains relatively rare. This can be attributed to the complex nature of the mathematical models involved. It is this particular area of endeavor that motivates our present study.

In this paper, we utilize complex variable methods to analyze the thermal stress in the vicinity of an elliptic hole present in a thermoelectric plate. Our study allows us to propose different strategies for dealing with induced thermal stress in thermoelectric materials. Firstly, our numerical analyses show that a simple adjustment of electric current can dramatically suppress the thermal stress in a thermoelectric medium while having little influence on the conversion efficiency. Secondly, additional electric current in the vertical direction is shown to be effective in entirely neutralizing the thermal stress at a particular point; for example, the thermal stress singularity at a crack tip can be eliminated by the introduction of electric current in the vertical direction. Each of these findings are significant in that they provide relatively simple yet effective ways of dealing with thermal stress in thermoelectric devices.

2. Governing equations

2.1. *Electric fields.* Consider a two-dimensional thermoelectric material occupying a Cartesian plane described by a generic point (x, y). The coupled transport of electric current and heat flux means that the temperature field and the electric potential in the material depend explicitly on position and are thus here denoted by $T(x, y)$ and $\phi(x, y)$, respectively. We assume further that all material parameters are temperature independent so that, in particular, the electric conductivity σ and Seebeck coefficient S for this thermoelectric material are taken to be uniform. The governing equation for the electric current density J in the thermoelectric material can then be expressed as [Milton 2002]

$$-J = \sigma \nabla \phi + \sigma S \nabla T. \tag{1}$$

Since the charge is restricted in a standalone system, the electric current is conserved. Consequently,

$$\nabla \cdot J = 0. \tag{2}$$

Substituting (1) into (2), we have

$$\nabla^2(\phi + ST) = 0. \tag{3}$$

The general solution of (3) is written in terms of the analytic function $f(z)$ of the complex variable $z = x + iy$ as

$$\phi + ST = \text{Re}[f(z)]. \tag{4}$$

Substituting (4) into (1), the components of the electric current density can be expressed as

$$J_x = -\tfrac{1}{2}\sigma(f'(z) + \overline{f'(z)}), \tag{5}$$

$$J_y = -\tfrac{1}{2}\sigma i(f'(z) - \overline{f'(z)}), \tag{6}$$

so that

$$J_x - i J_y = -\sigma f'(z). \tag{7}$$

2.2. *Thermal fields.* In a thermoelectric material, the heat flux $\boldsymbol{Q}$ is induced by the coupled electric current and negative local temperature gradient and is written as [Callen 1960]

$$\boldsymbol{Q} = TS\boldsymbol{J} - \kappa \nabla T, \tag{8}$$

where κ is the thermal conductivity. In contrast to heat conduction in traditional materials, the heat flux in a thermoelectric material is not conserved as a result of Joule heating. Both the electric power and heat flux constitute the total energy flux $\boldsymbol{U}$ such that [Yang et al. 2012]

$$\boldsymbol{U} = \boldsymbol{Q} + \phi \boldsymbol{J} = (\phi + ST)\boldsymbol{J} - \kappa \nabla T. \tag{9}$$

We restrict our system to be conserved, such that the energy flux is divergence-free,

$$\nabla \cdot \boldsymbol{U} = 0. \tag{10}$$

Substituting (9) into (10), and noting (4), we have

$$\nabla^2 T + \frac{\sigma}{\kappa} f'(z) \overline{f'(z)} = 0, \tag{11}$$

where the overbar denotes the complex conjugate. Solving (11), the temperature field can be expressed in the form

$$T = -\frac{\sigma}{4\kappa} f(z) \overline{f(z)} + g(z) + \overline{g(z)} + N, \tag{12}$$

where $g(z)$ is an arbitrary analytic function and N is an arbitrary real constant which denotes the uniform temperature field. The electric potential can be derived by substituting (12) into (4) as

$$\phi = \frac{\sigma S}{4\kappa} f(z) \overline{f(z)} + \tfrac{1}{2}(f(z) + \overline{f(z)}) - S(g(z) + \overline{g(z)}) - SN. \tag{13}$$

Finally, the thermal flux and energy flux can be deduced from (8) and (9) as

$$Q_x - iQ_y = \sigma f'(z)\left[\tfrac{1}{2}\overline{f(z)}\left(\frac{\sigma S}{2\kappa} f(z) + 1\right) - S(2\,\mathrm{Re}[g(z)] + N)\right] - 2\kappa g'(z), \tag{14}$$

$$U_x - iU_y = -\tfrac{1}{2}\sigma f(z) f'(z) - 2\kappa g'(z). \tag{15}$$

Since the temperature/electric potential and electric current/heat/energy flux have been expressed in terms of the two analytic functions $f(z)$ and $g(z)$, the corresponding thermal-electric problems in a two-dimensional thermoelectric system will be solved completely if the two analytic functions f and g are identified.

2.3. *Stress field.* The corresponding Airy (thermal) stress function Φ should satisfy the following compatibility equation [Parkus 1968; Timoshenko and Goodier 1951]

$$\nabla^4 \Phi + E\alpha \nabla^2 T = 0, \tag{16}$$

where α is the thermal expansion coefficient and E is Young's modulus. The general solution of (16) consists of the general solution of the biharmonic equation denoted here by Φ_0 added to a particular solution Φ_p of (16):

$$\Phi = \Phi_0 + \Phi_p. \tag{17}$$

In fact [Muskhelishvili 1975],

$$\Phi_0 = \tfrac{1}{2}(\bar{z}\,\varphi(z) + z\,\overline{\varphi(z)} + \theta(z) + \overline{\theta(z)}), \tag{18}$$

where $\varphi(z)$ and $\theta(z)$ are two analytic functions. Noting (12), the particular solution of (16) can be chosen as

$$\Phi_p = \frac{E\alpha\sigma}{16\kappa} h(z)\,\overline{h(z)}, \tag{19}$$

where

$$h(z) = \int f(z)\,dz. \tag{20}$$

Thus, the solution Φ can be expressed as

$$\Phi = \tfrac{1}{2}(\bar{z}\,\varphi(z) + z\,\overline{\varphi(z)} + \theta(z) + \overline{\theta(z)}) + \frac{E\alpha\sigma}{16\kappa} h(z)\overline{h(z)}. \tag{21}$$

We introduce the complex function $\psi(z)$ as the derivative of $\theta(z)$ with respect to z, thus the stress components can be deduced from (21) as

$$\sigma_{11} + \sigma_{22} = 4\frac{\partial^2 \Phi}{\partial z\,\partial \bar{z}} = 2(\varphi'(z) + \overline{\varphi'(z)}) + \frac{E\alpha\sigma}{4\kappa} f(z)\,\overline{f(z)}, \tag{22}$$

$$\sigma_{22} - \sigma_{11} + 2i\sigma_{12} = 4\frac{\partial^2 \Phi}{\partial z^2} = 2(\bar{z}\,\varphi''(z) + \psi'(z)) + \frac{E\alpha\sigma}{4\kappa} f'(z)\,\overline{h(z)}. \tag{23}$$

3. Solution for a thermoelectric plate weakened by an elliptic hole

3.1. *Boundary conditions.* We consider an infinite plane thermoelectric continuum containing an elliptic hole as shown in Figure 1 (left). The major and minor semiaxes of the elliptic hole are denoted by a and b, respectively. The infinite region outside the elliptic hole is referred to as the "matrix", which is subjected to prescribed remote electric current densities J_x^∞ and J_y^∞ as well as energy flux U_x^∞ and U_y^∞ at the far field. We assume that the boundary of the hole is impervious to both electrons and heat. Thus, the boundary conditions for the electric current and energy flux on the boundary of the hole can be expressed as

$$\int_P^Q J_r\,ds = 0, \tag{24}$$

$$\int_P^Q U_r\,ds = 0, \tag{25}$$

where J_r and U_r are the normal electric current density and energy flux, respectively, while P and Q are arbitrary points on the boundary of the hole. Since there is no applied loading on the boundary, both normal and shear stresses are zero, that is,

$$i\int_P^Q (X + iY)\,ds = 0, \tag{26}$$

where X and Y are the components of surface force on the boundary, respectively [Timoshenko and Goodier 1951].
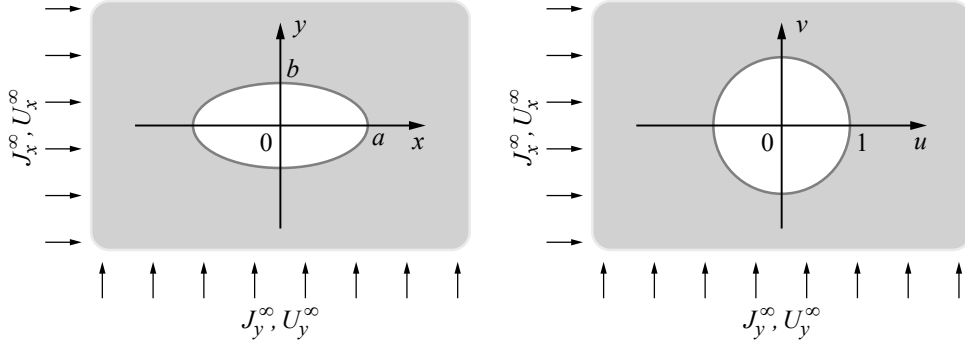
Figure 1. Left: elliptic hole embedded in an infinite thermoelectric plate. Right: the ω-plane after conformal mapping.

Our goal is to determine the temperature and thermal stress distributions around the hole. To this end, consider the conformal mapping

$$z = \omega(w) = R(w + m/w), \tag{27}$$

where $R = \frac{1}{2}(a+b)$, $m = (a-b)/(a+b)$, which maps the interior of the elliptic hole in the z-plane into the unit circle in the ω-plane where $w = u + iv$, as illustrated in Figure 1 (right).

3.2. *Electric and thermal fields.* Given the prescribed remote electric current density, the complex function $f(z)$ in the matrix can be expressed as

$$f(z) = A_1' z + f_0(z), \tag{28}$$

where $f_0(z)$ is an analytic function, and the coefficient A_1' can be determined by the value of the remote electric current density. The complex function $f(w)$ obtained from (28) via (27) can now be represented in the form

$$f(w) = A_1 w + \sum_{k=0}^{\infty} A_{-k} w^{-k}, \tag{29}$$

where $A_1 = -R(J_x^\infty - i J_y^\infty)/\sigma$. Substituting (7) into the boundary condition (24), we have

$$\int J_r \, ds = \int J_x \, dy - J_y \, dx = \tfrac{1}{2}\sigma i (f(w) - \overline{f(w)}) = 0. \tag{30}$$

Solving (30) using (29) yields

$$f(w) = A_1 w + A_{-1}/w, \tag{31}$$

where $A_{-1} = \bar{A}_1$. Similarly, $g(z)$ can be written as

$$g(z) = B_2' z^2 + B_1' z + g_0(z), \tag{32}$$

and the complex function $g(w)$ in the ω-plane can be represented by

$$g(w) = B_2 w^2 + B_1 w + \sum_{k=0}^{\infty} B_{-k} w^{-k}, \tag{33}$$

where $B_1 = -R(U_x^\infty - iU_y^\infty)/2\kappa$, $B_2 = -\sigma A_1^2/8\kappa$ according to the energy flux prescribed at infinity. Noting (15), the boundary condition (25) can be rewritten as

$$\int U_r\, ds = \int U_x\, dy - U_y\, dx = \tfrac{1}{8}\sigma i(f(w)^2 - \overline{f(w)^2}) + i\kappa(g(w) - \overline{g(w)}) = 0. \tag{34}$$

Comparing coefficients of like powers of w^k, $g(w)$ can be determined from (34) as

$$g[w] = B_2 w^2 + B_1 w + \frac{B_{-1}}{w} + \frac{B_{-2}}{w^2}, \tag{35}$$

where $B_{-1} = \bar{B}_1$, $B_{-2} = \bar{B}_2$. This set of equations solves completely the thermal-electric problems of an infinite thermoelectric continuum containing an elliptic hole leading to the complete determination of the field distributions in closed-form. In particular, the temperature and electric potential are determined as

$$T = -\frac{\sigma}{4\kappa}|A_1 w + A_{-1}/w|^2 + 2\,\mathrm{Re}\left[B_2 w^2 + B_1 w + \frac{B_{-1}}{w} + \frac{B_{-2}}{w^2}\right] + N, \tag{36}$$

$$\phi = \mathrm{Re}[A_1 w + A_{-1}/w] + \frac{\sigma S}{4\kappa}|A_1 w + A_{-1}/w|^2 - 2S\,\mathrm{Re}\left[B_2 w^2 + B_1 w + \frac{B_{-1}}{w} + \frac{B_{-2}}{w^2}\right] - SN, \tag{37}$$

and the electric current density, thermal flux and energy flux are given by

$$J_x - iJ_y = -\frac{\sigma(A_1 w^2 - A_{-1})}{R(w^2 - m)}, \tag{38}$$

$$Q_x - iQ_y = \frac{\sigma(A_1 w^2 - A_{-1})}{2R(w^2 - m)}$$
$$\times\left\{\left(\frac{\sigma S}{2\kappa}\left|A_1 w + \frac{A_{-1}}{w}\right|^2 + \bar{A}_1\bar{w} + \frac{\bar{A}_{-1}}{\bar{w}}\right) - 4S\,\mathrm{Re}\left[B_2 w^2 + B_1 w + \frac{B_{-1}}{w} + \frac{B_{-2}}{w^2}\right] - 2SN\right\}$$
$$- \frac{2\kappa(2B_2 w^4 + B_1 w^3 - B_{-1}w - 2B_{-2})}{Rw(w^2 - m)}, \tag{39}$$

$$U_x - iU_y = -\frac{\sigma(A_1 w^2 - A_{-1})(A_1 w^2 + A_{-1})}{2Rw(w^2 - m)} - \frac{2\kappa(2B_2 w^4 + B_1 w^3 - B_{-1}w - 2B_{-2})}{Rw(w^2 - m)}. \tag{40}$$

3.3. Stress distributions. It is assumed that the matrix is not constrained at infinity and can therefore expand freely there. Integrating $f(z)$ in (31), $h(z)$ is found from (20) to be

$$h(z) = R\left[\tfrac{1}{2}A_1 w^2 + \frac{mA_{-1}}{2w^2} + (A_{-1} - mA_1)\ln w\right]. \tag{41}$$

Noting the multivalued term appearing in $h(z)$, the functions $\varphi(z)$ and $\psi(z)$ in (22) and (23) can be expressed in the form

$$\varphi(z) = \varphi(w) = \eta_1 \ln w + \varphi_0(w), \tag{42}$$

$$\psi(z) = \psi(w) = \eta_2 \ln w + \psi_0(w). \tag{43}$$

According to (21), the boundary condition in (26) can be rewritten as

$$i \int_P^Q (X + iY) \, ds = \varphi(z) + z \overline{\varphi'(z)} + \overline{\psi(z)} + \frac{E\alpha\sigma}{8\kappa} h(z) \overline{f(z)} = 0. \tag{44}$$

Substituting (31), (41), (42), and (43) into (44), the unknown functions $\varphi(w)$ and $\psi(w)$ are found to be

$$\varphi[w] = -\frac{E\alpha\sigma \, R m \bar{A}_1}{16\kappa} \left(\frac{A_1}{w} + \frac{\bar{A}_1}{w^3} \right), \tag{45}$$

$$\psi[w] = \frac{E\alpha\sigma \, R}{8\kappa} (A_1 - m\bar{A}_1) \left(A_1 w + \frac{\bar{A}_1}{w} \right) \ln w - \frac{E\alpha\sigma \, R \bar{A}_1}{16\kappa} \left(\frac{A_1}{w} + \frac{\bar{A}_1}{w^3} \right)$$
$$- \frac{E\alpha\sigma \, m R \bar{A}_1 (1 + m w^2)}{16\kappa (w^2 - m)} \left(\frac{A_1}{w} + \frac{3\bar{A}_1}{w^3} \right). \tag{46}$$

The stress distributions in (22) and (23) can now be determined completely:

$$\sigma_{11} + \sigma_{22} = \frac{E\alpha\sigma m}{4\kappa} \mathrm{Re} \left[\frac{\bar{A}_1 (A_1 w^2 + 3\bar{A}_1)}{w^2 (w^2 - m)} \right] + \frac{E\alpha\sigma}{4\kappa} \left(A_1 w + \frac{\bar{A}_1}{w} \right) \left(\bar{A}_1 \bar{w} + \frac{A_1}{\bar{w}} \right), \tag{47}$$

$$\sigma_{22} - \sigma_{11} + 2i\sigma_{12}$$
$$= \frac{E\alpha\sigma m \bar{A}_1}{w^2 - m} \left[\frac{A_1 w^4 + 6\bar{A}_1 w^2 - 3m\bar{A}_1}{4\kappa w (w^2 - m)^2} \left(\bar{w} + \frac{m}{\bar{w}} \right) + \frac{A_1 w^2 + 3\bar{A}_1}{8\kappa w^2} \right]$$
$$+ \frac{E\alpha\sigma m \bar{A}_1}{8\kappa} \frac{A_1 (m w^6 + m^2 w^4 + 3 w^4 - m w^2) + 3\bar{A}_1 (3 m w^4 - m^2 w^2 + 5 w^2 - 3m)}{w^2 (w^2 - m)^3}$$
$$+ \frac{E\alpha\sigma}{4\kappa} \frac{A_1 w^2 - \bar{A}_1}{(w^2 - m)} \left[\tfrac{1}{2} \bar{A}_1 \bar{w}^2 + \frac{m A_1}{2\bar{w}^2} + (A_1 - m\bar{A}_1) \ln \bar{w} \right]$$
$$+ \frac{E\alpha\sigma (A_1 - m\bar{A}_1)[A_1 w^2 + \bar{A}_1 + (A_1 w^2 - \bar{A}_1) \ln w]}{4\kappa (w^2 - m)}. \tag{48}$$

Noting the expression for A_1, we see that the thermal stress is completely dependent on the applied electric current in the x and y directions, which makes it possible to suppress the thermal stress by simply adjusting the applied electric current itself.

4. Methods for suppressing thermal stress

4.1. *Suppressing thermal stress by adjusting the electric current.* In a thermoelectric material, the conversion efficiency H is the main parameter of interest. When the electric current and heat flux flow through a thermoelectric medium, the conversion efficiency can be calculated from the measured physical quantities. Here we select a finite square region of side L containing an elliptic hole (see Figure 2). Without loss of generality, we apply the electric current and energy flux in the y-direction, the conversion efficiency can then be derived as [Harman and Honig 1967]

$$H = \frac{\int_t \phi_2 J_{y2} \, dx - \int_s \phi_1 J_{y1} \, dx}{\int_s U_{y1} \, dx}, \tag{49}$$
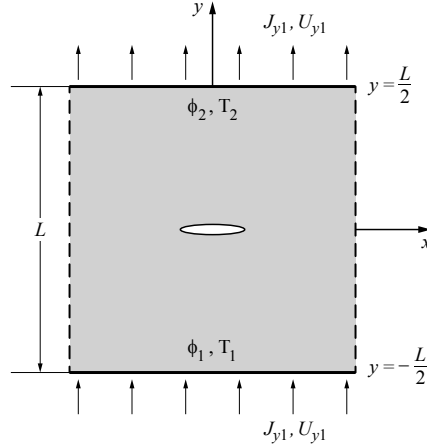
Figure 2. Finite thermoelectric model subjected electric current and energy flux in y-direction.

where s and t denote the entire surface corresponding to $y = -\frac{1}{2}L$ and $y = \frac{1}{2}L$, respectively, while the subscripts 1 and 2 denote the corresponding quantities on s and t, respectively. The conversion efficiency can be optimized with respect to electric current density for given temperatures. For example, if the temperatures on s and t are T_1 and T_2, respectively, the optimal electric current density for this system is [Yang et al. 2013]

$$J_{\text{opt}} = \frac{\sqrt{2\kappa}\,\sigma\,S(T_1 - T_2)}{\left[\sqrt{2\kappa} + \sqrt{2\kappa\sigma S^2(T_1 + T_2)}\right]L}. \tag{50}$$

In other words, the highest conversion efficiency requires the accompaniment of optimal electric current density J_{opt}.

On the other hand, the components of thermal stress in polar coordinates are given by the coordinate transformation formulas [Muskhelishvili 1975]:

$$\sigma_{\rho\rho} + \sigma_{\theta\theta} = \sigma_{11} + \sigma_{22}, \tag{51}$$

$$\sigma_{\theta\theta} - \sigma_{\rho\rho} + 2i\sigma_{\rho\theta} = \frac{w^2\omega'(w)}{\rho^2\,\overline{\omega'(w)}}(\sigma_{22} - \sigma_{11} + 2i\sigma_{12}), \tag{52}$$

where $\sigma_{\rho\rho}$, $\sigma_{\theta\theta}$, and $\sigma_{\rho\theta}$ are the corresponding normal and shear components in polar coordinates. Since both $\sigma_{\rho\rho}$ and $\sigma_{\rho\theta}$ are zero on the boundary of the elliptic hole, we focus only on the component $\sigma_{\theta\theta}$, which can be derived from (51) and (52) as

$$\sigma_{\theta\theta} = \frac{1}{2}\left[\sigma_{11} + \sigma_{22} + \frac{w^2\omega'(w)}{\rho^2\,\overline{\omega'(w)}}(\sigma_{22} - \sigma_{11} + 2i\sigma_{12})\right]. \tag{53}$$

The expanded form of (53) shows that $\sigma_{\theta\theta}$ is a monotonically increasing quadratic function of electric current density. Consequently, both the conversion efficiency and thermal stress depend on the electric current which is therefore confined to a particular range in order to achieve higher conversion efficiency and lower thermal stress.

sample	σ (Sm^{-1})	ε (VK^{-1})	κ (Wm^{-1}K^{-1})	E (GPa)	α (K^{-1})	μ
Bi$_2$Te$_3$	100000	0.00022	1.1	63.00	1.3×10^{-5}	0.23

Table 1. Material parameters of thermoelectric sample [Wu et al. 2014].

4.2. *Suppressing thermal stress through vertical electric current.* Back to the infinite thermoelectric plate: although the thermal stress can be mitigated by adjusting the electric current, it has a fairly limited role. In order to avoid the influence of electric current on the conversion efficiency, the vertical electric current can be applied to suppress thermal stress around an elliptic hole. For example, consider the case when $\sigma_{\theta\theta}$ has the value

$$\sigma_{\theta\theta} = -\frac{E\alpha m R^2 J_y^{\infty 2}}{2\sigma\kappa(1-m)}, \tag{54}$$

at the point $z = a$ when the material is loaded with a remote electric current in the y-direction. With the additional electric current in the x-direction, $\sigma_{\theta\theta}$ can be shown to be

$$\sigma_{\theta\theta} = \frac{E\alpha R^2 (2J_x^{\infty 2} - m J_y^{\infty 2})}{2\sigma\kappa(1-m)}. \tag{55}$$

It can be seen that $\sigma_{\theta\theta}$ can be suppressed or totally eliminated by additional electric current at the point $z = a$. More importantly, if the elliptic hole degenerates into a crack, the thermal stress will have a singularity at the crack tip which gives rise to the stress intensity factor corresponding to $\sigma_{\theta\theta}$:

$$K_{\theta\theta} = \lim_{z \to \alpha} \sqrt{2\pi(z-a)}\,\sigma_{\theta\theta} = \frac{E\alpha\sqrt{\pi a^5}}{32\sigma\kappa}(2J_x^{\infty 2} - J_y^{\infty 2}). \tag{56}$$

The thermal stress singularity at the crack tip can be eliminated when subjected to the electric current density $J_x^{\infty} = J_y^{\infty}/\sqrt{2}$.

5. Results and discussion

Numerical analyses have been undertaken to further illustrate the effects of electric current on thermal stresses with the material parameters of the corresponding samples listed in Table 1. We first consider the model described in Figure 2. The length of the semimajor axis of the elliptic hole is 0.01 m, while the length and width of the selected sample region are relatively much larger than the size of the elliptic hole. The temperatures on s and t are $T_1 = 800$ K and $T_2 = 300$ K, respectively. Thus, the optimal electric current density can be approximately determined as $J_{\text{opt}} = 1.93 \times 10^5$ A/m^2, as the elliptic hole has little influence on the conversion optimization efficiency of this system due to its relatively small size.

Under these conditions, the stress component $\sigma_{\theta\theta}$ on the boundary of the elliptic hole is shown in Figure 3 for the difference b, where θ is the angle measured up from the x-axis. It can be seen that the maximum value of positive stress decreases while the maximum negative stress increases as b decreases. Additionally, the stress distribution on the boundary is symmetric around the origin, thereby reducing the amount of computation required in what follows.

Due to the symmetry of the stress field on the boundary, we select two points, $z = a$ and $z = ib$, as samples to analyze the influence of the electric current on the conversion efficiency and corresponding stress
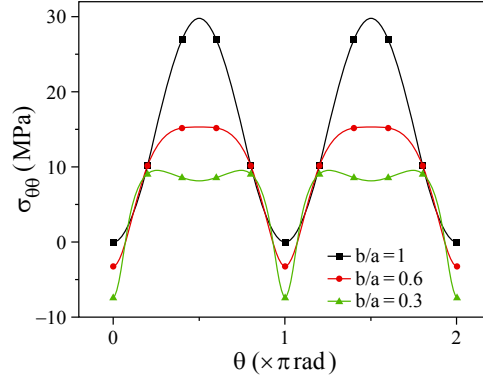
**Figure 3.** Thermal stress $\sigma_{\theta\theta}$ on the boundary of elliptic hole.
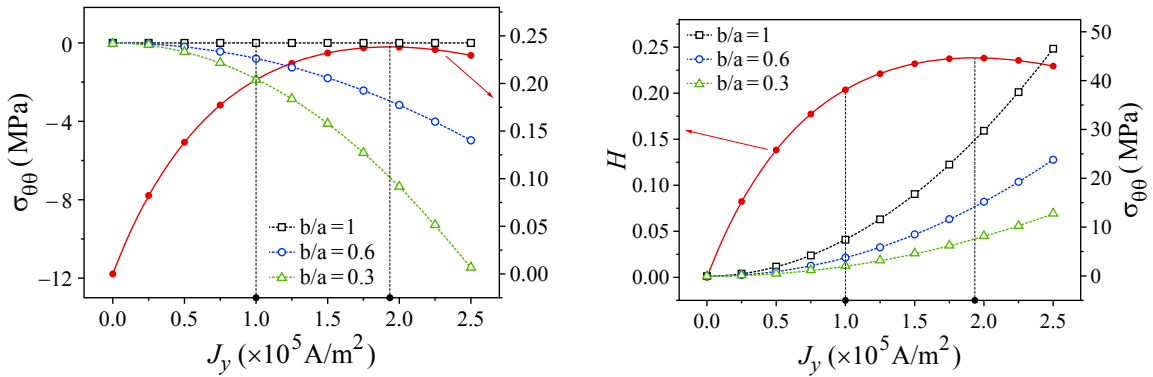
Figure 4. Conversion efficiency versus electric current density: $\sigma_{\theta\theta}$ at the point $z = a$ (left) and $\sigma_{\theta\theta}$ at the point $z = ib$ (right).

distributions. As we can see from Figure 4, the optimal electric current leads to maximum conversion efficiency but also corresponds to higher stresses. Fortunately, the change in the stress distributions is sharper than the conversion efficiency around the optimal electric current. For example, if we decrease the electric current density from J_{opt} to 10^5 A/m^2, the conversion efficiency will decrease by 14.5%, while all of the stress distributions at the two selected points will decrease by 73.2%. The huge difference between conversion efficiency and thermal stress makes it possible to minimize thermal stress by adjusting the electric current.

Apart from adjusting the electric current in the y-direction, the additional electric current in the x-direction also has the potential to suppress thermal stress. In fact, it has the added advantage of having no effect on the conversion efficiency in the vertical direction and totally neutralizing the thermal stress at a particular point. From Figure 5 we see that the stresses at the point $z = a$ decrease with the increase of J_x^∞ for different values of the semiminor axis of the elliptic hole while maintaining the semimajor axis at $a = 0.01$ m and, in fact, both can be entirely neutralized by electric current.

As noted in Section 4.2, crack tips correspond to singular points of thermal stress in a thermoelectric material but the singularity can be eliminated by additional electric current in the vertical direction. In order to further investigate this phenomenon, we analyze the stress $\sigma_{\theta\theta}$ on the upper boundary of the
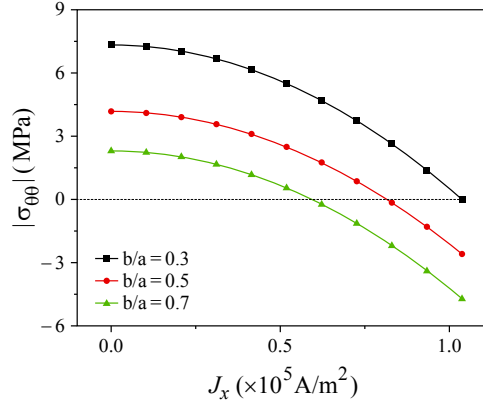
Figure 5. Stress field at the point $z = a$ versus electric current density J_x^∞.
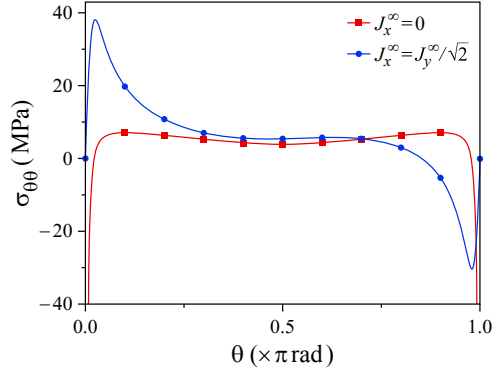
Figure 6. Stress field on the upper boundary of elliptic hole while $b \ll a$.

elliptic hole for the case $b \ll a$ (see Figure 6). The results show that the values of $\sigma_{\theta\theta}$ tend towards negative infinity at the points $z = a$ and $z = -a$ while $J_x^\infty = 0$, and $\sigma_{\theta\theta}$ is totally neutralized by the additional electric current density $J_x^\infty = J_y^\infty/\sqrt{2}$ despite the fact that it also leads to a considerable positive stress.

6. Conclusions

In contrast to traditional heat conduction in common materials, the coupled transport of heat flux and electric current allows for the existence of thermal stress in a simply connected thermoelectric medium which then affects the reliability of thermoelectric devices. Consequently, it becomes important to develop methods for the suppression of thermal stresses in thermoelectric media. In this paper, we have addressed this question in the case of a thermoelectric plate weakened by an elliptic hole. The results show that the thermal stress on the boundary of an elliptic hole can be suppressed by both adjusting the value of the electric current and adding additional vertical electric current. Each method is effective in improving reliability and prolonging the life of thermoelectric devices.

Acknowledgements

References

[Callen 1960] H. B. Callen, *Thermodynamics: an introduction to the physical theories of equilibrium thermostatics and irreversible thermodynamics*, Wiley, New York, 1960.

[Choi et al. 2011] H.-S. Choi, W.-S. Seo, and D.-K. Choi, "Prediction of reliability on thermoelectric module through accelerated life test and Physics-of-failure", *Electron. Mater. Lett.* **7** (2011), 271.

[Göktun 36] S. Göktun, "Design considerations for a thermoelectric refrigerator", *Energy Convers. Manage.* **36**:12 (36), 1197–1200.

[Harman and Honig 1967] T. C. Harman and J. M. Honig, *Thermoelectric and thermomagnetic effects and applications*, McGraw Hill, New York, 1967.

[Kim and Chun 2007] T.-S. Kim and B.-S. Chun, "Microstructure and thermoelectric properties of n-and p-type Bi_2Te_3 alloys by rapid solidification processes", *J. Alloys Compd.* **437**:1-2 (2007), 225–230.

[Kim et al. 2006] W. Kim, J. Zide, A. Gossard, D. Klenov, S. Stemmer, A. Shakouri, and A. Majumdar, "Thermal conductivity reduction and thermoelectric figure of merit increase by embedding nanoparticles in crystalline semiconductors", *Phys. Rev. Lett.* **96**:4 (2006), 045901.

[Liu 2012] L. Liu, "A continuum theory of thermoelectric bodies and effective properties of thermoelectric composites", *Int. J. Eng. Sci.* **55** (2012), 35–53.

[Milton 2002] G. W. Milton, *The theory of composites*, Cambridge University Press, 2002.

[Muskhelishvili 1975] N. I. Muskhelishvili, *Some basic problems of mathematical theory of elasticity*, Noordhoff, Leyden, 1975.

[Okamura et al. 2010] C. Okamura, T. Ueda, and K. Hasezaki, "Preparation of single-phase ZnSb thermoelectric materials using a mechanical grinding process", *Mater. Trans.* **51**:5 (2010), 860–862.

[Omer and Infield 1998] S. A. Omer and D. G. Infield, "Design optimization of thermoelectric devices for solar power generation", *Sol. Energy Mater. Sol. Cells* **53**:1 (1998), 67–82.

[Parkus 1968] H. Parkus, *Thermoelasticity*, Blaisdell Pub. Co., Waltham, MA, 1968.

[Pei et al. 2011] Y. Pei, A. LaLonde, S. Iwanaga, and G. J. Snyder, "High thermoelectric figure of merit in heavy hole dominated PbTe", *Energy Environ. Sci.* **4**:6 (2011), 2085–2089.

[Riffat and Ma 2003] S. B. Riffat and X. Ma, "Thermoelectrics: a review of present and potential applications", *Appl. Therm. Eng.* **23**:8 (2003), 913–935.

[Song et al. 2015] H.-P. Song, C.-F. Gao, and J. Li, "Two-dimensional problem of a crack in thermoelectric materials", *J. Therm. Stress* **38**:3 (2015), 325–337.

[Song et al. 2017] K. Song, H. P. Song, and C. F. Gao, "Macro-performance of multilayered thermoelectric medium", *Chinese Phys. B* **26** (2017), 127307.

[Timoshenko and Goodier 1951] S. P. Timoshenko and J. N. Goodier, *Theory of elasticity*, McGraw Hill, New York, 1951.

[Tritt and Subramanian 2006] T. M. Tritt and M. A. Subramanian, "Thermoelectric materials, phenomena, and applications: a bird's eye view", *MRS Bulletin* **31**:3 (2006), 188–198.

[Wu et al. 2014] Y. Wu, T. Ming, X. Li, T. Pan, K. Peng, and X. Luo, "Numerical simulations on the temperature gradient and thermal stress of a thermoelectric power generator", *Energy Convers. Manage.* **88** (2014), 915–927.

[Xuan 2002] X. C. Xuan, "Optimum design of a thermoelectric device", *Semicond. Sci. Technol.* **17**:2 (2002), 114.

[Yang et al. 2012] Y. Yang, S. H. Xie, F. Y. Ma, and J. Y. Li, "On the effective thermoelectric properties of layered heterogeneous medium", *J. Appl. Phys.* **111** (2012), 013510.

[Yang et al. 2013] Y. Yang, F. Y. Ma, C. H. Lei, Y. Y. Liu, and J. Y. Li, "Is thermoelectric conversion efficiency of a composite bounded by its constituents?", *Appl. Phys. Lett.* **102**:5 (2013), 053905.

[Yu et al. 2012] R. Yu, P. Zhai, G. Li, and L. Liu, "Molecular dynamics simulation of the mechanical properties of single-crystal bulk Mg$_2$Si", *J. Electron. Mater.* **41**:6 (2012), 1465–1469.

[Zhao and Tan 2014] D. Zhao and G. Tan, "A review of thermoelectric cooling: materials, modeling and applications", *Appl. Therm. Eng.* **66**:1-2 (2014), 15–24.

KUN SONG: ksong3@ualberta.ca
Institute of Aerospace, Nanjing University of Aeronautics and Astronautics, Nanjing, China

HAO-PENG SONG: hpsong@nuaa.edu.cn
Department of Software Engineering, Nanjing University of Aeronautics and Astronautics, Nanjing, China

PETER SCHIAVONE: pschiavo@ualberta.ca
Department of Mechanical Engineering, University of Alberta, Edmonton, AB, Canada

CUN-FA GAO: cfgao@nuaa.edu.cn
State Key Laboratory of Mechanics and Control of Mechanical Structures, Nanjing University of Aeronautics and Astronautics, Nanjing, China

SUBMISSION GUIDELINES

ORIGINALITY

Authors may submit manuscripts in PDF format online at the Submissions page. Submission of a manuscript acknowledges that the manuscript is original and has neither previously, nor simultaneously, in whole or in part, been submitted elsewhere. Information regarding the preparation of manuscripts is provided below. Correspondence by email is requested for convenience and speed. For further information, write to contact@msp.org.

LANGUAGE

Manuscripts must be in English. A brief abstract of about 150 words or less must be included. The abstract should be self-contained and not make any reference to the bibliography. Also required are keywords and subject classification for the article, and, for each author, postal address, affiliation (if appropriate), and email address if available. A home-page URL is optional.

FORMAT

Authors can use their preferred manuscript-preparation software, including for example Microsoft Word or any variant of TeX. The journal itself is produced in LaTeX, so accepted articles prepared using other software will be converted to LaTeX at production time. Authors wishing to prepare their document in LaTeX can follow the example file at www.jomms.net (but the use of other class files is acceptable). At submission time only a PDF file is required. After acceptance, authors must submit all source material (see especially Figures below).

REFERENCES

Bibliographical references should be complete, including article titles and page ranges. All references in the bibliography should be cited in the text. The use of BibTeX is preferred but not required. Tags will be converted to the house format (see a current issue for examples); however, for submission you may use the format of your choice. Links will be provided to all literature with known web locations; authors can supply their own links in addition to those provided by the editorial process.

FIGURES

Figures must be of publication quality. After acceptance, you will need to submit the original source files in vector format for all diagrams and graphs in your manuscript: vector EPS or vector PDF files are the most useful. (EPS stands for Encapsulated PostScript.)

Most drawing and graphing packages—Mathematica, Adobe Illustrator, Corel Draw, MATLAB, etc.—allow the user to save files in one of these formats. Make sure that what you're saving is vector graphics and not a bitmap. If you need help, please write to graphics@msp.org with as many details as you can about how your graphics were generated.

Please also include the original data for any plots. This is particularly important if you are unable to save Excel-generated plots in vector format. Saving them as bitmaps is not useful; please send the Excel (.xls) spreadsheets instead. Bundle your figure files into a single archive (using zip, tar, rar or other format of your choice) and upload on the link you been given at acceptance time.

Each figure should be captioned and numbered so that it can float. Small figures occupying no more than three lines of vertical space can be kept in the text ("the curve looks like this:"). It is acceptable to submit a manuscript with all figures at the end, if their placement is specified in the text by means of comments such as "Place Figure 1 here". The same considerations apply to tables.

WHITE SPACE

Forced line breaks or page breaks should not be inserted in the document. There is no point in your trying to optimize line and page breaks in the original manuscript. The manuscript will be reformatted to use the journal's preferred fonts and layout.

PROOFS

Page proofs will be made available to authors (or to the designated corresponding author) at a Web site in PDF format. Failure to acknowledge the receipt of proofs or to return corrections within the requested deadline may cause publication to be postponed.

Journal of Mechanics of Materials and Structures